

UNIVERSITY OF CALIFORNIA

Los Angeles

Computational Fluid Dynamics and Machine Learning Modeling,
Operation and Control of Steam Methane Reforming Reactors and Furnaces

A dissertation submitted in partial satisfaction of the
requirements for the degree Doctor of Philosophy
in Chemical Engineering

by

Anh Tuan Tran

2018

ABSTRACT OF THE DISSERTATION

Computational Fluid Dynamics and Machine Learning Modeling,
Operation and Control of Steam Methane Reforming Reactors and Furnaces

by

Anh Tuan Tran

Doctor of Philosophy in Chemical Engineering

University of California, Los Angeles, 2018

Professor Panagiotis D. Christofides, Chair

Hydrogen is proposed by many to be the fuel of the future as it is the key ingredient in a transition from a fossil fuel-based economy toward a zero carbon emission and sustainable energy economy. Hydrogen can serve as an efficient energy carrier for hydrogen-based technologies (e.g., fuel cells and hydrogen internal combustion engine) and lead to substantial reduction of greenhouse gas emissions and great environmental benefits. Hydrogen can be produced by a variety of technologies (e.g., steam methane reforming (SMR), coal gasification, biomass gasification, electrolysis, partial oxidation, solar thermal cracking) from fossil (e.g., natural gas), non-fossil (e.g., biogas) and non-carbon (e.g., water) sources, which highlights the great potential and flexibility of a hydrogen-based economy. Additionally, hydrogen is a key feedstock for the petroleum refining and fine chemical manufacturing industries. With current state-of-the-art technology, hydrogen is produced almost exclusively from fossil fuels by SMR. At SMR-based hydrogen plants, the reformers are the most expensive equipment in terms of the maintenance and operating costs, and thus, even a small improvement in the reformer thermal efficiency to lower operating costs of the reformer without compromising the expected service life of the reformer is expected to allow the plants to achieve a significant profit.

Motivated by these considerations, a systematic framework for creating and simulating a computational fluid dynamics (CFD) model for an industrial-scale reformer at an SMR-based hydrogen plant and, subsequently, a framework for designing and evaluating a real-time furnace balancing scheme are developed in this dissertation. Specifically, a CFD model for an industrial-scale reformer is created in ANSYS Fluent, which is used to improve our understanding of the physiochemical processes in the tube side and the furnace side of the reformer as well as their thermal interactions during the catalytic conversion of methane. Then, a furnace balancing scheme is developed to optimize the reformer input at the nominal total furnace-side feed (FSF) flow rate that minimizes the inherent variability in the outer tube wall temperature (OTWT) distributions along the reforming tube length. Subsequently, a statistical-based model identification is developed to create a computationally efficient and robust model for the OTWT distribution as a function of the FSF distribution, total FSF flow rate and interactions among neighboring reforming tubes so that the optimized reformer input can be identified in real-time. Finally, a real-time furnace-balancing scheme is developed to optimize the reformer input such that the reformer thermal efficiency is maximized without compromising the expected service life of the reformer.

The dissertation of Anh Tuan Tran is approved.

Dante A. Simonetti

James F. Davis

Xiaolin Zhong

Panagiotis D. Christofides, Committee Chair

University of California, Los Angeles

2018

Contents

List of Figures	vii
List of Tables	xv
1 Introduction	1
1.1 Hydrogen Economy	1
1.2 Dissertation Objectives and Structure	6
2 CFD Modeling of a Reformer	10
2.1 Introduction	10
2.2 Reformer geometry	12
2.3 Reformer mesh	14
2.4 Furnace chamber modeling	20
2.4.1 Combustion kinetic model and turbulence-chemistry model	20
2.4.2 Radiative heat transfer modeling	23
2.5 Reforming tube modeling	30
2.5.1 Reforming Reaction Kinetic Model	30
2.5.2 Porous Zone Design	33
2.6 Equation of state and turbulence-chemistry interaction model	36
2.7 Governing equations of reformer	41
2.7.1 Furnace Chamber	42
2.7.2 Reforming Tube	46
2.8 Process simulation	48
2.9 Simulation results	50
2.10 Discussion	51
2.11 Conclusion	69
3 Temperature Balancing in Reformer	74
3.1 Introduction	74
3.2 Furnace-balancing scheme	77
3.2.1 Data generation	79
3.2.2 Model Identification	82
3.2.3 Valves and flow rate relation	88
3.2.4 Model-based furnace-balancing optimizer	92
3.3 Simulation Results	98

3.3.1	Case study A	99
3.3.2	Case study B	101
3.4	Conclusion	115
4	Statistical-based Model Identification	116
4.1	Introduction	116
4.2	Reformer CFD database	122
4.3	Overview of the prediction and correction model identification scheme	124
4.4	Prediction models	127
4.4.1	Bayesian variable selection	133
4.4.2	Bayesian model averaging	138
4.4.3	Sparse nonlinear regression	139
4.5	Correction models	148
4.6	Combined model uniting prediction and correction models	160
4.7	Results	162
4.8	Conclusion	178
5	Advance Temperature Balancing in Reformer	180
5.1	Introduction	180
5.2	Overview of the furnace-balancing scheme	183
5.3	Reformer CFD model	185
5.4	Statistical-based model identification	190
5.5	Valve-to-flow-rate converter	195
5.6	Balancing Procedure	198
5.6.1	Furnace-balancing optimizer	201
5.7	Parallel Processing	208
5.8	Simulation results	211
5.8.1	Validation of data-driven model for the OTWT distribution	211
5.8.2	Dynamic response of the reformer	214
5.8.3	Validation of the furnace-balancing scheme	223
5.9	Conclusion	236
6	Conclusions	238
	Bibliography	243

List of Figures

2.1	The isometric view of an industrial-scale, top-fired, co-current reformer with 336 reforming tubes, which are symbolized by 336 smaller circles, 96 burners, which are denoted by 96 larger circles, and 8 flue gas tunnels, which are represented by 8 rectangular intrusions. The outer-lane burners are burners on the right and left boundaries of the figure, while the inner-lane burners are slightly larger than the outer-lane burners in the figure.	13
2.2	Isometric view of the hexahedral structured mesh of the outer-lane burner (a), inner-lane burner (b) and reforming tube (c). This figure demonstrates that the meshes of both the inner-lane and outer-lane burners, as well as the mesh of the reforming tubes, created by the O-grid Block function of ANSYS ICEM have the exact geometries of the corresponding components. In Fig. 2.2(c), the radial direction of the reforming tube is scaled up by 20 times for display purposes.	17
2.3	A sample of the top view of the hexahedral structured mesh of the reformer, where a row of reforming tubes is adjacent to two inner-lane burners. In Fig. 2.3, the reforming tube inlets and burner inlets are assigned with different color for display purposes.	18
2.4	A sample of the vertical cross section of the hexahedral structured mesh of the reformer.	19
2.5	Step-by-step converging strategy designed to resolve the initial instability issue of the reformer CFD simulation, accelerate the rate of convergence and minimize the required computing time to obtain the converged solution of the reformer CFD model in which the models with \checkmark are activated, and those with \mathcal{X} are disabled.	51
2.6	The frontal and lateral cross-sectional plane of the combustion chamber.	52
2.7	Lateral (left) and frontal (right) furnace-side temperature contour maps predicted by the reformer CFD simulation in which the parameters of the tube-side feed, furnace-side feed and combustion chamber refractory walls are consistent with typical plant data [35].	53
2.8	Lateral (left) and frontal (right) contour maps of energy released by the furnace-side oxidation predicted by the reformer CFD simulation in which the parameters of the tube-side feed, furnace-side feed and combustion chamber refractory walls are consistent with typical plant data [35].	54
2.9	Lateral (left) and frontal (right) contour maps of the furnace-side velocity magnitude predicted by the reformer CFD simulation in which the parameters of the tube-side feed, furnace-side feed and combustion chamber refractory walls are consistent with typical plant data [35].	55

2.10	Lateral (left) and frontal (right) methane mole fraction contour maps inside the combustion chamber predicted by the reformer CFD simulation in which the parameters of the tube-side feed, furnace-side feed and combustion chamber refractory walls are consistent with typical plant data [35].	56
2.11	Lateral (left) and frontal (right) hydrogen mole fraction contour maps inside the combustion chamber predicted by the reformer CFD simulation in which the parameters of the tube-side feed, furnace-side feed and combustion chamber refractory walls are consistent with typical plant data [35].	57
2.12	Lateral (left) and frontal (right) carbon monoxide mole fraction contour maps inside the combustion chamber predicted by the reformer CFD simulation in which the parameters of the tube-side feed, furnace-side feed and combustion chamber refractory walls are consistent with typical plant data [35].	58
2.13	Lateral (left) and frontal (right) oxygen mole fraction contour maps inside the combustion chamber predicted by the reformer CFD simulation in which the parameters of the tube-side feed, furnace-side feed and combustion chamber refractory walls are consistent with typical plant data [35].	59
2.14	Tube-side pressure contour map predicted by the reformer CFD simulation in which the parameters of the tube-side feed, furnace-side feed and combustion chamber refractory walls are consistent with typical plant data [35].	60
2.15	Radial-weighted average tube-side compositions predicted by the reformer CFD simulation in which the parameters of the tube-side feed, furnace-side feed and combustion chamber refractory walls are consistent with typical plant data [35].	61
2.16	Average temperature profiles of the furnace-side flow (solid line), outer reforming tube wall (dashed line), inner reforming tube wall (dash-dotted line) and tube-side flow (dotted line) predicted by the reformer CFD simulation in which the parameters of the tube-side feed, furnace-side feed and combustion chamber refractory walls are consistent with typical plant data [35].	62
2.17	Radial-weighted average tube-side compositions along the reforming tubes produced by the reformer CFD model (black) versus those derived from typical plant data of SMR (red) [35].	65
2.18	Average temperature profiles of the furnace-side flow and outer reforming tube wall produced by the reformer CFD model (black) versus those derived from typical plant data of SMR (red) [13].	65
2.19	Description of the layout of the OTWT distribution, in which each grid contains an average OTWT of the corresponding reforming tube recorded by a system of IR cameras situated around the reformer.	67
2.20	Distribution of the percent difference in the OTWT between the reformer CFD data and the plant data provided by the third party. The percent difference of each reforming tube is computed by the ratio of the deviation of the CFD data from the corresponding plant data to the corresponding plant data.	68
3.1	Flowchart of the furnace-balancing scheme.	78

3.2	The isometric view of an industrial-scale, top-fired, co-current reformer with 336 reforming tubes, which are represented by 336 slender cylinders, 96 burners, which are represented by 96 frustum cones, and 8 flue-gas tunnels, which are represented by 8 rectangular intrusions.	83
3.3	The velocity vector field of the furnace-side flow pattern in the vicinity of the 4 th burner row in the reformer is constructed from the reformer CFD data reported in Chapter 2. The outlets of the reformer are situated at the bottom right corner and are placed in the direction of the velocity vectors inside the flue-gas tunnels.	88
3.4	The temperature contour map of the 4 th flue-gas tunnel, which is situated directly under the 4 th burner row in the reformer, is shown. This contour map is created from the reformer CFD data in Chapter 2. In Fig. 3.4, the outlets of the reformer are situated at the bottom right corner.	89
3.5	A representation of a burner heating zone which is created by the highlighted burner in red. The burner heating zones are displayed by a blue cylindrical volume (where the reforming tubes are heated via thermal radiation from the furnace-side flow) and a green rectangular volume (where the reforming tubes are heated via thermal radiation from the neighboring flue-gas tunnels). It is assumed that only the reforming tubes located within the burner heating zones have the outer wall temperature values dependent on the FSF flow rate of the burner.	90
3.6	Evolution of the maximum, average and minimum temperature values of the OTWT distribution at a distance 6.5 m away from the reforming tube inlets during the first 6 iterations of the furnace-balancing scheme, which are generated by the reformer CFD model (black symbols) and by the data-driven model (red symbols).	103
3.7	Evolution of the standard deviation of the OTWT distribution at a distance 6.5 m away from the reforming tube inlets during the first 6 iterations of the furnace-balancing scheme, which are obtained from the reformer CFD model. The percent reduction in the magnitude of the standard deviation of the <i>i</i> th iteration with respect to the 0 th iteration (i.e., $\frac{\sigma_i - \sigma_0}{\sigma_0}$) in the first 6 iterations is also shown.	104
3.8	Evolution of the OTWT distribution at a distance 6.5 m away from the reforming tube inlets during the first 6 iterations of the furnace-balancing scheme, which are obtained from the reformer CFD model, is displayed by comparing the OTWT distributions in the 0 th (a), 2 nd (b), 4 th (c) and 6 th (d) iterations. In Fig. 3.8, the top row of each subfigure corresponds to the reforming tubes that are the closest to the reformer outlets, and the bottom row of each subfigure corresponds to the reforming tubes that are the furthest away from the reformer outlets.	105
3.9	Evolution of the overall maximum outer wall temperature along the reforming tube length among 336 reforming tubes in the reformer during the first 6 iterations of the furnace-balancing scheme, which are obtained from the reformer CFD model.	106

3.10	Comparison between the OTWT distributions at a distance 6.5 m away from the reforming tube inlets generated from the 7 th iteration when the FSF distribution is altered by the single-valve disturbance (a), and from the 8 th iteration when the FSF distribution is reoptimized to counter the impact of the single-valve disturbance (b). In Fig. 3.10, the top row of each subfigure corresponds to the reforming tubes that are the closet to the reformer outlets, and the bottom row of each subfigure corresponds to the reforming tubes that are the furthest away from the reformer outlets.	111
3.11	Comparison between the OTWT distributions at a distance 6.5 m away from the reforming tube inlets generated from the 9 th iteration when the FSF distribution is altered by the three-valve disturbance (a), and from the 10 th iteration when the FSF distribution is reoptimized to counter the impact of the three-valve disturbance (b). In Fig. 3.11, the top row of each subfigure corresponds to the reforming tubes that are the closet to the reformer outlets, and the bottom row of each subfigure corresponds to the reforming tubes that are the furthest away from the reformer outlets.	113
4.1	The isometric view of an industrial-scale, top-fired, co-current reformer. The right and back refractory walls with respect to the flue gas tunnel exits in Fig. 5.2 are removed to expose the interior of the reformer, which consists of 336 reforming tubes, which are represented by 336 cylinders, 96 burners, which are represented by 96 frustum cones, and 8 flue-gas tunnels, which are represented by 8 rectangular intrusions.	123
4.2	Flowchart of the regressor collection layer in the prediction step.	144
4.3	Flowchart of the regressor classification layer in the prediction step.	145
4.4	A virtual reformer geometry that is created based on the information generated by the location identifier in the regressor collection layer and consists of the <i>i</i> th reforming tube represented by a cylindrical tube and 96 burners represented by the frustum cones.	146
4.5	The first stage of the multistage affecting zone that is created based on R_{iZ}^1 and the virtual reformer geometry in the first iteration of the prediction step. In Fig. 4.5, the checked predictors in S_{iC}^1 are represented by the four shaded frustum cones and can be visually identified.	146
4.6	The first stage of the multistage affecting zone that is created based on R_{iZ}^j and the virtual reformer geometry in the <i>j</i> th iteration of the prediction step.	147
4.7	The first stage of the multistage affecting zone that is created based on R_{iZ}^{j+1} , R_{iZ}^j and the virtual reformer geometry in the (<i>j</i> + 1)th iteration of the prediction step.	147
4.8	The scatter plot of OTWTs of all reforming tubes in six training data sets versus the corresponding distance to the 77th reforming tube, which is referred to as the 77th lag. It is noted that not all reformer CFD data sets in the training data are shown in Fig. 4.8 to avoid cluttering.	154
4.9	The isometric view of the ordinary Kriging neighborhood of the <i>i</i> th reforming tube that is denoted as S_i^K and is defined as an 8 m by 8 m region centered at the <i>i</i> th tube, inside which the underlying process that gives rise to the variations in the OTWT distribution is assumed to be intrinsically stationary.	155

4.10	Omnidirectional sample semivariograms for \mathbf{S}_{77}^K computed by the classical estimator as shown in Eq. 4.22 using the training data. It is noted that not all results generated using reformer CFD data sets in the training data are displayed in Fig. 4.10 to avoid cluttering.	156
4.11	Omnidirectional average sample semivariograms for \mathbf{S}_{77}^K computed by Eqs. 4.22 and 4.23 using information of all reforming tube pairs in \mathbf{S}_{77}^K from the training data.	157
4.12	East-West anisotropic average sample semivariograms for \mathbf{S}_{77}^K computed by Eqs. 4.22 and 4.23 using information of the East-West pairs in \mathbf{S}_{77}^K from the training data. . .	158
4.13	North-South anisotropic average sample semivariograms for \mathbf{S}_{77}^K computed by Eqs. 4.22 and 4.23 using information of the North-South pairs in \mathbf{S}_{77}^K from the training data. .	159
4.14	Summary of LOO cross validation for selecting the optimal value of λ_{77} from \mathbf{S}_λ in which the mean squared prediction errors are denoted by the empty red circles and the mean squared fitting errors are denoted by the filled black squares.	166
4.15	Comparison of the 77th OTWT between reformer CFD data from the training data and BMA predicted estimates generated from the prediction model for the 77th reforming tube.	167
4.16	Residuals between reformer CFD data from the training data and BMA predicted estimates generated from the prediction model for the 77th reforming tube.	168
4.18	A plot of the mean squared prediction error associated with each of the four theoretical semivariogram models considered in the LOO cross validation to select the best theoretical semivariogram to model the spatial correlation among reforming tubes in the \mathbf{S}_{77}^K . The values on the horizontal axis, i.e., 0, 1, 2, and 3, correspond to the linear omnidirectional, linear anisotropic, exponential omnidirectional, and exponential anisotropic theoretical semivariogram models, respectively. Fig. 4.18 indicates that the linear omnidirectional model has the least mean squared prediction error and is considered the best model.	168
4.17	Reformer CFD data from the training data versus BMA predicted estimates generated from the prediction model for the 77th reforming tube scatter plots.	169
4.19	Comparison of the 77th OTWT between reformer CFD data from the training data and corrected estimates generated from the correction model for the 77th reforming tube.	169
4.20	Residuals between reformer CFD data from the training data and corrected estimates generated from the correction model of the 77th reforming tube.	170
4.21	Reformer CFD data from the training data versus corrected estimates generated from the correction model for the 77th reforming tube scatter plots.	170
4.22	Summary of LOO cross validation for selecting the optimal value of w^P from \mathbf{S}_w in which the mean squared prediction errors are denoted by the empty red circles and the mean squared fitting errors are denoted by the filled black squares.	173
4.23	Comparison of the maximum (T_{max}), average (T_{ave}) and minimum (T_{min}) OTWTs in each pair of data sets between reformer CFD data in the training data, which are represented by the filled black symbols, and estimates generated from the data-driven model for the OTWT distribution, which are represented by the empty red symbols.	175

4.24	Comparison of the OTWT distributions between the 7th data set in the training data (a) and its corresponding estimate generated from the data-driven model for the OTWT distribution (b). In Fig. 4.24, the layout of 336 reforming tubes in the reformer is represented by a table consisting of 336 rectangular cells, in which each cell corresponds to a unique reforming tube in the reformer, i.e., a cell at the bottom right corner of the table represents the 48th reforming tube in the reformer as shown in Fig. 5.2.	176
4.25	Comparison of the maximum (T_{max}), average (T_{ave}) and minimum (T_{min}) OTWTs in each pair of data sets between reformer CFD data in the testing data, which are represented by the filled black symbols, and estimates generated from the data-driven model for the OTWT distribution, which are represented by the empty red symbols.	177
5.1	Flowchart of the furnace-balancing scheme.	184
5.2	Isometric view of the reformer in which the right and back refractory walls are made transparent to display the interior components. The reformer includes 336 reforming tubes (represented by 336 cylinders), 96 burners (represented by 96 frustum cones), and 8 flue-gas tunnels (represented by 8 rectangular intrusions).	189
5.3	Flowchart of the balancing procedure.	205
5.4	Average value of the OTWT distribution when the reformer is operated under the nominal fuel flow rate and varying valve distributions.	206
5.5	Average value of the OTWT distribution when the reformer is operated under varying fuel flow rates and varying valve distributions.	207
5.6	RMS fitting and forecasting errors associated with the proposed values of λ_{64} generated from the two times 10-fold cross-validation study in the derivation of M_{64}^P are plotted in empty squares and black circles, respectively.	214
5.7	RMS fitting and forecasting errors associated with the proposed values of λ_{161} generated from the two times 10-fold cross-validation study in the derivation of M_{161}^P are plotted in empty squares and black circles, respectively.	215
5.8	RMS fitting and forecasting errors associated with each of the four theoretical semivariogram models (given on the horizontal axis as 0, 1, 2, and 3, which correspond to linear omnidirectional, linear anisotropic, exponential omnidirectional, and exponential anisotropic theoretical semivariogram models, respectively) considered in the two times 10-fold cross-validation study in the derivation of M_{64}^C are plotted in gray and black, respectively.	216
5.9	RMS fitting and forecasting errors associated with each of the four theoretical semivariogram models (given on the horizontal axis as 0, 1, 2, and 3, which correspond to linear omnidirectional, linear anisotropic, exponential omnidirectional, and exponential anisotropic theoretical semivariogram models, respectively) considered in the two times 10-fold cross-validation study in the derivation of M_{161}^C are plotted in gray and black, respectively.	217
5.10	RMS fitting errors associated with the proposed values of w^P generated from the two times 10-fold cross-validation study in the derivation of M are plotted in black circles.	218

5.11	RMS fitting errors associated with the proposed values of w^P generated from the two times 10-fold cross-validation study in the derivation of M are plotted in black circles.	219
5.12	Comparison of the maximum, average and minimum values in the OTWT distribution between the plant data (represented by filled black symbols) and the corresponding estimate computed by M (represented by the empty red symbols) at varying total fuel flow rates. In Fig. 5.12, we use jitter to add a small uniform random number on the range from -2% to 2% of the original total flow rate to itself for visual clarity.	220
5.13	Fitting errors of the maximum, average and minimum OTWTs between the estimated OTWT distribution, which is computed using the plant inputs and M , and the corresponding plant data. In Fig. 5.13, we use jitter to add a small uniform random number on the range from -2% to 2% of the original total flow rate to itself for visual clarity.	221
5.14	Comparison of the estimated OTWT distribution (a), which is generated by using M and the optimized reformer fuel input at the nominal total fuel flow rate, to the respective plant data (b). In Fig. 5.14, each cell represents a unique reforming tube, the location of each cell in the table corresponds to that of the respective reforming tube in the combustion chamber, of which orientation can be visualized by the keywords along the edges and Fig 5.2, and the color of each cell represents the value of the respective OTWT, which is specified by the colorbar.	223
5.15	Isometric view of the reformer in which the right and back refractory walls are made transparent to display the reforming tubes of which OTWTs at a fixed distance of 6.5 m away from the reformer ceiling are monitored to track the convergence progress of the transient simulations of the reformer CFD model.	224
5.16	The transient response of the OTWTs at a fixed distance of 6.5 m away from the reformer ceiling of the reforming tubes at the 17th position across all rows inside the combustion chamber as shown in Fig. 5.15 to a positive step change of 21.6 kg s^{-1} in the total fuel flow rate from the nominal value.	225
5.17	The transient response of the OTWTs at a fixed distance of 6.5 m away from the reformer ceiling of six representative reforming tubes along the 3rd row inside the combustion chamber as shown in Fig. 5.15 to a positive step change of 21.6 kg s^{-1} in the total fuel flow rate from the nominal value.	226
5.18	Transient response of the maximum OTWTs across the reforming tube length of seven representative reforming tubes at different regions inside the combustion chamber to a positive step change of 21.6 kg s^{-1} in the total fuel flow rate from the nominal value.	227
5.19	Transient response of the hydrogen and unreacted steam mole fractions in the synthesis gas to a positive step change of 1.8 kg s^{-1} in the total fuel flow rate from the nominal value.	228
5.20	Transient response of the hydrogen and unreacted steam mole fractions in the synthesis gas to a positive step change of 21.6 kg s^{-1} in the total fuel flow rate from the nominal value.	229

5.21	Comparison of the maximum, average and minimum values in the OTWT distribution between the plant data (represented by filled black symbols) and the corresponding forecasting estimate (represented by the empty red symbols) computed by M , the two proposed total fuel flow rates and the optimized valve distribution identified in Chapter 3.	230
5.22	Comparison of the estimated OTWT distribution (a), which is generated by using M , the proposed total fuel flow rate for the second case study and the optimized valve distribution identified in Chapter 3, to the respective plant data (b). In Fig. 5.22, each cell represents a unique reforming tube, the location of each cell in the table corresponds to that of the respective reforming tube in the combustion chamber, of which orientation can be visualized by the keywords along the edges and Fig 5.2, and the color of each cell represents the value of the respective OTWT, which is specified by the colorbar.	231
5.23	Temperature difference between the maximum OTWT along the reforming tube length among all reforming tube ($T_{wall}^{max,*}$) and the maximum value of the OTWT distribution ($T_{wall}^{max,*}$) when the reformer is operated under varying total fuel flow rates and varying valve distributions.	232
5.24	Total fuel flow rate generated by the aggressive flow rate generator (represented by the filled symbols) and by the conservative flow rate generator (represented by the empty symbols) in an effort to determine the maximized total fuel flow rate to achieve the desired reformer firing rate without causing premature failure of the reforming tubes.	233
5.25	Maximum, average and minimum values of the estimated OTWT distribution, which is computed using M with the total fuel flow rate and the respective optimized valve distribution proposed by the aggressive search (represented by the filled symbols) and by the conservative search (represented by the empty symbols) in the process of estimating the maximized total fuel flow rate to achieve the desired reformer firing rate without causing premature failure of the reforming tubes.	234
5.26	Maximum, average and minimum OTWT profile along the reforming tube length among all reforming tubes generated by the reformer CFD model in which the boundary conditions are adjusted based on the maximized total fuel flow rate and the corresponding optimized valve distribution that are identified by the balancing procedure.	235

List of Tables

2.1	Mesh quality of the reformer mesh.	17
2.2	Furnace-side inlet operating conditions of the inner-lane burner in which $x_{comb,inlet}^i$ represents the mole fraction of species i in the furnace-side feed.	24
2.3	Empirical constants of the correlation of the furnace-side flow total emissivity with temperature. These constants are used in the calculation of a_i (Eq. 2.5a) [43].	29
2.4	Properties of the combustion chamber refractory walls.	29
2.5	Johnson Matthey’s Katalco 23 – 4Q catalyst properties.	35
2.6	Simulation results of the original and simplified tube CFD models in which $\bar{P}_{tube,inlet}$ and $\bar{x}_{tube,outlet}^i$ represent the radial-weighted average inlet pressure and outlet mole fraction of species i in the tube-side flow.	40
2.7	Validation of reformer CFD model.	66
2.8	Validation of reformer CFD model by available plant data from literature	66
2.9	Notations	73
3.1	Reformer mesh quality	84
3.2	OTWT distribution obtained from the reformer CFD model in which the uniform FSF distribution is used as the boundary condition.	102
3.3	OTWT distribution obtained from the reformer CFD model in the 6 th iteration in which the optimized FSF distribution is used as the boundary condition.	103
3.8	Summary of the valve position distributions in the 0 th , 6 th , 7 th , 8 th , 9 th and 10 th iterations, in which the highlighted values represent the stuck positions of the defective valves due to the common valve-related disturbances.	110
3.4	OTWT distribution obtained from the reformer CFD model in the 7 th iteration when the FSF distribution is altered by the single-valve disturbance.	112
3.5	OTWT distribution obtained from the reformer CFD model in the 8 th iteration when the FSF distribution is reoptimized to counter the impact of the single-valve disturbance.	112
3.6	OTWT distribution obtained from the reformer CFD model in the 9 th iteration when the FSF distribution is altered by the three-valve disturbance.	114
3.7	OTWT distribution obtained from the reformer CFD model in the 10 th iteration when the FSF distribution is reoptimized to counter the impact of the three-valve disturbance	114
4.1	Distance from burners in S_{77R} to the 77 th reforming tube	165

4.2	Lags, Kriging weights, and directionality of reforming tubes used in the weighted average correction step in calculating the 77th OTWT.	171
4.3	Analysis of the deviations between reformer CFD data in the training data and estimates generated from the data-driven model for the OTWT distribution.	174
4.4	Analysis of the deviations between reformer CFD data in the testing data and estimates generated from the data-driven model for the OTWT distribution.	176
5.1	Comparison of representatives of the monitored transport variables documented at the last sampling time in the transient simulation of the reformer that is subjected to the positive step change of 21.6 kg s^{-1} in the total fuel flow rate from the nominal value to those extracted from the converged solutions of the corresponding steady-state simulation.	222

ACKNOWLEDGEMENTS

First and foremost, I would like to express my sincere gratitude to my advisor, Professor Panagiotis D. Christofides, for his patience, immense knowledge and continuous support of my graduate study. I would like to thank Professor Christofides for encouraging my research, for teaching me how to approach a problem by systematic thinking as an engineer and for allowing me to grow as a research scientist. Your advice on both research as well as on my career have been invaluable. I could not have imagined having a better advisor and mentor for my Ph.D study.

I would like to thank my undergraduate advisor, Professor Gerassimos Orkoulas, for giving me an opportunity to have my firsthand research experience in his laboratory during my undergraduate studies and for believing in me when I didn't believe in myself. For that, I can never thank you enough. Furthermore, I would like to thank my graduate student mentor, Michael Nayhouse, for introducing me to programming, bash scripting and computational research, and for mentoring me both in my undergraduate and graduate studies. I would like to acknowledge that Professor Orkoulas and Michael have made a profound impact on my character and my career goals.

I would like to thank Marquis Grant Crose for being an amazing friend, roommate, labmate and colleague over the years and for his willingness to help filtering my research ideas. I would like to also thank Helen Durand and Zhe Wu for being my outstanding colleagues who worked closely with me on many of my research projects. In addition, I would like to thank my undergraduate student researcher, Madeleine Pont, whom I have had the pleasure of advising, along with all the hard work she helped me with over the years. Furthermore, I would like to thank all of my past and present labmates whom I have had the pleasure to work alongside from my graduate career are Matt Ellis, Liangfeng Lao, Joseph Sangil Kwon, Larry Gao, Fahad Albalawi, Andres Aguirre, Anas Wael Alanqar, Carlos Garcia, Zhihao Zhang, Yangyao Ding, Scarlett Chen, and Mohammed Alhajeri, who were great labmates in addition to being good friends throughout my time at UCLA. Also, a special thanks in particular to both Zhe Wu and Zhihao Zhang for their comments in proofreading my dissertation.

I was also fortunate to meet and get to know a number of people outside of my research group

during my time at UCLA which made the experience much more enjoyable. I would like to thank Prakashan Korambath from the Institute for Digital Research and Education for his help on managing the Hoffman2 computing cluster. I would like to thank Dr. Nicolas Christou for his valuable inputs on the spatial modeling chapter of this dissertation.

I would like to thank my parents, Tran Van Tuan and Chau Thi Thuy, my brothers, Anh Thien-Tam Tran and Kevin Zimmerman, and my best friend, Uyen Tran, for their encouragement of me throughout my PhD and for always doing so much to help me. I hope you know that you have made an incredible impact on my life. It has occurred to me that without you, I don't think I would have grown to be the person I am or to have achieved all the accomplishments that I have.

I would also like to thank Professor James Davis, Professor Dante Simonetti, and Professor Xiaolin Zhong for serving on my doctoral committee.

Finally, financial support from the National Science Foundation (NSF), the Department of Energy (DOE), and a Dissertation Year Fellowship from UCLA's graduate division are gratefully acknowledged.

With regard to the research that forms the foundation for this work:

Chapter 2 contains a version of: A. Tran, A. Aguirre, H. Durand, M. Crose and P. D. Christofides. CFD Modeling of an Industrial-scale Steam Methane Reforming Furnace. *Chem. Eng. Sci.*, 171:576–598, 2017.

Chapter 3 is a version of: A. Tran, A. Aguirre, M. Crose, H. Durand and P. D. Christofides. Temperature Balancing in Steam Methane Reforming Furnace via an Integrated CFD/Data-Based Optimization Approach. *Comp. & Chem. Eng.*, 104:185–200, 2017.

Chapter 4 is a version of: A. Tran, M. Pont, A. Aguirre, H. Durand, M. Crose and P. D. Christofides. Bayesian Model Averaging for Estimating the Spatial Temperature Distribution in a Steam Methane Reforming Furnace. *Chem. Eng. Res. & Des.*, 131:465–487, 2018.

Chapter 5 contains a version of the manuscript: A. Tran, M. Pont, M. Crose and P. D. Christofides. Real-Time Furnace Balancing of Stem Methane Reforming Furnaces. *Chem. Eng. Res. & Des.*, 134:238–256, 2018.

VITA

- 2011–2014 Bachelor of Science, Chemical and Biomolecular Engineering
Department of Chemical and Biomolecular Engineering
Bachelor of Science, Biochemistry
Department of Chemistry and Biochemistry
University of California, Los Angeles
- 2014–2015 Master of Science, Chemical and Biomolecular Engineering
Department of Chemical and Biomolecular Engineering
University of California, Los Angeles
- 2014–2018 Graduate Student
Department of Chemical and Biomolecular Engineering
University of California, Los Angeles
- 2015–2018 Teaching Assistant/Associate
Department of Chemical and Biomolecular Engineering
University of California, Los Angeles
- 2018–2019 Dissertation of the Year
Department of Chemical and Biomolecular Engineering
University of California, Los Angeles

JOURNAL PUBLICATIONS

1. M. Crose, W. Zhang, A. Tran, and P. D. Christofides. Multiscale three-dimensional CFD modeling for PECVD of amorphous silicon thin films. *Comp. & Chem. Eng.*, 113:184–195, 2018.
2. M. Crose, W. Zhang, A. Tran, and P. D. Christofides. Run-to-Run Control of PECVD Systems: Application to a Multiscale Three-Dimensional CFD Model of Thin Film Silicon Solar Cell Deposition. *AIChE J.*, in press, 2018.
3. A. Tran, M. Pont, M. Crose and P. D. Christofides. Real-Time Furnace Balancing of Steam Methane Reforming Furnaces. *Chem. Eng. Res. & Des.*, 134:238–256, 2018.
4. A. Tran, M. Pont, A. Aguirre, H. Durand, M. Crose and P. D. Christofides. Bayesian Model Averaging for Estimating the Spatial Temperature Distribution in a Steam Methane Reforming Furnace. *Chem. Eng. Res. & Des.*, 131:465–487, 2018.
5. M. Crose, A. Tran, and P. D. Christofides. Multiscale Computational Fluid Dynamics: Methodology and Application to PECVD of Thin Film Solar Cells. *Coatings*, 7:22–54, 2017.
6. Z. Wu, A. Aguirre, A. Tran, H. Durand, D. Ni and P. D. Christofides. Model Predictive Control of a Steam Methane Reforming Reactor Described by a CFD Model. *Ind. & Eng. Chem. Res.*, 56:6002–6011, 2017.

7. A. Tran, A. Aguirre, H. Durand, M. Crose and P. D. Christofides. CFD Modeling of an Industrial-scale Steam Methane Reforming Furnace. *Chem. Eng. Sci.*, 171:576–598, 2017.
8. A. Tran, A. Aguirre, M. Crose, H. Durand and P. D. Christofides. Temperature Balancing in Steam Methane Reforming Furnace via an Integrated CFD/Data-Based Optimization Approach. *Comp. & Chem. Eng.*, 104:185–200, 2017.
9. M. Crose, JSI. Kwon, A. Tran, and P. D. Christofides. Multiscale modeling and run-to-run control of PECVD of thin film solar cells. *Renewable Energy*, 100:129–140, 2017.
10. L. Lao, A. Aguirre, A. Tran, Z. Wu, H. Durand and P. D. Christofides. CFD Modeling and Control of a Steam Methane Reforming Reactor. *Chem. Eng. Sci.*, 148:78–92, 2016.
11. M. Crose, JSI. Kwon, A. Tran, and P. D. Christofides. Multiscale modeling and operation of PECVD of thin film solar cells. *Chem. Eng. Sci.*, 136:50–61, 2015.
12. M. Nayhouse, A. Tran, JSI. Kwon, M. Crose, G. Orkoulas and P. D. Christofides. Modeling and control of ibuprofen crystal growth and size distribution. *Chem. Eng. Sci.*, 134:414–422, 2015.
13. V. Heng, M. Nayhouse, M. Crose, A. Tran and G. Orkoulas. Direct determination of triple-point coexistence through cell model simulation. *J. Chem. Phys.*, 137:141101, 2012.

Chapter 1

Introduction

1.1 Hydrogen Economy

High levels of atmospheric carbon dioxide, which is a known consequence of extensive use of fossil fuels as the primary sources of energy in the last century, are adversely affecting climate patterns across the world. In a global effort to reduce carbon emissions to mitigate some of the effects of climate change stricter emissions regulations have passed, which have motivated the need for alternative fuels such as hydrogen. A vision of a carbon-emission-free and sustainable energy system shared by many [4, 37] is aligned with a future hydrogen economy, in which hydrogen is used as a transportation fuel. This is because a hydrogen economy holds the potential to allow a nation to achieve energy security, i.e., to become independent of the limited and constantly depleting foreign crude oil supplies and on political stability of countries with large crude oil reservoirs, and to resolve some effects of climate change without halting economic growth. This vision of a carbon-emission-free and sustainable hydrogen economy is viable because hydrogen can be synthesized from a myriad of commercial thermal pathways (e.g., steam reforming, partial oxidation, gasification, cracking, pyrolysis, and biological reactions) that start from a diverse array of primary energy sources including fossil fuels, biomass and renewable energy. Additionally, physical and chemical properties, e.g., a high diffusivity, a high specific energy content and a wide

range of flammability, of hydrogen make it an efficient transportation fuel. For instance, hydrogen can diffuse rapidly into air to create a uniform combustible mixture while releasing 2.75 times greater heat of combustion per unit mass than hydrocarbon fuels [4].

In addition to the vision of a carbon-emission-free and sustainable hydrogen economy, the current demand for hydrogen is large, e.g., the annual world-wide hydrogen production in 2008 was ~ 500 billion Nm^3 , which is equivalent to 44.5 million metric tons, and corresponded to a global market of more than \$40 billion. The demand for hydrogen is also expected to grow at an annual rate of 5 to 10% because hydrogen is widely used as precursor across a variety of manufacturing industries. In petroleum refineries, refining catalytic processes account for approximately 37% hydrogen world-wide hydrogen consumption [4]. For example, the hydro-treating process uses hydrogen to convert olefins to paraffins, and the hydro-cracking process uses hydrogen to cleave sigma carbon-carbon bonds; these refining processes serve the same purpose of increasing the hydrogen to carbon ratio in the downstream process reactants, allowing these downstream processes to have higher efficiency. Additionally, the hydro-desulfurization process uses hydrogen to remove thiol compounds from the raw natural gas feedstock to prevent the catalysts of downstream processes from being deactivated. In fine chemical manufacturing industries, hydrogen is the main component of synthesis gas; e.g., the production of ammonia accounts for approximately 49% hydrogen world-wide hydrogen consumption. In semiconductor manufacturing industries, hydrogen is used as the gas carrier; for example, the feedstock to a plasma enhanced chemical vapor deposition reactor is typically composed of 90% hydrogen and 10% silane [11]. Moreover, hydrogen is also a clean and efficient energy carrier for hydrogen-based technologies. Thus, solving challenges encountered in commercial production of hydrogen and optimizing the production line has become of particular interest to both academia and industry [4].

It is noted that although hydrogen can be derived from a diverse array of primary energy sources with a variety of commercial processes, only a few are economically feasible. With current state-of-the-art technology, hydrogen is produced almost exclusively from fossil fuels, e.g., $\sim 96\%$ of the world-wide hydrogen production activity uses fossil fuels as starting materials [4], by ther-

mochemical processes. Our literature survey recognizes that steam methane reforming (SMR), an endothermic conversion of methane and superheated steam into hydrogen, is by far the most common commercial hydrogen production process and accounts for the largest share of the world-wide hydrogen production [27, 6, 18]; in 2007, SMR was responsible for up to 85% of the world-wide hydrogen production [55]. The reasons for the prevalent usage of centralized SMR-based facilities to meet the large and growing demand for hydrogen are twofold: (1) SMR can achieve up to 90% thermal efficiency on the metric of high heating value [50] and up to 82% of methane conversion [14], and (2) centralized SMR-based facilities with the production rates over 1 million Nm³ per day are reported to require the least capital investment [6] and have a low production cost (e.g., \$6.90 per gigajoule (GJ)) compared to hydrogen plants that use competing technologies, e.g., the production cost via electrolysis can be as high as \$98 per GJ [37]. Barreto et al. [6] speculated that SMR would remain the leading technology in world hydrogen production in 2050.

In practice, the process is simultaneously catalyzed and carried out under high operating temperatures inside hundreds of nickel-based catalyst filled tubular reactors to achieve a high conversion of methane in a finite packed-bed length, which allows the SMR-based facilities to become economically viable. To create the high temperature environment necessary to achieve a high conversion of methane, the reforming tubes are housed inside an insulated combustion chamber (which is referred to as a “reformer” in this dissertation) where the recycled effluent from the purification units and the fresh natural gas undergo a lean combustion process. Reformers can be categorized with respect to the location of burners: top-fired, side-fired, bottom-fired and terrace wall-fired reformer, which in turn dictates interactions between the tube side and furnace side, the temperature distribution characteristics of the furnace-side flow inside the reformer and the heat flux profile along the reforming tubes, e.g., bottom-fired reformers are characterized by a constant heat flux along the reforming tubes [19]. For SMR, the reformer configurations that facilitate a high heat transfer rate to the tube side near the reforming tube inlet are expected to require the shortest reforming tube length to achieve a desired set-point of the methane conversion and are preferable. Therefore, the top-fired configuration is frequently employed at SMR-based hydrogen

plants and is the subject of this dissertation.

SMR-based hydrogen plants typically consist of two major sections: the synthesis section and the purification section [24]. In the synthesis section, fresh natural gas feedstock is treated in a desulfurization unit to remove thiol compounds preventing catalysts used in downstream processes from being poisoned. Then, the effluent of the desulfurization unit typically undergoes a catalytic prereforming process to convert higher hydrocarbons in the treated feedstock into methane and byproducts (i.e., carbon oxides and hydrogen), preventing these high hydrocarbons from decomposing inside the reforming tubes, which causes coke formation and catalyst deactivation. Next, the treated feedstock (i.e., the effluent of the prereforming process) and high pressure superheated steam are fed into the reformer to undergo SMR producing hydrogen. The synthesis gas (i.e., the effluent of the reformer) is treated in a water-shift reactor to remove carbon monoxide and to produce a small additional amount of hydrogen, and the effluent of the water-shift reactor enters the purification section in which the process stream is stripped off of unreacted reactants and byproducts (i.e., carbon dioxide) to produce high purity product. At SMR-based hydrogen plants, the reformers are the most expensive equipment in terms of the maintenance and operating costs compared to other major equipment such as the hydrotreating, prereforming, water-shift and purification units. For instance, the re-tubing cost of the reformer is $\sim 10\%$ of the total capital investment [13], and the annual investment to procure fresh natural gas for a SMR-based hydrogen plant with a production rate of 2.7 million Nm^3 per day is \$62 million [13]. Therefore, even a small improvement in the reformer efficiency is expected to significantly lower the reformer operating cost and improve the plant efficiency, which results in significant financial benefits [32, 56, 13].

Despite the potential economic gain, under the standard operating policy of the reformer, the nominal operating condition is often suboptimal and is calibrated to maintain the expected reformer service life by reducing the total fired duty and compromising the hydrogen production rate of the SMR-based plant to keep the reformer in a safe operating regime. This is because hydrogen manufacturing industry recognizes that the degradation of the microstructure of the reforming tube wall due to temperature aging accelerates, if the outer tube wall temperature (OTWT) at any location

along the reforming tube length exceeds its design value [23, 2, 22]. Specifically, the evolution of the microstructure of the reforming tube wall starting from precipitation of primary and secondary carbides in the austenitic matrix, which leads to creep cavitation damage presented in the form of isolated cavities and coalesce cavities, followed by the formation of microcracks which propagate to form macrocracks occurs in an accelerated timeline leading to premature failure of the reforming tubes. It has been documented that the reformer service life of 100,000 h can be reduced by half under an operating condition that allows the maximum OTWT to exceed its design value by 20 K for an extended period of time [49]. This explains the relationship between the reformer service life and the maximum operating temperature of the reformer or in particular the maximum outer tube wall temperature (OTWT) along the reforming tube length among all reforming tubes. For this reason, the SMR-based hydrogen plant uses a system of infrared cameras to periodically sample the OTWTs of the reforming tubes at a few discrete locations along the reforming tube length to monitor the reformer service life; each set of measurements collected at the fixed height is typically defined as an OTWT distribution. Experimental plant data of OTWT distributions have revealed that the OTWTs within each OTWT distribution are nonuniform with a fluctuating range between 30 K to 110 K [32], and OTWT profiles along the reforming tube length can vary noticeably among the reforming tubes. This nonuniformity in OTWT distributions poses a major challenge in the estimation of the optimized firing rate due to the high risk of accelerating the degradation of the microstructure of the reforming tube wall. Specifically, the maximum OTWT along the reforming tube length among all reforming tubes in the reformer operated under a suboptimal fuel distribution can be higher than that in a reformer operated under an optimized fuel distribution with the same total fuel flow rate [56]. Consequently, the optimized firing rate may not be implemented without the proper distribution of the optimized total fuel flow rate, and the SMR-based hydrogen plant throughput is compromised to retain the reformer service life and to reduce the risk of suffering substantial capital and production losses.

1.2 Dissertation Objectives and Structure

Motivated by the objective to increase the reformer thermal efficiency while maintaining the expected service life of the reformer in the presence of the inherent nonuniformity in OTWT distributions, this dissertation is structured as follows.

Chapter 2 focuses on developing a computational fluid dynamics (CFD) model for an industrial-scale reformer in ANSYS Fluent so that we can achieve an in-depth understanding of the physiochemical processes in the tube side and the furnace side as well as their thermal interactions during the catalytic conversion of methane to hydrogen. Specifically, the effects of turbulence on the furnace-side transport variables is simulated by the standard $k - \varepsilon$ turbulence model with ANSYS enhanced wall treatment function. Additionally, the lean combustion of the furnace-side feed is modeled by the finite rate/eddy dissipation turbulence-chemistry interaction model and the global reaction schemes with the premixed combustion assumption. Next, the absorption coefficient of the furnace-side flow is modeled by an empirical correlation for estimating the radiative properties of a homogeneous gas flow, Kirchhoff's law, and Lambert Beer's law, and thermal radiative heat transfer rate between the interior combustion chamber, the outer reforming tube wall and the furnace-side flow is modeled by the discrete ordinate method. Similarly, the effects of turbulence on the tube-side transport variables is also simulated by the standard $k - \varepsilon$ turbulence model with ANSYS enhanced wall treatment function. Additionally, the catalytic bed of the reforming reactor is modeled by the continuum approach with ANSYS porous zone function, the effectiveness factor and catalyst packing factor. It is noted that the effectiveness factor is used to simulate the heat and mass transfer resistances between the bulk fluid and the surface of the catalyst. Next, the wall of the reforming reactor is modeled by ANSYS thin wall function, and SMR is modeled by the global reaction scheme. Subsequently, publicly available SMR-based plant data is used to derive equivalent boundary conditions of the reformer CFD model namely the tube inlet, the burner inlet and the energy leakage through the combustion chamber refractory wall, etc. As a result, the simulation data generated by the CFD model for the reformer and the corresponding SMR-based plant data

can be used to validate our proposed assumptions and CFD model.

Chapter 3 focuses on developing a furnace-balancing scheme to determine an optimized FSF distribution at the nominal total FSF flow rate that minimizes the inherent nonuniformity in the OTWT distribution such that the reformer thermal efficiency can be subsequently increased while maintaining the expected service life of the reformer. Initially, the CFD model for an industrial-scale reformer outlined in Chapter 2 is used to explore the steady-state behavior of the reformer at the nominal total FSF flow rate with varying FSF distributions. Then, a model identification in which the algorithm is formulated based on the least squares regression method, properties of thermal radiative heat transfer, the reformer geometry and the furnace-side flow pattern is proposed. Next, the relationship between the FSF distribution and the flow control system of the reformer is formulated under the linear valve assumption, and the fundamental differences between properly functional and defective flow control valves (i.e., constituents of the flow control system) is discussed. Subsequently, a model-based furnace-balancing optimizer, which is formulated as an optimization problem with the valve position distribution as the decision variable, and minimizing the sum of the weighted squared deviations of the OTWTs from a set-point value for all reforming tubes with the least the penalty term on the deviation of the valve positions from their fully open positions as the objective function, is proposed. Finally, simulation data generated in this study will be used to demonstrate that the optimized FSF distribution created by the furnace-balancing scheme can significantly reduce the nonuniformity in the OTWT distribution in the combustion chamber even when the reformer is under the influence of common valve-related disturbances.

Chapter 4 focuses on developing a statistical-based model identification that can be used to derive a high-fidelity model for the OTWT distribution as a function of the FSF distribution, total FSF flow rate and interactions among neighboring reforming tubes from simulation data generated by the CFD model for the reformer outlined in Chapter 2. The model identification is structured to have two distributed components, namely, a prediction step and a correction step, which can be used simultaneously and independently to derive the prediction and correction models for the OTWT distribution. Initially, an algorithm for the prediction step based on Bayesian variable se-

lection, Bayesian model averaging, sparse nonlinear regression, reformer geometry and properties of thermal radiation is proposed so that for each reforming tube, the prediction step can systematically identify predictors for the OTWT and simultaneously collect a corresponding library of sub-prediction models, which are subsequently combined to yield the prediction model for the OTWT of the reforming tube. A collection of prediction models for all reforming tubes is defined as a prediction model for the OTWT distribution, which is expected to capture the dependence of the OTWT distribution on the FSF distribution and total FSF flow rate. Next, an algorithm for the correction step designed based on the ordinary Kriging is proposed so that for each reforming tube, the correction step creates a spatial model allowing the OTWT to be estimated from the predicted OTWT of the neighboring reforming tubes. A collection of correction models for all reforming tubes is defined as a correction model for the OTWT distribution, which is expected to adjust the predicted OTWT distribution to account for interactions among neighboring reforming tubes. Subsequently, the data-driven model for the OTWT distribution is created using the prediction and correction models for the OTWT distribution, which allows the model to account for the effect of interactions among neighboring reforming tubes while estimating the OTWT distribution based on the FSF distribution and total FSF flow rate. The model identification is executed on the Hoffman2 shared computing cluster at UCLA to construct the data-driven model for the OTWT distribution, and the results from the goodness-of-fit and out-of-sample prediction tests of the data-driven model are used to demonstrate the effectiveness of the scheme outlined in Chapter 4.

Chapter 5 focuses on developing a real-time furnace-balancing scheme that simultaneously maximizes total FSF flow rate and identifies the corresponding optimized valve distribution in real-time such that the reformer thermal efficiency is maximized within the physical limitation of the reforming tube wall material. Initially, the framework for the furnace-balancing scheme, the valve-to-flow-rate converter and the statistical-based model identification outlined in Chapters 2, 4 and 3 are integrated with a heuristic search algorithm to create a real-time balancing procedure, which recursively proposes different total FSF flow rate followed by optimizing the correspond valve distribution until key operational specifications, e.g., the reformer throughput is maximized,

and the OTWT along the reforming tube length of all reforming tubes must not exceed the design temperature of the reforming tube wall, are satisfied. Subsequently, a CFD model for the reformer outlined in Chapter 2 is used to represent the on-line unit at the SMR-based hydrogen plant and is used to characterize the previously unstudied dynamic response of the reformer to a step change input in the total FSF flow rate, based on which an optimal strategy to implement the optimized total FSF flow rate to maximize the reformer throughput without causing additional damage to the reforming tubes in the process is proposed. Finally, a case study in which the balancing procedure is implemented on the reformer initially operated under the nominal reformer input is discussed, and the results are used to demonstrate that the furnace-balancing scheme successfully determines the optimized reformer fuel input to increase the reformer throughput while meeting the OTWT limits.

Chapter 6 summarizes the main results of the dissertation.

Chapter 2

CFD Modeling of a Reformer

2.1 Introduction

In Chapter 1, we have established that the reformer service life is sensitive to the maximum operating temperature of the reformer and more specifically the maximum outer tube wall temperature (OTWT) along the reforming tube length and among all reforming tubes. Due to the inherent variability in the OTWT distribution and the risk of accelerating the temperature aging process of the reforming tube wall as outlined in Chapter 1, the maximized fired duty cannot be implemented without an optimized spatial distribution of the total FSF flow rate in a sense of minimizing the nonuniformity in the OTWT distribution. Therefore, as a preliminary step to developing a robust real-time tool to maximize the reformer thermal efficiency, this Chapter focuses on developing a CFD model for an industrial-scale reformer (details given in Section 2.2) in ANSYS Fluent so that we can achieve an in-depth understanding of the physiochemical processes in the tube side and the furnace side as well as their thermal interactions during the catalytic conversion of methane to hydrogen. Initially, we discuss the modeling methodology for creating the reformer CFD model which explains the selection of appropriate models to simulate all essential transport phenomena and chemical reactions typically observed in the reformer with an affordable computational cost and reasonable computing time. Specifically, the standard $k - \varepsilon$ turbulence model with the AN-

ANSYS enhanced wall treatment function, finite rate/eddy dissipation (FR/ED) turbulence-chemistry interaction model and global kinetic models of combustion [5] [46] are integrated to simulate the non-premixed combustion characteristics (details given in Section 2.4.1). Additionally, an empirical correlation [43], Kirchhoff's law and Lambert Beer's law are used to simulate the furnace-side radiative properties as a function of the furnace-side temperature, and the discrete ordinate method [3] is used to simulate the rates of radiative heat transfer between the furnace-side flow, the combustion chamber refractory walls and the outer reforming tube walls (details given in Section 2.4.2). In the reforming tubes, the effects of turbulence on the tube-side transport variables is simulated by the standard $k - \epsilon$ turbulence model with ANSYS enhanced wall treatment function. Additionally, the catalytic bed of the reforming reactor is modeled by the continuum approach with ANSYS porous zone function, the effectiveness factor and catalyst packing factor. It is noted that the effectiveness factor is used to simulate the heat and mass transfer resistances between the bulk fluid and the surface of the catalyst. Next, the wall of the reforming reactor is modeled by ANSYS thin wall function, and SMR is modeled by the global reaction scheme. The boundary conditions for the reforming tube inlet (referred to in the following text as "tube-side feed"), burner inlet (referred to in the following text as "furnace-side feed"), and combustion chamber refractory walls are derived from typical plant data [35]. Finally, the simulation results generated by the reformer CFD model are rigorously validated by comparing them with the available data in the literature, converged solution produced by a single reforming tube CFD model [34] and simulation results generated by a reforming Gibbs reactor of a commercial steady-state process simulator.

2.2 Reformer geometry

The reformer investigated in this work is developed based on an industrial-scale top-fired, co-current reformer designed by Sela Fluid Processing Corporation (Fig. 3.2). The reformer is approximately 16 m wide, 16 m long and 13 m tall and produces 2.83 million Nm^3 of high-purity hydrogen along with 1.7 million kg of superheated steam (i.e., 663.15 K and 4,580 kPa) per day [35]. The reformer contains seven rows of forty-eight reforming tubes of which the external diameter, internal diameter and exposed length are 14.6 cm, 12.6 cm and 12.5 m, respectively. Inside these reforming tubes, commercial nickel-based catalyst pellets (e.g., alpha-alumina-supported nickel oxide denoted as $\text{NiO} - \alpha\text{Al}_2\text{O}_3$) are used as packing material. At the combustion chamber ceiling, these rows of reforming tubes are separated by eight rows of twelve burners which are fed with a furnace-side feed composed of a fuel stream containing methane, hydrogen and carbon monoxide, and an oxidizer stream containing combustion air. The rows of burners which are adjacent to the combustion chamber refractory walls and a single row of reforming tubes (for brevity these burners are denoted as “outer-lane burners”), are fed with a lower FSF flow rate than the rows of burners which are adjacent to two rows of reforming tubes (for brevity, these burners are denoted as “inner-lane burners”). Specifically, the FSF flow rate of the outer-lane burners is 60% of that of the inner-lane burners to avoid causing “over-firing” in the outer lanes and “under-firing” in the inner lanes, which would occur if the total FSF flow rate were evenly distributed to all burners. At the reformer floor, the rows of reforming tubes are separated by the rectangular intrusions known as flue gas tunnels or coffin boxes which extend from the front to the back of the combustion chamber along the rows of reforming tubes with a height of 3 m from the floor. Additionally, there are thirty-five extraction ports evenly distributed in a row along each side of the flue gas tunnels that allow the furnace-side flow to enter the flue gas tunnels, and then to exit the combustion chamber through the front openings of the flue gas tunnels. In this work, we will focus on the development of a CFD model of the reformer described above.

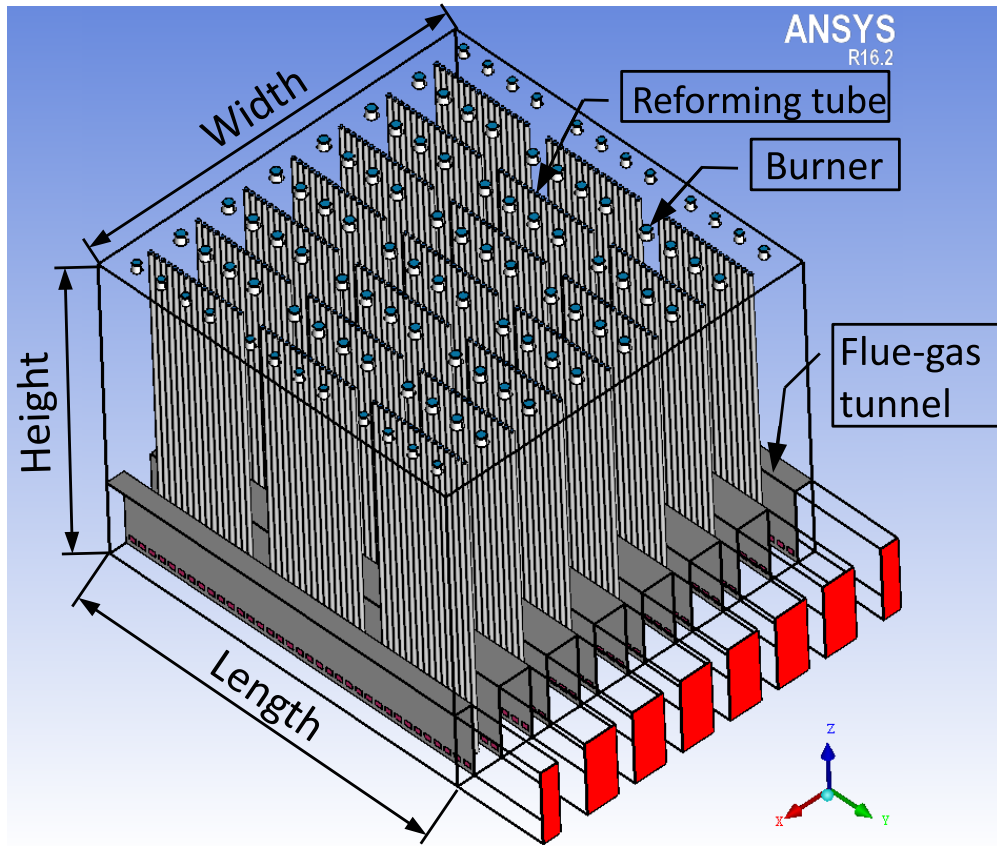


Figure 2.1: The isometric view of an industrial-scale, top-fired, co-current reformer with 336 reforming tubes, which are symbolized by 336 smaller circles, 96 burners, which are denoted by 96 larger circles, and 8 flue gas tunnels, which are represented by 8 rectangular intrusions. The outer-lane burners are burners on the right and left boundaries of the figure, while the inner-lane burners are slightly larger than the outer-lane burners in the figure.

2.3 Reformer mesh

In the CFD study of the reformer, the reformer volume is divided into small and discrete subdomains also known as grids (a collection of grids is referred to as a mesh), within which spatial variations are, though not negligible, significantly less drastic than those in the overall domain. Then, the reformer mathematical model (i.e., two sets of highly non-linear coupled integro-differential equations with seven independent variables) is numerically solved by the finite volume method within each grid to characterize the fluid-flow and temperature fields. Then, the numerical solutions of the grids are patched together to reconstruct the solution of the original domain. Hence, creating a mesh with acceptable mesh quality is a critical task that determines the success level of CFD modeling because a CFD model built from a poor quality mesh has a slow speed of convergence [7] and is more likely to converge to an inaccurate solution as mesh quality directly determines solver discretization error [3].

There are two common meshing strategies in ANSYS ICEM, i.e., the unstructured tetrahedral meshing strategy (for simplicity, it is denoted as “unstructured meshing”) and the multiblock structured hexahedral meshing strategy (for simplicity, it is denoted as “structured meshing”). The unstructured meshing procedure creates a collection of predominantly tetrahedral grids that are arranged in an irregular pattern, while the structured meshing procedure creates a collection of hexahedral grids that are arranged in a pattern specified by the user of the mesh creation software. Although unstructured meshing is generally more proficient at approximating complicated geometries than structured meshing, the ANSYS ICEM environment offers an O-grid Block function that can be utilized to enhance the ability of structured meshing to approximate curvy geometry characteristics by re-arranging existing grid lines into an *O* shape to effectively improve the overall hexahedral mesh quality. In the creation of the reformer hexahedral mesh in this work, the O-grid Block function can be used for meshing of the burner geometries, which have a frustum-like structure, and the reforming tubes, which have a cylindrical structure. As shown in Figs. 2.2(a), 2.2(b) and 2.2(c), the structured meshing procedure with the O-grid Block function can capture

the geometries of the reformer components (e.g., the inner-lane burners, outer-lane burners and reforming tubes) that cannot be represented with straight lines. Therefore, because we can capture all aspects of the reformer geometry with the structured meshing technique, and because for wall-bounded systems like the reforming tubes, a CFD model built from structured meshing generally generates a converged solution closer to experimental data and also is expected to have a superior speed of convergence compared to other CFD models built from unstructured meshing when the system is decomposed into the same number of discrete grids [3, 34, 15]. Therefore, the reformer mesh is created using structured meshing in this work. The good agreement of our CFD results (presented in Section 2.8) with typical plant data (compared in Section 2.10) utilizing this meshing strategy shows that the meshing method employed was adequate for obtaining results that are consistent with typical plant data.

In the reformer mesh, the grids are not uniformly distributed and are more dense in regions expected to have large momentum, material, and temperature gradients, such as in the neighborhood of the reforming tube walls (where heat transfer from the furnace side to the tube side is expected to create temperature gradients that must be captured through a denser mesh as shown in Fig. 2.3) and in the regions directly under the burners that correspond to the flames (where the mixing-limited nature of non-premixed combustion is expected to create species and flow characteristics that should be captured with a denser mesh as shown in Fig 2.4). This design of the reformer mesh aims to reduce the stiffness of the spatial gradients of the transport variables, which allows the ANSYS Fluent CFD solver to obtain the numerical solution of the reformer CFD model with a shorter computing time.

In CFD, the reformer mesh must be discretized into a sufficient number of grids so that the CFD simulation data becomes mesh-independent. In this effort, three multiblock structured hexahedral meshes with the approximate sizes of 13, 29 and 41 million cells are used for the mesh-independent study to estimate the baseline size of the grid, and three corresponding reformer CFD models are created and denoted as the coarse-mesh CFD model, CFD model and fine-mesh CFD model, respectively. It is worth noting that the simulation of the coarse-mesh CFD model is unstable

even when a conservative mode of ANSYS Fluent solver is used. The converged CFD simulation results generated by the reformer CFD models are used to determine the appropriate mesh size for the present work. The difference between the simulation results (e.g., the average temperature profiles of the furnace-side flow) of the coarse-mesh CFD model and CFD model is noticeable. The comparison between the simulation results of the CFD model and fine-mesh CFD model shows that they are nearly identical while the fine-mesh CFD model requires a longer computing time to obtain the converged solution. Our studies shows that a mesh size of about 29 million cells produces mesh-independent results. Specifically, the reformer mesh contains 29,099,252 hexahedral grids, 88,798,168 quadrilateral faces and 30,584,930 nodes.

The quality of the resulting mesh is evaluated utilizing the three mesh quality evaluation criteria (the minimum orthogonal factor, maximum ortho skew and aspect ratio) suggested by the manufacturer ANSYS Inc. of the commercial CFD software package utilized to develop the reformer CFD model in this work (other potential mesh evaluation criteria not specified by ANSYS Inc. were not utilized because ANSYS Inc. did not indicate recommended ranges for such properties that would suggest appropriate mesh quality based on such other criteria). ANSYS Inc. suggests that if the values of the three suggested criteria for all subdomains (i.e., mesh quality) are within the recommended ranges shown in Table 2.1, the mesh can be considered to have reasonably good quality and can be used to generate CFD results. Because the values of the minimum orthogonal factor, maximum ortho skew, and maximum aspect ratio among all subdomains are within the ranges recommended by ANSYS Inc., the mesh of the industrial-scale reformer is considered to have reasonably good quality (this is further validated by the good agreement of the CFD data generated using this mesh and typical plant data as discussed in Section 2.10). Although the minimum orthogonal factor and maximum ortho skew of the reformer mesh are close to the lower limits as shown in Table 2.1, the average orthogonal factor (0.965) and average ortho skew (0.035) of the reformer mesh are close to the ideal values of 1.000 and 0.000, respectively. Hence, we use the reformer mesh with approximately 29 million cells to create the reformer CFD model.

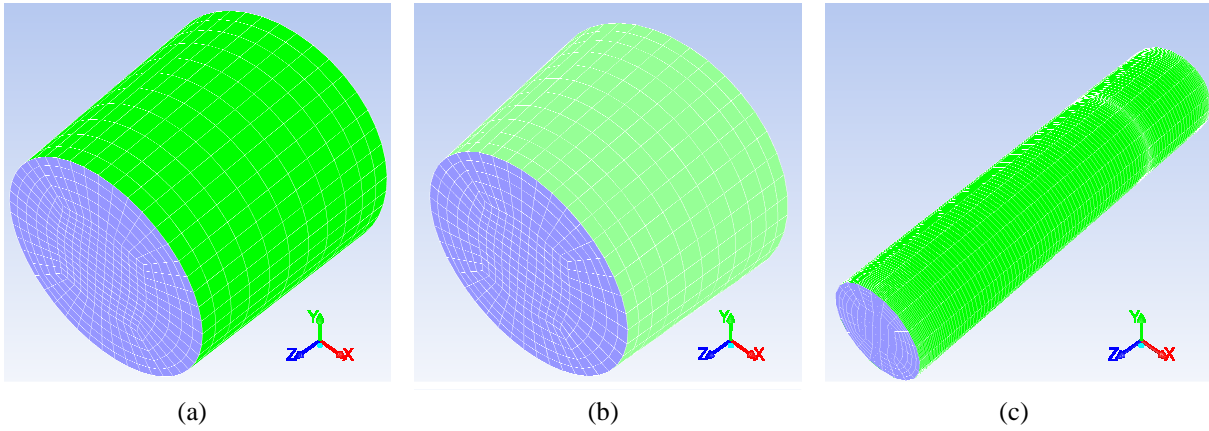


Figure 2.2: Isometric view of the hexahedral structured mesh of the outer-lane burner (a), inner-lane burner (b) and reforming tube (c). This figure demonstrates that the meshes of both the inner-lane and outer-lane burners, as well as the mesh of the reforming tubes, created by the O-grid Block function of ANSYS ICEM have the exact geometries of the corresponding components. In Fig. 2.2(c), the radial direction of the reforming tube is scaled up by 20 times for display purposes.

Table 2.1: Mesh quality of the reformer mesh.

	The reformer mesh	Recommended range
Minimum orthogonal factor	0.181	0.167 – 1.000
Maximum ortho skew	0.819	0.000 – 0.850
Maximum aspect ratio	28.5	1.000 – 100.0

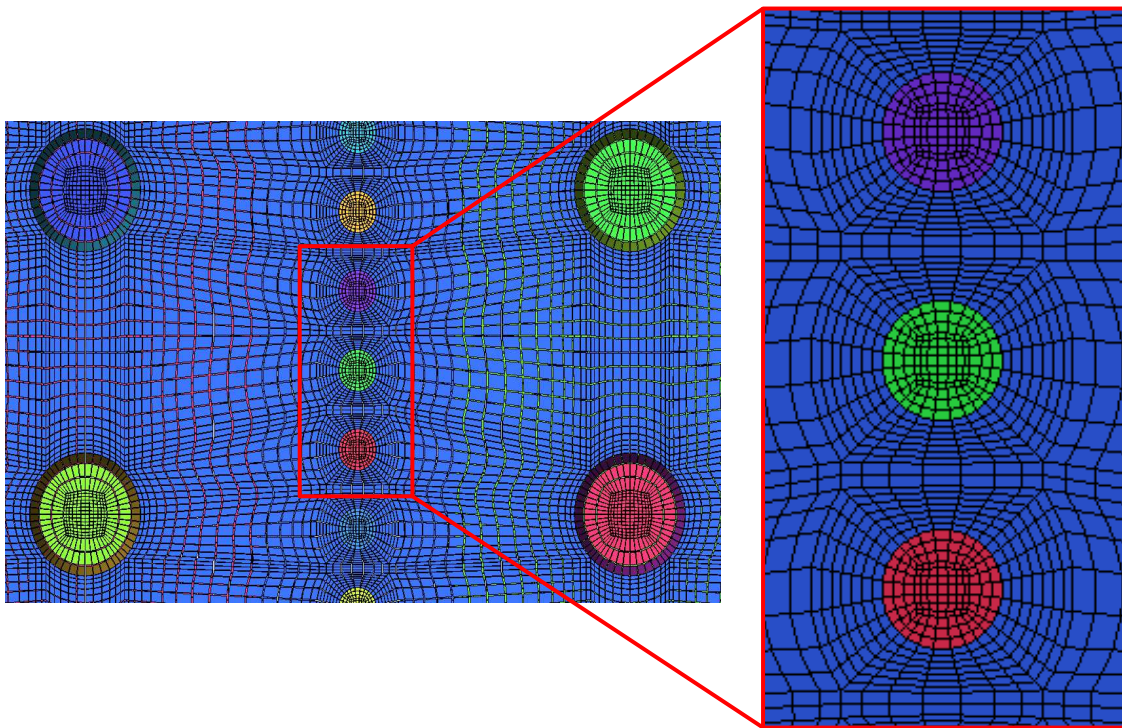


Figure 2.3: A sample of the top view of the hexahedral structured mesh of the reformer, where a row of reforming tubes is adjacent to two inner-lane burners. In Fig. 2.3, the reforming tube inlets and burner inlets are assigned with different color for display purposes.

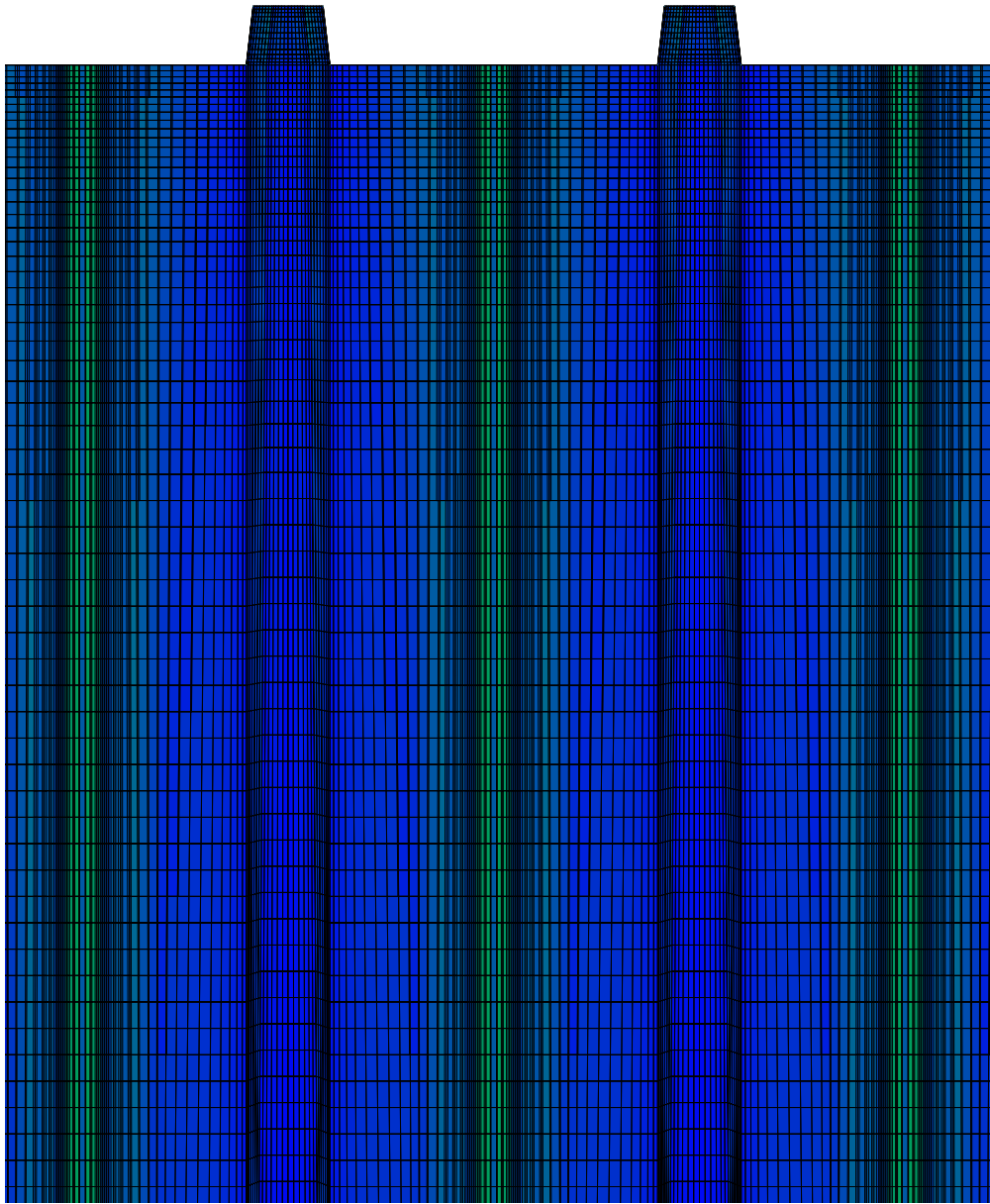


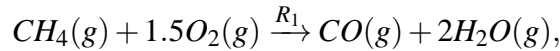
Figure 2.4: A sample of the vertical cross section of the hexahedral structured mesh of the reformer.

2.4 Furnace chamber modeling

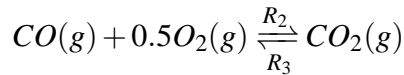
2.4.1 Combustion kinetic model and turbulence-chemistry model

In the combustion chamber, reducing agents in the furnace-side feed are oxidized to their highest oxidation states generating carbon dioxide, water and a large amount of thermal energy, which is used to drive SMR inside the reforming tubes. The chemistry of the combustion phenomena is a complex network of sequential elementary reactions governed by the concentrations of free radicals. For instance, the complete mechanism of the hydrogen combustion phenomena generating water involves more than 20 elementary reactions with various intermediates, and the corresponding detailed kinetic model consists of more than 20 distinct reaction rates [59]. Although it is possible to implement such a detailed kinetic model in the reformer CFD model, the CFD model would be no longer meaningful for industrial applications as it would take a long computing time to generate the CFD simulation data. As a result, global kinetic models for the combustion of methane [46] and hydrogen [5] are used to model the combustion of the furnace-side feed to reduce the computational requirement for simulating the reformer CFD model:

Global kinetic model of methane combustion:



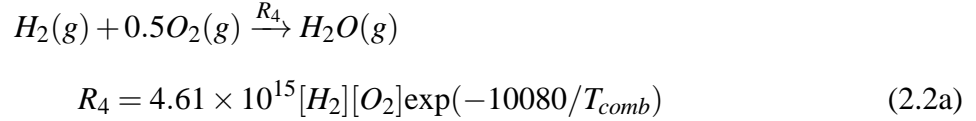
$$R_1 = 10^{15.22}[CH_4]^{1.46}[O_2]^{0.5217}\exp(-20643/T_{comb}) \quad (2.1a)$$



$$R_2 = 10^{14.902}[CO]^{1.6904}[O_2]^{1.57}\exp(-11613/T_{comb}) \quad (2.1b)$$

$$R_3 = 10^{14.349}[CO_2]\exp(-62281/T_{comb}) \quad (2.1c)$$

Global kinetic model of hydrogen combustion:



where R_1, R_2, R_3 and R_4 ($\text{kmol m}^{-3} \text{ s}^{-1}$) are the intrinsic volumetric reaction rates, T_{comb} (K) and $[i]$, $i = CO_2, CO, CH_4, H_2, O_2$ (kmol m^{-3}) are the temperature and species molar concentrations of the furnace-side flow. It is worth noting that because the empirical kinetic formulas (Eqs. 2.1–2.2) are in the Arrhenius form, they can be directly integrated into the reformer CFD model.

In the reformer, the furnace-side feed composed of two separate streams, i.e., the fuel stream and the oxidizer stream, is combusted inside the combustion chamber to generate the required fired duty for SMR. The intrinsic nature of non-premixed combustion is turbulent mixing-controlled, i.e., the rate of the chemical reactions is relatively faster than that of mixing on which the observed reaction rates of furnace-side species depend. In the remainder of this section, we demonstrate a modeling strategy that allows the reformer CFD model to simulate the behavior of non-premixed combustion processes of the furnace-side feed. Specifically, in the reformer CFD model, the fuel stream and air stream of the furnace-side feed are assumed to be well-mixed as shown in Table 2.2 prior to being fed into the combustion chamber, and the combustion phenomena of methane and hydrogen are modeled by the premixed combustion model. However, the intrinsic nature of non-premixed combustion phenomena must be shown in the simulation results generated by the reformer CFD model. This issue is resolved by using the finite-rate/eddy-dissipation (FR/ED) model as the turbulence-chemistry interaction model to simulate the reaction rates of the furnace-side species. In particular, the FR/ED model utilizes the global kinetic models of combustion phenomena (shown in Eqs. 2.1 and 2.2), finite rate formula (shown in Eq. 2.3c) and eddy-dissipation rates (shown in Eqs. 2.3a–2.3b) to estimate the observed reaction rates of the furnace-side species [3]. The formulation of the FR/ED model is presented as follows:

$$R_{i,j} = v_{i,j} M_i A \rho_{comb} \frac{\epsilon_{comb}}{k_{comb}} \min_{\mathcal{R}} \left(\frac{Y_{\mathcal{R}}}{v_{\mathcal{R},j} M_{\mathcal{R}}} \right) \quad (2.3a)$$

$$R_{i,j} = v_{i,j} M_i A B \rho_{comb} \frac{\epsilon_{comb}}{k_{comb}} \frac{\sum_{\mathcal{P}} Y_{\mathcal{P}}}{\sum_n^N v_{n,j} M_n} \quad (2.3b)$$

$$R_{i,j} = v_{i,j} M_i R_j \quad (2.3c)$$

where $R_{i,j}$ ($\text{kg m}^{-3} \text{s}^{-1}$) and $v_{i,j}$ are the observed reaction rate and stoichiometric coefficient of species i in reaction j , M_i (kg kmol^{-1}) is the molecular weight of species i , $Y_{\mathcal{R}}$ and $M_{\mathcal{R}}$ are the mass fraction and molecular weight of a specified reactant \mathcal{R} , $v_{\mathcal{R},j}$ is the stoichiometric coefficient of a specified reactant \mathcal{R} in reaction j , $A = 4.0$ and $B = 0.5$ are the default empirical constants of the FR/ED model [42], k_{comb} ($\text{m}^2 \text{s}^{-2}$) and ϵ_{comb} ($\text{m}^2 \text{s}^{-3}$) are the turbulence kinetic energy and dissipation rate (which will be discussed in Section 2.7), $Y_{\mathcal{P}}$ is the mass fraction of a product species \mathcal{P} in reaction j , R_j ($\text{kmol m}^{-3} \text{s}^{-1}$) is the intrinsic volumetric reaction rate of reaction j from Eqs. 2.1–2.2, ρ_{comb} (kg m^{-3}) is the density of the furnace-side flow, n is the index of the product species involved in reaction j and N represents the number of chemical species in reaction j [3]. When the FR/ED model is integrated in the reformer CFD model, the reaction rate of each furnace-side species is calculated based on the three different methods presented in Eqs. 2.3a, 2.3b and 2.3c for which the smallest estimate corresponding to the slowest rate is set as the observed rate [38]. In other words, in the reaction-limited zone, the observed reaction rates of the furnace-side species are computed by the finite rate formula (Eq. 2.3c), whereas in the transport-limited zone, they are computed by the eddy-dissipation formulas (Eqs. 2.3a and 2.3b). Particularly, because the furnace-side temperature of 532.9 K at the inner-lane/outer-lane burner inlets is relatively low compared to the typical operating furnace-side temperature, the finite rate formula is expected to predict slower reaction rates of furnace-side species than those estimated by the eddy-dissipation formulas. This is because the activation temperature values of combustion phenomena derived from the chosen kinetic models (Eqs. 2.1–2.2) are substantially larger than the FSF temperature, and the concentrations of reacting species are diluted by the presence of inert

furnace-side species (i.e., nitrogen and argon), which account for $\sim 61\%$ of the FSF molar flow rate. Furthermore, the contour plots of furnace-side compositions and energy released from the combustion of the furnace-side feed (presented in Section 2.8) generated by the reformer CFD model indicate that the oxidation rates of methane and hydrogen detected in the vicinity of the inner-lane/outer-lane burner inlets are slow, which matches well with the expected observations. The results suggest that the reaction rates of furnace-side species estimated by the FR/ED model in these regions mimic the effect of initial mixing of fuel and oxidizer streams in non-premixed combustion phenomena. As the oxidation of the furnace-side feed gradually proceeds to produce combustion products (i.e., carbon dioxide and water), the enthalpy of reactions is released causing the temperature of the furnace-side flow to increase, which allows the combustion phenomena to eventually overcome the activation energy barrier. Therefore, in the flame bodies, the finite rate formula is expected to yield higher estimates for the reaction rates of the furnace-side species than those based on the eddy-dissipation formulas. As a result, the premixed combustion model coupled with the FR/ED model allows the reformer CFD model to simulate the turbulent-mixing controlled characteristics of non-premixed combustion phenomena.

2.4.2 Radiative heat transfer modeling

In high-temperature applications such as SMR, the contribution of thermal radiation to the total heat transfer rate cannot be neglected. In Olivieri et al. [47], thermal radiation has also been reported as the dominant mode of heat transfer in a reformer as it accounts for about $\sim 95\%$ of the total heat transfer rate to the tube side. This is because the rates at which thermal energy is transferred by conduction and convection are known to be approximately proportional to the difference in temperature, while the rate of thermal energy transferred by radiation is proportional to the difference between the temperatures raised to the fourth power. Therefore, in the high-temperature combustion chamber of the reformer, thermal radiation would be expected to contribute significantly to heat transfer.

The study of radiative heat transfer is not often conducted experimentally for reformers because

Table 2.2: Furnace-side inlet operating conditions of the inner-lane burner in which $x_{comb,inlet}^i$ represents the mole fraction of species i in the furnace-side feed.

Pressure (kPa)	131.3
Temperature (K)	532.9
Flow rate (kg/s)	1.1358
$x_{comb,inlet}^{H_2O}$	0.0039
$x_{comb,inlet}^{O_2}$	0.1610
$x_{comb,inlet}^{Ar}$	0.0071
$x_{comb,inlet}^{N_2}$	0.6008
$x_{comb,inlet}^{H_2}$	0.0592
$x_{comb,inlet}^{CO_2}$	0.0972
$x_{comb,inlet}^{CO}$	0.0208
$x_{comb,inlet}^{CH_4}$	0.0501

of the severe operating temperature of 2050 K inside the reformer and the absence of an accurate means to measure the radiative heat transfer rate. Additionally, the only experimental data type related to the total heat transfer rate which can be collected from an on-line reformer may be the OTWT at a finite number of designated locations (e.g., three along the heated tube length of 12.5 m) [13]. This data is expected to carry a high degree of uncertainty because of the way by which the OTWT is measured, which involves a system of infrared cameras that gains access into the reformer to monitor the OTWT through peepholes in the combustion chamber refractory walls [35]. Therefore, the study of radiative heat transfer in reformers has been conducted primarily by a modeling approach.

To model thermal radiation, it is essential that the role of radiating media in thermal radiation is well understood. Specifically, radiating media, which can consist of various particle types (e.g., neutral molecules, ionic molecules, free electrons and atoms), participate in thermal radiation by absorbing or emitting radiative energy in the form of electromagnetic waves for which the

corresponding energy content denoted by E_{wave} can be evaluated as follows:

$$E_{wave} = h \cdot \nu_{wave} \quad (2.4)$$

where h is Planck's constant and ν_{wave} (s^{-1}) is the frequency of an electromagnetic wave. When a radiating particle absorbs/emits radiative energy, it absorbs/emits an electromagnetic wave, and its energy increases/decreases correspondingly by the amount of the electromagnetic wave. In air-fired reformers, radiating media (e.g., the furnace-side flow) can be assumed to be neutral molecules, and thus, the furnace-side flow can absorb an electromagnetic wave if the radiative energy content of the electromagnetic wave is equal to the transition energy required for the energy level to elevate to higher discrete bound states which correspond to the vibrational, rotational and electronic modes. Hence, radiative heat transfer in the furnace-side flow is spectrum dependent because the furnace-side flow only absorbs/emits radiative energy at certain frequencies in the entire spectrum. In the furnace-side flow, monatomic molecules (e.g., argon) and diatomic molecules (e.g., oxygen, nitrogen, hydrogen and carbon monoxide) can be considered to be transparent to radiation [43]. As a result, the furnace-side flow can be treated as a $H_2O - CO_2$ flow in the sense that the radiative properties of the furnace-side flow can be considered to depend only on those of H_2O and CO_2 (i.e., the furnace-side flow must be modeled as a radiatively participating medium with radiative properties developed from those of H_2O and CO_2).

The combustion modeling literature suggests that the radiative properties of the furnace-side flow can be estimated with the line-by-line model (LBLM), statistical narrow band model (SNBM) and exponential wide band model (EWBM); nevertheless, because of the excessively high required computational cost of utilizing these models for large-scale systems, they are not compatible with CFD models developed for industrially-oriented applications [43]. In the present work, a more computationally efficient empirical model developed in [43], which is designed for air-fired combustion systems, is utilized. The empirical model uses the temperature, composition and total pressure of the furnace-side flow and the characteristic dimension of the combustion chamber in the estimation of the total emissivity of the furnace-side flow. The results reported in [43] show

that the total emissivity of an air-fired combustion system calculated from the empirical model is within $\pm 5\%$ of the data generated by the SNBM, and the computing time is decreased by a factor of at least ten. Hence, the following empirical model for the total emissivity of the furnace-side flow is expected to offer a significant reduction in the computing time and to predict sufficiently accurate estimates of the furnace-side total emissivity:

$$a_i = a_{10,i} + a_{11,i} \cdot x_{comb}^{H_2O} + a_{12,i} \cdot x_{comb}^{CO_2} + a_{13,i} \cdot x_{comb}^{H_2O} \cdot x_{comb}^{CO_2} \quad (2.5a)$$

$$L = 3.6 \cdot \frac{V_{comb}}{A_{comb}} \quad (2.5b)$$

$$\begin{aligned} \varepsilon_{rad} = & a_1 + a_2 \cdot \ln(T_{comb}) + a_3 \cdot \ln(P_{comb}^t L) + a_4 \cdot [\ln(T_{comb})]^2 \\ & + a_5 \cdot [\ln(P_{comb}^t L)]^2 + a_6 \cdot \ln(T_{comb}) \cdot \ln(P_{comb}^t L) \end{aligned} \quad (2.5c)$$

where $a_{j,i}$ and a_i are the model constants of the empirical model as shown in Table 2.3, $x_{comb}^{H_2O}$ and $x_{comb}^{CO_2}$ are the mole fractions of water and carbon dioxide in the furnace-side flow, $V_{comb} \sim 3303.5 \text{ m}^3$, $A_{comb} \sim 5204.4 \text{ m}^2$ and $L \sim 2.3 \text{ m}$ are the volume, total surface area and characteristic dimension of the combustion chamber, respectively, and P_{comb}^t and ε_{rad} are the total pressure and total emissivity of the furnace-side flow. The empirical model of the furnace-side total emissivity is designed for air-fired combustion systems, and as a result, the total pressure inside the furnace chamber in [43] as well as in the present work is assumed to be constant and is taken to be near atmospheric pressure of 100 kPa (i.e., 1 bar).

Though the correlation of Eq. 2.5 depends on $x_{comb}^{CO_2}$ and $x_{comb}^{H_2O}$, which vary in the flame region of the furnace-side, the flame physical volume (i.e., the reaction zones of the combustion of the furnace-side feed) accounts for a small fraction of the total volume of the combustion chamber. Therefore, the region within which ε_{rad} would vary due to the changes in a_i , $i = 1, \dots, 6$, would be expected to be small compared to the dimensions of the furnace-side within which radiation is occurring. Furthermore, the difference in the furnace-side composition between the combustion product and the furnace-side feed is small, which is due to the fact that the inert gases (i.e., nitrogen

and argon) of the furnace-side feed account for $\sim 61.0\%$ of the total molar flow rate, while the fuel (i.e., methane and hydrogen) only accounts for $\sim 11.0\%$. Specifically, the differences in the average mole fractions of H_2O and CO_2 between the furnace-side feed and the combustion product change from 0.0039 to ~ 0.170 and from 0.0972 to ~ 0.175 , respectively. As a result, the change in ϵ_{rad} between its value at the furnace-side inlet conditions and the complete oxidation condition of the furnace-side feed is not expected to be necessary to account for within the radiation calculations, especially given the small flame volume over which ϵ_{rad} varies. Therefore, to reduce computation time, $x_{comb}^{H_2O}$ and $x_{comb}^{CO_2}$ are both approximated as constants at 0.170 and 0.175, respectively, in calculating ϵ_{rad} according to Eq. 2.5. Moreover, the characteristic dimension L of the reformer, which is estimated by Eq. 2.5b based on the volume and total enclosure surface area of the combustion chamber, is also a constant, as is P_{comb}^t . As a result, the furnace-side total emissivity reduces to a function only of the furnace-side temperature (it is noted that the approximation of a constant furnace-side composition in calculating ϵ_{rad} does not imply that other properties of the furnace-side flow should be modeled to be independent of composition; modeling the composition of the furnace-side is important in capturing, for example, the observed reaction rates of the furnace-side species, which determines the heat release profile of the combustion of the furnace-side feed).

Next, the absorption coefficient of the furnace-side flow is related to the value of ϵ_{rad} from the empirical model of Eq. 2.5 through Kirchhoff's law and Lambert Beer's Law as follows:

$$\sigma_a = -\frac{\ln(1 - \epsilon_{rad})}{L} \quad (2.6)$$

where σ_a is the absorption coefficient of the furnace-side flow. It is important to note that the correlation of the absorption coefficient in Eq. 2.6 inherits all assumptions that are used to develop the correlation of the total emissivity, and therefore, it is also a function of only the furnace-side temperature. Subsequently, an absorption coefficient data set within the operating temperature range of the reformer is obtained by the correlations of Eqs. 2.5 and 2.6 and is fit with a second-order polynomial function by using a least-squares linear regression method. The result of this fit is

$$\sigma_a = 2.10 \times 10^{-8} \cdot T_{comb}^2 - 2.06 \times 10^{-4} \cdot T_{comb} + 0.456, \quad (2.7)$$

which will be utilized in the reformer CFD model.

The next step in modeling radiation within the furnace side is choosing a suitable radiation model. The present work is facilitated by the ANSYS Fluent CFD solver, which only supports a limited number of thermal radiation models. Specifically, ANSYS Fluent uses one of five radiative heat transfer models (i.e., Rosseland, $P - 1$, discrete transfer radiation model (DTRM), surface to surface (S2S) model and discrete ordinate model (DOM)) to estimate the energy transferred by thermal radiation in high-temperature applications in which thermal radiation cannot be ignored. Among the five radiative heat transfer models, the DOM is the most versatile model [3]. In particular, the DOM can estimate heat transfer by radiation within absorbing, emitting and scattering media and between the participating media and opaque/semi-transparent walls. In addition, unlike the Rosseland and $P - 1$ approximation which are only applicable for high optical thickness systems, the DOM can be used in any high-temperature application including the reformer in which the optical thickness is not well-defined because of the complex reformer interior. Unlike the S2S model which ignores the presence of the participating media, the DOM can account for the effect of the absorbing and emitting furnace-side flow. Additionally, unlike the DTRM which uses the ray tracing technique and is more prone to error due to ray effects, the DOM converts the partial integro-differential radiative transfer equation (RTE) with seven independent variables into a finite number of transport equations of radiation intensity, which depends on the solid angle discretization parameters of the DOM. In particular, by default in each octant space the azimuthal division is equal to two, and the polar division is equal to two, which allows the DOM to generate 32 partial differential equations of radiation intensity corresponding to 32 discrete direction vectors \vec{s} specifying the directions at which energy is transferred by radiation. As a result, the radiative heat transfer rate obtained by solving the equations of radiation intensity is expected to require a relatively lower computational cost than is required to directly solve the RTE. In this work, radiative heat transfer between the furnace-side flow, combustion chamber refractory walls and outer

Table 2.3: Empirical constants of the correlation of the furnace-side flow total emissivity with temperature. These constants are used in the calculation of a_i (Eq. 2.5a) [43].

a_i	$a_{10,i}$	$a_{11,i}$	$a_{12,i}$	$a_{13,i}$
$i = 1$	-2.756	-12.091	-2.074	8.90
$i = 2$	1.0155	3.827	0.649	-2.48
$i = 3$	0.284	-1.024	0.421	-0.64
$i = 4$	-0.085	-0.286	-0.047	0.17
$i = 5$	0.0104	-0.067	-0.016	0.19
$i = 6$	-0.0272	0.162	-0.061	0.08

reforming tube walls will be quantified by the discrete ordinate method (DOM). The description of the DOM of an absorbing, emitting and non-scattering gray gas can be found in [3].

It is critical to a successful modeling task to realize that the internal emissivity of the wall surface is an intrinsic property of the surface, and therefore, it only depends on the surface's characteristics, e.g., the surface texture, instead of the surface material. In the reformer CFD model, the emissivity coefficients for the wall surfaces are assumed to be independent of the furnace-side temperature and are constant. Specifically, the emissivity coefficients of the reforming tubes, refractory wall and tunnel wall are chosen to be 0.85, 0.65 and 0.65, respectively, and additional physical properties of the refractory wall and tunnel wall are shown in Table 2.4 [35].

Table 2.4: Properties of the combustion chamber refractory walls.

Density (kg m^{-3})	3950
Heat Capacity ($\text{J kg}^{-1} \text{K}^{-1}$)	718
Thermal Conductivity ($\text{W m}^{-1} \text{K}^{-1}$)	2.6
Emissivity	0.65

2.5 Reforming tube modeling

In the present work, the 336 reforming tubes are modeled by the pseudo-homogeneous reactor model, the reforming tube walls are modeled by the ANSYS thin wall model, the catalyst network is modeled by the continuum approach and its effects on the tube-side flow are modeled by the ANSYS porous zone function. These modeling strategies were utilized due to their success in generating CFD data with good agreement with typical plant data for a single reforming tube with an assumed OTWT profile (i.e., the furnace-side and its interactions through heat transfer with the tube-side were not simulated) in [34]. In the remainder of this section, the modeling strategies of the kinetic model of SMR and the catalyst network are presented.

2.5.1 Reforming Reaction Kinetic Model

On the macroscopic scale, SMR consumes the thermal energy produced by the combustion of the furnace-side feed to convert steam and methane into hydrogen and carbon oxides in the presence of a nickel-based catalyst network, and the tube-side composition is reported to be close to the equilibrium composition at the reforming tube exit [64]. On the microscopic scale, the reactants are transported from the bulk of the tube-side flow to the surface of the catalyst network by convective mass transfer driven primarily by the reactant concentration gradients, which are generated by the external diffusion resistance of the catalyst network. Then, they diffuse down the second reactant concentration gradients from the surface of the catalyst network through the catalyst medium to the catalyst active sites, where SMR occurs to generate the desired hydrogen along with carbon oxides. The reactant concentration gradients within the catalyst are generated by the internal diffusion resistance of the catalyst network. Finally, the products diffuse from the catalyst active sites back to the surface of the catalyst network, and eventually emerge back into the tube-side flow. A kinetic model that provides a rate formula for each microscopic event of SMR is unsuitable for the reformer CFD simulation because it would be expected to require a significant computation time. Therefore, a global kinetic model of SMR proposed in [64], which is derived based

on the Langmuir-Hinshelwood mechanism (i.e., the heterogeneous catalysis kinetic model) and is formulated in $\text{kg} (\text{kg of catalyst})^{-1} \text{ s}^{-1}$, is utilized to lessen the computational demand without substantially sacrificing the accuracy of the simulation results:

$$\begin{aligned}
 & \text{CH}_4(\text{g}) + \text{H}_2\text{O}(\text{g}) \rightleftharpoons \text{CO}(\text{g}) + 3\text{H}_2(\text{g}), \\
 R_5 &= \frac{k_1}{\left(p_{\text{H}_2}^{\text{H}_2}\right)^{2.5}} \left(p_{\text{CH}_4}^{\text{CH}_4} p_{\text{H}_2\text{O}}^{\text{H}_2\text{O}} - \frac{\left(p_{\text{H}_2}^{\text{H}_2}\right)^3 p_{\text{CO}}^{\text{CO}}}{K_1} \right) / \text{DEN}^2 \quad (2.8a)
 \end{aligned}$$

$$\begin{aligned}
 & \text{CO}(\text{g}) + \text{H}_2\text{O}(\text{g}) \rightleftharpoons \text{CO}_2(\text{g}) + \text{H}_2(\text{g}), \\
 R_6 &= \frac{k_2}{p_{\text{H}_2}^{\text{H}_2}} \left(p_{\text{CO}}^{\text{CO}} p_{\text{H}_2\text{O}}^{\text{H}_2\text{O}} - \frac{p_{\text{H}_2}^{\text{H}_2} p_{\text{CO}_2}^{\text{CO}_2}}{K_2} \right) / \text{DEN}^2 \quad (2.8b)
 \end{aligned}$$

$$\begin{aligned}
 & \text{CH}_4(\text{g}) + 2\text{H}_2\text{O}(\text{g}) \rightleftharpoons \text{CO}_2(\text{g}) + 4\text{H}_2(\text{g}), \\
 R_7 &= \frac{k_3}{\left(p_{\text{H}_2}^{\text{H}_2}\right)^{3.5}} \left(p_{\text{CH}_4}^{\text{CH}_4} \left(p_{\text{H}_2\text{O}}^{\text{H}_2\text{O}}\right)^2 - \frac{\left(p_{\text{H}_2}^{\text{H}_2}\right)^4 p_{\text{CO}_2}^{\text{CO}_2}}{K_3} \right) / \text{DEN}^2 \quad (2.8c)
 \end{aligned}$$

$$\text{DEN} = 1 + \frac{K_{\text{H}_2\text{O}} p_{\text{H}_2\text{O}}^{\text{H}_2\text{O}}}{p_{\text{H}_2}^{\text{H}_2}} + K_{\text{CO}} p_{\text{CO}}^{\text{CO}} + K_{\text{H}_2} p_{\text{H}_2}^{\text{H}_2} + K_{\text{CH}_4} p_{\text{CH}_4}^{\text{CH}_4} \quad (2.8d)$$

where K_{H_2} , K_{CH_4} and K_{CO} are adsorption constants for H_2 , CH_4 and CO , $K_{\text{H}_2\text{O}}$ is a dissociative adsorption constant of H_2O , K_1 , K_2 , and K_3 are equilibrium constants of the reactions in Eqs. 2.8a, 2.8b and 2.8c, k_1 , k_2 and k_3 are forward kinetic constant coefficients of the reactions in Eqs. 2.8a, 2.8b, and 2.8c, respectively, DEN is a dimensionless parameter and $p_{\text{H}_2}^{\text{H}_2}$, $p_{\text{CH}_4}^{\text{CH}_4}$, $p_{\text{H}_2\text{O}}^{\text{H}_2\text{O}}$, $p_{\text{CO}}^{\text{CO}}$ and $p_{\text{CO}_2}^{\text{CO}_2}$ are the partial pressures of H_2 , CH_4 , H_2O , CO and CO_2 in the tube-side flow, respectively. This kinetic model is widely accepted [33] and is frequently used in CFD modeling and first-principles modeling of SMR because it accounts for the amount of the available catalyst. The kinetic model can also be modified to account for the external and internal diffusion resistances of the catalyst network by multiplying the kinetic formulas with a universal effectiveness factor of 0.1 [62]. However, unlike the global kinetic models of the methane and hydrogen combustion

phenomena, because the empirical kinetic formulas shown in Eq. 2.8 are not in the Arrhenius form, they cannot be directly integrated into the reformer CFD model. Nevertheless, ANSYS Fluent allows these non-Arrhenius form kinetic formulas to be integrated into the CFD model by means of user-defined functions, i.e., *DEFINE_VR_RATE* and *DEFINE_NET_REACTION_RATE*, to simulate the formation and consumption rates of the tube-side components. In [64], the complete list of the possible chemical reactions in SMR is provided, which does not contain any gas phase reaction. Additionally, the components of the tube-side flow (i.e., methane, superheated steam, carbon oxides and hydrogen) of SMR are naturally stable and will not undergo chemical reaction in the absence of the nickel-based catalyst. Therefore, gas phase reactions are not considered in the present work.

Inside the reforming tubes, the catalyst network with a uniform packing pattern disrupts the tube-side flow and enhances the mixing processes of the tube-side flow, and the Reynolds number at the reforming tube entrances is calculated to be $\sim 70,000$ based on the tube-side feed information detailed in [34]. Therefore, the tube-side flow is expected to be turbulent, and it is necessary to utilize a suitable turbulence-chemistry interaction model to simulate the tube-side species reaction rates under the influence of turbulent effects. Two turbulence-chemistry interaction models offered by ANSYS Fluent that may be appropriate for modeling turbulent effects on the tube-side species reaction rates are the FR/ED model and the EDC model. On one hand, the FR/ED model is expected to require less computation time, but is known to estimate observed reaction rates that deviate significantly from experimental data for some reactions with multiple dependent elementary reaction rates [3]. In contrast, the EDC model is expected to be more accurate because it can utilize detailed multi-step reaction kinetic models to determine the formation and consumption rates of the tube-side species in the turbulent reacting flow, but is computationally expensive. Additionally, the EDC model with default parameters is a robust turbulence-chemistry interaction model, and can be directly applied for a wide variety of reaction-limited and diffusion-limited systems [41]. The description of the EDC model can be found in [3]. Although the observed reaction rates of the tube-side species calculated from the EDC model are expected to have higher accuracy than those

calculated from the FR/ED model of Eq. 2.3, it is preferable for industrial applications to avoid integrating the EDC model in the reformer CFD model when that does not significantly impact the solution accuracy due to the corresponding increase in the required computational cost. In Section 2.6, the numerical error associated with the FR/ED model in the solution of the reformer CFD model is evaluated to determine that the FR/ED model is an appropriate chemistry-turbulence interaction model for the tube-side flow.

2.5.2 Porous Zone Design

In the reforming tubes, the nickel-based catalyst pellets are used as the packing material, and hence, it is essential to the development of the reformer CFD model that the effects of the catalyst network on SMR are well understood. Specifically, the catalyst network facilitates the formation of hydrogen from the naturally stable and slowly-reacting tube-side reactants, i.e., steam and methane, and it also enhances the rate of convective energy transfer from the reforming tube walls to the tube-side flow by increasing the contact area. Additionally, the catalyst network interferes with the tube-side flow, increases the residence time of the tube-side species and reduces the free volume. Furthermore, a pressure difference between the tube-side flow at the reforming tube inlet and outlet cannot be neglected due to the presence of the catalyst network inside the reforming tubes. Therefore, the effects of the catalyst on the momentum and energy transport equations of the tube-side must be accounted for. In the present work, the reforming tubes are modeled by the pseudo-homogeneous reactor model in which the solid phase (i.e., the catalyst network) is modeled by the continuum approach, and the effects of the catalyst network on the tube-side flow are modeled by the ANSYS porous zone function. The porous zone function modifies the standard governing equations of the pseudo-homogeneous reactor model to account for the presence and effects of the catalyst network on the tube-side flow (which will be discussed in Section 2.7.2). Although the modeling strategy does not require the catalyst pellets and the random packing pattern of the catalyst network to be modeled, the simulation data generated by the reforming tube CFD model is expected to capture the gradients of the tube-side composition and state variables at

the macroscopic scale typically larger than the equivalent dimension of the catalyst pellet [45]. The modeling strategy has been shown to be valid for packed-bed reactors in which the effective characteristic dimension of the catalyst pellets is less than 5 mm [54]. We have found that a reforming tube CFD model created from this modeling approach can simulate the macroscopic effects of the catalyst network on the tube-side flow (e.g., the pressure drop across the catalyst network and the increase of the tube-side residence time generated by the reforming tube CFD model are consistent with the typical plant data) [34]. In the reformer CFD model, the modeling parameters of the porous zone function are estimated from the semi-empirical Ergun equation [17]:

$$\frac{\Delta P_{tube}}{L_{tube}} = \frac{150\mu_{tube}}{D_p^2} \frac{(1-\gamma)^2}{\gamma^3} v_{\infty,tube} + \frac{1.75\rho_{tube}}{D_p} \frac{(1-\gamma)}{\gamma^3} v_{\infty,tube}^2 \quad (2.9)$$

where ΔP_{tube} (kPa) is the pressure difference of the tube-side flow across the catalyst network, $v_{\infty,tube}$ (m s^{-1}), ρ_{tube} (kg m^{-3}) and μ_{tube} ($\text{kg m}^{-1} \text{s}^{-1}$) are the average superficial velocity, density and viscosity of the tube-side flow at the reforming tube inlet and outlet, respectively, L_{tube} of 12.5 m is the reforming tube length, $\gamma=0.609$ is the porosity of the catalyst network and D_p (m) is an effective diameter of the catalyst pellets. Based on the pressure drop of the tube-side flow across the catalyst network from typical plant data, reforming tube geometry and available physical properties of the catalyst network reported in [34], the Ergun equation is employed to estimate the effective diameter of the catalyst pellets. Then, the modeling parameters of the porous zone function required by the reformer CFD model are calculated as follows,

$$\alpha = \frac{D_p^2}{150} \frac{\gamma^3}{(1-\gamma)^2} \quad (2.10a)$$

$$\beta = \frac{3.5}{D_p} \frac{(1-\gamma)}{\gamma^3} \quad (2.10b)$$

where $\alpha^{-1} \sim 8,782,800 \text{ m}^{-2}$ is the viscous resistance coefficient of the catalyst network and $\beta \sim 1,782 \text{ m}^{-1}$ is the inertial resistance coefficient of the catalyst network. It is noteworthy that because the semi-empirical Ergun equation is suitable for a wide range of Reynolds numbers and various

packing patterns [3], it is not necessary to model the detailed packing of the catalyst network within the reformer. In this CFD model, the catalyst network inside each reforming tube is assumed to have a uniform packing structure and to be functioning properly (i.e., no deactivation or sintering occurs). Hence, the coefficients of viscous resistance and inertial resistance of the catalyst network can be assumed to be constant and uniform along the axial and radial directions.

Table 2.5: Johnson Matthey's Katalco 23 – 4Q catalyst properties.

Density (kg m^{-3})	3960
Heat Capacity ($\text{J kg}^{-1} \text{K}^{-1}$)	880
Thermal Conductivity ($\text{W m}^{-1} \text{K}^{-1}$)	33
Particle Diameter (mm)	3.5

2.6 Equation of state and turbulence-chemistry interaction model

In this section, we present the procedure by which the thermodynamic and turbulence-chemistry interaction models are selected for the reformer CFD model. The modeling considerations that motivate the analysis of multiple equations of state and turbulence-chemistry interaction models are discussed. Finally, a strategy to obtain the necessary numerical evidence, which is subsequently analyzed to determine the solutions for the modeling challenges, is proposed.

The first modeling consideration is the choice of an equation of state for describing the thermodynamics of the furnace-side and tube-side flows in the reformer. In the combustion chamber of the reformer, the maximum temperature of the furnace-side flow is approximately 2050 K due to the thermal energy released by the rapid oxidation of the furnace-side feed, and the operating pressure is designed to be nearly at atmospheric pressure at ~ 132 kPa. Therefore, the furnace-side flow can be assumed to possess incompressible ideal gas characteristics. On the contrary, the thermodynamic behavior of the tube-side flow is speculated to deviate significantly from that governed by the incompressible ideal gas law due to the high operating pressure inside the reforming tubes (i.e., $\sim 3,000$ kPa), which is ~ 25 - 28 times higher than that of the combustion chamber [35]. Specifically, the tube-side density at high operating pressure of the reforming tubes is expected to be significantly different from the estimated density by the incompressible ideal gas law using the reference state of 298 K. It is critical to the development of the reformer CFD model that the adopted equation of state accurately predicts the thermodynamics of turbulent reacting flows inside both the combustion chamber and reforming tubes because SMR is expected to reach equilibrium at the reforming tube outlets. In an effort to choose an appropriate equation of state, two potential thermodynamic models, i.e., the compressible ideal gas and the real gas Soave-Redlich-Kwong (SRK) equations of state, are selected. It is important to note that the real gas SRK model predicts more accurate fluid properties than the compressible ideal gas model and is frequently employed for determining fluid thermodynamic properties for industrial applications. Nevertheless, the required computational cost of the real gas SRK model is higher than that of the compressible ideal gas

model; the former thermodynamic model should be integrated into the reformer CFD model only when the latter model is proven to be inadequate for obtaining accurate results.

The second modeling consideration is the selection of an appropriate turbulence-chemistry interaction model. As discussed in Secs. 2.4.1 and 2.5.1, the FR/ED and EDC models are two viable models for these phenomena, but the FR/ED model may produce inaccurate results, though it is expected to have a lower computational time than the EDC model.

To evaluate whether the less computationally intensive modeling strategies (compressible ideal gas and FR/ED models) can be expected to produce sufficiently accurate results, we could develop one reformer CFD model that uses the more computationally intensive modeling strategies (i.e., the SRK and EDC models) and one that uses the less computationally intensive modeling strategies. The results could then be compared to analyze the impact on the CFD numerical results of utilizing the more rigorous SRK and EDC models compared to utilizing the less accurate (but more suitable in terms of computational cost, computing time, and memory capacity for industrial applications) compressible ideal gas and FR/ED models. Nevertheless, the available computational power (i.e., 80 cores on UCLA's Hoffman2 Cluster) and memory capacity (i.e., 20.0 GB on UCLA's Hoffman2 Cluster) are not expected to be sufficient to simulate the reformer CFD model with the more computationally intensive modeling strategies in a timely manner because the reformer mesh is composed of 29,099,252 hexahedral grids, 88,798,168 quadrilateral faces and 30,584,930 nodes. Consequently, it is not practical to employ the reformer CFD model that uses the more computationally intensive modeling strategies as a means to obtain the necessary numerical evidence, which would subsequently be used as a basis for selection of the appropriate models. As an alternative for assessing the expected order of magnitude of differences in the CFD numerical results when employing the more computationally intensive versus less computationally intensive modeling strategies, we would like to use a part of the reformer domain (e.g., a single reforming tube) to analyze both types of thermodynamic and chemistry-turbulence interaction models. However, the transport phenomena of the reforming tubes of the reformer CFD model are coupled and thus a single reforming tube from the reformer model could not be simu-

lated individually. Therefore, a CFD model of a single industrial-scale reforming tube developed from our previous work [34] using modeling strategies similar to those employed for modeling the reforming tubes of the reformer CFD model is readily available and will be used in the remainder of this section for assessing whether the more or less computationally intensive modeling strategies will be chosen for the reformer CFD model.

Before utilizing the industrial-scale reforming tube from [34] to assess the appropriateness of the more and less computationally intensive thermodynamic and turbulence-chemistry interaction models for the reformer CFD model, the differences between the industrial-scale reforming tube mesh and modeling strategies and those of the reformer CFD model are discussed to demonstrate the large reduction in the computation time offered by the industrial-scale reforming tube CFD model. Three key differences between the reformer mesh and industrial-scale reforming tube mesh are the shape of the subdomains, the number of the subdomains and the mesh quality. Specifically, the industrial-scale reforming tube mesh developed in [34] is the 2-D axisymmetric quadrilateral structured mesh, and the reformer CFD mesh is the 3-D hexahedral structured mesh. Additionally, the industrial-scale reforming tube mesh consists of ~ 23 thousand subdomains, and the reformer mesh has ~ 29 million subdomains, which corresponds to a cell count that is ~ 1264 times higher than that of the former mesh. Moreover, the mesh quality of the industrial-scale reforming tube mesh reported in [34] is nearly ideal based on the three suggested criteria (i.e., the orthogonal factor, aspect ratio and ortho skew) and is better than that of the reformer mesh shown in Table 2.1. Therefore, the industrial-scale reforming tube CFD model serves as an effective tool to quantify the magnitude of the numerical error introduced in the CFD simulation data when the computationally less intensive modeling strategies (i.e., the compressible ideal gas model and the FR/ED model) are implemented, and the industrial-scale reforming tube CFD model is expected to have a faster speed of convergence than that of the reformer CFD model, making the analysis possible in a reasonable time frame.

In this effort, two industrial-scale reforming tube CFD models are developed, one of which utilizes the SRK and EDC models, and the other of which uses the compressible ideal gas and

FR/ED models (for brevity, the former and latter CFD models will be referred to as the original and simplified tube CFD models, respectively). In this study, all boundary conditions of the tube CFD models (i.e., the OTWT and the tube-side feed conditions) are derived from typical plant data [34], and the modeling strategies are identical to those of the reformer CFD model. The simulation results generated by the original and simplified tube CFD models are shown in Table 2.6. The deviations of the simulation results generated by the simplified tube CFD model with respect to the data generated by the original tube CFD model are considered to be insignificant. However, the computational benefits of utilizing the simplified tube CFD model compared to using the original tube CFD model are noticeable. Specifically, the original tube CFD model takes 1100 iterations and 650 seconds of computing time to reach the converged solution, while the simplified tube CFD model only takes 871 iterations and 320 seconds. This result shows that the simplified tube CFD model offers a 20% reduction in the number of iterations and a 50% reduction in the computing time required for the simulation to reach the converged solution and yields similar simulation data compared to the original tube CFD model. As a result, the compressible ideal gas and FR/ED models are integrated in the reformer CFD model to describe the thermodynamics and reaction rates of individual species in the turbulent reacting flows of both the tube-side and furnace-side flows.

The most prominent difference in the modeling strategies of the industrial-scale reforming tube mesh and of a reforming tube in the reformer CFD model is that the industrial-scale reforming tube assumes a tube wall temperature profile along the reforming tube length whereas the reforming tubes in the reformer exhibit a temperature profile dependent on the furnace-side environment which is simultaneously calculated. Though these differences in the mesh and modeling strategies exist, they are not expected to significantly impact the order of magnitude of numerical differences in the CFD results for the industrial-scale reforming tube using the more and less computationally intensive modeling strategies compared to the order of magnitude of the differences that would be observed using a reforming tube from the reformer model. Furthermore, the order of magnitude of the results utilizing a single reforming tube would be expected to be indicative of the order of

Table 2.6: Simulation results of the original and simplified tube CFD models in which $\bar{P}_{tube,inlet}$ and $\bar{x}_{tube,outlet}^i$ represent the radial-weighted average inlet pressure and outlet mole fraction of species i in the tube-side flow.

	Original tube CFD model [*]	Simplified tube CFD model	Difference (% , with respect to *)
ΔP_{tube} (kPa)	204.2	210.3	3.00
$\bar{P}_{tube,inlet}$ (kPa)	2958.2	2964.3	0.21
Average heat flux (kW m ⁻²)	69.506	68.423	1.56
$\bar{x}_{tube,outlet}^{H_2}$	0.470	0.469	0.33
$\bar{x}_{tube,outlet}^{H_2O}$	0.341	0.341	0.00
$\bar{x}_{tube,outlet}^{CH_4}$	0.043	0.044	3.44
$\bar{x}_{tube,outlet}^{CO}$	0.088	0.087	1.18
$\bar{x}_{tube,outlet}^{CO_2}$	0.058	0.059	1.43

magnitude of differences that would be expected on the furnace-side as well, particularly since the equation of state is not expected to pose an issue on the furnace side due to the relatively low pressures in that domain.

2.7 Governing equations of reformer

The reformer mathematical model consists of two sets of highly non-linear coupled partial integro-differential equations with seven independent variables as discussed in Section 2.1. Specifically, one of the two equation sets represents the combustion chamber model, and the other is the reforming tube model. In this section, we present the equations of continuity and of momentum, energy, and species material conservation that employ parameters or variables calculated from the modeling strategies discussed in the prior sections to characterize the mass, flow, heat and species transport within the reformer. The physical properties of individual species in these equations in the tube-side and furnace-side flows are imported from the ANSYS Fluent database materials. Subsequently, the physical properties of the tube-side and furnace-side flows are computed based on those of the corresponding constituents, ideal gas mixing law (in the case of the thermal conductivities and viscosities) and kinetic theory (in the case of the diffusion coefficients). Inside the combustion chamber and reforming tubes, the flow profiles are speculated to be turbulent as discussed in Secs. 2.4.1 and 2.5.1, and thus, the state variables (e.g., temperature, pressure, internal energy, enthalpy, and entropy) and fluid properties (i.e., velocity, density and species concentration) fluctuate about their corresponding time-averaged values. In the present work, the standard $k - \varepsilon$ turbulence model developed from the Reynolds-averaged Navier-Stokes (RANS) equations and the Boussinesq hypothesis is integrated in the reformer CFD model to characterize the furnace-side and tube-side turbulent reacting flows, which allows the reformer CFD model to simulate the effects of turbulence on the transport and chemical reaction phenomena [29, 36, 3]. The standard $k - \varepsilon$ model is selected because it is a robust turbulence model, it requires lower computational resources compared to the realizable $k - \varepsilon$ model (i.e., relatively longer computing time), RNG $k - \varepsilon$ model (i.e., 15% more computing time) and Reynolds stress model (i.e., 50%-60% more computing time), and it is expected to yield reasonably accurate predictions for a wide range of turbulent flows [3]. Additionally, the $k - \varepsilon$ model is expected to be suitable when there are not extreme pressure gradients within the fluid [3], which we do not expect to observe on either the

tube side or furnace side of the reformer because the ratios between the pressure drop and the inlet pressure of the tube-side feed and furnace-side feed are $\sim 5\%$ and $\sim 0\%$, respectively, based on the typical plant data [35]. In the present work, the enhanced wall treatment option of the standard $k - \varepsilon$ model is used to improve the model accuracy at the regions near the walls. Therefore, though the ideal dimensionless distance from the wall to the first interior node (denoted by y^+) everywhere in the reformer mesh is recommended by ANSYS Fluent to be ~ 1 , the use of the $k - \varepsilon$ model with enhanced wall treatment allows the accuracy of the CFD data to be less sensitive to the y^+ value, which allows for the y^+ value of the reformer mesh to be greater than 1 and allows the cell count in the reformer mesh to be reduced compared to the case that the y^+ value is ~ 1 . In the present work, the initial guess of the grid size is obtained from NASA's viscous grid spacing calculator based on the Reynolds number of the furnace-side flow at the inner-lane burner inlet ($Re = 240,000$), the diameter of the inner-lane burner inlet and the desired value of y^+ , which varies between 30 and 60. The grid size is further adjusted by a trial-and-error approach during the trial simulations of the reformer CFD model to ensure that the convergence criteria defined in Section 2.8 can be reached. From the simulation results, the average y^+ values at the outer reforming tube wall and the interior wall of the combustion chamber obtained from the CFD simulation data were 20.8 and 58.9, respectively. The reformer mathematical model accounts for transport phenomena frequently observed in high-operating-temperature applications in addition to the essential reformer-related considerations discussed at length in Secs. 2.4.1, 2.4.2, 2.5.1 and 2.5.2. In the remainder of this section, the combustion chamber model and the reforming tube model are presented.

2.7.1 Furnace Chamber

The combustion chamber model developed in this work can simulate the mixing-controlled characteristics of non-premixed combustion phenomena, radiative heat transfer between the furnace-side flow, outer reforming tube walls and combustion chamber refractory inner walls, in addition to other heat transfer mechanisms observed in reformers (e.g., convective and conductive heat transfer). Based on the above considerations and those discussed in Section 2.4 and Section 2.6,

the combustion chamber model including the continuity equation (Eq. 2.11a), the momentum (Eq. 2.11b), energy (Eq. 2.11c) and species (Eq. 2.11d) conservation equations, and the turbulence model (Eq. 2.11e and Eq. 2.11f) required for characterizing the heat and fluid-flow fields as well as composition inside the combustion chamber are formulated as follows:

Continuity equation:

$$\frac{\partial}{\partial t}(\rho_{comb}) + \nabla \cdot (\rho_{comb} \vec{v}_{comb}) = 0 \quad (2.11a)$$

Momentum conservation equation:

$$\frac{\partial}{\partial t}(\rho_{comb} \vec{v}_{comb}) + \nabla \cdot (\rho_{comb} \vec{v}_{comb} \vec{v}_{comb}) = -\nabla P_{comb} + \nabla \cdot \bar{\bar{\tau}}_{comb} + \rho_{comb} \vec{g} \quad (2.11b)$$

Energy conservation equation:

$$\begin{aligned} \frac{\partial}{\partial t}(\rho_{comb} E_{comb}) + \nabla \cdot (\vec{v}_{comb}(\rho_{comb} E_{comb} + P_{comb})) = \\ \nabla \cdot \left[k_{comb}^{eff} \nabla T_{comb} - \left(\sum_i h_{comb}^i \vec{J}_{comb}^i \right) + (\bar{\bar{\tau}}_{comb} \cdot \vec{v}_{comb}) \right] + S_{comb}^{h,rxn} + \nabla \cdot \vec{q}_{rad} \end{aligned} \quad (2.11c)$$

Species material conservation equation:

$$\frac{\partial}{\partial t}(\rho_{comb} Y_{comb}^i) + \nabla \cdot (\rho_{comb} \vec{v}_{comb} Y_{comb}^i) = -\nabla \cdot (\vec{J}_{comb}^i) + R_{comb}^i \quad (2.11d)$$

Transport equations of the standard $k - \varepsilon$ turbulence model:

$$\frac{\partial}{\partial t}(\rho_{comb} k_{comb}) + \nabla \cdot (\rho_{comb} k_{comb} \vec{v}_{comb}) = \quad (2.11e)$$

$$\nabla \cdot \left[\left(\mu_{comb} + \frac{\mu_{comb}^t}{\sigma_k} \right) \nabla k_{comb} \right] + G_{comb}^k + G_{comb}^b - \rho_{comb} \varepsilon_{comb}$$

$$\frac{\partial}{\partial t}(\rho_{comb} \varepsilon_{comb}) + \nabla \cdot (\rho_{comb} \varepsilon_{comb} \vec{v}_{comb}) = \quad (2.11f)$$

$$\nabla \cdot \left[\left(\mu_{comb} + \frac{\mu_{comb}^t}{\sigma_\varepsilon} \right) \nabla \varepsilon_{comb} \right] + C_{1\varepsilon} \frac{\varepsilon_{comb}}{k_{comb}} G_{comb}^k - C_{2\varepsilon} \rho_{comb} \frac{\varepsilon_{comb}^2}{k_{comb}} \quad (2.11g)$$

$$\vec{J}_{comb}^i = \left(\rho_{comb} D_{comb}^{m,i} + \frac{\mu_{comb}^t}{Sc_{comb}^t} \right) \nabla Y_{comb}^i \quad (2.12a)$$

$$\bar{\tau}_{comb} = \mu_{comb} \left[(\nabla \vec{v}_{comb} + \nabla \vec{v}_{comb}^T) - \frac{2}{3} \nabla \cdot \vec{v}_{comb} I \right] \quad (2.12b)$$

$$E_{comb} = h_{comb} + \frac{v_{comb}^2}{2} - \frac{P_{comb}}{\rho_{comb}} \quad (2.12c)$$

$$h_{comb} = \sum_j Y_{comb}^j h_{comb}^j \quad (2.12d)$$

$$h_{comb}^j(T_{comb}) = \int_{T_{ref}}^{T_{comb}} C_{p,comb}^j dT \text{ with } T_{ref} = 298.15 \text{ K} \quad (2.12e)$$

$$S_{comb}^{h,rxn} = - \sum_j \frac{h_j^f}{M_j} R_{comb}^j \quad (2.12f)$$

$$R_{comb}^j = \sum_k^3 v_{comb}^{k,j} R_{comb}^{k,j} \quad (2.12g)$$

$$k_{comb}^{eff} = k_{comb}^l + k_{comb}^t \quad (2.12h)$$

$$k_{comb}^t = \frac{C_{p,comb} \mu_{comb}^t}{Pr_t} \quad (2.12i)$$

$$\mu_{comb}^t = \rho_{comb} C_\mu \frac{k_{comb}^2}{\epsilon_{comb}} \quad (2.12j)$$

$$G_{comb}^k = - \rho_{comb} \frac{v_{comb,i}' v_{comb,j}'}{\partial x_i} \frac{\partial v_{comb,j}}{\partial x_i} \quad (2.12k)$$

$$G_{comb}^b = \beta' g_i \frac{\mu_{comb}^t}{Pr_t} \frac{\partial T_{comb}}{\partial x_i} \quad (2.12l)$$

where \vec{v}_{comb} (m s^{-1}), μ_{comb} ($\text{kg m}^{-1} \text{s}^{-1}$), μ_{comb}^t ($\text{kg m}^{-1} \text{s}^{-1}$), k_{comb}^{eff} ($\text{W m}^{-1} \text{K}^{-1}$), k_{comb}^l ($\text{W m}^{-1} \text{K}^{-1}$), k_{comb}^t ($\text{W m}^{-1} \text{K}^{-1}$), $C_{p,comb}$ ($\text{J kg}^{-1} \text{K}^{-1}$), T_{comb} (K) and P_{comb} (kPa) are the furnace-side flow mass-averaged velocity, laminar flow viscosity, turbulent flow viscosity (calculated as shown in Eq. 2.12j), effective thermal conductivity (estimated as shown in Eq. 2.12h), laminar thermal conductivity, turbulent thermal conductivity (estimated as shown in Eq. 2.12i), specific heat capacity, temperature and pressure of the furnace-side flow in the combustion chamber, respectively, \vec{g} is the universal gravitational acceleration, $\bar{\tau}_{comb}$ is the stress tensor (estimated as shown in Eq. 2.12b), and I is the unit tensor. The combustion chamber model accounts for all reformer-relevant modes

of momentum, energy and material transport phenomena under the influence of chemical phenomena and turbulence to characterize the dynamics of the chamber. Specifically, the turbulent mass diffusion flux of species i , \vec{J}_{comb}^i , driven by concentration gradients, is shown in Eq. 2.12a, where Y_{comb}^i and $D_{comb}^{m,i}$ are the furnace-side mass fraction and laminar mass diffusion coefficient of species i , respectively. It is necessary to note that the ratio $\frac{\mu_{comb}^t}{Sc_{comb}^t}$, in which Sc_{comb}^t and μ_{comb}^t are the turbulent Schmidt number and turbulent viscosity of the furnace-side flow, is used to account for the effect of turbulence on the mass diffusion flux of species i , and therefore, it can be written as $\rho_{comb} D_{comb}^{m,t}$ where $D_{comb}^{m,t}$ is the turbulent mass diffusion coefficient. Additionally, the specific internal energy (E_{comb}) of the furnace-side flow which can be computed as the sum of the furnace-side specific sensible enthalpy (h_{comb}) which depends on the furnace-side specific sensible enthalpy of species j at temperature T_{comb} ($h_{comb}^j(T_{comb})$), specific kinetic energy ($v_{comb}^2/2$) and external work per unit weight of the furnace-side flow ($-P_{comb}/\rho_{comb}$), is shown in Eq. 2.12c, Eq. 2.12d and Eq. 2.12e. It is important to note that the value of $T_{ref} = 298.15 K$ in Eq. 2.12e is chosen automatically by ANSYS Fluent's parallel/pressure based solver, and $C_{p,comb}^j$ is the heat capacity of species j in the combustion chamber. In addition, from Eq. 2.11c, $\nabla \cdot (k_{comb}^{eff} \nabla T_{comb})$, $-\nabla \cdot (\sum_i h_{comb}^i \vec{J}_{comb}^i)$, $\nabla \cdot (\bar{\tau}_{comb} \cdot \vec{v}_{comb})$ and $\nabla \cdot \vec{q}_{rad}$ represent four distinct mechanisms, i.e., conduction, species diffusion, viscous dissipation and radiation respectively, through which energy is transferred. Furthermore, the overall rate at which thermal energy is released from combustion processes inside the combustion chamber, $S_{comb}^{h,rxn}$, is computed as shown in Eq. 2.12f in which R_{comb}^j and h_j^f represent the overall volumetric consumption/formation rate and enthalpy of formation of species j , and $v_{comb}^{k,j}$ and $R_{comb}^{k,j}$ are the stoichiometric coefficient and volumetric consumption/formation rate of species j in reaction k . It is noteworthy that $R_{comb}^{k,j}$ is determined by the FR/ED turbulence-chemistry interaction model (Section 2.4.1). Transport equations of the standard $k - \varepsilon$ turbulence model are presented in Eq. 2.11e and Eq. 2.11f, in which k_{comb} and ε_{comb} are the turbulence kinetic energy and turbulence dissipation rate of the furnace-side flow, β' is the coefficient of thermal expansion of the furnace-side flow, $\sigma_k = 1.3$ and $\sigma_\varepsilon = 1.0$ are the default values of the turbulent Prandtl numbers for k_{comb} and ε_{comb} , $C_{1\varepsilon} = 1.44$, $C_{2\varepsilon} = 1.92$, $C_\mu = 0.09$ and

$Pr_t = 0.85$ are default constants of the standard $k - \varepsilon$ turbulence model, respectively, and G_{comb}^k and G_{comb}^b represent the generation of turbulence kinetic energy in the furnace-side flow due to the mean velocity gradients (Eq. 2.12k) and buoyancy effect (Eq. 2.12l). The standard $k - \varepsilon$ turbulence model can capture the characteristic parameters of turbulent reacting flow profiles. Specifically, in Eq. 2.12k, the term $-\rho_{comb} \overline{v'_{comb,i} v'_{comb,j}}$ is the Reynolds stress representing the effect of turbulence on the velocity profile of the furnace-side flow that arises from the RANS equations, and $\overline{v'_{comb,i}}$ is the time-averaged fluctuating component of \vec{v}_{comb} in the x_i direction. It is worth noting that all default constants of the standard $k - \varepsilon$ turbulence model are determined empirically by experiments for fundamental turbulent flows, and have been shown to be suitable for a wide range of wall-bounded and free shear flow applications [3].

2.7.2 Reforming Tube

In the present work, the effects of the catalyst network on the tube-side transport phenomena are accounted for by the ANSYS porous zone function, which includes the additional momentum sink term in the momentum conservation equation of the reforming tube model to simulate the interference effect of the catalyst network, which decreases the superficial velocity and increases the residence time of the tube-side species. In addition, the energy conservation equation of the reforming tube model is affected by the porous zone function to include an additional transient term to account for the thermal inertia of the catalyst network and to use the effective thermal conductivity to account for the presence of the catalyst network. Moreover, the tube-side species material balances of the reforming tube model use the overall effectiveness factor (η) to account for the internal and external mass transfer resistances of the catalyst network and the catalyst packing factor ($(1 - \gamma) \rho_{cat}$) to convert the surface reaction rates from Eq. 2.8 to volumetric reaction rates (i.e., $\text{kg m}^{-3}\text{h}^{-1}$) that are employed within the FR/ED turbulence-chemistry interaction model for use within the species material balances. These approximations of the effects of the catalyst network on the transport equations and species balances were also utilized in the development of the industrial-scale reforming tube CFD model for which the simulation results have been shown

to be in good agreement with typical plant data [34], and thus these approximations are expected to be sufficient for the reforming tubes of the reformer CFD model. The reforming tube walls are modeled by the ANSYS thin wall model in which the thermal resistance of the reforming tube wall and the temperature profile across the reforming tube wall thickness can be estimated without meshing the reforming tube wall explicitly. In the simulation of the reforming tube CFD model, the ANSYS thin wall model creates an artificial wall thickness for the reforming tubes, and the ANSYS Fluent solver utilizes the 1-D steady heat conduction equation to determine the reforming tube wall thermal resistance based on the specified artificial wall thickness and material of the reforming tubes. This modeling strategy is utilized because the wall thickness is negligible compared to other dimensions of the system (the ratio of the reforming tube exposed length and wall thickness is $\sim 1250:1$, and the ratio of the reforming tube diameter and wall thickness is $\sim 13:1$). This modeling strategy for the tube wall affects the boundary conditions of the reforming tube walls when solving the heat transfer equations. Radiation is neglected in the energy balance equation for the tube side [54, 33, 45] because the nickel-based catalyst network expands the contact area between the tube-side flow and the inner reforming tube wall, with the result that convective heat transfer is expected to be the dominant mode. Based on the above considerations and those discussed in Section 2.5 and Section 2.6, the governing equations including the continuity equation and the momentum, energy and tube-side species balances, and the turbulence model required to simulate SMR inside the reforming tubes, are constructed in a similar manner to that of the combustion chamber, which has been described in Section 2.7.1. Additionally, the governing equations of the tube-side flow have also been explicitly presented in our recent publication [34], and therefore, they are not repeated here for brevity.

2.8 Process simulation

Intuitively, the CFD solution of the reformer CFD model would be obtained by simulating the reformer CFD model until convergence criteria are satisfied. However, the reformer CFD model has been found to be very sensitive to the initial guess (e.g., the simulation of the reformer CFD model with the initial guess automatically generated by the ANSYS Fluent standard initialization function based on the boundary conditions of the CFD model is often unstable and is likely to quickly diverge). Although ANSYS Fluent allows a conservative mode of the ANSYS Fluent solver to be selected to prevent the reformer CFD simulation from diverging, this strategy often results in a substantial increase in the required computing time to calculate the converged solution of the reformer CFD model, and therefore, forfeits the potential of the reformer CFD model for industrial interests. In this work, a step-by-step converging strategy that allows the implementation of an aggressive mode of the ANSYS Fluent solver to compute the reformer CFD steady-state solution is proposed as shown in Fig. 2.5. Specifically, the step-by-step converging strategy is an optimized procedure that is designed to resolve the instability issue of the reformer CFD simulation, to accelerate the rate of convergence and to minimize the required computing time to obtain the converged solution of the reformer CFD model. Initially, an isothermal, non-reacting (INR) reformer CFD model is created by deactivating the combustion phenomena, radiative heat transfer and SMR kinetic models in addition to excluding the energy conservation equations from the furnace-side and tube-side models. Then, the simulation of the INR reformer CFD model is initialized with the initial guess generated by the ANSYS Fluent standard initialization function based on the tube-side and furnace-side feeds, and is solved by the aggressive mode of the ANSYS Fluent solver. In this work, the reformer CFD simulation is said to reach the converged solution when the global normalized residuals of all transport variables computed over all subdomains of the reformer between two consecutive iterations are less than 10^{-4} , the mass flow rate integrated over all boundaries of the reformer CFD model is approximately zero, the total heat transfer rate integrated over all boundaries of the reformer CFD model is less than 1% of the reformer total fired duty and the absolute

residuals of the furnace-side temperature at five different locations inside the combustion chamber are less than 1 K. Next, the converged solution of the INR reformer CFD model is utilized as an initial guess for the succeeding non-reacting (NR) CFD model because even though the composition and temperature fields in the INR reformer CFD model are different from those in the NR reformer CFD model, their velocity and turbulence fields are expected to be similar [3, 60]. Analogously, the converged reformer CFD solution in each preceding step is utilized as an initial guess for the reformer CFD model in the subsequent step until the converged solution of the complete reformer CFD model is obtained.

The solution of the reformer CFD model is obtained after ~ 72 hours of computing time by the ANSYS Fluent parallel solver with a computational power of 80 cores on UCLA's Hoffman2 Cluster. During the initialization procedure of the reformer CFD model, the ANSYS Fluent solver arbitrarily selects one of the available 80 cores as a host process and designates the remaining 79 cores as compute-node processes. It is noteworthy that the host process is only responsible for interpreting the user's commands given in the graphical user interface (GUI), then redistributing them to all compute-node processes by a message-passing library, e.g., the Message Passing Interface (MPI). Thus, the reformer mesh is partitioned into 79 parts corresponding to the number of available compute-node processes, and each partition consisting of $\sim 368,345$ grids is assigned to a different compute-node process. Then, the compute-node processes consider each grid within the corresponding partitions as an open system in which the reformer mathematical model is discretized by the finite volume method and numerically solved until the convergence criteria are satisfied. The corresponding solutions of the grids are recombined to generate the simulation results of the reformer CFD model.

2.9 Simulation results

In this section, the steady-state simulation results of the reformer CFD model with the furnace-side and tube-side operating conditions and properties as shown in Tables 2.2–2.7 are presented.

Two cross-sectional planes (i.e., the frontal and lateral planes) of the combustion chamber as shown in Fig. 2.6 are designated along which the properties of the furnace-side flow are presented. Specifically, the furnace-side temperature contour maps (lateral and frontal planes) are shown in Fig. 2.7. The contour maps of the thermal energy released by the oxidation of the furnace-side feed are shown in Fig. 2.8. In addition, the furnace-side velocity magnitude vector plots are shown in Fig. 2.9, and the furnace-side species contour maps are shown in Figs. 2.10–2.13.

The properties of the interior of a reforming tube are displayed for a cross-sectional plane along the axial direction of a reforming tube. Because the dimension of the heated reforming tube length is ~ 85 times longer than that of the reforming tube diameter, the radial dimension of the reforming tube cross section is scaled up by 20 times for display purposes. The tube-side pressure contour map is shown in Fig. 2.14. The radially uniform pressure profile inside the reforming tubes is the result of the uniformly packed catalyst network assumption, and the definition of the porous zone with uniform coefficients of viscous resistance and inertial resistance of the catalyst network along the axial and radial directions as presented in Section 2.5.2.

Lastly, the average composition profiles of the tube-side flow are shown in Fig. 2.15, and the average temperature profiles of the outer and inner reforming tube walls and the furnace-side and tube-side flows are shown in Fig. 2.16. Fig. 2.16 suggests that the maximum temperature of the outer reforming tube wall of ~ 1180 K is below the maximum allowable operating temperature of ~ 1300 K [53]; if the outer reforming tube wall were to exceed the maximum temperature for a sufficient length of time, the reforming tube would rupture more quickly than if it were kept below

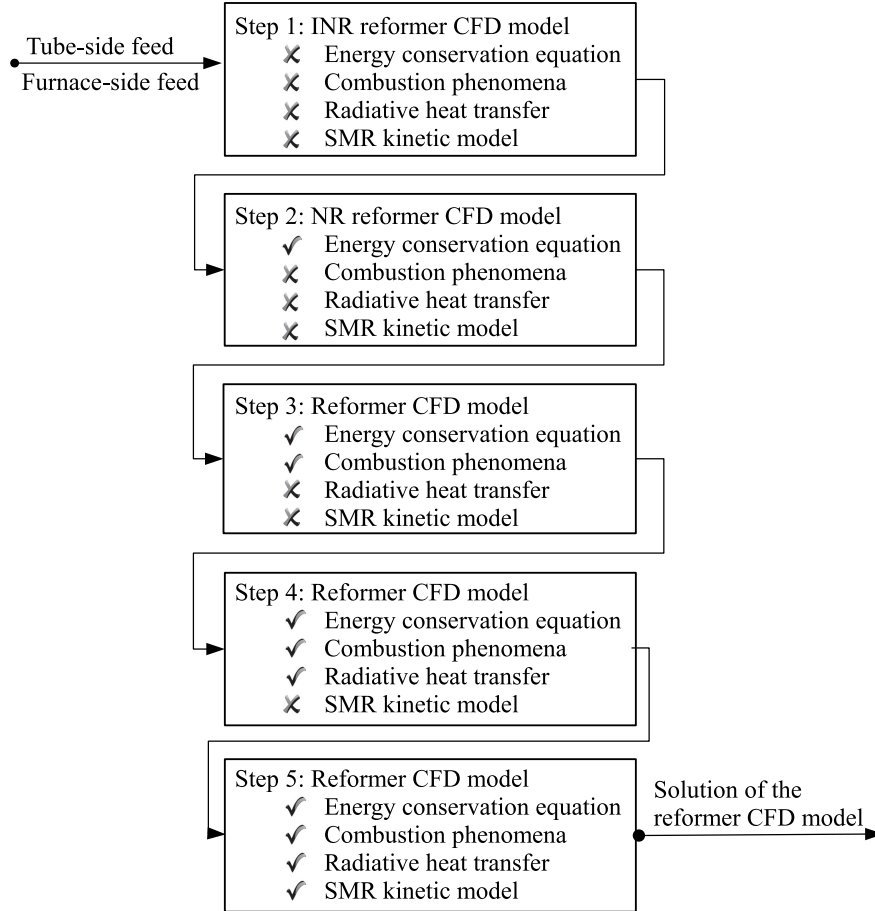


Figure 2.5: Step-by-step converging strategy designed to resolve the initial instability issue of the reformer CFD simulation, accelerate the rate of convergence and minimize the required computing time to obtain the converged solution of the reformer CFD model in which the models with ✓ are activated, and those with ✗ are disabled.

this maximum temperature.

2.10 Discussion

In computational fluid dynamics study, a converged solution is not necessarily a physically correct solution, and therefore, the simulation results produced by the reformer CFD model are inspected by the well-established knowledge of the phenomena typically observed in reformers and validated by the typical plant data [35, 13, 52, 16, 21, 49] in the remainder of this section.

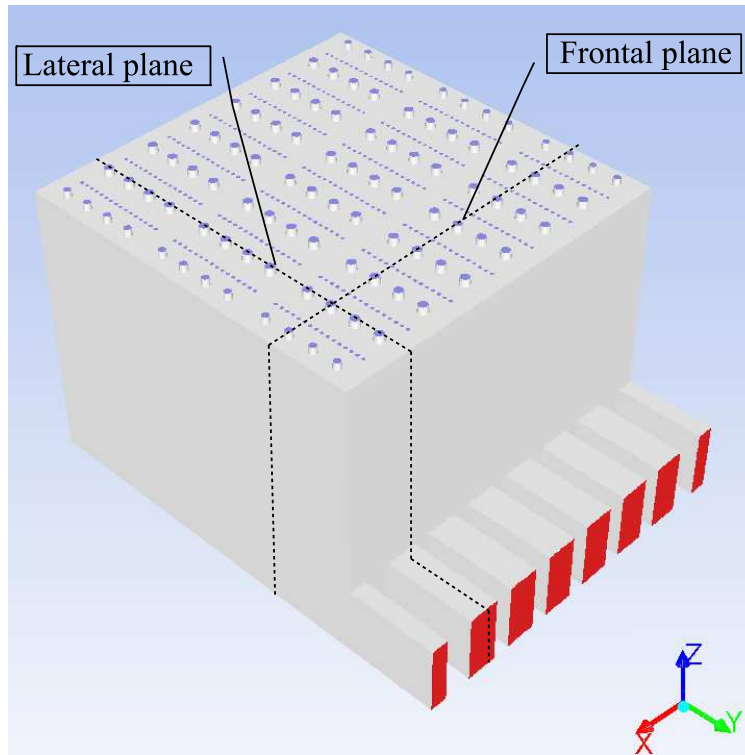


Figure 2.6: The frontal and lateral cross-sectional plane of the combustion chamber.

We begin by checking that the modeling strategies employed produced the effects expected. For instance, the furnace-side feed composition in Table 2.2 indicates that it is lean-fuel (i.e., the ratio of air to fuel of the furnace-side feed is higher than the stoichiometric ratio). Therefore, it is expected that the fuel will be fully oxidized and that oxygen will remain in the flue gas. Figs. 2.10, 2.11 and 2.12 demonstrate that the composition of the furnace-side reducing agents in the CFD solution are effectively zero everywhere except in the reaction zones, and Fig. 2.13 shows that oxygen is not completely consumed, as expected. Additionally, the characteristics of non-premixed combustion phenomena that are expected in the furnace-side as discussed in Section 2.4.1 can be observed in the converged reformer CFD solution. In particular, Figs. 2.10–2.12 reveal that the furnace-side compositions in the vicinities of the inner-lane and outer-lane burners are almost identical to those in the furnace-side feed, and Fig. 2.8 shows that the oxidation rate of the furnace-side feed in these regions is close to zero. These results suggest that the reformer CFD model correctly simulates the initial mixing of the fuel and air streams of the furnace-side feed, in which

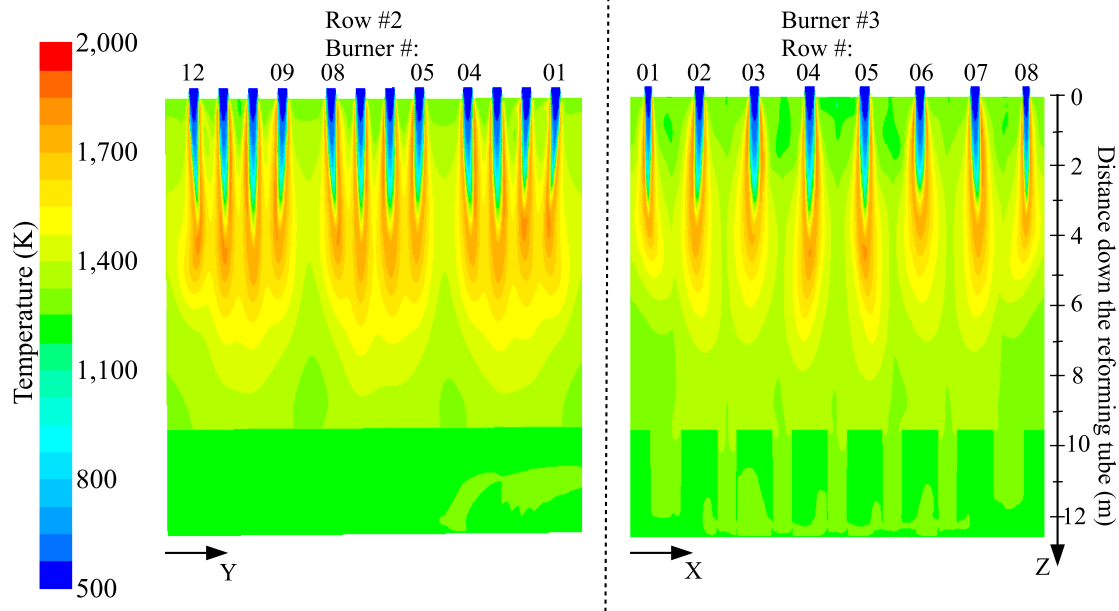


Figure 2.7: Lateral (left) and frontal (right) furnace-side temperature contour maps predicted by the reformer CFD simulation in which the parameters of the tube-side feed, furnace-side feed and combustion chamber refractory walls are consistent with typical plant data [35].

the observed oxidation rate of the furnace-side species is expected to be relatively slow. Moreover, the characteristics of top-fired reformers can be seen in the presented solution of the reformer CFD model. Particularly, Figs. 2.7 and 2.16 indicate that the maximum furnace-side temperature is located in the upper part of the reformer [12, 13], and Fig. 2.8 demonstrates that the flame length is consistent with the typical values between ~ 4.5 m and ~ 6 m [35]. Furthermore, the simulation data of the reformer CFD model indicates that approximately 55.1% of the thermal energy released by this process is transferred to the reforming tubes, 3% of which dissipates to the surrounding air through the chamber refractory walls and the remainder of which exits the reformer at the combustion chamber outlets, which is in close agreement with typical plant data [35, 12]. Finally, the solution of the reformer CFD model suggests that SMR is near equilibrium at the reforming tube outlets as expected. Specifically, Fig. 2.15 shows that the slopes of the composition profiles, which are indicative of the net reaction rates of the tube-side species at the reforming tube outlet, are close to zero.

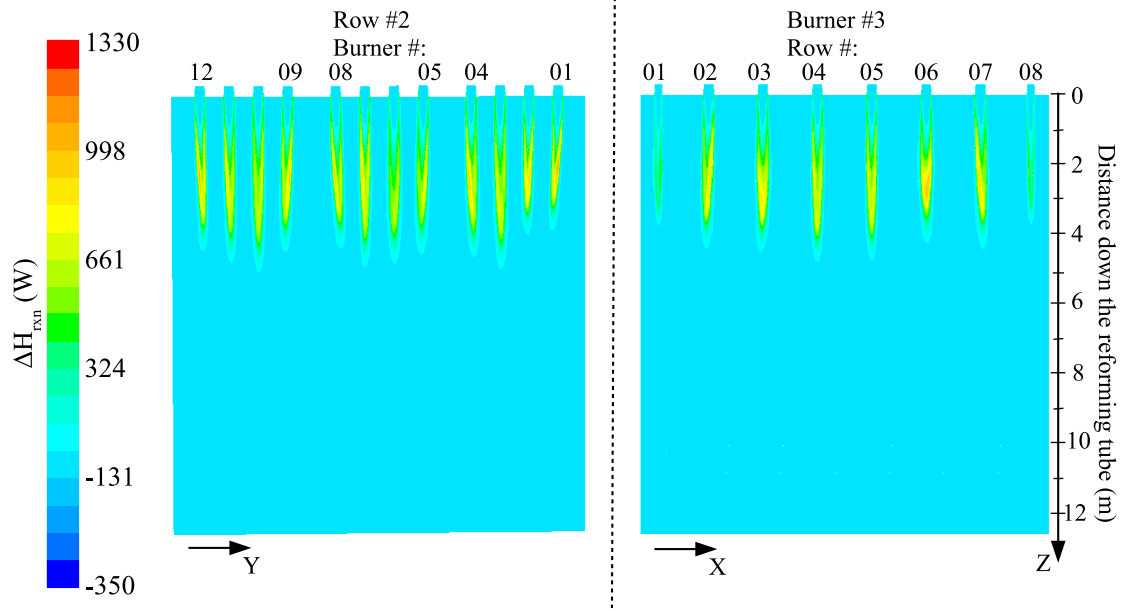


Figure 2.8: Lateral (left) and frontal (right) contour maps of energy released by the furnace-side oxidation predicted by the reformer CFD simulation in which the parameters of the tube-side feed, furnace-side feed and combustion chamber refractory walls are consistent with typical plant data [35].

We next compare our numerical results with those from typical plant data. When typical plant data is employed to justify the validity of the simulation results produced by the reformer CFD model, the data needs to be normalized to unity as follows:

$$\bar{z}^* = \frac{\bar{z} - \bar{z}_{min}}{\bar{z}_{max} - \bar{z}_{min}} \quad (2.13)$$

where \bar{z} and \bar{z}^* are the original data and corresponding normalized data, respectively, and \bar{z}_{max} and \bar{z}_{min} are the maximum and minimum values of the data set of interest. This is because many variations of top-fired reformer geometries are employed in the previous experimental and computational works of SMR, and the typical plant data are commonly reported in deviation forms for proprietary reasons. Fig. 2.17 and Fig. 2.18 compare the normalized CFD data with the normalized typical plant data presented in [35] and [13]. It is noted that we refer to the data from [35] and [13] as typical plant data though it is generated from a first-principles reformer

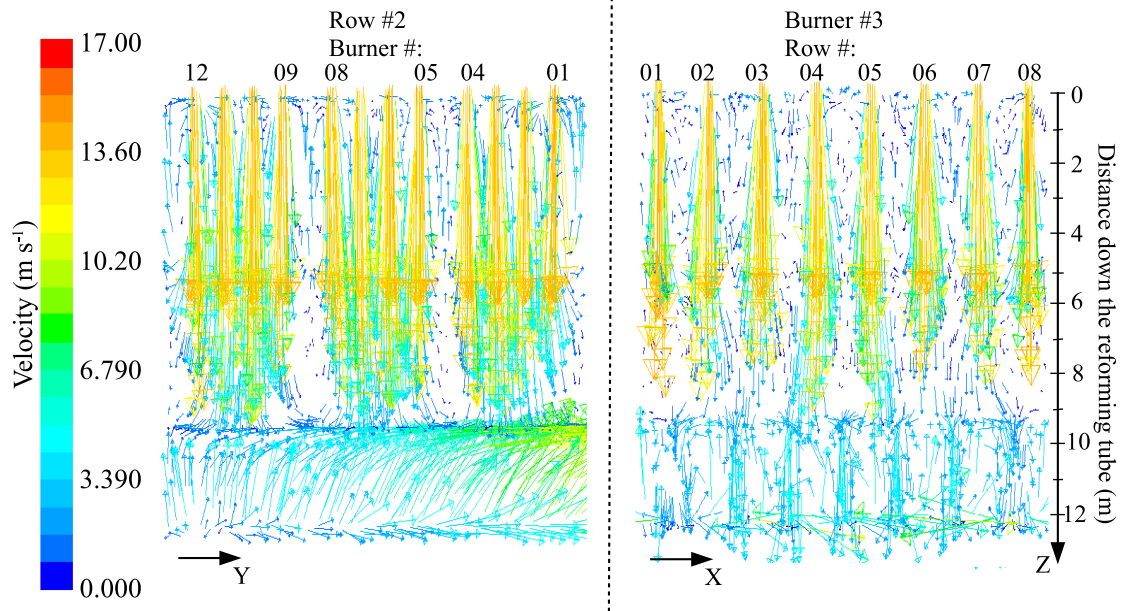


Figure 2.9: Lateral (left) and frontal (right) contour maps of the furnace-side velocity magnitude predicted by the reformer CFD simulation in which the parameters of the tube-side feed, furnace-side feed and combustion chamber refractory walls are consistent with typical plant data [35].

model in which the combustion of the furnace-side feed was not simulated simultaneously with the reforming tubes, and a predefined heat released profile was used. In addition, the reforming tube models from those works are modeled by the 1-D plug flow reactor model and thus ignore the radial spatial gradients of transport variables and the effect of the flow pattern on the reforming tubes. Nevertheless, the models from [35] and [13] employ a number of adjustable empirical constants (e.g., the heat-release length, the predefined parabolic heat-release profile, the gray gas model, and the convective heat transfer coefficients) that are tuned so that the estimated temperature profile of the outer reforming tube wall is consistent with the experimental data recorded by the high-cost monitoring IR cameras of an on-line reformer. Thus, we consider that the data from these works can be considered to be sufficiently close to experimental plant data to be utilized in validating the reformer CFD model. Therefore, the data from [35] and [13] is used to validate the proposed modeling strategies that lead to the development of the reformer CFD model from Section 2.4, Section 2.5, Section 2.6 and 2.7. Specifically, Fig. 2.17 shows that the com-

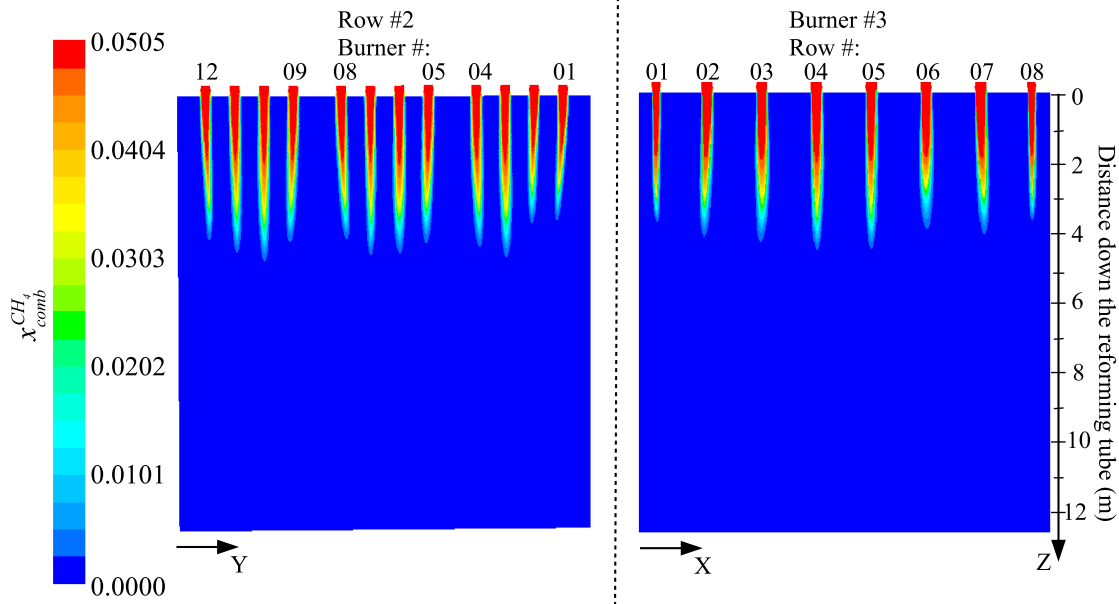


Figure 2.10: Lateral (left) and frontal (right) methane mole fraction contour maps inside the combustion chamber predicted by the reformer CFD simulation in which the parameters of the tube-side feed, furnace-side feed and combustion chamber refractory walls are consistent with typical plant data [35].

position profiles of the tube-side species along the reforming tube length vary in a manner that is consistent with the previous work, which justifies the choice of the global kinetic model of SMR with the universal effectiveness factor and the FR/ED model for accounting for turbulence-chemistry interaction. Additionally, Fig. 2.18 demonstrates that the average temperature profiles of the furnace-side flow and outer reforming tube wall along the length of the reforming tube closely resemble the corresponding profiles reported in the previous reformer study, which validates the choice of the radiative property correlation and heat transfer model, as well as the neglect of radiation in the tube side and the use of the porous zone function for modifying the heat transfer equations in the reforming tubes. Specifically, the OTWTs from the reformer CFD model and [13] are similar, and the temperature profiles for the furnace-side flow have a similar shape in the sense that both demonstrate a maximum furnace-side temperature that is located in the upper part of the reformer (i.e., a characteristic of top-fired reformers). Differences between the furnace-side flow

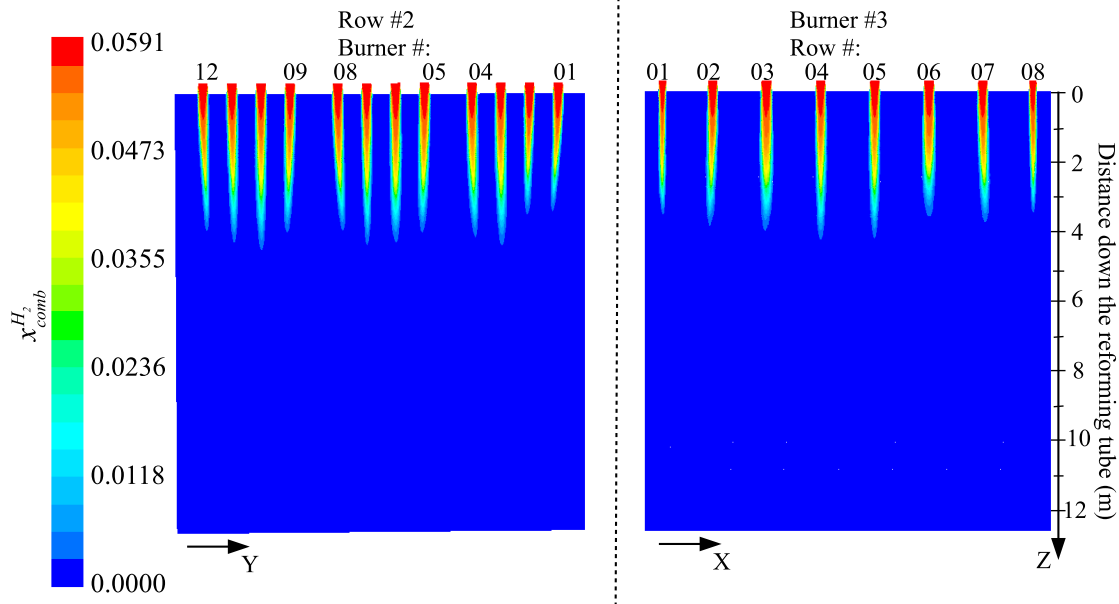


Figure 2.11: Lateral (left) and frontal (right) hydrogen mole fraction contour maps inside the combustion chamber predicted by the reformer CFD simulation in which the parameters of the tube-side feed, furnace-side feed and combustion chamber refractory walls are consistent with typical plant data [35].

temperature profiles of the CFD simulation and [13] are expected since in [13], the effects of the furnace-side flow pattern on the temperature of the furnace-side flow are ignored as the combustion chamber is assumed to behave like a plug flow reactor. As additional validation of the reformer CFD simulation results, the values of a number of properties of the tube-side flow from [35] are compared with those from the reformer CFD model in Table 2.7 and show good agreement.

The converged reformer CFD solution is validated by the CFD data generated by the industrial-scale reforming tube CFD model developed in [34]. The industrial-scale reforming tube CFD model is updated with the same modeling parameters as described in Section 2.2, Section 2.5 and Section 2.6, and implemented with the tube-side feed conditions and outer reforming tube wall profile (Fig. 2.16) of the reformer CFD model. Table 2.7 indicates that the differences between the CFD data generated by the reformer CFD model and updated industrial-scale reforming tube CFD model are not significant.

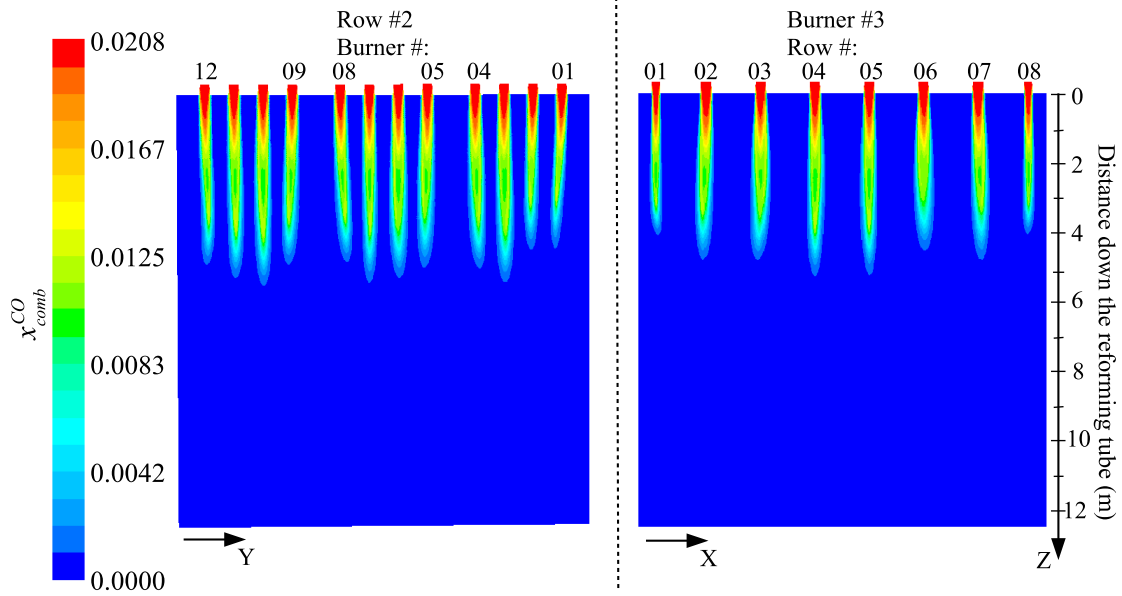


Figure 2.12: Lateral (left) and frontal (right) carbon monoxide mole fraction contour maps inside the combustion chamber predicted by the reformer CFD simulation in which the parameters of the tube-side feed, furnace-side feed and combustion chamber refractory walls are consistent with typical plant data [35].

Furthermore, the converged reformer CFD solution is validated by the data generated by a standard reforming Gibbs reactor model of a steady-state process simulator (e.g., Pro/II) as shown in Table 2.7. Because the tube-side reactions have been demonstrated above through Fig. 2.15 to have approximately reached equilibrium at the reactor outlet, it is expected that the mole fractions at the tube outlet from the CFD simulation would correspond with the results from the Gibbs reactor simulation. The reforming Gibbs reactor model is provided with the Gibbs reactor feed stream and duty, which are set to the tube-side feed and the average thermal energy absorbed by each reforming tube of 345.090 kW derived from the reformer CFD solution, respectively. The differences in the results between the reformer CFD model and the reforming Gibbs reactor model are demonstrated in Table 2.7 to be small. It is important to note that the solution of the reforming Gibbs reactor model can only be obtained after the solution of the reformer CFD model has already been computed from which the total energy absorbed by each reforming tube is extracted.

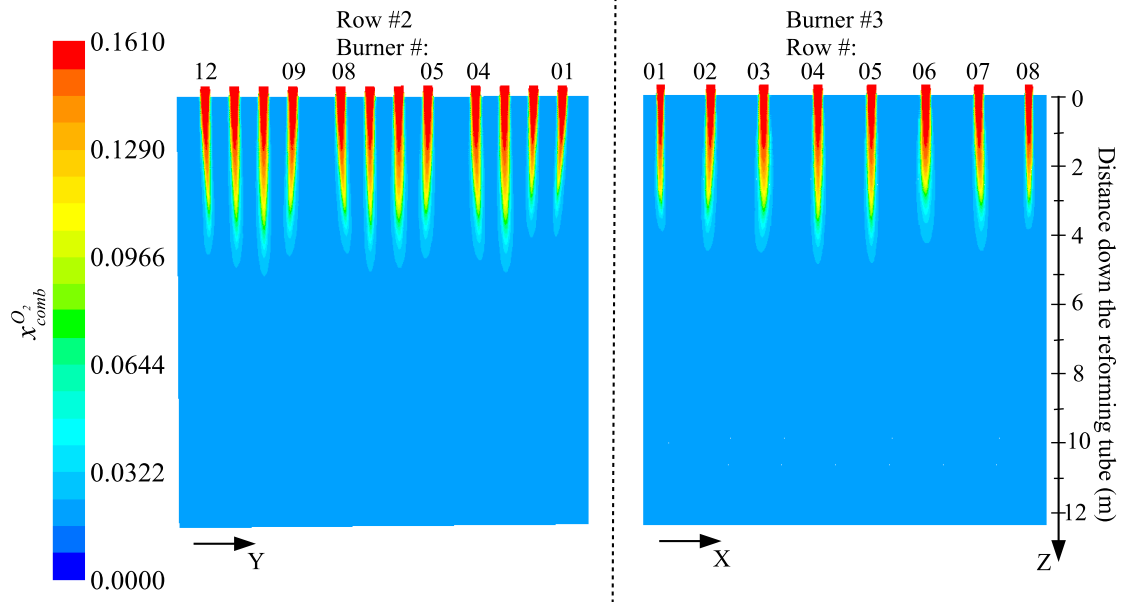


Figure 2.13: Lateral (left) and frontal (right) oxygen mole fraction contour maps inside the combustion chamber predicted by the reformer CFD simulation in which the parameters of the tube-side feed, furnace-side feed and combustion chamber refractory walls are consistent with typical plant data [35].

One might suggest that the total energy absorbed by each reforming tube can be back-calculated given the tube-side composition at the reforming tube outlets; however, prior to the completion of the reformer CFD simulation, neither the amount of thermal energy absorbed by the reforming tubes (i.e., the energy uptake of a reforming Gibbs reactor model) nor the tube-side composition at the reforming tube outlets (i.e., the approximated yield of SMR) are available to be used as inputs. Hence, it is evident that the reforming Gibbs reactor model is not designed to replace the reformer CFD model.

Next, the area-weighted average heat flux across the reforming tube wall predicted by the reformer CFD model is compared to that of the typical plant data reported in the literature as shown in Table 2.8. The average heat flux in Table 2.8 from [35] is estimated based on the outer and inner reforming tube wall temperature profiles reported in that work, the reforming tube thermal conductivity of $106,500 \text{ J m}^{-1} \text{ h}^{-1} \text{ K}^{-1}$ and the typical reforming tube wall thickness

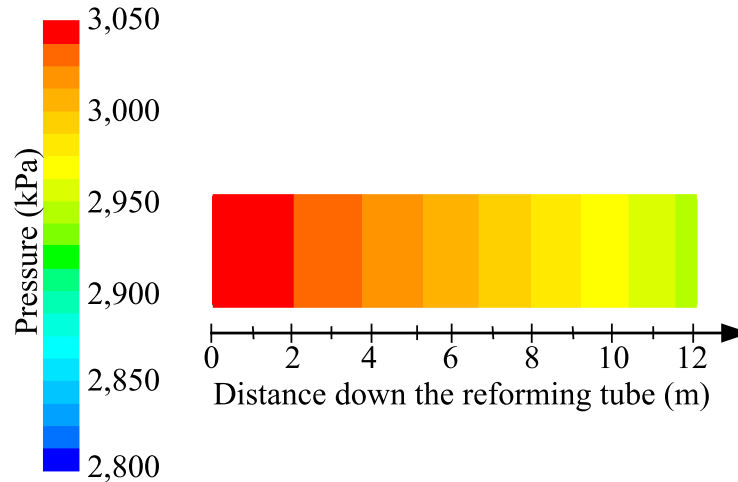


Figure 2.14: Tube-side pressure contour map predicted by the reformer CFD simulation in which the parameters of the tube-side feed, furnace-side feed and combustion chamber refractory walls are consistent with typical plant data [35].

of 0.015 m. From Table 2.8, the area-weighted average heat flux across the reforming tube wall predicted by the reformer CFD model is consistent with that of the typical plant data.

Finally, the reformer CFD model is implemented with the furnace-side feed distribution of an on-line reformer provided by a third party, and the corresponding converged CFD data is obtained by the proposed step-by-step convergence strategy as discussed in Section 2.8. Subsequently, the CFD data is compared with the recorded plant data, which is an OTWT distribution at a fixed axial location (as shown in Fig. 2.19) and is collected by a system of IR cameras situated around the reformer as discussed in Section 2.4.2. The OTWT distribution constructed based on the CFD simulation and information of the approximate views of the IR cameras is consistent with the plant data provided by the third party as the maximum deviation at any location is $\sim 3\%$ and the average deviation is $\sim 1.2\%$ as shown in Fig. 2.20. The blank spaces shown in Fig. 2.20 represent reforming tubes for which no temperature measurements were provided from the reported data. However, from the good agreement of our CFD data with the available data, we can be confident that our CFD results for these additional reforming tubes are indicative of the actual operating conditions. This highlights the utility of CFD modeling for obtaining information regarding operating conditions

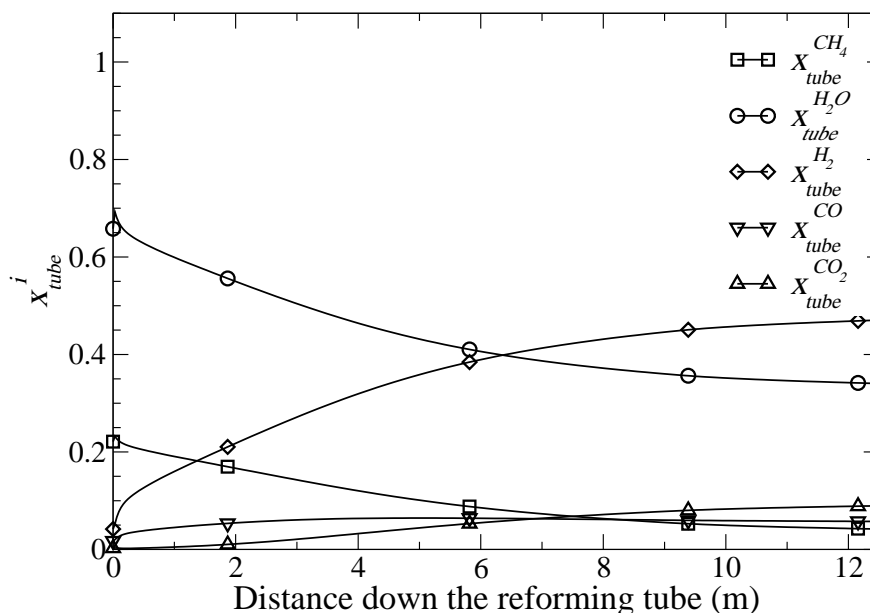


Figure 2.15: Radial-weighted average tube-side compositions predicted by the reformer CFD simulation in which the parameters of the tube-side feed, furnace-side feed and combustion chamber refractory walls are consistent with typical plant data [35].

that are perhaps not available from standard process monitoring techniques (e.g., the outer wall temperature at all z locations down the reforming tube length, for every reforming tube) which may be required for assessing whether potentially dangerous operating conditions exist (e.g., any reforming tube outer wall temperature exceeding the maximum operating temperature at any z location) and modifying the process inputs to ameliorate such conditions when they are detected.

Based on the above, the simulation results produced by the reformer CFD model are demonstrated to be consistent with phenomena observed in reformers and to be in close agreement with the typical plant data. As a result, the converged solution of the reformer CFD model can be considered to be a reasonably reliable representation of experimental data and can be utilized to characterize the velocity, turbulence, composition and temperature fields inside the reformer.

In this work, we focus on presenting only modeling strategies that are expected to be most suitable for modeling the expected transport and reaction phenomena among the choices offered by Fluent for the purpose of demonstrating how a high-fidelity CFD model of a reformer can be devised. Showing how initial modeling strategies can be selected for reasonably accurate results

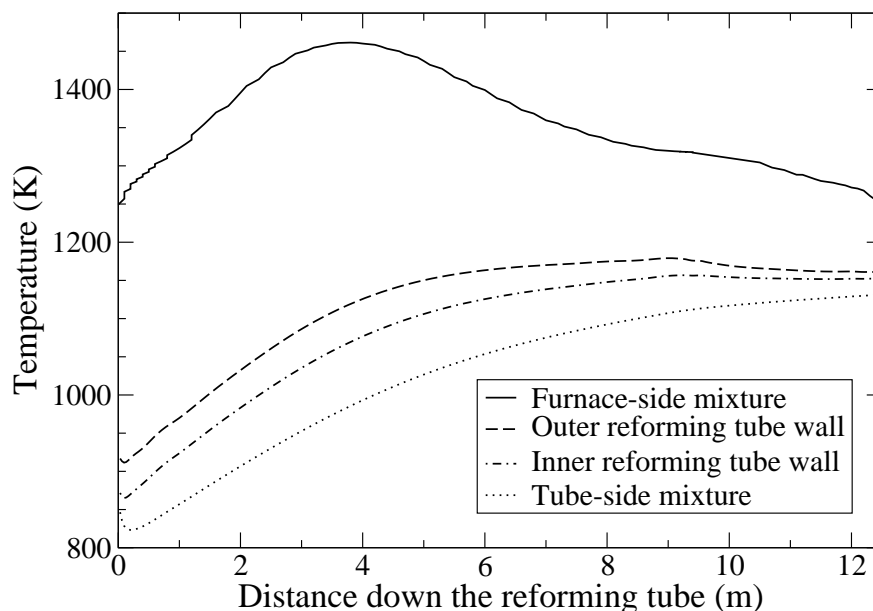


Figure 2.16: Average temperature profiles of the furnace-side flow (solid line), outer reforming tube wall (dashed line), inner reforming tube wall (dash-dotted line) and tube-side flow (dotted line) predicted by the reformer CFD simulation in which the parameters of the tube-side feed, furnace-side feed and combustion chamber refractory walls are consistent with typical plant data [35].

within a reasonable time frame is a significant contribution of the present work, because the coupling between the various transport and reaction phenomena in and between the tube and furnace sides prevents CFD results of the entire SMR from being generated for comparison with typical plant data until all phenomena have been included within the CFD simulation. Therefore, we focus only on the selection of initial modeling strategies that allow CFD data to be obtained that shows good agreement with typical plant data. Fine-tuning of the models for various phenomena (e.g., re-running the CFD simulation with alternative models such as alternative turbulence-chemistry interaction models to analyze whether this improves the agreement of the CFD results with typical plant data) could be performed, particularly by industry with significant plant data that can be used for distinguishing between the differences in accuracy at this fine-tuning step, but given the already significant agreement with typical plant data, changing the modeling strategies chosen would not conceptually change the novelty of the work (developing a step-by-step guide for ob-

taining a high-fidelity CFD model of an industrial-scale reformer), and thus is not pursued. The good agreement of the typical plant data with our CFD simulation results indicates that all simplifications and assumptions made in the development of the reformer CFD modeling strategies and meshing as described in Secs. 2.2-2.7 were sufficient for obtaining a CFD model that can be considered to be a reasonable substitute for experimental data.

In this work, we assume that the furnace-side feed is uniformly distributed among all inner-lane burners and among all outer-lane burners, which results in symmetry in the furnace-side feed distribution and geometry that could have been exploited for the simulation. However, the intended application of the reformer CFD model is for allowing the evaluation of reformer operating parameters to improve the economics of operation when such operating changes cannot be fully evaluated any other way (for example, furnace balancing, which is optimizing the furnace-side feed distribution so that the temperature distribution of the outer reforming tube wall at a given length down the reforming tubes becomes more uniform). Evaluating the most optimal operating conditions may require the flexibility of simulating asymmetry within the reactor (e.g., an asymmetrical furnace-side feed distribution). Furthermore, the FSF flow rate to each burner is controlled by the percent opening of the corresponding valve, and therefore, valve-related disturbances (e.g., the valve stickiness) can cause an unintended asymmetric furnace-side feed distribution. For such reasons, it is beneficial to simulate the entire reformer, without exploiting symmetry, in the development of the reformer CFD model.

The comparison of the Gibbs reactor simulation results and those from the outlet of a reforming tube in the reformer CFD model in Table 2.7 does not indicate that steady-state simulations that are standard in the chemical process industries can serve as substitutes for a CFD model of a reformer. The CFD simulations reveal details about the reactor operation (e.g., the flame length, maximum and minimum temperatures of the reforming tube walls at any given axial location in the reformer, and the effect of changes in the burner feed flow rates on these maximum and minimum temperatures) that cannot be obtained from steady-state simulations such as a Gibbs reactor, and cannot even be obtained from standard experimental measurements that are taken at SMR plants

(e.g., temperatures of specific reforming tube walls at specific axial locations determined from infrared cameras). It is also notable that due to the effects of the geometry on the flows and heat transfer within the SMR (for example, asymmetry in the flow field within the furnace side is observed in Fig. 2.9 due to the flue gas tunnel exits being located on only one side of the reformer, which creates non-identical environments for the reforming tubes throughout the reformer despite the fact that they are fed with identical feeds), as well as the interactions of the flow and heat transfer with the observed reaction rates, our prior works ([34, 1]) cannot predict the effects seen in a reformer as the present work can because they utilize different geometries and modeling strategies. Therefore, the novelty of the present work hinges on the fact that because it demonstrates how a reformer CFD model can be developed and validated (i.e., it develops neither a simplified model like a Gibbs reactor nor even a smaller-scale CFD model), it demonstrates a methodology for obtaining high-fidelity data regarding the operating conditions throughout a reformer that can be considered to be representative of the actual conditions within the SMR but cannot be obtained any other way. The development of such a model is significant therefore for industry, because it provides a methodology for optimizing process operation with highly reliable data that is not otherwise available and allows problematic operating conditions to be evaluated and mitigated. Furthermore, the discussion of why the CFD modeling strategies were chosen demonstrates how expected phenomena within a reactor can be evaluated to allow for appropriate modeling strategies to be chosen for CFD simulation of other reactors of industrial interest for which such high-fidelity data would be beneficial.

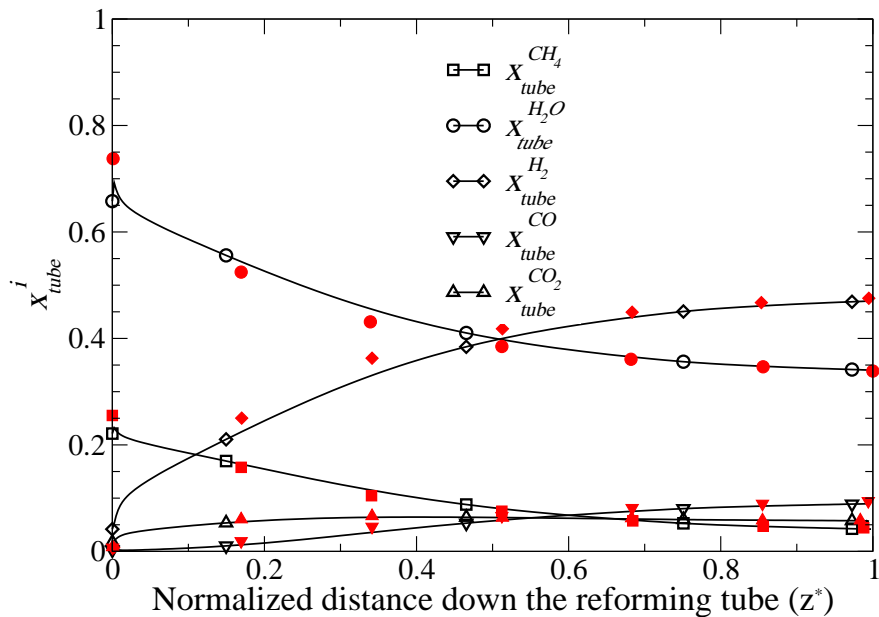


Figure 2.17: Radial-weighted average tube-side compositions along the reforming tubes produced by the reformer CFD model (black) versus those derived from typical plant data of SMR (red) [35].

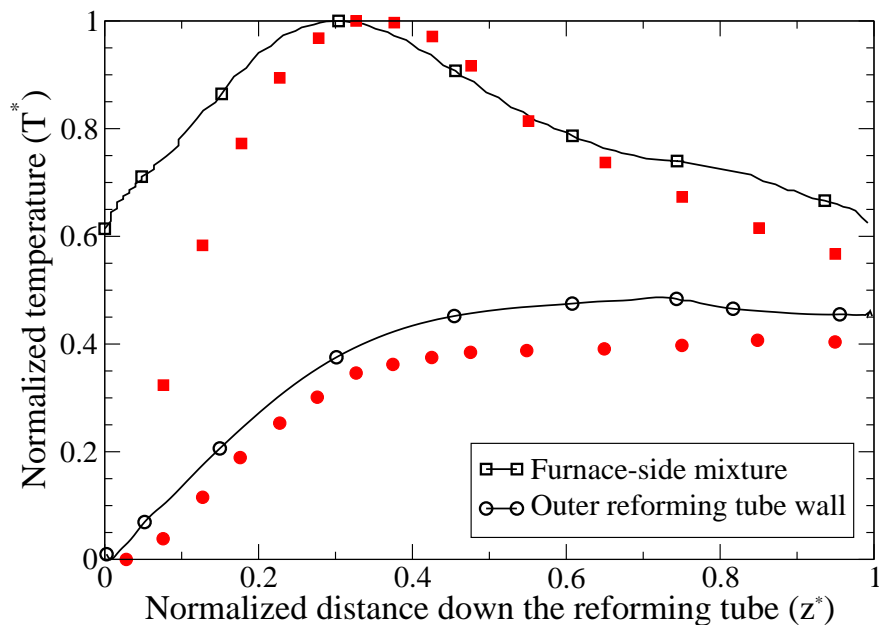


Figure 2.18: Average temperature profiles of the furnace-side flow and outer reforming tube wall produced by the reformer CFD model (black) versus those derived from typical plant data of SMR (red) [13].

Table 2.7: Validation of reformer CFD model.

	Industrial-scale reforming tube CFD model	Reformer CFD model	Reforming Gibbs reactor model	Typical plant data [35]
ΔP_{tube} (kPa)	194.29	106.22	N/A	146.9
$\bar{P}_{tube,outlet}$ (kPa)	2955.2	3044.0	N/A	2879.8
Average heat flux (kW m^{-2})	70.659	69.523	N/A	67.125
$\bar{x}_{tube,outlet}^{H_2}$	0.4734	0.4687	0.4686	0.4713
$\bar{x}_{tube,outlet}^{H_2O}$	0.3380	0.3419	0.3411	0.3377
$\bar{x}_{tube,outlet}^{CH_4}$	0.0389	0.0430	0.0433	0.0453
$\bar{x}_{tube,outlet}^{CO}$	0.0905	0.0883	0.0872	0.0889
$\bar{x}_{tube,outlet}^{CO_2}$	0.0574	0.0576	0.0589	0.0559

Table 2.8: Validation of reformer CFD model by available plant data from literature

	Average heat flux (kW m^{-2})
Reformer CFD model	70
Industrial-scale reforming tube CFD model [34]	71
[35]	67
[52]	45–90
[16]	79
[21]	76
[49]	< 80

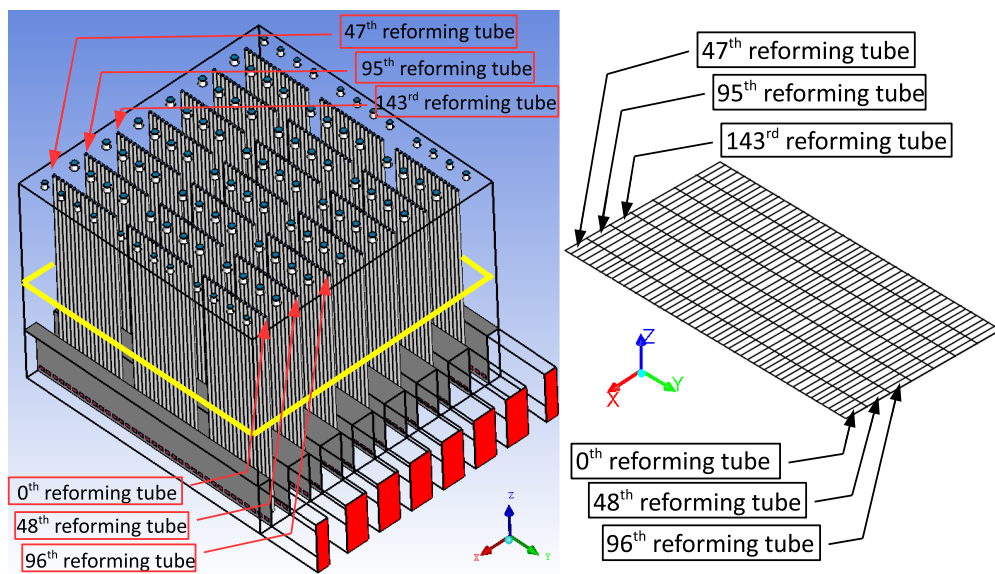


Figure 2.19: Description of the layout of the OTWT distribution, in which each grid contains an average OTWT of the corresponding reforming tube recorded by a system of IR cameras situated around the reformer.

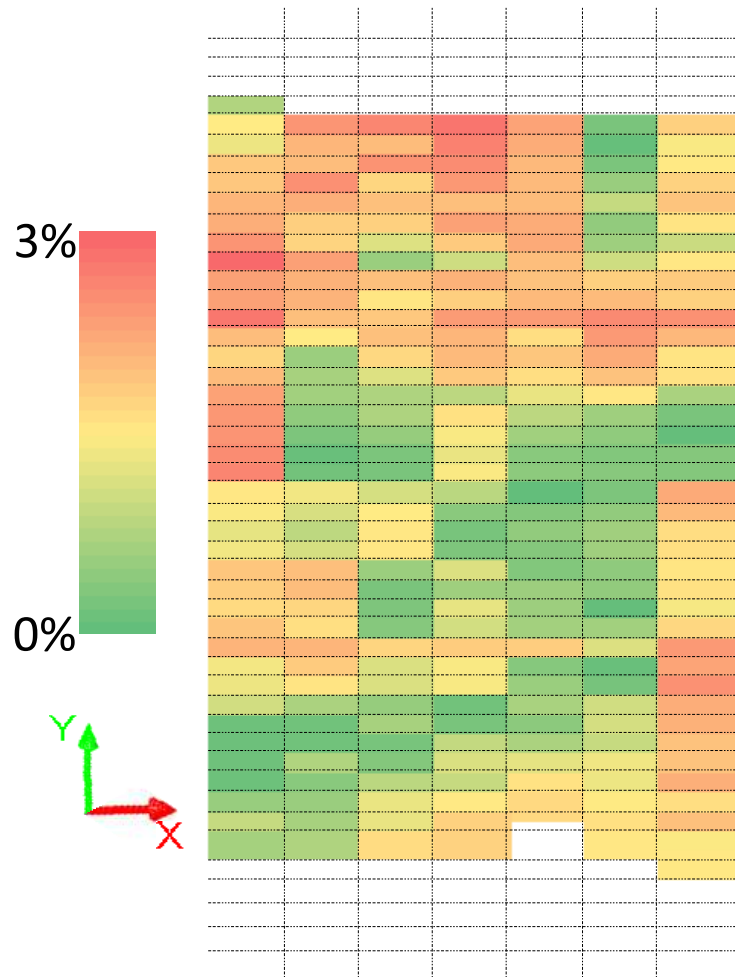


Figure 2.20: Distribution of the percent difference in the OTWT between the reformer CFD data and the plant data provided by the third party. The percent difference of each reforming tube is computed by the ratio of the deviation of the CFD data from the corresponding plant data to the corresponding plant data.

2.11 Conclusion

The present work detailed the development of a CFD model of a steam methane reformer and presented a methodology for analyzing expected transport and reaction phenomena to choose modeling strategies within the CFD software that result in CFD simulation data that can be considered to be a substitute for experimental data. The reformer model simulates the essential transport phenomena observed in industrial high-temperature applications as well as reformer-relevant physical and chemical phenomena. Specifically, the standard $k - \varepsilon$ turbulence model, FR/ED model and global kinetic models of hydrogen/methane combustion were selected to simulate the non-premixed combustion characteristics, the reaction rates of the furnace-side species and the thermal energy released from the oxidation of the furnace-side feed under the influence of turbulence. Then, a correlation between the furnace-side radiative properties and temperature, Kirchhoff's law, Lambert Beer's law and the discrete ordinate method were chosen to simulate radiative heat transfer within the furnace-side flow and between the furnace-side flow and solid surfaces inside the reformer. Next, the standard $k - \varepsilon$ turbulence model, FR/ED model and global kinetic model of SMR were utilized to simulate the reaction rates of the tube-side species under the influence of turbulence. Lastly, the modeling strategy of the reforming tubes utilized an approximate representation of the catalyst network to simulate the presence of catalyst particles inside the reforming tube and the effect of internal and external diffusion limitations on the observed reaction rates of the tube-side species. We recognize that the computing time required to complete a simulation of the reformer CFD model by ANSYS Fluent on 80 cores of UCLA's Hoffman2 cluster is significant (i.e., approximately three full days), yet the upfront investment (i.e., time) makes it possible for us to determine the optimized operating conditions of the reformer. Specifically, the simulation results generated by the reformer CFD model with the tube-side and furnace-side feed derived from typical plant data are demonstrated to be consistent with phenomena observed in reformers and to be in close agreement with typical plant data. In addition, the simulation data generated by the reformer CFD model, in which the tube-side and furnace-side feed distributions provided by a

third party are used as boundary conditions, is shown to be in close agreement with the plant data recorded from the on-line reformer at the hydrogen manufacturing plant. Therefore, the reformer CFD model can be considered to be an adequate representation of the on-line reformer and can be used to determine the risk to operate the on-line reformer at un-explored and potentially more beneficial operating conditions.

A_{comb}	total surface area of the combustion chamber (m^2)
C_p	specific heat capacity of the furnace-side flow ($J\ kg^{-1}\ K^{-1}$)
$C_{p,comb}^j$	heat capacity of species j in the furnace-side flow ($J\ kg^{-1}\ K^{-1}$)
D_p	effective diameter of the catalyst pellets (mm)
$D_{comb}^{m,i}$	mass diffusion coefficient of the species i in the furnace-side flow ($m^2\ s^{-1}$)
$D_{comb}^{m,t}$	turbulent mass diffusion coefficient of the furnace-side flow ($m^2\ s^{-1}$)
E_{comb}	specific internal energy of the furnace-side flow ($J\ kg^{-1}$)
E_{wave}	energy of electromagnetic waves (J)
P_{comb}	pressure of the furnace-side flow (kPa)
P_{tube}^i	partial pressure of the species i in the tube-side flow (kPa)
\vec{g}	universal gravitational acceleration vector ($m\ s^{-2}$)
h	Plank's constant
h_{comb}	specific sensible enthalpy of the furnace-side flow ($J\ kg^{-1}$)
h_{comb}^j	specific sensible enthalpy of species j in the furnace-side flow ($J\ kg^{-1}$)
K_{H_2}	adsorption constants for H_2 (bar^{-1})
K_{CH_4}	adsorption constants for CH_4 (bar^{-1})
K_{CO}	adsorption constants for CO (bar^{-1})
K_{H_2O}	dissociative constants for H_2O
K_1	equilibrium constant of the reaction 5 (bar^2)
K_2	equilibrium constant of the reaction 6
K_3	equilibrium constant of the reaction 7 (bar^2)

k_1	forward kinetic constant coefficient of the reaction 5 ($\text{kmol bar}^{1/2} (\text{kg of catalyst})^{-1} \text{h}^{-1}$)
k_2	forward kinetic constant coefficient of the reaction 6 ($\text{kmol (kg of catalyst)}^{-1} \text{h}^{-1}$)
k_3	forward kinetic constant coefficient of the reaction 7 ($\text{kmol bar}^{1/2} (\text{kg of catalyst})^{-1} \text{h}^{-1}$)
k_{comb}^{eff}	effective thermal conductivity of the furnace-side flow ($\text{W m}^{-1} \text{K}^{-1}$)
k_{comb}^l	thermal conductivity of the furnace-side flow ($\text{W m}^{-1} \text{K}^{-1}$)
k_{comb}^t	turbulent thermal conductivity of the furnace-side flow ($\text{W m}^{-1} \text{K}^{-1}$)
k_{comb}	turbulence kinetic energy of the furnace-side flow ($\text{m}^2 \text{s}^{-2}$)
I	unit tensor (kPa)
\vec{j}_{comb}^i	turbulent mass diffusion flux of species i of the furnace-side flow ($\text{kg m}^{-2} \text{s}^{-1}$)
$R_i, i = 1, \dots, 4$	intrinsic volumetric reaction rate of the i^{th} reaction ($\text{kmol m}^{-3} \text{s}^{-1}$)
$R_i, i = 5, \dots, 7$	intrinsic volumetric reaction rate of the i^{th} reaction ($\text{kmol (kg of catalyst)}^{-1} \text{s}^{-1}$)
$R_{i,j}$	observed volumetric rate of species i in reaction j ($\text{kg m}^{-3} \text{s}^{-1}$)
M_i	molecular weight of species i (kg kmol^{-1})
$M_{\mathcal{R}}$	molecular weight of a specified reactant \mathcal{R} (kg kmol^{-1})
L	characteristic dimension of the combustion chamber (m)
L_{tube}	heated reforming tube length (m)
Sc_{comb}^t	turbulent Schmidt number of the furnace-side flow
T_{comb}	temperature of the furnace-side flow (K)
T_{wall}	temperature of the solid surfaces (K)
T_{ref}	reference temperature (K)
$[i]$	molar concentrations of the species i of the furnace-side flow (kmol m^{-3})
x_{tube}^i	mole fractions of species i in the tube-side flow
x_{comb}^i	mole fractions of species i in the furnace-side flow

Y_i	mass fraction of species i
Y_{comb}^i	mass fraction of species i in the furnace-side flow
$Y_{\mathcal{R}}$	mass fraction of a specified reactant \mathcal{R} in reaction j
$Y_{\mathcal{P}}$	mass fraction of a specified product species \mathcal{P} in reaction j
V_{comb}	volume of the combustion chamber (m^3)
$v_{\infty,tube}$	superficial velocity of the tube-side flow (m s^{-1})
\vec{v}_{comb}	mass-averaged velocity vector of the furnace-side flow (m s^{-1})
$v_{comb}^2/2$	specific kinetic energy of the furnace-side flow (J kg^{-1})
α	permeability coefficient of the catalyst network (m^2)
β	inertial resistance coefficient of the catalyst network (m^{-1})
β'	coefficient of thermal expansion of the furnace-side flow (K^{-1})
$\nu_{i,j}$	stoichiometric coefficient of species i in reaction j
$\nu_{\mathcal{R},j}$	stoichiometric coefficient of a specified reactant \mathcal{R} in reaction j
ν_{wave}	frequency of electromagnetic waves (s^{-1})
ρ_{tube}	density of the tube-side flow (kg m^{-3})
ρ_{comb}	density of the furnace-side flow (kg m^{-3})
ε	total emissivity of the furnace-side flow
ε_{comb}	dissipation rate of the furnace-side flow ($\text{m}^2 \text{s}^{-3}$)
ε_{wall}	internal emissivity coefficient of the solid surfaces
σ_a	absorption coefficient of the furnace-side flow
$\overline{\tau}_{comb}$	stress tensor (kPa)
γ	porosity of the catalyst network
μ_{comb}	molecular viscosity of the furnace-side flow ($\text{kg m}^{-1} \text{s}^{-1}$)
μ_{comb}^t	eddy viscosity of the furnace-side flow ($\text{kg m}^{-1} \text{s}^{-1}$)
μ_{tube}	molecular viscosity of the tube-side flow ($\text{kg m}^{-1} \text{s}^{-1}$)
$-\nabla \cdot \vec{q}_{rad}$	radiative heat transfer rate ($\text{J m}^{-3} \text{s}^{-1}$)
ΔP_{tube}	pressure difference of the tube-side flow across the catalyst network (kPa)

Table 2.9: Notations

Chapter 3

Temperature Balancing in Steam Methane Reforming Furnace via an Integrated CFD/Data-Based Optimization Approach

3.1 Introduction

In Chapter 2, a CFD model for an industrial-scale reformer is developed in ANSYS Fluent to further our understanding of the physiochemical processes in the tube side and the furnace side as well as their thermal interactions during the catalytic conversion of methane to hydrogen, which allows us to investigate the root causes of the inherent variability in the outer tube wall temperature (OTWT) distribution among the reforming tubes at a fixed height as outlined in Chapter 1. Specifically, a potential root cause is found to be an asymmetric furnace-side flow pattern as speculated in the SMR literature; for example, Zheng et al. [65] shows that a maldistribution of the furnace-side flow in the reformer can cause flame impingement, which creates local hot-spots along the reforming tube length and causes the OTWT distribution to have a higher degree of variability. The hot-spot temperatures may significantly exceed the design temperature of the reforming tube walls, which consequently reduces the reformer service life. Using the reformer CFD model, we

have found that the asymmetric furnace-side flow pattern is the result of an asymmetric reformer geometry. For example, the reformer considered in this work, developed and validated in Chapter 2 and shown in Fig. 3.2, is designed such that the furnace-side outlets of the combustion chamber are situated on the front side of the refractory wall. Hence, the asymmetric furnace-side flow pattern is an intrinsic characteristic of the reformer and cannot be resolved without having to redesign the reformer geometry and to rebuild the reformer. However, Oprins et al. [48] demonstrates that the nonuniformity in the OTWT distribution under the influence of the asymmetric furnace-side flow pattern can be reduced by redistributing the “furnace-side feed” whose definition is restated in Section 3.2.1, so that the total FSF flow rate can be subsequently increased to improve the reformer thermal efficiency.

Motivated by the above considerations, this Chapter focuses on developing a model-based furnace-balancing scheme to determine an optimized furnace-side feed (FSF) distribution at the nominal total FSF flow rate to lessen the variability in the OTWT distribution along the reforming tube length in the reformer. The concept of ‘furnace balancing’ is well-founded, and in particular, Kumar et al. [32] and [31] are noteworthy examples of many proofs of concept in literature, which address the problem of the optimized FSF distribution. Nevertheless, the features of the high-fidelity reformer CFD model, model identification process and furnace-balancing optimizer clearly differentiate this work from those in literature. The remainder of this manuscript is structured as follows: in Section 3.2, an overview of the model-based furnace-balancing scheme is presented, of which the algorithm of each component is detailed in Secs. 3.2.1, 3.2.2, 3.2.3 and 3.2.4. In Section 3.2.1, the physical description, process modeling and process simulation of the high-fidelity reformer CFD model are presented. Specifically, the reformer CFD model is created from a multiblock structured hexahedral reformer mesh with ~ 41 million grids that has a reasonably acceptable mesh quality, and the corresponding CFD data generated from the simulations of the reformer CFD model is verified to be mesh-independent. The modeling strategies of the reformer CFD model are selected from a pool of potential models such that the chosen models can simulate characteristics of the transport and chemical reaction phenomena observed

inside the reformer during hydrogen production and require a reasonable computational resource. In addition, Chapter 2 demonstrates that the CFD simulation data generated from the simulations of the reformer CFD model is in good agreement with various sources in the literature. In Section 3.2.2, the impact of the furnace-side flow pattern on the OTWT distributions along the reforming tubes is investigated, and the concept of a heating zone is introduced and is utilized to allow the model identification process to embed the characteristics of the reformer geometry and knowledge of the potential effects of the furnace-side flow pattern on the OTWT distribution into the data-driven model. The data-driven model derived from this ‘hybrid’ model identification process (i.e., a model identification strategy that uses information on the reformer geometry and effects of the furnace-side flow pattern on the OTWT distributions), which represents the reasonably accurate relationship between the OTWT distribution and the FSF distribution inside the reformer CFD model, can be obtained from a small set of CFD training data. This feature of the model identification process highlights contributions of the present work to the existing SMR modeling literature. In Section 3.2.3, the relationship between the FSF distribution and the flow control system of the reformer and the fundamental differences between properly functional and defective flow control valves (i.e., constituents of the flow control system) are presented. In Section 3.2.4, the algorithm of the furnace-balancing optimizer, of which the decision variables are the valve positions of the properly functional flow control valves, is presented. Then in Section 3.3.1, the proposed furnace-balancing scheme is deployed with the assumption that the reformer is properly functional, and the CFD data corresponding to the optimized FSF distribution generated by the proposed furnace-balancing scheme is used to evaluate its performance. Finally in Section 3.3.2, the proposed furnace-balancing scheme is deployed for the case in which the reformer is subjected to two different valve-related disturbances, and the CFD data corresponding to the reoptimized FSF distribution, generated by the proposed furnace-balancing scheme, is used to evaluate its ability to compensate for the additional constraints imposed by the disturbances.

3.2 Furnace-balancing scheme

The furnace-balancing scheme consists of four processes denoted by the rectangular boxes in Fig. 3.1 (i.e., data generation, model identification, a model-based furnace-balancing optimizer and a termination checker). It is designed to search for the optimized FSF distribution such that the nonuniformity in OTWT distributions along the reforming tubes and the overall maximum outer reforming tube wall temperature (i.e., the maximum radially averaged outer wall temperature among all reforming tubes along their heated length) are minimized, which facilitate the subsequent increase of the total FSF flow rate to the reformer to achieve higher production rates of hydrogen and superheated steam without shortening the reformer service life.

Ideally, the initial FSF distribution used by the furnace-balancing scheme is chosen to be the nominal FSF distribution of the on-line reformer at hydrogen manufacturing plants; however, the industrial data concerning reformer operational settings is limited, e.g., although the total FSF flow rate is available for public access, to the extent of our knowledge the FSF distribution of the reformer has never been reported. Additionally, it is evident that the OTWT distribution is dependent on the asymmetric furnace-side flow pattern as discussed in Section 3.1, and the quantitative relationship between them has not yet been revealed; therefore, we do not have sufficient information to form an educated initial guess of the optimized FSF distribution. As a result, the initial guess of the optimized FSF distribution is assumed to be a uniform distribution (i.e., the furnace-side feed is uniformly distributed among the inner-lane burners and among the outer-lane burners, and this distribution is referred to as the uniform FSF distribution.) Hence, the reformer CFD simulation result computed using the uniformly distributed furnace-side feed serves as a basis for this investigation. Initially, the uniform FSF distribution is implemented as the boundary condition of the reformer CFD model in the data generation process of Fig. 3.1. The corresponding CFD data generated from the simulation of the reformer CFD model is stored in the reformer CFD database (which is the Hoffman2 computing cluster at UCLA in this work). Subsequently, the CFD data in the reformer CFD database is used by the model identification process to derive a data-driven

model, which is a single input/single output (SISO) model that quantifies the impact of the FSF distribution on the OTWT distribution. Next, the model-based furnace-balancing optimizer utilizes the data-driven model to predict the optimized FSF distribution such that the degree of nonuniformity in the OTWT distribution is minimized. Then, the optimized FSF distribution is re-applied as the boundary condition of the reformer CFD model in the data generation process and is also used as the input of the data-driven model to generate two sets of the optimized OTWT distribution. Thereafter, the termination checker process utilizes the corresponding two data sets to evaluate the accuracy of the data-driven model and the performance of the furnace-balancing scheme such that when the difference between the two data sets is within 1%, or when the performance of the furnace-balancing scheme is no longer improved, the termination checker process signals for the furnace-balancing scheme to be terminated and the last optimized FSF distribution to be applied to the on-line reformer. In the remainder of this section, the data generation, model identification and model-based furnace-balancing optimizer processes will be presented.

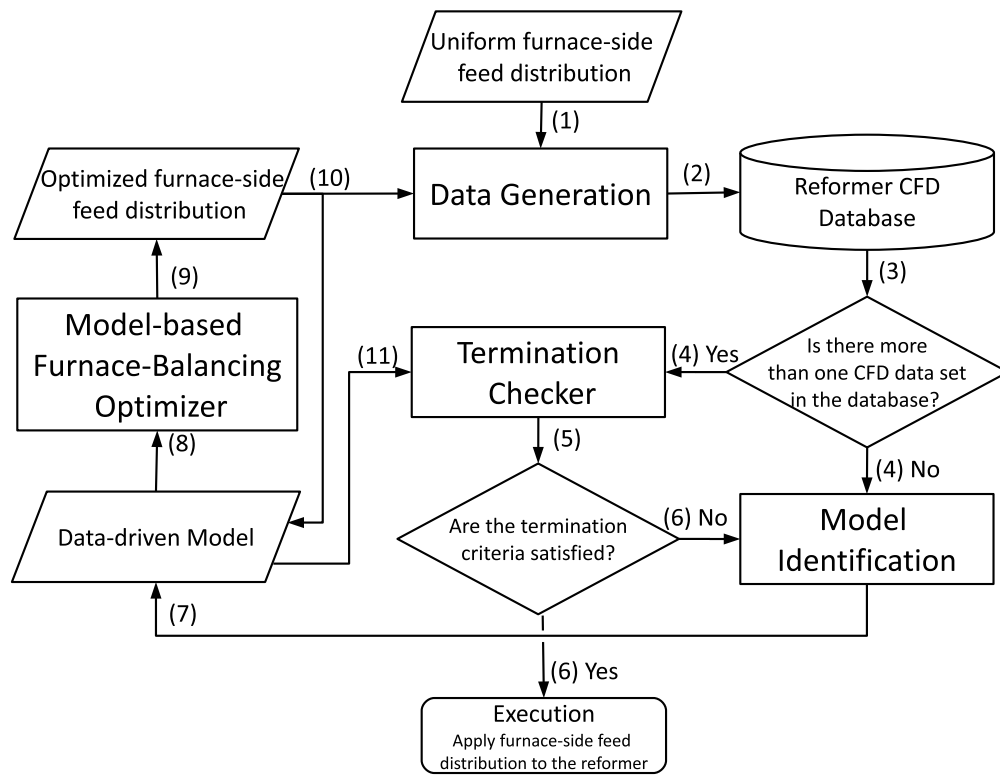


Figure 3.1: Flowchart of the furnace-balancing scheme.

3.2.1 Data generation

The first step of the furnace-balancing scheme (i.e., the data generation process) utilizes a reformer CFD model developed in Chapter 2 from which the CFD simulation data is generated and is consistent with various sources in the literature.

The reformer has a width of ~ 16 m, length of ~ 16 m and height of ~ 13 m. This unit consists of 336 reforming tubes, 96 burners and 8 flue-gas tunnels as shown in Fig. 3.2. Inside the reformer, 336 reforming tubes are arranged as seven rows of 48 units inside which commercial nickel-based catalyst pellets are used as packing material. At the ceiling of the reformer, 96 burners are positioned as eight rows of 12 units. Among the 96 burners, there are 24 outer-lane burners which are adjacent to one row of 48 reforming tubes and 72 inner-lane burners which are adjacent to two rows of 48 reforming tubes. The outer-lane burners are designed to be smaller and to have lower maximum flow capacity compared to the inner-lane burners. At the floor of the reformer, eight flue-gas tunnels are placed parallel to the rows of reforming tubes. On each side of the flue-gas tunnels, there is a row of 35 evenly spaced rectangular extraction ports. The reformer produces $2,800,000 \text{ Nm}^3$ of high-purity hydrogen and $1,700,000 \text{ kg}$ of superheated steam per day with an annual operating cost of $62,000,000$ dollars.

In CFD study, mesh generation is the most critical and time-consuming process because a CFD model created from a poor quality grid requires more computational resources and a longer computational time to calculate a converged simulation result, and the result is likely to carry a large numerical error [3]. The choice of meshing strategy (i.e., the structured multi-block hexahedral meshing) for creating the reformer mesh and the criteria (i.e., maximum orthogonal factor, minimum ortho skew, and maximum aspect ratio) for evaluating the reformer mesh quality are identical to those in Chapter 2 and, therefore, will not be repeated for brevity. However, the current reformer mesh in this work is designed to be finer than that in Chapter 2 (i.e., the total number of grids is increased from ~ 29 million to ~ 41 million) and to have significantly better mesh quality compared to the mesh in Chapter 2 as shown in Table 3.1. Although the reformer CFD model built from

the finer reformer mesh is expected to require a longer computational time than the reformer CFD model in Chapter 2 with the computational resources that we have at our disposal (i.e., 80 cores on the Hoffman2 cluster), the CFD data generated by the current reformer CFD model is expected to be a more accurate representation of the experimental data. The increased accuracy resulting in the increased computational time is essential because the magnitude of the reduction in the overall maximum outer reforming tube wall temperature in a balanced reformer is expected to be small (if not negligible) compared to its typical value. It is important to note that though the current multiblock structured hexahedral reformer mesh with ~ 41 million grids has a minimum orthogonal factor of 0.459 and a maximum ortho skew of 0.541, which may not appear to be suitable when the accuracy of the CFD data is the primary interest, its average orthogonal factor of 0.964 and average ortho skew of 0.036 are nearly ideal, which dismiss the initial concern of the impact of the mesh quality of the CFD data accuracy.

In Chapter 2, the modeling strategies of the reformer are chosen based on the transport and chemical reaction phenomena expected inside the reformer during hydrogen production and are selected to require a reasonably powerful computational resource and moderate computing time to create the reformer CFD model. In particular, the reformer CFD model is able to simulate the non-premixed combustion characteristics of the furnace-side fuel stream by using the standard $k - \epsilon$ turbulence model with the ANSYS enhanced wall treatment, finite rate/eddy dissipation (FR/ED) model and global volumetric kinetic models of methane/hydrogen combustion in air [5, 46]; therefore, burners in the reformer CFD model are supplied with the well-mixed feed (i.e., the furnace-side feed), which is created by mixing the fuel stream and the combustion air stream. Additionally, the reformer CFD model is capable of simulating radiative heat transfer between within the furnace-side flow, combustion chamber refractory walls and outer reforming tube walls by using an empirical correlation between the furnace-side radiative properties and temperature [43], Lambert Beer's law, Kirchoff's law and the discrete ordinate method [3]. Furthermore, the reformer CFD model can simulate the SMR process in the tube side by means of the standard $k - \epsilon$ turbulence model, FR/ED model and global kinetic model of the SMR process [64]. Moreover, the reformer

CFD model can also simulate the effects of the catalyst network on the tube side flow by employing the ANSYS porous zone function for which the parameters are estimated from the semi-empirical Ergun equation and relevant typical industrial data [34].

It has been established that the simulation of the reformer CFD model is sensitive to initial guesses (e.g., when the simulation of the reformer CFD model is initialized by the ANSYS standard initialization based on the boundary conditions of the CFD model, it quickly diverges), and for that reason in Chapter 2, a step-by-step converging strategy is proposed to counter the numerical instability issue and to accelerate the rate of convergence of the simulation, which reduces the computational time devoted to generate the converged CFD data. Hence, the converging strategy is again utilized in the present work to obtain the CFD data of the reformer CFD model in which the uniform FSF distribution is implemented as the boundary condition, and the CFD data is expected to be determined by the ANSYS Fluent parallel solver after ~ 3 days on the 80 private cores on UCLA's Hoffman2 Cluster. Although subsequent simulations of the reformer CFD model, in which the optimized FSF distribution is implemented as the boundary condition, could be executed with the converging strategy, we have found that we can further reduce the computational time to slightly more than a day by utilizing a CFD data set stored in the reformer CFD database as an initial guess for the simulations and executing with a two-step converging strategy. Specifically, the data generation process of each iteration of the furnace-balancing scheme begins with the simulation of the isothermal, non-reacting (INR) reformer CFD model, which is initialized based on the reformer CFD data and is solved by the aggressive mode of the ANSYS Fluent solver to generate an intermediate solution that contains information of the new flow fields (i.e., the velocity and turbulence fields of the furnace-side and tube-side flows) of the balanced reformer CFD model. This is because despite the differences in the composition and temperature fields of the furnace-side and tube-side flows computed by the INR reformer CFD model and the reformer CFD model, their furnace-side and tube-side flow fields are expected to be similar [3, 60]. Finally, the simulation of the (complete) reformer CFD model is initialized based on the intermediate CFD data (which contains information of the new flow fields in addition to the temperature and species fields from

the reformer CFD data of a prior iteration) and is solved by the aggressive mode of the ANSYS Fluent solver until the convergence criteria, which are adopted from Chapter 2 and described in the next paragraph, are met.

Typically, after the global normalized residuals of the conserved transport variables are on the order of 10^{-4} , the total mass flow rate integrated over all boundaries of the reformer CFD model is $\sim 0 \text{ kg s}^{-1}$, the total heat transfer rate integrated over all boundaries of the reformer CFD model is less than 1% of the reformer total fired duty, and the absolute residuals of the temperature of the furnace-side flow at five different locations inside the combustion chamber are less than 1 K, the simulations would be terminated. In the present work, the simulations are continued because we recognize that the global normalized residuals are nonzero which indicates that the CFD data fluctuates around the true steady-state solution of the reformer CFD model, and therefore, the averaged CFD data of many converged CFD data sets is the most accurate representation of the reformer steady-state solution. In the effort of acquiring the more accurate CFD data for each reformer CFD model, the simulation is kept running for an additional 300 iterations, which correspond to $\sim 5\% - 10\%$ of the total computational time, and the corresponding CFD data is periodically saved in the reformer CFD database every 100 iterations creating a total of four CFD data sets for each reformer CFD model, of which the average CFD data is utilized by subsequent processes of the furnace-balancing scheme. Although the effort to obtain the more accurate CFD data results in increased computational time, the trade-off is critical because the reduction in the maximum outer reforming tube wall temperature due to the optimized FSF distribution is expected to be substantially smaller than the overall average outer wall temperature of the reforming tubes.

3.2.2 Model Identification

The second step of the furnace-balancing scheme (i.e., the model identification process) utilizes the cumulative reformer CFD database collected from the data generation process to derive a data-driven model describing the relationship between the OTWT distribution at a specified distance away from the reforming tube inlets and the FSF distribution. In the present work, we have found

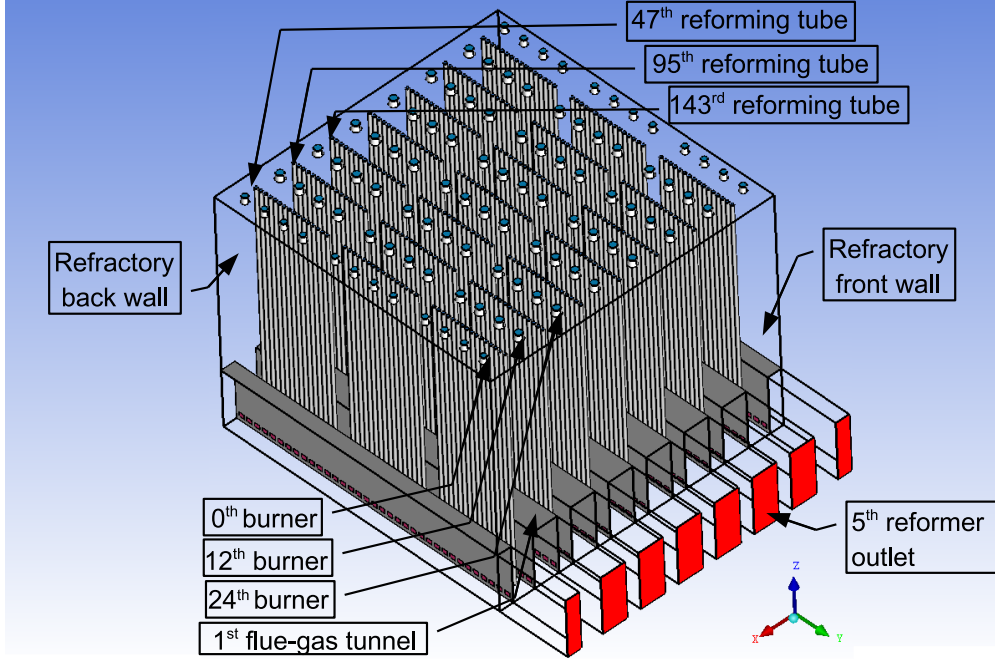


Figure 3.2: The isometric view of an industrial-scale, top-fired, co-current reformer with 336 reforming tubes, which are represented by 336 slender cylinders, 96 burners, which are represented by 96 frustum cones, and 8 flue-gas tunnels, which are represented by 8 rectangular intrusions.

that the relationship can be assumed to be linear, and the data-driven model can still provide a reasonably accurate prediction of the OTWT distribution, which is generated by the reformer CFD model, given a sufficiently large reformer CFD database. Therefore, the radially average outer reforming tube wall temperature of the i^{th} reforming tube at the fixed distance away from the reforming tube inlet (T_i (K)), which is an element of the OTWT distribution, can be approximated by a linear combination of the FSF flow rates of all 96 burners (i.e., the FSF distribution) as follows,

$$T_i = \sum_{j=0}^{95} \alpha_{ij} F_j \quad (3.1)$$

where F_j (kg s^{-1}) is the furnace-side feed flow rate of the j^{th} burner and α_{ij} ($\text{K kg}^{-1}\text{s}$) is the empirical coefficient of the data-driven correlation corresponding to the i^{th} reforming tube and j^{th} burner, which is to be determined by the model identification process. In this study, the outer-lane/inner-lane burners and reforming tubes are indexed from $0^{th} - 95^{th}$ and $0^{th} - 335^{th}$ in the specified

Table 3.1: Reformer mesh quality

	Current mesh	Mesh in Chapter 2	Recommended range
Number of grids (millions)	41	29	
Min orthogonal factor	0.459	0.181	0.167–1.000
Max ortho skew	0.541	0.819	0.000–0.850
Max aspect ratio	28.5	28.5	1–100

patterns as shown in Fig. 3.2. As a result, the model identification process created based on our assumption of the linear relationship between the OTWT and FSF distributions is an optimization problem with 32256 decision variables. Due the sheer number of decision variables, the model identification process is expected to be a computationally expensive algorithm. Hence, in the remainder of this section, the concept of a heating zone is introduced in an effort to decrease the computational time for deriving the data-driven model, and a modified formulation of the model identification process is presented.

In high-temperature applications, thermal radiation is the dominant mode of heat transfer, and the reformers are commonly referred to as radiant heat exchangers [32]. Olivieri et al. [47] shows that radiative heat transfer accounts for $\sim 95\%$ of the total heat transfer in the top-fired reformer investigated in that work, which suggests that the OTWT distribution is primarily controlled by thermal radiation. This is because the rate of energy transferred by thermal radiation between two blackbodies at different temperatures is commonly modeled as being proportional to the difference in temperatures raised to the fourth power (i.e., $\Delta(T^4)$), while the rate of heat transfer by conduction and convection between them is proportional to the temperature difference (i.e., $\Delta(T)$). However, the rate of heat transfer by thermal radiation decreases drastically with increasing distance between two blackbodies because it is proportional to the radiation intensity, which is inversely proportional to the distance between the two blackbodies raised to the second power. This idea allows us to assume that when the distance between a specified burner and reforming tube is sufficiently large, the furnace-side feed flow rate of the burner has negligible impact on

the average outer reforming tube wall temperature. In this study, the distance between a specified burner and reforming tube is defined as the distance between the projection of the burner centroid and the projection of the reforming tube centroid onto any 2-D horizontal cross-sectional plane. To quantitatively determine the local radiative heating effect on the OTWT distribution due to the furnace-side feed flow rate of each burner, we consider the following simplifying assumptions: each burner creates a heating zone represented by a blue cylindrical volume as shown in Fig. 3.5, the heating zones of the burners have an identical size and shape, and the FSF flow rate of the j^{th} burner only affects the average outer wall temperature values of the reforming tubes which are located inside the heating zone of the j^{th} burner.

On the other hand, it has been established that the furnace-side flow pattern can influence the OTWT distribution, e.g., a maldistribution of the furnace-side flow pattern in the reformer can potentially cause flame impingement, which might make the outer wall temperature values of some reforming tubes to exceed the design temperature, causing the OTWT distribution to have a higher degree of nonuniformity as discussed in Section 3.1. Hence, it is desired that the model identification process can create a data-driven model that is also capable of accounting for the effect of the furnace-side flow pattern on the OTWT distribution. We begin by utilizing the existing reformer CFD data reported in Chapter 2 to construct the velocity vector fields of the furnace-side flow pattern as shown in Fig. 3.3, which allows us to form a hypothesis regarding the underlining mechanism by which the furnace-side flow field affects the OTWT distribution. Specifically, Fig. 3.3 indicates that the hot combustion products (i.e., the furnace-side flow) enter the flue-gas tunnels through the extraction ports and move toward the reformer outlets. The existing furnace-side flow pattern appears to cause the wall temperature of the flue-gas tunnels to increase with decreasing distance toward the reformer outlets as shown in Fig. 3.4. Additionally, Fig. 3.4 shows that the minimum wall temperature of the flue-gas tunnel of 1240 K is greater than the maximum temperature of the reforming tube wall of 1183 K as reported in Chapter 2, so it is reasonable to assume that the reforming tubes might receive additional radiative heating from the neighboring flue-gas tunnels. However, the magnitude of the additional heating transferred to each

reforming tube from the neighboring flue-gas tunnels depends on the location of the reforming tube with respect to the reformer outlets. Particularly, because the flue-gas tunnels are at higher temperature toward the reformer outlets, the reforming tubes that are situated closer to the reformer outlets are expected to receive higher amounts of additional radiative heating from the neighboring flue-gas tunnels. It is important to note that the existing furnace-side flow pattern (Fig. 3.3) also suggests that the additional radiative heating received by the reforming tubes that are situated near the reformer outlets can be from the combustion products of the burner that is situated near the reformer back wall. The analysis motivates us to develop heating zones with the shape shown in Fig. 3.5 in the effort of making the data-driven model aware of the furnace-side flow pattern and its effects on the OTWT distribution. It is important to note that when a larger cylindrical heating zone is utilized in the model identification process, each burner is assumed to influence more surrounding reforming tubes in addition to those that are situated in the direction toward the reformer outlets and in the two adjacent rows of reforming tubes, which may allow the data-driven model to be more accurate with respect to the reformer CFD data at the cost of increased computational time. We conducted a study with various dimensions of the burner heating zone to determine the appropriate dimension of the cylindrical volume (i.e., r_{cyl}), and we have found that at $r_{cyl} \sim 3.4$ m, we are able to form 336 sets of the tube-burner relationships, which are denoted by S_i and $i \in [0, 335]$ such that S_i contains the FSF flow rates of the burners on which the outer wall temperature of the i^{th} reforming tube depends. The tube-burner relationships reduce the number of decision variables of the model identification algorithm from 32256 to 6865 and, thus, allow the data-driven model to be created within a reasonable computing time interval.

The data-driven model is designed to account for the reformer geometry characteristics (i.e., the burner and reforming tube arrangements) and is designed to have the potential to account for the influence of the furnace-side flow pattern on the OTWT distribution by using the concept of a heating zone. The data-driven model utilizes a given FSF distribution to predict an OTWT distribution that is close to that taken from a reformer CFD simulation result in the least squares sense. The model identification process based on n sets of the reformer CFD data taken from the

reformer CFD database is formulated as follows,

$$\min_{\alpha_{i,j} \in [0, \infty)} \sum_{m=0}^{n-1} \left(\sum_{k=0}^{335} (T_{k,m} - T_{k,m}^{est})^2 \right)^2 \quad (3.2)$$

subject to

$$T_{k,m}^{est} = \sum_{j=0}^{95} \alpha_{kj} F_{j,m} \quad (3.3a)$$

$$\alpha_{kj} = 0 \quad \text{if } F_{j,m} \notin S_k \quad (3.3b)$$

$$\alpha_{kj} = \alpha_{ki} \quad \text{if } F_{j,m}, F_{i,m} \in S_k \text{ and } d_{kj} = d_{ki} \quad (3.3c)$$

$$\left(\frac{d_{kj}}{d_{ki}} \right)^\beta \cdot \alpha_{kj} \geq \alpha_{ki} \geq \alpha_{kj} \quad \text{if } F_{j,m}, F_{i,m} \in S_k \text{ and } d_{kj} > d_{ki} \quad (3.3d)$$

where $T_{k,m}$ and $T_{k,m}^{est}$ are the average outer wall temperature of the k^{th} reforming tube taken from the m^{th} reformer CFD data set and the corresponding value generated by the data-driven model given the m^{th} furnace-side feed distribution as shown in Eq. 3.3a, respectively, $F_{j,m}$ is the furnace-side feed flow rate of the j^{th} burner derived from the m^{th} reformer CFD data set, $\beta = 4.0$ is an empirical constant of the data-driven model estimated from the study of the burner heating zone, d_{kj} is the distance between the k^{th} reforming tube and the j^{th} burner and d_{ki} is the distance between the k^{th} reforming tube and the i^{th} burner. In Eqs 3.3a–3.3d, the ranges of k , i , j and m are $0 - 335$, $0 - 95$, $0 - 95$ and $0 - n$, respectively. The cost function (Eq. 3.2) of the model identification penalizes the deviation of the average outer wall temperature of each reforming tube generated by the data-driven model from that derived from the corresponding reformer CFD data set. Specifically, Eq. 3.3b suggests that if the k^{th} reforming tube is not situated within the heating zone of the j^{th} burner ($T_{k,m} \neq T_{k,m}(F_{j,m})$), the data-driven model will assume that the furnace-side feed flow rate of the j^{th} burner does not affect the k^{th} outer reforming tube wall temperature. Additionally, Eq. 3.3c indicates that if the distance between the k^{th} reforming tube and the j^{th} burner is equal to that

between the k^{th} reforming tube and the i^{th} burner, the data-driven model then presumes that the effects of the burners on the k^{th} outer reforming tube wall temperature are the same. Similarly, Eq. 3.3d shows that if the distance between the k^{th} reforming tube and the j^{th} burner is greater than that between the k^{th} reforming tube and the i^{th} burner, the data-driven model then infers that the effects of the j^{th} burner on the k^{th} outer reforming tube wall temperature are weaker than those of the i^{th} burner.

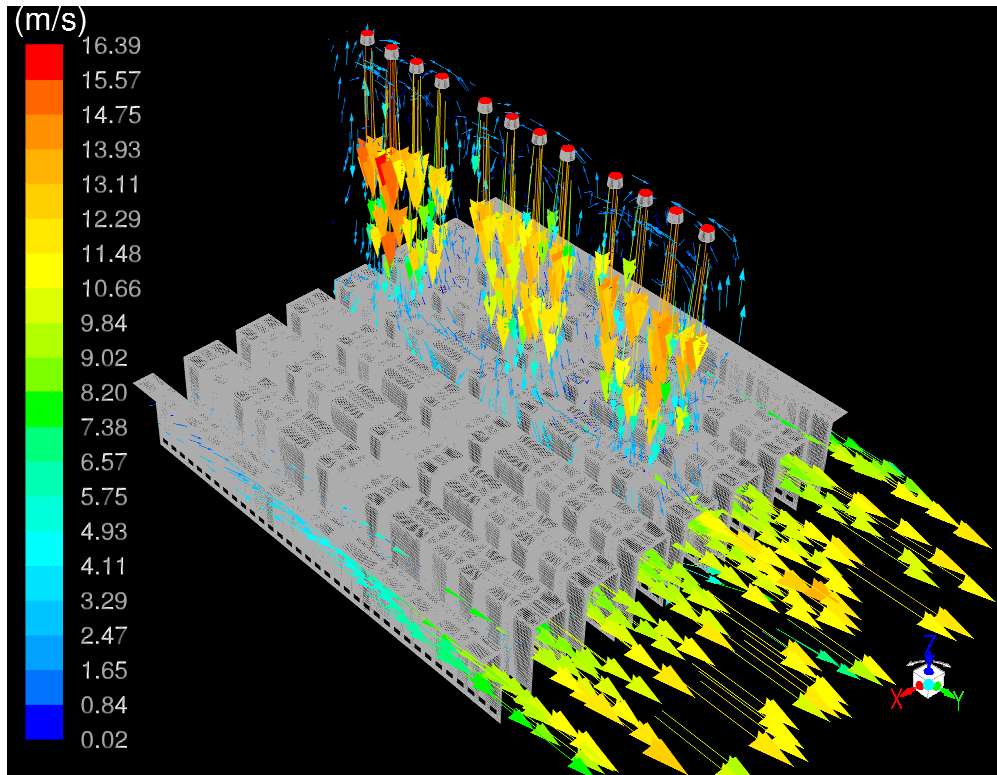


Figure 3.3: The velocity vector field of the furnace-side flow pattern in the vicinity of the 4th burner row in the reformer is constructed from the reformer CFD data reported in Chapter 2. The outlets of the reformer are situated at the bottom right corner and are placed in the direction of the velocity vectors inside the flue-gas tunnels.

3.2.3 Valves and flow rate relation

Although the FSF distribution is used as the boundary condition of the high-fidelity reformer CFD model and is chosen as the input of the data-driven model, it cannot be directly controlled and is

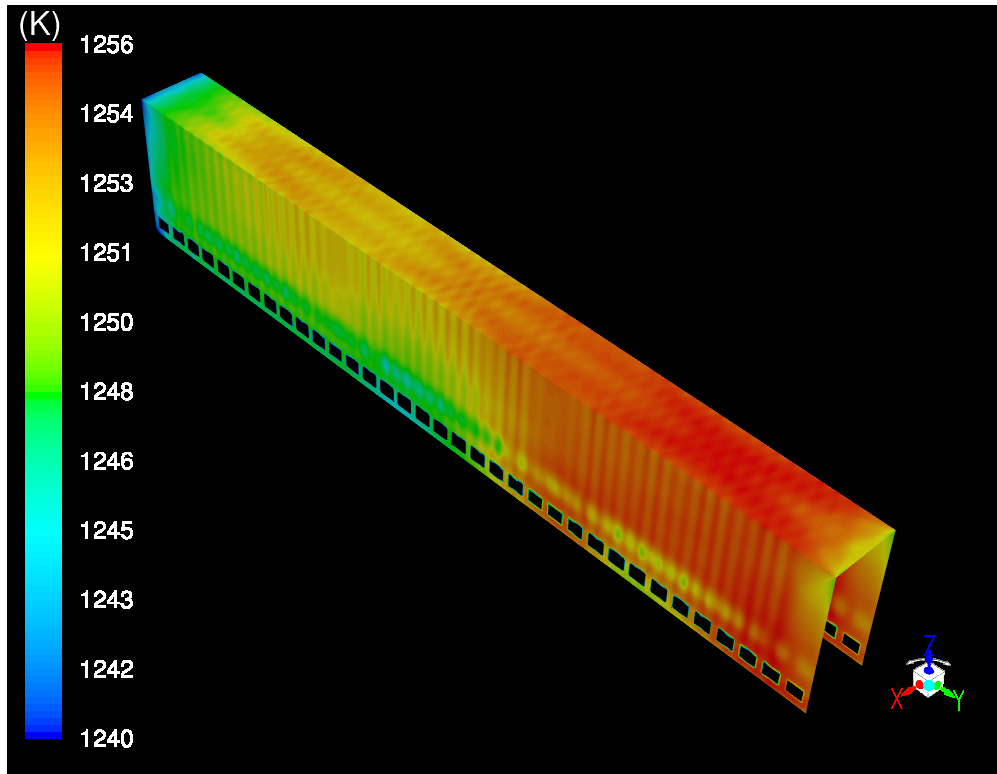


Figure 3.4: The temperature contour map of the 4th flue-gas tunnel, which is situated directly under the 4th burner row in the reformer, is shown. This contour map is created from the reformer CFD data in Chapter 2. In Fig. 3.4, the outlets of the reformer are situated at the bottom right corner.

not typically measured in industrial practice. Indeed, the FSF distribution is controlled by a system of flow regulators consisting of a finite number of flow control valves. Specifically, because the burners in the reformer are interconnected, a fractional amount of the FSF flow rate of the j^{th} burner can be redistributed to other units by partially closing the corresponding flow control valve. This suggests that the optimized FSF distribution can be produced by appropriately adjusting the percent open positions of all flow control valves in the flow regulator system, which is referred to as the valve position distribution. Hence, the merit of the high-fidelity reformer CFD model and of the data-driven model for the furnace-balancing application, which aims to reduce the degree of the temperature nonuniformity in the combustion chamber and to increase the reformer thermal efficiency, is evident.

In an industrial setting of commercial-scale hydrogen production, it is unconventional for a

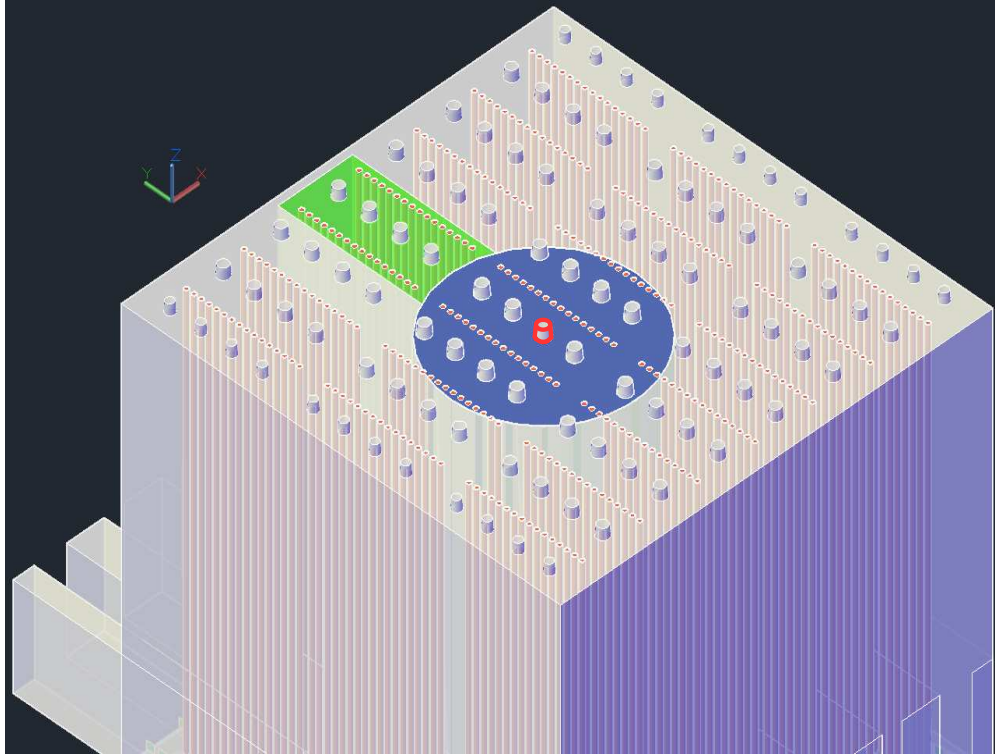


Figure 3.5: A representation of a burner heating zone which is created by the highlighted burner in red. The burner heating zones are displayed by a blue cylindrical volume (where the reforming tubes are heated via thermal radiation from the furnace-side flow) and a green rectangular volume (where the reforming tubes are heated via thermal radiation from the neighboring flue-gas tunnels). It is assumed that only the reforming tubes located within the burner heating zones have the outer wall temperature values dependent on the FSF flow rate of the burner.

furnace-side feed flow rate of a burner in the reformer to be individually regulated due to the sheer number of burners. In the present work, we assume that every set of two consecutive burners in a row of twelve burners is controlled by a flow control valve, and therefore, it is also reasonable to assume that the same FSF flow rate is delivered to these burners. Additionally, we assume that the FSF distribution is regulated by two distinct linear flow control valve models with different maximum capacities. Among the flow control valve models, one valve model with a larger maximum capacity is used for the inner-lane burners, and the other valve model with a smaller maximum capacity is implemented in the outer-lane burners such that when valves are at the same opening position, the FSF flow rate of the outer-lane burners is 60% of that of the inner-lane burners. Based

on the burner arrangement in the reformer and the capacity ratio of the inner-lane valve model and the outer-lane valve model, the valve-position-to-flow-rate converter is formulated as follows,

$$[F] = \delta \cdot [X] \cdot [Y] \cdot [V] \quad (3.4)$$

subject to

$$[V] \in \mathbb{R}^{48 \times 1} \quad (3.5a)$$

$$[X] \in \mathbb{R}^{96 \times 96} \quad (3.5b)$$

$$X_{ij} = 0.6; \quad i = j \text{ where } i \in [0, 11] \cup [84, 95]$$

$$X_{ij} = 1.0; \quad i = j \text{ where } i \in [12, 93]$$

$$X_{ij} = 0.0; \quad i \neq j$$

$$[Y] \in \mathbb{R}^{96 \times 48} \quad (3.5c)$$

$$Y_{ij} = 1.0; \quad i = 2j \cup i = 2j + 1 \text{ where } j \in [0, 47]$$

$$Y_{ij} = 0.0; \quad i \neq 2j \cap i \neq 2j + 1 \text{ where } j \in [0, 47]$$

$$[F] \in \mathbb{R}^{96 \times 1} \quad F_i \geq 0 \quad \forall i \in [0, 95] \quad (3.5d)$$

$$\delta = \frac{F_{tot}}{\|[X] \cdot [Y] \cdot [V]\|_1} \quad (3.5e)$$

where F_{tot} (kg s^{-1}) is the total mass flow rate of the furnace-side feed to the reformer, δ is the valve-to-flow-rate proportionality coefficient and is dependent on the valve position distribution, $[F]$ is a vector of the FSF flow rate through each burner (the FSF distribution), $[X]$ is a transformation matrix that identifies the types of the flow control valves (i.e., the inner-lane and outer-lane valves) in the reformer, $[Y]$ is a transformation matrix that describes the burner arrangement in the reformer and $[V]$ is a vector of valve positions (the valve position distribution). A characteristic of the valve-to-flow-rate converter is that an FSF distribution can be produced by different valve position distributions by changing the inlet pressure of the furnace-side feed to the reformer. To illustrate

this idea, we utilize a fictitious simplified interconnected flow system which consists of four inner-lane burners and is supplied with the constant total FSF mass flow rate of $4.0 \text{ (kg s}^{-1}\text{)}$. When both flow control valves regulating the four inner-lane burners are at 100% open, the total FSF flow rate to the simplified interconnected flow system is evenly distributed, i.e., the FSF flow rate to each inner-lane burner is expected to be $1.0 \text{ (kg s}^{-1}\text{)}$. When both flow control valves regulating the four inner-lane burners are 80% open, the FSF flow rate to each inner-lane burner is still required to be $1.0 \text{ (kg s}^{-1}\text{)}$ to maintain the constant total FSF mass flow rate of $4.0 \text{ (kg s}^{-1}\text{)}$ because of the two following reasons: the FSF flow rates of the two inner-lane flow control valves that are at the same valve position are equal, and the FSF flow rates of the two inner-lane burners that are regulated by a flow control valve are also assumed to be equal. The primary difference between the two case studies is in plant's efficiency, as the magnitude of the inlet pressure of the furnace-side feed to the reformer is expected to be higher in the second case study, which corresponds to a higher energy input to the compressor system leading to an increase in the operating cost of the reformer and a reduction in the plant's efficiency.

In the reformer, the flow control system has 48 flow control valves among which 36 valves are designated to regulate the FSF flow rates of the 72 inner-lane burners, and the valve position of each flow control valve must be adjusted to create the optimized FSF distribution. Therefore, the reformer thermal efficiency becomes susceptible to common valve-related problems (e.g., valve stickiness) as these disturbances prevent the valve position distribution that is designed to produce the optimized FSF distribution from being implemented. In this study, when a flow control valve is said to become defective, we assume that the flow control valve becomes stuck, and hence, the valve position cannot be adjusted, which prevents the furnace-side feed from being distributed according to the optimized distribution.

3.2.4 Model-based furnace-balancing optimizer

The third step of the furnace-balancing scheme (i.e., the model-based furnace-balancing optimizer) utilizes the data-driven model (Eq. 3.10b), the valve-position-to-flow-rate converter (Eq. 3.10a)

to derive an optimized FSF distribution that aims to reduce the degree of nonuniformity in the OTWT distribution. The furnace-balancing optimizer is designed as a multivariable optimization problem in which the decision variables are the positions of the properly functional flow control valves. Additionally, the furnace-balancing optimizer is designed to handle defective valves in the flow control system by adjusting the number of decision variables. For instance, if a flow control valve of the 0^{th} and 1^{st} outer-lane burners becomes defective, there are 47 functional valves in the flow control system, and therefore, the number of decision variables decreases from 48 (which corresponds to the total number of the flow control valves in the reformer) to 47. During the initialization of the furnace-balancing optimizer, a text file documenting the current status of the flow control valves is provided, based on which the furnace-balancing optimizer identifies the defective valve(s) and the corresponding stuck valve position(s) to determine the number of decision variables.

The decision variables of the furnace-balancing optimizer are subjected to the practical constraint of the flow control valves (i.e., Eq. 3.10f, which is enforced to avoid extinguishing the flame) and the physical constraint of the flow control valves (i.e., Eq. 3.10e). In addition, we assume that the total furnace-side feed derived based on typical industrial data is kept constant at F_{tot} (i.e., Eq. 3.10c), when the optimized FSF distribution is computed. This strictly controlled operating window of the reformer allows the radial average temperature of the i^{th} reforming tube at a fixed distance away from the reforming tube inlet to be expressed as a linear combination of the FSF distribution as shown in Eq. 3.10b.

In the development of the furnace-balancing optimizer, careful considerations regarding the characteristic of the valve-to-flow-rate converter must be given. Specifically, the valve-to-flow-rate converter allows a FSF distribution to be produced by different valve position distributions between which the primary difference is in the plant's efficiency because the valve position distribution deviates further away from the default distribution (i.e., in which flow control valves are fully open) and thus requires a higher inlet pressure of the furnace-side feed to the reformer leading to a higher energy input to the compressor system, an increase in the operating cost of the reformer and

a reduction in the plant's efficiency. In the present work, a quantitative assessment of the deviation of a valve position distribution ($[V]$) from the default distribution ($[V]_0$) is computed as the 1-norm of the difference between $[V]_0$ and $[V]$, i.e., $\|[V]_0 - [V]\|_1$. Therefore, the furnace-balancing optimizer is designed to minimize the degree of nonuniformity in the OTWT distribution in a manner that requires the least duty of the compressor system to maximize the plant's efficiency and reformer service life by penalizing the weighted quadratic deviation of the outer wall temperature values of all reforming tubes from the set-point temperature (T_{AVE}),

$$\sum_{k=0}^{335} w_k (T_{AVE} - T_k^{est})^2, \quad (3.6)$$

and also penalizing the deviation of the optimized valve position distribution ($[V]$) from $[V]_0$,

$$\|[V]_0 - [V]\|_1 = \sum_{i=0}^{47} (V_{i,max} - V_i). \quad (3.7)$$

The objective function of the furnace-balancing optimizer must signify that minimizing the degree of nonuniformity in the OTWT distribution has by far the highest priority and should not be compromised by the minor benefit of minimizing the duty of the compressor system. This idea is translated into mathematical expression of the penalty associated with the task of minimizing the compressor duty in the objective function of the furnace-balancing optimizer by normalizing the deviation of the optimized valve position distribution from $[V]_0$, which is subsequently scaled by multiplying with the product of the penalty associated with the task of minimizing the degree of nonuniformity in the OTWT distribution and a weighting factor (γ),

$$\gamma \cdot \sum_{k=0}^{335} w_k (T_{AVE} - T_k^{est})^2 \cdot \frac{\sum_{i=0}^{47} (V_{i,max} - V_i)}{\sum_{i=0}^{47} (V_{i,max} - V_{i,min})}. \quad (3.8)$$

As a result, the objective function of the furnace-balancing optimizer is formulated as shown in Eq. 3.9, in which the first term represents the penalty associated with the task of minimizing the

degree of nonuniformity in the OTWT distribution, and the second term represents the penalty associated with the task of minimizing the compressor duty. The set-point temperature (T_{AVE}) can be computed based on the OTWT distribution from any of the previous CFD data sets from the reformer CFD database as shown in Eq. 3.10d because the overall average outer wall temperature at the fixed distance away from the reforming tube inlets is expected to be constant despite the degree of nonuniformity in the OTWT distribution. Additionally, the initial guesses for the decision variables of the furnace-balancing optimizer are set to be 100% open (i.e., when the penalty on the control action is minimized) to allow the furnace-balancing optimizer to initially shift the focus on minimizing the degree of nonuniformity in the OTWT distribution and to avoid being stuck, which could happen when it is initially forced to accomplish both objectives simultaneously. The model-based furnace-balancing optimizer is formulated as follows,

$$\min_{\substack{V_j \in [60, 100] \\ j = \{0, \dots, 47\} \setminus V_{def}}} \sum_{k=0}^{335} w_k (T_{AVE} - T_k^{est})^2 + \gamma \sum_{k=0}^{335} w_k (T_{AVE} - T_k^{est})^2 \cdot \frac{\sum_{i=0}^{47} (V_{i,max} - V_i)}{\sum_{i=0}^{47} (V_{i,max} - V_{i,min})} \quad (3.9)$$

subject to

$$[F] = \delta \cdot [X] \cdot [Y] \cdot [V] \quad (3.10a)$$

$$T_k^{est} = \sum_{j=0}^{95} \alpha_{k,j} F_j \quad \forall F_j \in [F] \quad (3.10b)$$

$$\sum_{j=0}^{95} F_j = F_{tot}, j = \{0, \dots, 95\} \quad (3.10c)$$

$$T_{AVE} = \frac{1}{336} \sum_{k=0}^{335} T_{k,m} \quad (3.10d)$$

$$V_{i,max} = 100\% \quad i = \{0, \dots, 47\} \quad (3.10e)$$

$$V_{i,min} = 60\% \quad i = \{0, \dots, 47\} \quad (3.10f)$$

$$V_{i,max} \leq V_i \leq V_{i,max} \quad i = \{0, \dots, 47\} \setminus V_{def} \quad (3.10g)$$

$$V_{i,def} \quad (3.10h)$$

where V_{def} is the set of indices of defective control valves, w_k is the weighting factor of the k^{th} reforming tube (which is used to compute the penalty associated with the deviation of the predicted outer wall temperature of the k^{th} reforming tube (T_k^{est}) from T_{AVE}), γ is the weighting factor of the penalty associated with the control action, V_i (the i^{th} component of $[V]$) is the valve position of the i^{th} flow control valve (which regulates the FSF flow rates of the $(2i)^{th}$ and $(2i+1)^{th}$ burners) and F_j (the j^{th} component of $[F]$) is the optimized FSF flow rate of the j^{th} burner. The idea of assigning the deviations of T_k^{est} from T_{AVE} of the reforming tubes different weights in the penalty associated with the degree of nonuniformity in the OTWT distribution is motivated by the fact that the local environments of the reforming tubes are not all identical, and specifically, the additional radiative heating provided for the reforming tubes from the neighboring flue-gas tunnels is expected to decrease with increasing distance away from the reformer outlets. Hence, we want to compensate for the nonuniform additional radiative heating along the rows of 48 reforming tubes by giving the most weight to the offsets of the reforming tubes that are the furthest away from the reformer

outlets (e.g., the 47th reforming tube). Specifically, w_k is designed to monotonically decrease with the position (p_k) of the k^{th} reforming tube in a row of 48 reforming tubes as follows,

$$p_k = k - 48 \cdot \left\lfloor \frac{k}{48} \right\rfloor \quad k \in \{0, 1, \dots, 335\} \quad (3.11a)$$

$$w_k = w_k^{\text{max}} \cdot \exp[-\beta_w \cdot (47 - p_k)] \quad p_k \in \{0, 1, \dots, 47\} \quad (3.11b)$$

where $\lfloor \cdot \rfloor$ represents the ‘floor’ operator, and w_k^{max} and β_w are the parameters of w_k . These weights, combined with the form of the heating zones for the data-driven model discussed in Section 3.2.2, allow the furnace-balancing optimizer to account to some extent for the reformer geometry, furnace-side flow pattern and its potential influence on the OTWT distribution. Therefore, the furnace-balancing optimizer is expected to realize that the burners situated near the refractory back wall might have long range effects on the outer wall temperature of the reforming tubes near the reformer outlets. As a result, the optimized FSF distribution is expected to lessen the degree of nonuniformity in the OTWT distributions along the reforming tubes and to reduce the overall maximum temperature of the outer reforming tube wall, which creates room for improving the thermal efficiency of the reformer. It is important to note that $w_{k,1}^{\text{max}} = 10.0$, $\beta_w = 0.05$ and $\gamma = 0.1$ are determined based on a trial-and-error approach until the largest reduction in the degree of nonuniformity in the predicted OTWT distribution is observed.

3.3 Simulation Results

In this section, the average of four CFD data sets produced by the reformer CFD model, in which the uniform FSF distribution is used as the boundary condition, are utilized to analyze the existing degree of nonuniformity in OTWT distributions at different locations along the reforming tube length as shown in Table 3.2. We note that the spread of the OTWT distributions only raises our concerns about the reformer life service when the average temperature of the OTWT distribution at a fixed distance away from the reforming tube inlets is in the regime of the maximum value of average temperatures of the OTWT distributions along the reforming tube length. This is because if the average temperature of the OTWT distribution is high, the radially averaged maximum temperature is likely to exceed the design temperature of the reforming tube wall, and therefore, the service life of the reformer is shortened. Additionally, Kumar et al. [32] shows that OTWT distributions along the reforming tube length and the spatial distribution of the furnace-side temperature can be made to become more uniform by reducing the degree of nonuniformity in just one OTWT distribution. In the remainder of this section, we focus on the OTWT distribution that is ~ 6.5 m away from the reforming tube inlets as it has a relatively high overall average temperature (1165.08 K, which is $\sim 99\%$ of the maximum value in the average outer wall temperature profile), temperature range (67.7 K) and standard deviation (9.7 K). Only the OTWT distributions and the corresponding FSF distributions are utilized by the model identification to create the data-driven model as discussed in Section 3.2.2. Next, the model-based furnace-balancing optimizer uses the status of the flow control system, the valve-position-to-flow-rate converter and the most up-to-date data-driven model to search for the optimized FSF distribution to minimize the degree of nonuniformity in the OTWT distribution. We note that each data set utilized by the model identification process requires 3.64×10^{-4} GB of storage space, while the original reformer CFD data, from which the OTWT distribution and FSF distribution are extracted, requires 112 GB of storage space, and therefore, the data-driven model might not be able to precisely predict the behavior of the reformer when the training data set is not sufficiently large. Hence, once an optimized FSF

distribution is obtained from the furnace-balancing optimizer, the optimized FSF distribution is simultaneously used as the boundary condition of the reformer CFD and as the input of the data-driven model, and the corresponding data is utilized in the termination checker process, in which the accuracy of the data-driven model and the performance of the furnace-balancing scheme are evaluated. In the present work, the performance of the furnace-balancing scheme is assessed based on the percent reduction in the standard deviation of the OTWT distribution generated by the reformer CFD model, in which the optimized FSF distribution is used as the boundary condition, compared to that generated by the reformer CFD model, in which the uniform FSF distribution is used as the boundary condition.

Each iteration of the proposed furnace-balancing scheme solved by Ipopt [61] generates an optimized FSF distribution and quantitatively estimates the reduction of the degree of nonuniformity of the OTWT distribution within 30 hours using 80 cores of UCLA Hoffman2 Cluster, and $\sim 90\%$ of the computational time is designated to the data generation process. The termination checker process triggers a terminating signal after six iterations of the furnace-balancing scheme. It is worth noting that subsequent attempt to re-optimize the FSF distribution to compensate for the influences of common valve-related problems can be accomplished after fewer iterations of the furnace-balancing scheme as the data-driven model derived using the entire reformer CFD database is expected to accurately predict the reformer behavior.

3.3.1 Case study A

In this subsection, the performance of the furnace-balancing scheme is investigated under the assumption that the flow control system is fully functional (i.e., the furnace-balancing optimizer has 48 decision variables). The simulation results generated during the first six iterations of the furnace-balancing scheme are presented and discussed.

The evolution of the data-driven model is shown in Fig. 3.6, which indicates that the data-driven model progressively becomes a more accurate representation of the reformer CFD data

with more iterations of the furnace-balancing scheme due to a larger reformer CFD database. Fig. 3.6 shows the predicted OTWT distributions generated by the data-driven model match well with those generated by the reformer CFD model with just five training data sets from the reformer CFD database, which validates our hypotheses of the impact of the furnace-side flow pattern on the OTWT distribution, the size of the cylindrical heating zone, the altered shape of the heating zone and the assumption that the radial average temperature of the i^{th} reforming tube at a fixed distance away from the reforming tube inlet can be expressed as a linear combination of the FSF distribution.

Next, the evolution of the OTWT distribution at a distance 6.5 m away from the reforming tube inlets is shown in Figs. 3.6, 3.7 and 3.8, which reveal that the reformer CFD model, in which the optimized FSF distribution is used as the boundary condition, has a less severe degree of nonuniformity in the OTWT distribution after the first iteration of the furnace-balancing scheme. Fig. 3.8 is created to allow data visualization (allowing the 336 reforming tubes in the reformer to be represented by a table consisting of 336 rectangular cells, of which each location in the table maps to a unique reforming tube in the reformer) so that the performance of the furnace-balancing scheme and the degree of nonuniformity of the OTWT distribution can be evaluated qualitatively at a glance (e.g., if Fig. 3.8 has a high number of red and green cells, the OTWT distribution is highly nonuniform). Fig. 3.8 shows that the OTWT distribution gradually becomes more uniform with more iterations of the furnace-balancing scheme. Specifically, by the 2nd iteration, the under-heated region near the reformer outlets in the OTWT distribution of the 0th iteration (i.e., the reformer CFD model of which the uniform FSF distribution is used as the boundary condition) is completely eliminated, by the 4th iteration the other noticeable under-heated region near the refractory back wall in the OTWT distribution of the 0th iteration is completely removed, and by the 6th iteration the severity of the two over-heated regions in the OTWT distribution of the 0th iteration is reduced. Figs. 3.6 and 3.7 are utilized to quantitatively evaluate the performance of the furnace-balancing scheme and the degree of nonuniformity of the OTWT distribution. From the 2nd iteration onward, Figs. 3.6 and 3.7 show that the temperature range and standard deviation

of the OTWT distribution decrease compared to those of the 0th iteration. Specifically, at the 6th iteration of the furnace-balancing scheme, the temperature range and standard deviation of the OTWT distribution are reduced from 67.7 K and 9.7 K to 25.7 K and 4.8 K, respectively. The reduction in the standard deviation of the OTWT distribution due to the optimized FSF distribution with respect to the basis is 51%.

Finally, the evolution of the overall maximum outer wall temperature of the reforming tubes is shown in Fig. 3.9, which indicates that the reformer CFD model, in which the optimized FSF distribution (generated at any iteration of the furnace-balancing scheme) is used as the boundary condition, has a lower maximum outer reforming tube wall temperature compared to that of the 0th iteration. Specifically, at the 6th iteration of the furnace-balancing scheme, the overall maximum outer temperature of the reforming tubes is reduced from 1197.2 K to 1191.5 K (by 5.6 K). We would like to note that although the magnitude of the reduction in the overall maximum outer reforming tube wall temperature is much less than the overall average outer wall temperature of 1121.6 K, the contribution of our present work for industrial applications that strive to improve the thermal efficiency and service life of the reformer remains significant for the reason noted in Section 3.1. Due to the reduction in the overall maximum outer reforming tube wall temperature, the total FSF mass flow rate to the reformer can potentially be increased to achieve a higher operating temperature of the furnace-side flow without reducing the reformer service life, which leads to a lower rate of methane leakage (i.e., unreacted methane) and higher production rates of hydrogen and superheated steam. As a result, the thermal efficiency of the reformer is improved.

3.3.2 Case study B

In this subsection, the performance of the furnace-balancing scheme is analyzed when the flow control system is subjected to two different valve-related disturbances, which are categorized based on the number of defective valves. We consider the reformer from Case Study A after six iterations of the furnace balancing scheme have been executed with all valves fully functional. Though the termination checker of the furnace balancing scheme indicated that the balancing procedure could

Table 3.2: OTWT distribution obtained from the reformer CFD model in which the uniform FSF distribution is used as the boundary condition.

Distance down reforming tubes (m)	T_{AVE} (K)	T_{Max} (K)	T_{Min} (K)	Standard deviation (K)
1.0	971.9	998.7	948.3	10.8
2.0	1035.3	1064.3	1010.8	11.6
3.0	1086.0	1114.6	1052.1	11.5
4.0	1123.2	1150.1	1076.5	11.7
5.0	1149.4	1172.7	1097.1	11.2
6.0	1161.6	1179.6	1110.6	10.1
6.5	1165.1	1183.2	1115.5	9.7
7.0	1168.5	1186.5	1121.1	9.3
8.0	1174.0	1192.3	1130.5	8.8
9.0	1179.3	1197.2	1138.1	8.0
10.0	1168.8	1187.6	1128.7	7.9
11.0	1164.1	1183.4	1125.0	8.1
12.0	1162.5	1181.7	1124.6	8.2

be terminated after the 6^{th} iteration if no significant changes in the plant dynamics occurred, we assume that the valve-related disturbances occur after the 6^{th} iteration of the furnace-balancing scheme has been executed and that the furnace-balancing scheme is therefore required to continue iterating to determine an optimized FSF distribution given the change in the valve availability. The predicted optimized valve position distribution produced by the furnace-balancing optimizer in the 6^{th} when there were no defective valves cannot be utilized because the valve positions of the defective valves cannot be adjusted to the optimized positions. Hence, the valve position distribution that is sent to the valve-position-to-flow-rate converter to generate the boundary conditions of the reformer CFD model is non-optimal. As a result, the OTWT distributions obtained by implementing the FSF distribution determined at the 6^{th} iteration prior to the occurrence of the valve-related disturbances are expected to have a high degree of nonuniformity when implemented in a CFD model that accounts for the valve-related disturbances, and the furnace-balancing scheme is continue. We will impose two different valve-related disturbances after the 6^{th} iteration and will refer

Table 3.3: OTWT distribution obtained from the reformer CFD model in the 6th iteration in which the optimized FSF distribution is used as the boundary condition.

Distance down reforming tubes (m)	T_{AVE} (K)	T_{Max} (K)	T_{Min} (K)	Standard deviation (K)
6.0	1160.1	1177.9	1148.9	5.5
6.5	1163.4	1178.6	1152.9	4.8
7.0	1166.6	1180.0	1155.1	4.3
8.0	1171.8	1185.4	1160.1	4.5
9.0	1177.0	1191.5	1162.8	5.0
10.0	1166.8	1184.1	1155.1	4.9
11.0	1162.2	1181.4	1151.8	5.3
12.0	1160.7	1180.9	1150.2	5.6

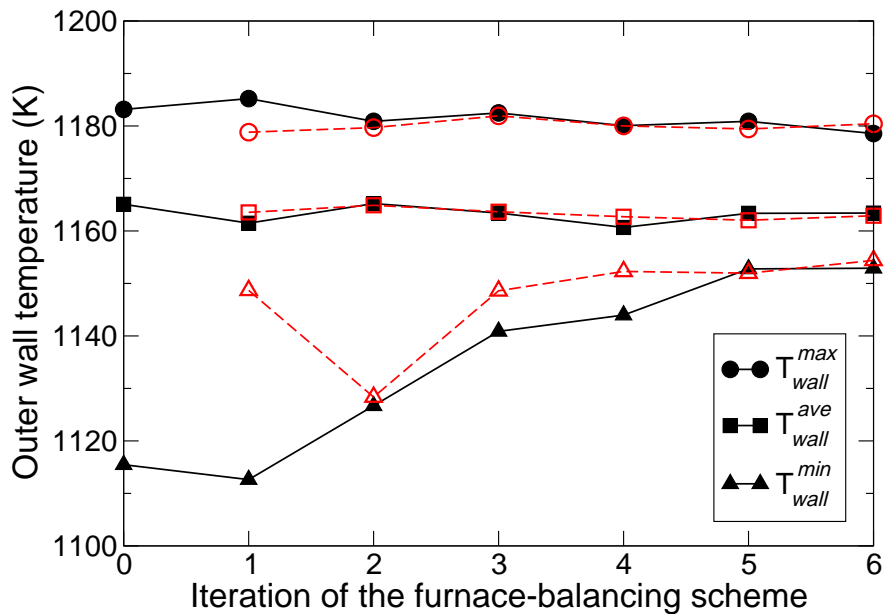


Figure 3.6: Evolution of the maximum, average and minimum temperature values of the OTWT distribution at a distance 6.5 m away from the reforming tube inlets during the first 6 iterations of the furnace-balancing scheme, which are generated by the reformer CFD model (black symbols) and by the data-driven model (red symbols).

to the iteration of the furnace-balancing scheme assuming the first type of valve-related disturbance occurs after the 6th iteration as the 7th iteration, and to the iteration of the furnace-balancing

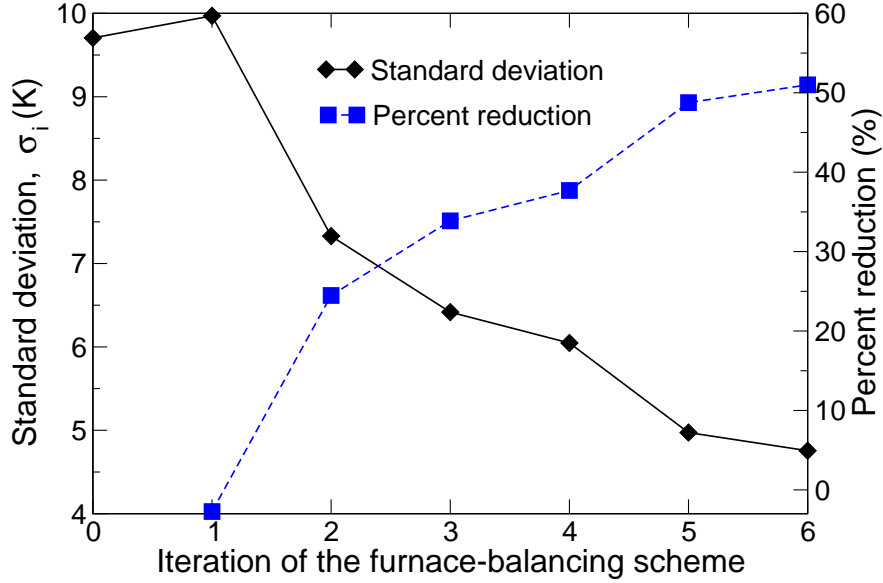


Figure 3.7: Evolution of the standard deviation of the OTWT distribution at a distance 6.5 m away from the reforming tube inlets during the first 6 iterations of the furnace-balancing scheme, which are obtained from the reformer CFD model. The percent reduction in the magnitude of the standard deviation of the i^{th} iteration with respect to the 0^{th} iteration (i.e., $\frac{\sigma_i - \sigma_0}{\sigma_0}$) in the first 6 iterations is also shown.

scheme assuming the second type of valve-related disturbance occurs after the 6^{th} iteration as the 9^{th} iteration (according to the above analysis, we expect significant OTWT distribution nonuniformity in both the 7^{th} and the 9^{th} iterations). In the re-balancing iterations of the furnace-balancing scheme (i.e., the 8^{th} and 10^{th} iterations), the text file documenting the status of the flow control system is updated, which notifies the furnace-balancing optimizer of the defective valves. Additionally, we simulate the two disturbances by assuming that the defective valves of the flow control system are arbitrarily selected, in which the corresponding stuck valve positions are modified from the optimized valve position by 5%–30%. The simulation results generated in the 7^{th} , 8^{th} , 9^{th} and 10^{th} iterations of the furnace-balancing scheme are presented and discussed.

In the case in which the reformer CFD model is subjected to a single-valve disturbance, a flow control valve is assumed to become defective. In particular, the valve regulating the FSF mass flow rates of the 48^{th} and 49^{th} inner-lane burners is chosen; and while the 6^{th} iteration of the furnace-

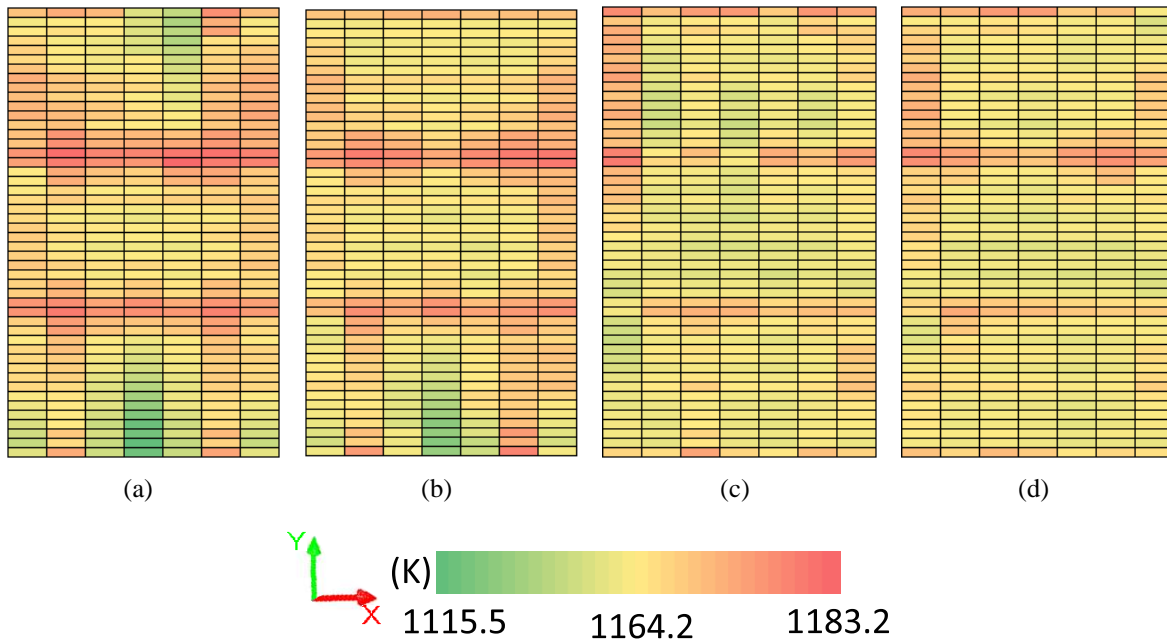


Figure 3.8: Evolution of the OTWT distribution at a distance 6.5 m away from the reforming tube inlets during the first 6 iterations of the furnace-balancing scheme, which are obtained from the reformer CFD model, is displayed by comparing the OTWT distributions in the 0th (a), 2nd (b), 4th (c) and 6th (d) iterations. In Fig. 3.8, the top row of each subfigure corresponds to the reforming tubes that are the closest to the reformer outlets, and the bottom row of each subfigure corresponds to the reforming tubes that are the furthest away from the reformer outlets.

balancing scheme suggests that the optimized valve position is 97%, the stuck valve position is 70%. The CFD data generated by the reformer CFD model, in which the flow control system is under the influence of the single-valve disturbance, is used to analyze the degree of nonuniformity of the OTWT distributions in the high temperature regions along the reforming tube length. Comparing Table 3.4 with Table 3.3 reveals that the OTWT distributions expectedly become more nonuniform at the 7th iteration compared to the 6th iteration. Specifically, the temperature range and standard deviation of the OTWT distribution at the location 6.5 m away from the reforming tube inlets in the 7th iteration increase by 34.6 K and 4.6 K. The results suggest that the furnace-balancing scheme must be made aware of the constraint imposed by the single-valve disturbance to properly reoptimize the FSF distribution.

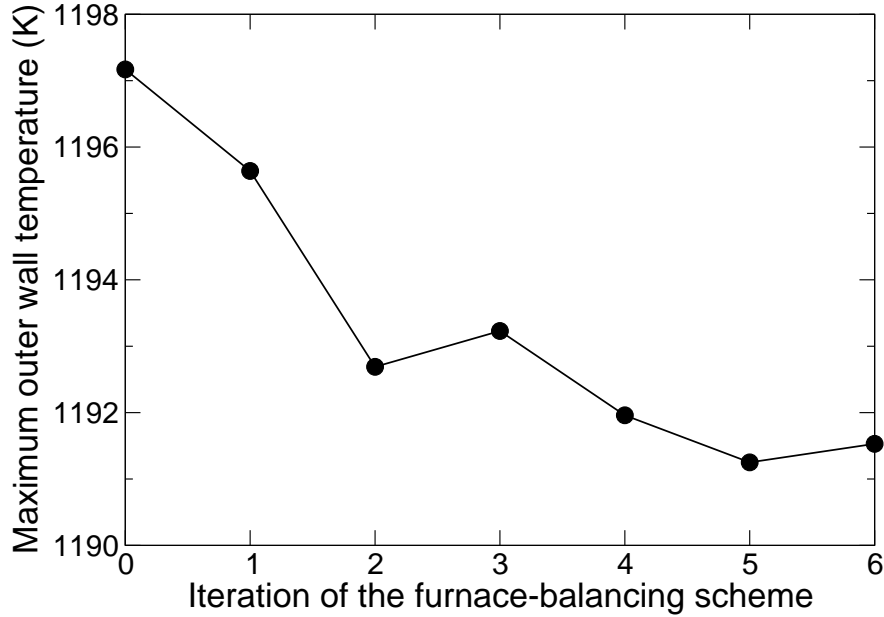


Figure 3.9: Evolution of the overall maximum outer wall temperature along the reforming tube length among 336 reforming tubes in the reformer during the first 6 iterations of the furnace-balancing scheme, which are obtained from the reformer CFD model.

In the 8th iteration, as the text file documenting the status of the flow control system has been updated, the furnace-balancing optimizer is aware of the defective valve, which allows the number of decision variables to be reduced from 48 to 47 as discussed in Section 3.2.4. We note that the furnace-balancing optimizer is designed to handle a varying number of decision variables, and this ability of the furnace-balancing optimizer makes the furnace-balancing scheme especially appealing for industrial applications that are interested in control and automation. The CFD data generated by the reformer CFD model, in which the reoptimized FSF distribution is used as the boundary condition, is used to investigate the ability of the furnace-balancing scheme to compensate for the impact of the single-valve disturbance occurring in the flow control system.

Fig. 3.10 shows that the OTWT distribution at a distance 6.5 m away from the reforming tube inlets produced in the 8th iteration is more uniform than that produced in the 7th iteration. Specifically, the under-heated region near the reformer outlets in the OTWT distribution of the 7th iteration is completely resolved in the 8th iteration, and the severity of the over-heated region in the 7th iteration is significantly lessened in the 8th iteration. Additionally, the OTWT distribution

in the 8th iteration shown in Fig. 3.10(b) resembles the optimized OTWT distribution in the 6th iteration shown in Fig. 3.8(d) even though the corresponding optimized valve position distributions are completely different as shown in Table 3.8. This is because the FSF distributions produced by these optimized valve position distributions in the 6th and 8th iterations are very similar. Moreover, Table 3.5 shows that the degree of nonuniformity in the OTWT distributions in the high temperature regions along the reforming tube length in the 8th iteration is reduced with respect to the corresponding quantities in the 7th iteration. Specifically, in the OTWT distribution at the location 6.5 m away from the reforming tube inlets of the 8th iteration, the temperature range and standard deviation decrease to 24.1 K and 4.5 K. Therefore, the qualitative assessment (Fig. 3.10) and quantitative analysis (Table 3.5) of the degree of nonuniformity in the OTWT distribution between the 6th, 7th and 8th iterations indicates that the furnace-balancing scheme compensates for the impact of the single-valve disturbance occurring in the flow control system.

In the case when the reformer CFD model is subjected to a three-valve disturbance after the 6th iteration, three flow control valves become defective. In particular, the three valves which control the FSF mass flow rates of the 0th and 1st outer-lane burners and of the 42nd, 43rd, 82nd and 83rd inner-lane burners are selected, and the corresponding stuck valve positions are 70%, 80% and 90%, respectively, as oppose to their optimized valve positions of 86%, 87% and 81% in the 6th iteration of the furnace-balancing scheme. The only difference between the two disturbances occurring in the flow control system is the number of defective valves, and therefore, the analysis which is used to investigate the effects of the single-valve disturbance on the degree of nonuniformity in OTWT distributions along the reforming tube length and the ability of the furnace-balancing scheme to compensate for the constraint imposed by the single-valve disturbance during the search for the reoptimized FSF distribution is also utilized.

The quantitative assessment of the effects of the three-valve disturbance on OTWT distributions in the high temperature region of the reforming tube length is presented in Table 3.6, which shows that the OTWT distributions of the 9th iteration are more nonuniform compared to the corresponding ones in the 6th iteration; and specifically, the temperature range and standard deviation

of the OTWT distribution at the location 6.5 m away from the reforming tube inlets increase by 19.9 K and 1.9 K, respectively. Subsequently, the information of the three-valve disturbance is utilized to update the text file documenting the status of the flow control system in the 10th iteration, which notifies the furnace-balancing optimizer of the three defective valves and allows the number of decision variables to be reduced from 48 to 45. The CFD data generated by the reformer CFD model, in which the reoptimized FSF distribution is used as the boundary condition, is used to create Fig. 3.11 and Table 3.7 to investigate the ability of the furnace-balancing scheme to compensate for the impact of the three-valve disturbance. Specifically, Fig. 3.11 shows that the OTWT distribution produced in the 10th iteration is more uniform than that produced in the 9th iteration as the over-heated region near the left corner of the refractory back wall in the OTWT distribution of the 9th iteration is completely resolved in the 10th iteration, and the severity of the under-heated region near the reformer outlets in the 9th iteration is significantly lessened in the 10th iteration. Moreover, Table 3.7 shows that the degree of nonuniformity in most of OTWT distributions in the high temperature regions along the reforming tube length in the 10th iteration is reduced compared to those in the 9th iteration, and specifically, the temperature range and standard deviation in the OTWT distribution at the location 6.5 m away from the reforming tube inlets decrease to 36.5 K and 5.9 K, respectively. Although the 10th iteration appears to be able to compensate for the impacts of the three-valve disturbance, which are observed in the 9th iteration, the OTWT distribution in the 10th iteration shown in Fig. 3.11(b) appears to have a higher degree of nonuniformity than the optimized OTWT distribution in the 6th iteration shown in Fig. 3.8(d). Therefore, the qualitative assessment (Fig. 3.11) and quantitative analysis (Table 3.7) of the degree of nonuniformity in the OTWT distribution between the 6th, 9th and 10th iterations indicates that the furnace-balancing scheme can compensate for the impact of the three-valve disturbance occurring in the flow distribution system.

V_i \ iteration	0 th	6 th	7 th	8 th	9 th	10 th
V_0	100	86	86	68	70	70
V_1	100	94	94	71	94	99

V_2	100	88	88	68	88	87
V_3	100	84	84	67	84	85
V_4	100	85	85	66	85	83
V_5	100	92	92	72	92	93
V_6	100	88	88	69	88	98
V_7	100	73	73	60	73	69
V_8	100	81	81	65	81	79
V_9	100	89	89	69	89	84
V_{10}	100	87	87	69	87	85
V_{11}	100	81	81	64	81	77
V_{12}	100	92	92	71	92	83
V_{13}	100	85	85	66	85	78
V_{14}	100	94	94	73	94	91
V_{15}	100	86	86	68	86	87
V_{16}	100	78	78	61	78	77
V_{17}	100	100	100	78	100	100
V_{18}	100	87	87	71	87	92
V_{19}	100	78	78	62	78	79
V_{20}	100	91	91	70	91	93
V_{21}	100	86	86	68	80	80
V_{22}	100	89	89	71	89	87
V_{23}	100	82	82	65	82	79
V_{24}	100	97	70	70	97	91
V_{25}	100	86	86	67	86	82
V_{26}	100	85	85	68	85	80
V_{27}	100	86	86	68	86	86

V_{28}	100	84	84	65	84	84
V_{29}	100	100	100	78	100	100
V_{30}	100	86	86	71	86	88
V_{31}	100	78	78	61	78	78
V_{32}	100	92	92	72	92	95
V_{33}	100	88	88	69	88	85
V_{34}	100	86	86	68	86	84
V_{35}	100	92	92	72	92	82
V_{36}	100	86	86	66	86	79
V_{37}	100	81	81	61	81	83
V_{38}	100	84	84	66	84	77
V_{39}	100	82	82	65	82	81
V_{40}	100	86	86	67	86	84
V_{41}	100	81	81	64	90	90
V_{42}	100	90	90	71	90	92
V_{43}	100	90	90	74	90	85
V_{44}	100	87	87	68	87	89
V_{45}	100	91	91	72	91	88
V_{46}	100	86	86	69	86	84
V_{47}	100	95	95	74	95	86

Table 3.8: Summary of the valve position distributions in the 0^{th} , 6^{th} , 7^{th} , 8^{th} , 9^{th} and 10^{th} iterations, in which the highlighted values represent the stuck positions of the defective valves due to the common valve-related disturbances.

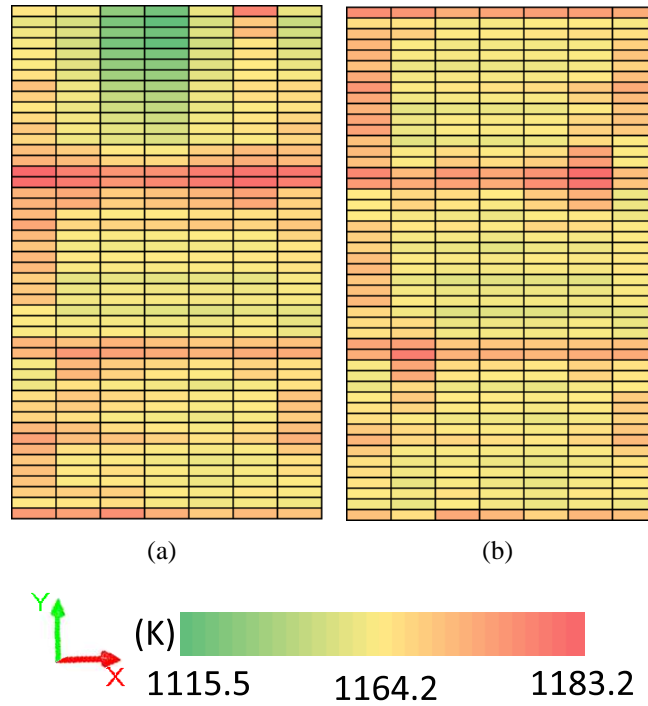


Figure 3.10: Comparison between the OTWT distributions at a distance 6.5 m away from the reforming tube inlets generated from the 7th iteration when the FSF distribution is altered by the single-valve disturbance (a), and from the 8th iteration when the FSF distribution is reoptimized to counter the impact of the single-valve disturbance (b). In Fig. 3.10, the top row of each subfigure corresponds to the reforming tubes that are the closest to the reformer outlets, and the bottom row of each subfigure corresponds to the reforming tubes that are the furthest away from the reformer outlets.

Table 3.4: OTWT distribution obtained from the reformer CFD model in the 7th iteration when the FSF distribution is altered by the single-valve disturbance.

Distance down reforming tubes (m)	T_{AVE} (K)	T_{Max} (K)	T_{Min} (K)	Standard deviation (K)
6.0	1158.2	1177.2	1112.4	10.0
6.5	1161.6	1178.3	1118.1	9.3
7.0	1164.9	1180.4	1124.7	8.6
8.0	1170.2	1187.4	1134.9	8.0
9.0	1175.5	1194.3	1142.6	7.9
10.0	1165.4	1186.2	1134.7	7.8
11.0	1160.9	1182.4	1132.2	7.7
12.0	1159.5	1181.1	1132.9	7.4

Table 3.5: OTWT distribution obtained from the reformer CFD model in the 8th iteration when the FSF distribution is reoptimized to counter the impact of the single-valve disturbance.

Distance down reforming tubes (m)	T_{AVE} (K)	T_{Max} (K)	T_{Min} (K)	Standard deviation (K)
6.0	1160.1	1175.7	1148.6	5.3
6.5	1163.3	1177.8	1153.7	4.5
7.0	1166.4	1179.9	1157.5	4.1
8.0	1171.5	1185.0	1159.6	4.3
9.0	1176.6	1190.7	1162.8	4.7
10.0	1166.4	1182.6	1154.9	4.7
11.0	1161.8	1178.9	1151.4	5.0
12.0	1160.3	1177.8	1147.2	5.3

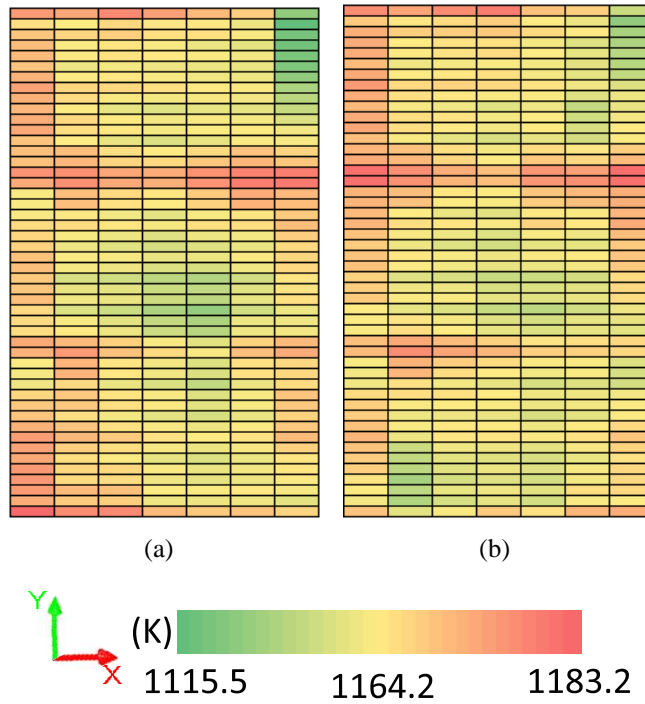


Figure 3.11: Comparison between the OTWT distributions at a distance 6.5 m away from the reforming tube inlets generated from the 9th iteration when the FSF distribution is altered by the three-valve disturbance (a), and from the 10th iteration when the FSF distribution is reoptimized to counter the impact of the three-valve disturbance (b). In Fig. 3.11, the top row of each subfigure corresponds to the reforming tubes that are the closet to the reformer outlets, and the bottom row of each subfigure corresponds to the reforming tubes that are the furthest away from the reformer outlets.

Table 3.6: OTWT distribution obtained from the reformer CFD model in the 9th iteration when the FSF distribution is altered by the three-valve disturbance.

Distance down reforming tubes (m)	T_{AVE} (K)	T_{Max} (K)	T_{Min} (K)	Standard deviation (K)
6.0	1159.4	1180.3	1129.6	7.5
6.5	1162.9	1180.9	1135.4	6.7
7.0	1166.3	1181.4	1142.1	6.0
8.0	1171.7	1187.4	1151.5	5.6
9.0	1177.0	1193.1	1158.9	5.7
10.0	1166.8	1184.5	1151.9	5.8
11.0	1162.2	1181.2	1147.9	5.9
12.0	1160.7	1180.6	1146.9	6.0

Table 3.7: OTWT distribution obtained from the reformer CFD model in the 10th iteration when the FSF distribution is reoptimized to counter the impact of the three-valve disturbance .

Distance down reforming tubes (m)	T_{AVE} (K)	T_{Max} (K)	T_{Min} (K)	Standard deviation (K)
6.0	1159.1	1179.5	1137.0	6.6
6.5	1162.7	1180.1	1143.6	5.9
7.0	1166.2	1183.1	1151.3	5.3
8.0	1171.6	1188.6	1158.2	5.1
9.0	1177.0	1194.9	1165.0	5.2
10.0	1166.9	1187.9	1152.8	5.6
11.0	1162.4	1185.0	1148.1	5.9
12.0	1160.9	1184.3	1147.1	6.2

3.4 Conclusion

In this work, we developed a robust model-based furnace-balancing scheme that can reduce the degree of nonuniformity in OTWT distributions along the reforming tubes inside the furnace of a steam methane reformer. To this end, we adopted a high-fidelity reformer CFD model created in our previous work and developed a model identification process based on the effects of thermal radiation, the furnace-side flow pattern, reformer CFD data and the least squares regression method to approximate the relationship between the OTWT distribution and the FSF distribution. Then, we introduced the model-based furnace-balancing optimizer that accounts for typical industrial operational constraints and physical constraints on the flow control valves while searching for an optimal FSF distribution based on the data-driven model. The CFD data showed that the optimized FSF distribution created by the proposed furnace-balancing scheme allowed the degree of nonuniformity of OTWT distributions in the high temperature region of the reforming tubes and the overall maximum outer wall temperature to be reduced compared to the case in which a uniform FSF distribution was used. This result demonstrated that the proposed furnace-balancing scheme allowed the spatial distribution of the furnace-side temperature inside the combustion chamber to also become more uniform, which was expected to enhance the radiative heat transfer efficiency in the reformer. We also demonstrated the effectiveness of the furnace-balancing scheme in reducing the degree of nonuniformity of OTWT distributions in the presence of defects of the valves regulating the amount of furnace-side feed to the burners. The proposed balancing scheme allows taking advantage of the reduction in the overall maximum outer reforming tube wall temperature and the more uniform OTWT distributions to increase the total FSF mass flow rate to the burners, thereby increasing hydrogen production and extending reforming tube lifetime.

Chapter 4

Bayesian Model Averaging for Estimating the Spatial Temperature Distribution in a Steam Methane Reforming Furnace

4.1 Introduction

In Chapter 2, a potential root cause of the inherent variation in the outer tube wall temperature (OTWT) distribution has been studied, and an ad hoc mitigation strategy is to re-calibrate total furnace-side feed (FSF) flow rate in an attempt to prevent the OTWT of all reforming tubes from exceeding the design temperature of the wall material and to maintain the expected service life of the reformer at the expense of the reformer efficiency. The hydrogen manufacturing industry reasons that this trade-off is necessary because when the OTWT of a reforming tube exceeds the design temperature of the reforming tube wall, the reformer might have a significantly shorter service life, e.g., Pantoleontos et al. [49] reports that an increase of 20 K above the design temperature of the reforming tube wall causes the reformer service life to be reduced by half, and the reforming tubes are at risk of rupturing; if rupture were to occur, it would lead to substantial production and capital losses. For decades, this ad hoc mitigation strategy has been a solution that prevents

significant unexpected capital costs as the cost of re-tubing is estimated to be approximately 10% of the total capital investment [13]. Then, in Chapter 3, the systematic mitigation strategy, i.e., the furnace balancing scheme, has been proposed to successfully reduce the variability in the OTWT distributions at a fixed height in the reformer for the nominal total FSF flow rate. Despite of this initial success, the simulation data shows that the conversions of methane via SMR in the reformer operated under varying spatial distributions of the fixed total fuel flow rate are constant. In the continuous effort to maximize the reformer thermal efficiency while maintaining the expected service life of the reformer, systematic mitigation strategies for varying total FSF flow rate is getting much attention from academics and industries. Therefore, it is apparent that an accurate relationship between the OTWT distribution at a fixed height, the FSF distribution and the total FSF flow rate of the reformer is required to design a robust furnace balancing method. The dependence of the OTWT distribution on the FSF distribution and the total FSF flow rate of the reformer can be constructed based on first principles modeling [13] and computational fluid dynamics (CFD) modeling of the reformer.

However, models derived from these modeling techniques are typically unsuitable for designing a robust real-time furnace-balancing scheme (for which the need is evident as the reformer is constantly subjected to various disturbances, e.g., ambient temperature) [32]. In particular, first principles modeling often uses an overwhelming number of simplifying assumptions in the development of reformer models, which causes prediction data generated by first principles models often to fall short in terms of accuracy. While CFD modeling does not have the same issue (e.g., the simulation data generated by the reformer CFD model developed in Chapter 2 have been shown to be a reasonably accurate representation of the experimental data recorded from an on-line unit), the significant computational time needed to create a single CFD data set makes it unsuitable for designing a real-time furnace balancing scheme because the CFD model is required to be repeatedly solved with different FSF distributions to search for the optimized FSF distribution. Therefore, data-driven modeling is an appealing alternative as data-driven models are computationally inexpensive and can have reasonable accuracy.

In this work, data-driven modeling is used to discover the dependence of the OTWT distribution on the FSF distribution and the total FSF flow rate of the reformer. A direct approach is to model the OTWT at a fixed height of each reforming tube as a function of the FSF distribution and total FSF flow rate (i.e., the FSF flow rates of all burners), and estimates of the parameters associated with the regressors in the data-driven model can be determined by the ordinary least squares (OLS) regression method in which the sum of squared residuals between the OTWT data and fitted data is minimized. This naive approach is expected to create an uninterpretable (in the sense that it is not representing physical relationships between burners and reforming tubes within the reformer) data-driven model for the OTWT distribution with high prediction errors due to over fitting. Specifically, Chapter 2 notes that in the high temperature reformer, thermal radiation is expected to be the dominant mode of heat transfer, and [47] shows that 95% of the total heat transfer rate to the tube side in the reformer of their investigation is due to thermal radiation. Additionally, the inverse square law for thermal radiation suggests that the OTWT of each reforming tube is governed by the FSF flow rates of the nearby burners. Therefore, a smaller set of important regressors for each reforming tube should be identified and used to construct a more computationally efficient data-driven model.

Standard statistical practice employs shrinkage and subset selection techniques (e.g., LASSO, nonnegative garotte and ridge regression) to search for the set of important regressors and to calculate the estimates of their corresponding parameters based on some criteria (e.g., minimizing the sum of squared residuals) to derive a single best data-driven model. Subsequently, this standard statistical practice assumes this data-driven model to be the true model for the relationship between the OTWT of a reforming tube, FSF distribution and total FSF flow rates, and then utilizes the chosen model exclusively to make predictions. The greatest flaw of the standard statistical practice is that the approach overlooks the importance of competing data-driven models. Specifically, [25] illustrates that two competing models with similar goodness of fit for a given training data can yield substantially different predictions and suggests that predictions made based on a single data-driven model are unreliable. Bayesian statistics provides systematic straightforward methods to

identify the set of important regressors for each reforming tube (i.e., Bayesian variable selection) and to account for model uncertainty in making predictions based on the observed database (i.e., Bayesian model averaging). Bayesian statistics is employed in many disciplines (e.g., chemistry, genetics, medicine and finance) and has led to over 587 publications between 1996 and 2014 [20].

In this work, we combine the Bayesian methods and sparse nonlinear regression technique (i.e., least absolute shrinkage and selection operator or LASSO) to derive a collection of data-driven models, each of which requires the minimum number of terms for a given basis set of regressors while revealing the dependence of the OTWT of each reforming tube on the FSF distribution and total FSF flow rate with a reasonable accuracy. Specifically, it is assumed that a data-driven model for the OTWT of each reforming tube has the form of a linear combination of nonlinear/linear transformations of the original regressors (i.e., sparse nonlinear regression) so that the nonlinear characteristics in the observed data can be adequately described [9, 63] For instance, [9] shows that sparse nonlinear regression can be used to create data-driven models that describe the underlying dynamics of nonlinear systems (e.g., nonlinear oscillators and the chaotic Lorenz system). A typical library of nonlinear transformations contains monomial, exponential, logarithmic and trigonometric functions.

Lastly, it is recognized that the OTWT of each reforming tube is spatially correlated to those of the nearby neighbors because thermal radiation inside the reformer is expected to occur between the furnace-side flow, reforming tube walls and refractory wall. It is also recognized from the reformer CFD simulation data reported in Chapter 3 that reforming tubes which are in close proximity to one another tend to have similar OTWTs. Therefore, it is logical to allow the data-driven model for the OTWT of each reforming tube to also utilize the information (i.e., the locations and OTWTs) of the neighboring reforming tubes, in addition to the FSF distribution and total FSF flow rate, to make predictions of the OTWT. In the geostatistics literature, there exist a variety of distance-weighted average interpolation algorithms (e.g., Kriging, triangulation and the inverse distance method), each of which can be used to estimate an OTWT of each reforming tube as a weighted average of the neighboring OTWTs based on a unique weighting function. In this work,

Kriging is selected as it provides a straightforward approach to adjust the predicted OTWT distribution estimated based on the FSF distribution and total FSF flow rate to account for the effect of interactions among neighboring reforming tubes on the OTWT distribution. Kriging can also be used for clustering data, which occurs due to the arrangement of the reforming tubes inside the reformer, i.e., the reforming tubes are arranged in an irregular grid pattern (e.g., seven rows of 48 units), in which reforming tubes are situated closely to one another along a row but are separated by a relatively large distance between rows. Additionally, the Kriging algorithm is designed to minimize the mean squared prediction error, which makes this interpolation algorithm more suitable for predicting the OTWT at unexplored operating conditions of the reformer.

Motivated by this, the present work focuses on developing a two-step prediction and correction model identification procedure that utilizes Bayesian methods with an efficient search algorithm (Occam's window), sparse nonlinear regression, Kriging, information on the reformer geometry and theories of thermal radiative heat transfer to derive a high-fidelity model from reformer data such that the model can account for interactions among neighboring reforming tubes in making predictions about the OTWT distribution based on the FSF distribution and total FSF flow rate. This manuscript is structured as followed: in Section 4.2, physical descriptions, process modeling and process simulation of a computational fluid dynamics (CFD) model of a reformer are briefly discussed to be used as supporting evidence that the reformer CFD data are adequate representations of the data from an on-line reformer, which allows us to use the reformer CFD model to facilitate the creation of the training and testing data. In Section 4.3, an overview of the integrated model identification scheme is presented, and the major components, namely, the prediction step and correction step, are introduced. In Section 4.4, a rundown of the prediction step that details the procedure for deriving the prediction model for the OTWT distribution from the training data is presented, and in Sections 4.4.1, 4.4.2, and 4.4.3 the integration of Bayesian variable selection, Bayesian model averaging, sparse nonlinear regression and theories of thermal radiation into an algorithm for the prediction step is described. In Section 4.5, a rundown of the correction step that details the procedure for creating the correction model for the OTWT distribution from the

training data using ordinary Kriging is presented. In Section 4.6, the procedure to generate the combined data-driven model for the OTWT distribution from the prediction and correction models is detailed. Finally in Section 4.7, the goodness of fit and out-of-sample predictive performance of the data-driven model for the OTWT distribution generated from the integrated model identification scheme proposed in this work are evaluated using the training and testing data, respectively, and are discussed to highlight the potential of this work for being used in developing more optimal operating conditions of a reformer in a computationally efficient manner, e.g., it may be considered for use as the data-driven model for an on-line robust furnace balancing optimizer.

4.2 Reformer CFD database

In the present work, the high-fidelity reformer CFD model developed in Chapter 2 is used to represent an on-line reformer designed by Selas Fluid Processing Corporation at a hydrogen plant [13]. This is because the geometry of the reformer model is created to have approximate dimensions of the on-line unit, which is 16 m wide, 16 m long and 13 m tall. The geometry of the reformer model also contains important features of its physical counterpart, which include the major components (i.e., 336 reforming tubes, 72 inner-lane burners, 24 outer-lane burners and 8 flue-gas tunnels) and the layout inside the reformer as shown in Fig. 5.2. Additional details of the reformer geometry can be found in Chapter 2. Furthermore, the mesh of the reformer CFD model has been verified to have acceptable mesh quality based on the criteria (i.e., min orthogonal factor and max ortho skew) suggested by ANSYS ICEM and to allow the reformer CFD model to produce mesh-independent solutions. The generation of the reformer mesh is detailed in Chapters 2 and 3. In addition, the modeling strategies for the known transport phenomena and chemical reactions associated with SMR and air combustion processes are used to create the reformer CFD model. For instance, the reformer CFD model is implemented with the empirical correlation for the furnace-side total emissivity [43], Lambert Beer's law, Kirchoff's law and the discrete ordinate method to simulate radiative heat transfer between the furnace-side flow, outer reforming tube walls and refractory walls. Readers who are interested in the details of the modeling strategies for the reformer CFD model, efficient step-by-step converging strategy and data collection procedure are recommended to refer Chapters 2 and 3. Moreover, the CFD simulation data generated by the reformer CFD model have been shown to be in good agreement with simulation data generated by a reforming Gibbs reactor model, with typical plant data in the SMR literature and with plant data provided by a third party collaborator, and therefore, can be considered as an adequate representation of plant data collected from an on-line unit.

In the present work, the reformer CFD model is utilized to facilitate the creation of the reformer database. Specifically, the reformer CFD model is initially implemented with varying FSF distri-

butions at a fixed typical total FSF flow rate and, subsequently, implemented with varying total FSF flow rates at the optimized FSF distribution reported in Chapter 3, which creates 21 CFD data sets. In this work, 18 CFD data sets (i.e., the training data), which is approximately 90% of the reformer database, are randomly chosen and used as inputs for the integrated model identification scheme to produce a data-driven model that adequately describes the dependence of the OTWT distribution on the FSF distribution and total FSF flow rate. The remaining 3 CFD data sets (i.e., the testing data), which is approximately 10% of the reformer database, are used to validate the performance on out-of-sample predictions of the data-driven model.

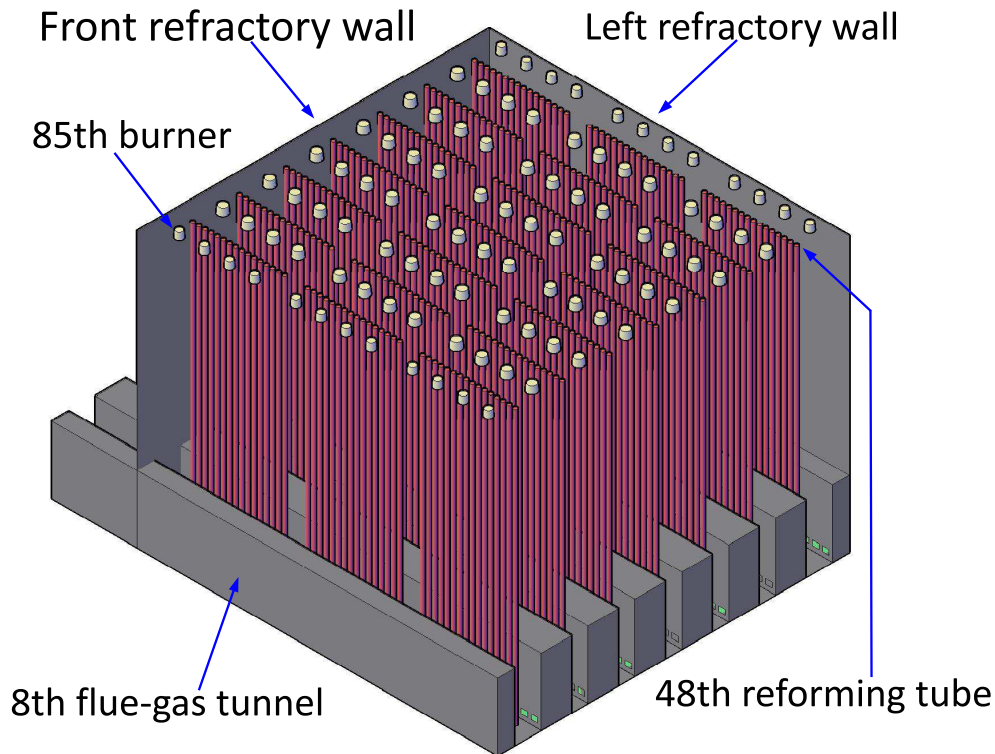


Figure 4.1: The isometric view of an industrial-scale, top-fired, co-current reformer. The right and back refractory walls with respect to the flue gas tunnel exits in Fig. 5.2 are removed to expose the interior of the reformer, which consists of 336 reforming tubes, which are represented by 336 cylinders, 96 burners, which are represented by 96 frustum cones, and 8 flue-gas tunnels, which are represented by 8 rectangular intrusions.

4.3 Overview of the prediction and correction model identification scheme

The statistical-based model identification scheme is a two step (i.e., prediction and correction) procedure that is designed to derive a model for the dependence of the OTWT distribution at a fixed distance of 6.5 m away from the reformer ceiling on the FSF distribution and total FSF flow rate from the training data of the reformer CFD database. In the prediction step, the model-building process for the i th OTWT as a function of the FSF distribution and total FSF flow rate from the training data is executed independently of other reforming tubes based on Bayesian methods, i.e., Bayesian variable selection and Bayesian model averaging (BMA), with an efficient search algorithm and sparse nonlinear regression (which will be further defined in Sections 4.4.1, 4.4.2 and 4.4.3). The data-driven model for the OTWT of the i th reforming tube generated by the prediction step is referred to as the i th prediction model and is formulated as follows,

$$\widehat{T}_i^{P,n} = \sum_{k=1}^{K_i} w_{i,k}^P \widetilde{T}_{i,k}^{P,n} \quad \forall n \in \{1, \dots, N\} \quad (4.1a)$$

subject to

$$\sum_{k=1}^{K_i} w_{i,k}^P = 1 \quad (4.1b)$$

$$\vec{F}^n = [F_1^n, F_2^n, \dots, F_{96}^n]^T \quad (4.1c)$$

$$\|\vec{F}^n\|_1 = F_{tot}^n \quad (4.1d)$$

$$\widetilde{T}_{i,k}^{P,n} = \sum_{g=1}^G (\vec{\alpha}_i^{kg}) \cdot f_g(\vec{F}^n) + \alpha_i^k \quad (4.1e)$$

where n is the index of the n th data set in the training data, N is the number of data sets in the training data, $\widehat{T}_i^{P,n}$ is the BMA predicted estimate of the i th OTWT based on the n th FSF distribution (\vec{F}^n) and n th total FSF flow rate (F_{tot}^n), $\widetilde{T}_{i,k}^{P,n}$ is the k th predicted estimate of the i th OTWT based on

\vec{F}^n , F_{tot}^n and the k th sub-prediction model for the i th reforming tube (where this model denoted is by $M_{i,k}$ and defined and developed in Section 4.4), K_i is the total number of sub-prediction models in the i th library, $w_{i,k}^P$ is the BMA weighting factor of $M_{i,k}$ (developed in Section 4.4.2), $f_g(\cdot)$ is the g th basis function in the library of transformation functions (developed in Section 4.4.3), G is the number of functions in the library of transformation functions (developed in Section 4.4.3), $\vec{\alpha}_i^{kg}$ is the empirical parameter vector of $M_{i,k}$ corresponding to $f_g(\cdot)$ (defined in Section 4.4.3) and α_i^k represents the estimated ambient temperature of $M_{i,k}$ (defined in Section 4.4.3). The prediction step in the model identification algorithm is parallelized to simultaneously create 336 prediction models, each of which corresponds to a reforming tube of the reformer, and subsequently, these prediction models are combined to create the data-driven model (i.e., the prediction model) for the OTWT distribution to describe the dependence of the OTWT distribution on the FSF distribution and total FSF flow rate. However, the prediction model for the OTWT distribution does not account for the effects of interactions between neighboring reforming tubes on the OTWT distribution, and hence, the correction step of the model identification procedure is created. In the correction step, the predicted estimate of the i th OTWT is adjusted based on information of the neighboring reforming tubes extracted from the reformer geometry and predicted OTWT distribution. The correction model for the i th reforming tube developed based on ordinary Kriging (to be further developed in Section 4.5) is formulated as follows,

$$\hat{T}_i^{C,n} = \sum_{\substack{j=1 \\ j \neq i}}^{336} w_{i,j}^C \hat{T}_j^{P,n} \quad (4.2)$$

where $\hat{T}_i^{C,n}$ is the corrected estimate of the i th OTWT and $w_{i,j}^C$ is the Kriging weighting factor of the j th reforming tube. Finally, the estimated OTWT of the i th reforming tube given \vec{F}^n and F_{tot}^n is computed as the weighted sum of the BMA predicted and corrected estimates as follows,

$$\hat{T}_i^n = w^P \hat{T}_i^{P,n} + (1 - w^P) \hat{T}_i^{C,n} \quad (4.3)$$

where w^P is the weighting factor of the BMA estimates, of which the optimal value is determined

by leave-out-one cross validation (developed in Section 4.6). In the remainder of this manuscript, the development of the prediction and correction model identification algorithm is elucidated in detail, and the accompanying assumptions are explicitly stated and demonstrated to be valid using the training data.

The decision to investigate the OTWT distribution at a fixed distance of 6.5 m away from the reformer ceiling was originally proposed in Chapter 3. In particular, this OTWT distribution has been found to have a high average OTWT, i.e., $\sim 99\%$ of the maximum value of the average OTWT profile (which is a collection of averages of OTWT distributions along the reforming tube length and is invariant at the fixed total FSF flow rate), so that in a scenario that the hydrogen plant is at risk of suffering significant capital and production losses due to the suboptimal FSF distribution, this OTWT distribution is expected to have high degree of nonuniformity (indicated by a wide temperature range and a high standard deviation), and the maximum value of the OTWT distribution at a distance of 6.5 m away from the reformer ceiling is expected to exceed the design temperature of the reforming tube wall. This rationale suggests that the reformer can be kept in a safe operating regime by reducing the degree of nonuniformity in the OTWT distribution and preventing the maximum value of the OTWT distribution from exceeding the design temperature, and therefore, a data-driven model for the OTWT distribution was created in the development of the furnace-balancing scheme in Chapter 3 that seeks to reduce the nonuniformity. In an anticipation that an application of the modeling method in this work may be to derive the data-driven model for a furnace-balancing algorithm as in Chapter 3, we consider a distance of 6.5 m away for the ceiling in this work for consistency with Chapter 3.

4.4 Prediction models

In this work, Bayesian methods are integrated in the algorithm for the prediction step because of the twofold advantage that these methods offer (Section 4.1): the Bayesian variable selection method provides a straightforward approach to identify the important regressors for each reforming tube, and BMA allows model-selection uncertainty to be accounted for in making predictions about the OTWT distribution given \vec{F}^n and F_{tot}^n [25]. In the prediction step, the prediction model for the i th OTWT is derived from the training data independently of the model-building process for the remaining OTWTs. This approach is expected to effectively reduce the total computational time devoted for constructing the prediction model for the OTWT distribution because the model-building process can be simultaneously executed for 336 reforming tubes. In this section, the important terminologies used in the description of the algorithm for the prediction step are explicitly defined, and then, the algorithm for the prediction step is discussed in the context of constructing the i th prediction model from the training data.

In the j th iteration of the prediction step,

1. Checked predictors are the burners that are in the neighborhood of the i th reforming tube, and a collection of checked predictors in the j th iteration of the prediction step is denoted as \mathbf{S}_{iC}^j . However, checked predictors may or may not have a significant impact on the i th OTWT.
2. Potential predictors are elements of a subset of \mathbf{S}_{iC}^j , which is denoted as \mathbf{S}_{iP}^j . Potential predictors are candidate regressors of the i th reforming tube model and will be characterized by the regressor classification layer. Potential predictors that are classified as important regressors by the regressor classification layer are added to the basis set of regressors (denoted as \mathbf{S}_{iR}).
3. Predictors are important regressors of the i th prediction model and are elements of \mathbf{S}_{iR} .
4. A sub-prediction model library of the i th reforming tube is a collection of models that allows the i th OTWT to be estimated based on \vec{F}^n and F_{tot}^n .

In addition, the concept of a multistage affecting zone is introduced to facilitate the search for and classification of checked predictors. Specifically, we define the multistage affecting zone of the i th reforming tube in the j th iteration of the prediction step as a cylindrical region with a radius that is denoted R_{iZ}^j and is evaluated as follows,

$$R_{iZ}^j = R_{iZ}^0 + j\Delta R_Z \quad \forall j = 1, 2, 3, \dots \quad (4.4)$$

where $R_{iZ}^0=0$ m is the initial radius of the multistage affecting zone of the i th reforming tube and $\Delta R_Z=1.5$ m is the corresponding step increment. The first stage of an affecting zone of the i th reforming tube is defined as a cylindrical volume of radius R_{iZ}^j centered at the i th reforming tube inside which burners are considered to be elements of \mathbf{S}_{iC}^j . The second stage of an affecting zone of the i th reforming tube is defined as a hollow cylindrical volume bounded by two concentric cylinders of radii R_{iZ}^j and R_{iZ}^{j-1} inside which burners are considered to be elements of \mathbf{S}_{iP}^j , which is defined as follows,

$$\mathbf{S}_{iP}^j = \mathbf{S}_{iC}^j \setminus \mathbf{S}_{iC}^{j-1}. \quad (4.5)$$

where $\mathbf{S}_{iC}^j \setminus \mathbf{S}_{iC}^{j-1}$ is defined as all elements that are in \mathbf{S}_{iC}^j but are not in \mathbf{S}_{iC}^{j-1} .

The algorithm for the prediction step consists of two layers, which are referred to as the regressor collection (Fig. 4.2) and regressor classification (Fig. 4.3) layers, respectively. The regressor collection layer is composed of five processes represented by five rectangular boxes, i.e., the location identifier, checked predictor identifier, potential predictor identifier, sparse nonlinear regression and termination checker. The layer is structured to have two sequential modes, which aim to obtain the default \mathbf{S}_{iR} and to search for potential predictors to be used as inputs for the regressor classification layer, respectively. We note that the second mode is proposed to avoid having to re-look at all the potential predictors that have already been evaluated. The search algorithm for the regressor collection layer is developed based on the inverse square law for thermal radiation. It makes use of two fundamental guidelines, namely, the burners separated from the i th reforming

tube by a significant distance should not be considered as potential predictors, and the nearby burners have greater influence on the i th OTWT than other burners that are situated farther away from the i th reforming tube, to reduce the regressor space and define a unique searching path, which will be elaborated later in this section. The search algorithm is the most critical development of the present work and allows the model identification based on the Bayesian framework to be computationally efficient. This is because the search algorithm selectively creates a small number of sub-prediction models for the i th OTWT to be used by the BMA in making predictions as opposed to 2^{96} ($\approx 7.9 \times 10^{28}$) sub-prediction models, which would be generated by the alternative, i.e., the exhaustive search algorithm, which if it was implemented would make the model identification scheme computationally infeasible. In this work, the distance between the i th reforming tube and j th burner is denoted as d_{ij} and is calculated as the Euclidean distance between the projections of their centroids on a horizontal plane, and we assume that the default \mathbf{S}_{iR} of the i th reforming tube consists of the four nearest burners.

In the first iteration of the prediction step, the regressor collection layer is operated under the first mode to obtain the default \mathbf{S}_{iR} . Initially, it begins with the location identifier, which calculates the relative distance from the i th reforming tube to burners inside the reformer, and simultaneously computes the radius of the affecting zone (denoted as R_{iZ}^1) of the i th reforming tube according to Eq. 4.4. Next, the checked predictor identifier uses the information about the relative location of the i th reforming tube to create a virtual reformer geometry, which consists of the i th reforming tube and 96 burners as shown in Fig 4.4, and uses R_{iZ}^1 to create the first stage of the affecting zone as shown in Fig. 4.5. The checked predictor identifier, then, uses the virtual reformer geometry and first-stage affecting zone to generate \mathbf{S}_{iC}^1 , which contains information (i.e., distance to the i th reforming tube, burner IDs and FSF flow rates) of the checked predictors. In the first iteration, the library of i th sub-prediction models is expected empty, and therefore, the cardinality of \mathbf{S}_{iC}^1 is evaluated. If the cardinality of \mathbf{S}_{iC}^1 is less than or equal to four, the prediction step is instructed to terminate the first iteration and to execute the next iteration. The second iteration of the prediction step begins to recompute the radius of the affecting zone (denoted as R_{iZ}^2) of the i th reforming

tube according to Eq. 4.4. As in the first iteration of the prediction step, the checked predictor identifier in the second iteration uses R_{iZ}^2 to create the updated first stage of the affecting zone and, then, uses it and the virtual reformer geometry created in the first iteration to generate \mathbf{S}_{iC}^2 . Thereafter, the cardinality of \mathbf{S}_{iC}^2 is also evaluated since the library of *ith* sub-prediction models is expected to remain empty, and if its result is still less than or equal to four, the prediction step is again instructed to terminate the second iteration and to execute the next iteration. This procedure is repeated until the number of elements in the checked predictor set of the *ith* reforming tube is strictly greater than four.

This discussion is continued with the assumption that in the *jth* iteration of the prediction step, the cardinality of \mathbf{S}_{iC}^j is greater than four as shown in Fig. 4.6. Initially, the four nearest burners to the *ith* reforming tube in \mathbf{S}_{iC}^j are used to create the default \mathbf{S}_{iR} , which is utilized by the sparse nonlinear regression algorithm to create the default sub-prediction model for the *ith* OTWT. Then, the model is stored in the *ith* library of sub-prediction models and is assigned an index of 1. The remaining elements in \mathbf{S}_{iC}^j , i.e., $\mathbf{S}_{iC}^j \setminus \mathbf{S}_{iR}$, are considered to be potential predictors, which are elements of \mathbf{S}_{iP}^j , and are used as inputs for the regressor classification layer, which is the secondary layer of the prediction step algorithm.

The regressor classification layer is structured based on the Bayesian variable selection framework to systematically update \mathbf{S}_{iR} using a given potential predictor set and to selectively create additional sub-prediction models for the *ith* OTWT. A brute-force Bayesian variable selection would require all possible hypothetical basis sets of regressors to be created from \mathbf{S}_{iP}^j and \mathbf{S}_{iR} , followed by using the sparse nonlinear regression to generate all possible hypothetical sub-prediction models, from which the important sub-prediction models would be selected. This approach is expected to be computationally intensive and will not be implemented. Instead, the layer is designed to exploit Occam's window [39] and the two fundamental guidelines that are used in the regressor collection layer to avoid generating all possible hypothetical basis sets of regressors from \mathbf{S}_{iP}^j and \mathbf{S}_{iR} in the process of identifying the important sub-prediction models by assessing the impact of each element in the potential predictor set on the goodness of fit of the sub-prediction model in a

step-wise fashion. Specifically, in the j th iteration of the regressor collection layer, the regressor classification layer starts out with the basis set constructor, which is programmed to strategically select an element in \mathbf{S}_{iP}^j followed by adding it to the existing \mathbf{S}_{iR} to create a hypothetical basis set of regressors (denoted as \mathbf{S}_{iR}^h), which is subsequently used by the sparse nonlinear regression to generate the corresponding hypothetical sub-prediction model. If the hypothetical sub-prediction model can explain the training data significantly better than the sub-prediction model created with \mathbf{S}_{iR} (in a sense related to Bayes factors to be made clear in Section 4.4.1), it is either stored in or used to replace the i th library of sub-prediction models based on the supporting evidence for the model, and \mathbf{S}_{iR}^h is used to replace \mathbf{S}_{iR} ; otherwise, the hypothetical sub-prediction model and \mathbf{S}_{iR}^h are discarded. In this work, the procedure of selecting an element in \mathbf{S}_{iP}^j encoded in the basis set constructor begins by ranking elements in \mathbf{S}_{iP}^j in the order of increasing distance to the i th reforming tube such that the potential predictor separated from the i th reforming tube by the shortest distance is considered to have the highest rank (i.e., the 1st rank), and the potential predictors separated from the i th reforming tube by an equal distance are considered to have the same rank. Then, the rank of each element in \mathbf{S}_{iP}^j is utilized by the basis set constructor as an indicator for the order that the element is selected to construct \mathbf{S}_{iR}^h . Specifically, the basis set constructor starts with the high-ranking elements in \mathbf{S}_{iP}^j because the burners that are situated closer to the i th reforming tube are expected to have greater influence on the i th OTWT than other burners that are situated farther away and are more likely to be considered as predictors; therefore, \mathbf{S}_{iR}^h is more likely to be accepted. When multiple elements of \mathbf{S}_{iP}^j have the same rank, the order that these elements are selected to construct \mathbf{S}_{iR}^h is trivial because our proposed model (Eq. 4.1a) does not contain any cross term, which suggests that burners are assumed to independently interact with the i th reforming tube. In this case, they are iteratively selected one by one to construct \mathbf{S}_{iR}^h before the potential predictors in the next lower rank are selected. This procedure is repeated until all elements in \mathbf{S}_{iP}^j are considered, then the updated \mathbf{S}_{iR} is sent back to the regressor collection layer.

Subsequently, in the regressor collection layer, the termination checker reviews R_{iZ}^j and the updated \mathbf{S}_{iR} created in the regressor classification layer to decide if the prediction step should be

terminated. Specifically, when R_{iZ}^j is less than the critical radius of the multistage affecting zone (denoted as R_Z^c), the termination checker always instructs the prediction step to execute the next iteration. In this work, R_Z^c is chosen to be 3.4 m to prevent the prediction step from exploring unnecessary regions in the regressor space because Chapter 3 shows that the faraway burners, which are defined as those separated from the i th reforming tube by a distance greater than 3.4 m, are expected to have small impact on the i th OTWT by demonstrating that data-driven models which include the faraway burners in the basis set of regressors have similar goodness of fit to that of the data-driven model that excludes the faraway burners from the basis set of regressors. On the contrary, when R_{iZ}^j becomes greater than or equal R_Z^c , the termination checker only allows the prediction step to execute the next iteration if at least one potential predictor in \mathbf{S}_{iP}^j is added to \mathbf{S}_{iR} . This design of the termination checker is proposed to account for the potential influence of the furnace-side flow pattern on the OTWT distribution that allows the faraway burners to have long range effects on the i th OTWT and to simultaneously prevent the prediction step from exploring unnecessary regions in the regressor space.

After the j th iteration of the prediction step, the regressor collection layer is operated under the second mode to exclusively search for potential predictors to be used as inputs for the regressor classification layer. Initially, it begins to compute R_{iZ}^{j+1} of the i th reforming tube according to Eq. 4.4, which is used by the checked predictor identifier in the $(j+1)$ th iteration to create the first stage of the affecting zone as done in the previous iterations of the prediction step. Next, the checked predictor identifier uses the first stage affecting zone and virtual reformer geometry created in the first iteration to generate \mathbf{S}_{iC}^{j+1} . In the $(j+1)$ th iteration of the prediction step, because the library of i th sub-prediction models is no longer empty, the potential predictor identifier is executed for the first time; this step is the key difference between the first and second modes of the regressor collection layer. Specifically, the potential predictor identifier uses R_{iZ}^{j+1} and R_{iZ}^j to create the second stage of the affecting zone as shown Fig. 4.7 and, then, uses it and the virtual reformer geometry to generate \mathbf{S}_{iP}^{j+1} , which contains information of the potential predictors. After that, \mathbf{S}_{iP}^{j+1} is used as an input for the regressor classification layer, which updates \mathbf{S}_{iR} . Finally, the

termination checker utilizes R_{iZ}^{j+1} and the updated \mathbf{S}_{iR} in the decision-making process of concluding the prediction step. This procedure is repeatedly executed until the radius of the multistage affecting zone is greater than or equal R_Z^c , and all elements in the potential predictor set of the i th reforming tube are rejected. Finally, BMA is utilized to determine the weighting factor for each member in the i th library of sub-prediction models (see Section 4.4.2).

4.4.1 Bayesian variable selection

In the present work, a Bayesian variable selection method with the search algorithm developed based on Occam's window and theories of thermal radiation is used to identify the predictors for the i th OTWT based on the training data and to simultaneously create a collection of sub-prediction models that can be used to explain the dependence of the i th OTWT on the FSF distribution and total FSF flow rate. At each step, an element in the set of potential predictors is added to \mathbf{S}_{iR} to create a \mathbf{S}_{iR}^h , which is subsequently used to create the corresponding hypothetical sub-prediction model as detailed earlier in this section (the sparse nonlinear regression algorithm used to develop the hypothetical sub-prediction models will be described in Section 4.4.3). Then, the layer quantitatively assesses the goodness of fit of two competing data-driven models of the i th reforming tube, i.e., the sub-prediction model (denoted as $M_{i,k}$ where k is the model index in the i th library of sub-prediction models) created with \mathbf{S}_{iR} and the hypothetical sub-prediction model denoted as $M_{i,h}$ created with \mathbf{S}_{iR}^h , by using the ratio of posterior model probabilities as the metric to determine if a potential predictor of interest can be classified as an important regressor. Specifically, the posterior model probability of $M_{i,k}$, which is denoted as $pr(M_{i,k} | \mathbf{T}_i)$ to represent the probability that $M_{i,k}$ is the true model for the dependence of the i th OTWT on the FSF distribution and total FSF flow rate after observing the training data, is computed as follows,

$$pr(M_{i,k} | \mathbf{T}_i) = \frac{pr(\mathbf{T}_i | M_{i,k}) pr(M_{i,k})}{\sum_{l=1}^{K_i} pr(\mathbf{T}_i | M_{i,l}) pr(M_{i,l})} \quad (4.6)$$

where $\mathbf{T}_i = \{T_i^1, T_i^2, \dots, T_i^N\}$ is the collection of all $N=18$ training data sets, T_i^j is the i th OTWT

extracted from the j th training data set, K_i is the total number of sub-prediction models in the i th library, $pr(M_{i,k})$ is the prior model probability of $M_{i,k}$ and $pr(\mathbf{T}_i|M_{i,k})$ is the model evidence in favor of $M_{i,k}$. It is worth noting that $pr(M_{i,k})$ reflects our beliefs that $M_{i,k}$ is the true model for the dependence of the i th OTWT on the FSF distribution and total FSF flow rate before observing the training data. If information about the true model for the i th reforming tube is available (e.g., the number of predictors in the true model is known), the prior model probability distribution could be designed to incorporate such information by assigning the sub-prediction models that have the same number of predictors as the true model with a higher prior model probability. However, this is typically not the case in practice. Therefore, the prior model probability distribution is chosen to be noninformative, which assigns equal prior probability to all sub-prediction models in the i th library and allows conclusions about the true model to be drawn directly from data. The noninformative prior model probability distribution for the i th reforming tube is designed as follows,

$$pr(M_{i,j}) = \frac{1}{K_i} \quad \forall j = 1, \dots, K_i. \quad (4.7)$$

Hence, the ratio of posterior model probabilities between $M_{i,h}$ and $M_{i,k}$ can be evaluated as follows,

$$\frac{pr(M_{i,h}|\mathbf{T}_i)}{pr(M_{i,k}|\mathbf{T}_i)} = \frac{pr(\mathbf{T}_i|M_{i,h}) pr(M_{i,h})}{pr(\mathbf{T}_i|M_{i,k}) pr(M_{i,k})} = \frac{pr(\mathbf{T}_i|M_{i,h})}{pr(\mathbf{T}_i|M_{i,k})} = B_{i,hk} \quad (4.8)$$

where $B_{i,hk}$ is defined as a Bayes factor for $M_{i,h}$ against $M_{i,k}$. Eq. 4.8 suggests that $B_{i,hk}$ and the ratio of posterior model probabilities between $M_{i,h}$ and $M_{i,k}$ under the assumption of the noninformative prior model probability distribution (Eq. 4.7) are equivalent, and therefore, the value of $B_{i,hk}$ can be used as the quantitative evidence in favor of incorporating the potential predictor into \mathbf{S}_{iR} . However, computing $B_{i,hk}$ is a nontrivial task because there is no analytical closed-form expression for computing $pr(\mathbf{T}_i|M_{i,k})$. Specifically, $pr(\mathbf{T}_i|M_{i,k})$ is computed by integrating over all possible values of the parameters of $M_{i,k}$ as follows,

$$pr(\mathbf{T}_i|M_{i,k}) = \int pr(\mathbf{T}_i|M_{i,k}, \vec{\alpha}_i^k) pr(\vec{\alpha}_i^k|M_{i,k}) d\vec{\alpha}_i^k \quad (4.9)$$

where $\vec{\alpha}_i^k = [\vec{\alpha}_i^{k1}, \dots, \vec{\alpha}_i^{kG}, \alpha_i^k]^T$ is the parameter vector of $M_{i,k}$ (see Section 4.4.3), $pr(\vec{\alpha}_i^k | M_{i,k})$ is prior probability density of $\vec{\alpha}_i^k$ and $pr(\mathbf{T}_i | M_{i,k}, \vec{\alpha}_i^k)$ is the likelihood function of \mathbf{T}_i . It is important to note that the likelihood function of \mathbf{T}_i is defined as the joint probability density function of $T_i^1, T_i^2, \dots, T_i^N$ and is dependent on $\vec{\alpha}_i^k$ of $M_{i,k}$ as follows,

$$pr(\mathbf{T}_i | M_{i,k}, \vec{\alpha}_i^k) = \prod_{j=1}^N pr(T_i^j | M_{i,k}, \vec{\alpha}_i^k) \quad (4.10)$$

where $pr(T_i^j | M_{i,k}, \vec{\alpha}_i^k)$ is the probability density function of T_i^j . In addition, the probability density function of T_i^j is assumed to be computed as follows,

$$pr(T_i^j | M_{i,k}, \vec{\alpha}_i^k) = \frac{1}{\sqrt{2\pi}(\sigma_i^j)^2} \exp\left(-\frac{(T_i^j - \widehat{T}_i^{P,j})^2}{2(\sigma_i^j)^2}\right) \quad (4.11)$$

where σ_i^j is the standard deviation of the noise in the i th OTWT in the j th training data set. Due to challenges in computing $B_{i,hk}$, many published works in the Bayesian statistics literature center on proposing methods to compute $pr(\mathbf{T}_i | M_{i,k})$ numerically, e.g., Markov Chain Monte Carlo, or to approximate it with an acceptable accuracy, e.g., Laplace approximation, Bayesian information criterion (BIC) approximation and maximum likelihood estimator (MLE) approximation [20]. In this work, the BIC approximation is favored for two reasons: the BIC approximation is expected to provide a good approximation of $\log B_{i,hk}$ for linear models [20] and allows us to avoid making assumptions about the prior probability density of $\vec{\alpha}_i^k$, which allows the decision to incorporate the potential predictor into \mathbf{S}_{iR} to be made based entirely on the training data [30]. Under the BIC approximation, $\log B_{i,hk}$ is computed as follows,

$$\log B_{i,hk} = \left[\log\left(pr(\mathbf{T}_i | M_{i,h}, \widehat{\vec{\alpha}}_i^h)\right) - \log\left(pr(\mathbf{T}_i | M_{i,k}, \widehat{\vec{\alpha}}_i^k)\right) \right] - \frac{1}{2}(d_h - d_k) \log(N) \quad (4.12)$$

where $\widehat{\vec{\alpha}}_i^k$ is the MLE of $\vec{\alpha}_i^k$ and d_k is the number of nonzero parameters of $\vec{\alpha}_i^k$ (see Section 4.4.3). It is important to note that the first term in Eq. 4.12 can be interpreted as the assessment of the goodness of fit between two sub-prediction models, and the second term can be interpreted as the penalty for using a model with higher complexity. The approximated value of $\log B_{i,hk}$ is the evidence in favor of $M_{i,h}$ extracted from the training data, and higher values of $\log B_{i,hk}$ imply that the training data provides more evidence in support of $M_{i,h}$ and against $M_{i,k}$. Therefore, the value of $\log B_{i,hk}$ can be used in the decision-making process for determining whether to incorporate a potential predictor into \mathbf{S}_{iR} . In the present work, the task of interpreting the value of $\log B_{i,hk}$ is especially challenging because the improvement in the model goodness of fit by incorporating an additional term into \mathbf{S}_{iR} is expected to be underestimated when a small number of training data sets is used. Hence, guidelines for interpreting Bayes factors proposed in the Bayesian statistics literature, namely, twice the natural logarithm of the Bayes factor suggested by [30], half unit on the logarithm of the Bayes factor suggested by [28], Occam's window with the lower bound of 1/20 and upper bound of 20 suggested by [51] and Occam's window with the lower bound of 1/20 and upper bound of 1 suggested by [40], were reviewed. In this work, Jeffreys' interpretation of the Bayes factor [28] is selected and is tailored to account for the impact of using the small number of training data sets on the value of $\log B_{i,hk}$ as follows: we reason that when an insignificant regressor is incorporated into \mathbf{S}_{iR} to create \mathbf{S}_{iR}^h , the two competing sub-prediction models are expected to have a similar goodness of fit, which causes the first term in Eq. 4.12 to be approximately zero, and the dimension of \mathbf{S}_{iR}^h is greater than that of \mathbf{S}_{iR} , which causes the second term in Eq. 4.12 to be negative due to the increased model complexity. Therefore, a negative $\log B_{i,hk}$ can be viewed as a strong evidence against $M_{i,h}$, which implies that the i th OTWT is independent of the potential predictor. In this case, the regressor classification layer is instructed to discard $M_{i,h}$ and to dismiss the attempt to incorporate the potential predictor into \mathbf{S}_{iR} . On the contrary, when $\log B_{i,hk}$ is non-negative and greater than 2.0, it can be viewed as a strong evidence against $M_{i,k}$, which indicates that the training data provides significant evidence in support of $M_{i,h}$ and against $M_{i,k}$ because $M_{i,h}$ has a significantly higher goodness of fit than $M_{i,k}$. In this case, the layer is instructed to discard

$M_{i,k}$ along with its nested sub-prediction models (i.e., the sub-prediction models created and stored throughout the prediction step in the process of generating $M_{i,k}$) in the i th sub-prediction model library followed by accepting the attempt to incorporate the potential predictor into \mathbf{S}_{iR} and storing $M_{i,h}$ in the i th library as the first sub-prediction model. It is worth noting that this action is inspired by the two principles of Occam's window, which suggests that when a sub-prediction model has a significantly lower goodness of fit than its competitor, it should be discredited [20]. Furthermore, in the remaining case, i.e., when $\log B_{i,hk}$ is nonnegative and less than or equal to 2.0, it can be viewed as a weak evidence against $M_{i,k}$, which indicates that the training data suggests there is weak evidence in support of $M_{i,h}$ and against $M_{i,k}$ because $M_{i,h}$ has a slightly higher goodness of fit than $M_{i,k}$; however, this evidence is insufficient to discredit $M_{i,k}$. In this case, the layer is instructed to accept the attempt to incorporate the potential predictor into \mathbf{S}_{iR} and store $M_{i,h}$ in the i th library as the $(k + 1)$ th sub-prediction model.

Although the reformer data (i.e., the training data and testing data) is generated by simulating the high-fidelity reformer CFD model, it is expected to exhibit some stochastic behavior because in all simulations of the reformer CFD model, the final global normalized residuals have small nonzero values which suggests that the reformer data fluctuates around the true steady-state. Furthermore, even though the training data and testing data are expected to exhibit some stochastic behavior, each reformer data set only has one realization, which prevents the magnitude of the noise from being estimated from the reformer data. In this work, the noise in OTWTs of all reforming tubes in the j th training data set is assumed to be normal, independent and identically distributed with a mean of zero and a standard deviation of σ^j , which is assumed to be 5%–10% of the corresponding OTWT range and is approximated as follows,

$$\sigma_i^j = \sigma^j = \eta_\sigma \left(\max(\vec{T}^j) - \min(\vec{T}^j) \right) \quad \forall i = 1, \dots, 336 \quad (4.13)$$

where $\max(\vec{T}^j)$ and $\min(\vec{T}^j)$ represent the maximum and minimum OTWT in the j th training data set, respectively, and η_σ is a hyperparameter, which has a random value between 0.05 and 0.1 generated by our in-house uniform random number generator.

4.4.2 Bayesian model averaging

In the present work, Bayesian model averaging is used to account for model uncertainty in making predictions about the i th OTWT based on the FSF distributions and total FSF flow rates. In this section, it is assumed that K_i sub-prediction models for the i th reforming tube, that capture the dependence of the i th OTWT on the FSF distribution and total FSF flow rate reasonably well, are derived from the training data based on the Bayesian variable selection approach, and T_i^* is to be estimated given \vec{F}^* and F_{tot}^* , which are the unexplored operating conditions of the reformer. Therefore, the posterior mean of T_i^* , which represents the most likely value of T_i^* that is expected to be observed based on the training data, can be computed as follows,

$$E\left(T_i^*|\mathbf{T}_i, \vec{F}^*, F_{tot}^*\right) = \sum_{k=1}^{K_i} pr(M_{i,k}|\mathbf{T}_i) E\left(T_i^*|\mathbf{T}_i, \vec{F}^*, F_{tot}^*, M_{i,k}\right) \quad (4.14)$$

where $E\left(T_i^*|\mathbf{T}_i, \vec{F}^*, F_{tot}^*, M_{i,k}\right)$ represents the posterior mean of T_i^* when $M_{i,k}$ is assumed to be the true model for the i th reforming tube. It is recognized that Eqs. 4.1a and 4.14 bear an uncanny resemblance, and therefore, it can be inferred that $pr(M_{i,k}|\mathbf{T}_i)$ is the BMA weighting factor of $M_{i,k}$,

$$pr(M_{i,k}|\mathbf{T}_i) = w_{i,k}^P. \quad (4.15)$$

In addition, $pr(M_{i,k}|\mathbf{T}_i)$ can be expressed in terms of Bayes factors by dividing the numerator and denominator of Eq. 4.6 by the posterior probability of an arbitrary model (e.g., $M_{i,1}$) chosen from the i th sub-prediction model library,

$$pr(M_{i,k}|\mathbf{T}_i) = \frac{B_{i,k1}}{\sum_{l=1}^{K_i} B_{i,l1}}. \quad (4.16)$$

Therefore, the BMA weighting factor of $M_{i,k}$ can be approximated by the BIC approximation (Eq. 4.12) using the training data, which allows $\widehat{T}_i^{P,*}$ to be computed as a weighted average of $\widetilde{T}_{i,k}^{P,*}$

generated by sub-prediction models of the i th reforming tube.

4.4.3 Sparse nonlinear regression

In the present work, sparse nonlinear regression with maximum likelihood estimation (MLE) is used to construct data-driven models of the i th reforming tube that can be used to explain nonlinearities in the dependence of the i th OTWT on the FSF distribution and total FSF flow rate. The idea is inspired by the work in [9] which uses sparse nonlinear regression to extract governing equations of nonlinear systems from observed data. Additionally, [9] notes that governing equations of many systems typically consist of a few nonzero terms, which makes sparse nonlinear regression an especially appealing approach. To derive sub-prediction models that can be used to describe the dependence of the i th OTWT on the FSF distribution and total FSF flow rate from the reformer data, a library of linear and nonlinear transformations is designed based on expected interactions between the i th OTWT and its predictors. For instance, if the j th burner is a predictor of the i th OTWT, any nonzero value of the j th burner FSF flow rate is expected to cause the i th OTWT to rise above the ambient temperature, and when the FSF flow rate of the burner is increased, the i th OTWT is also expected to increase. Therefore, the transformations are restricted to nonnegative, monotonically increasing and continuously differentiable classes of functions. In this work, the library of transformation functions is proposed to consist of monomial, root and exponential functions as follows,

$$f_1(\vec{F}^n) = [F_1^n, F_2^n, \dots, F_{96}^n]^T \quad (4.17a)$$

$$f_2(\vec{F}^n) = [(F_1^n)^2, (F_2^n)^2, \dots, (F_{96}^n)^2]^T \quad (4.17b)$$

$$f_3(\vec{F}^n) = [(F_1^n)^3, (F_2^n)^3, \dots, (F_{96}^n)^3]^T \quad (4.17c)$$

$$f_4(\vec{F}^n) = [\sqrt[2]{F_1^n}, \sqrt[2]{F_2^n}, \dots, \sqrt[2]{F_{96}^n}]^T \quad (4.17d)$$

$$f_5(\vec{F}^n) = [\sqrt[3]{F_1^n}, \sqrt[3]{F_2^n}, \dots, \sqrt[3]{F_{96}^n}]^T \quad (4.17e)$$

$$f_6(\vec{F}^n) = [\sqrt[4]{F_1^n}, \sqrt[4]{F_2^n}, \dots, \sqrt[4]{F_{96}^n}]^T \quad (4.17f)$$

$$f_7(\vec{F}^n) = [\sqrt[5]{F_1^n}, \sqrt[5]{F_2^n}, \dots, \sqrt[5]{F_{96}^n}]^T \quad (4.17g)$$

$$f_8(\vec{F}^n) = [\exp(F_1^n), \exp(F_2^n), \dots, \exp(F_{96}^n)]^T \quad (4.17h)$$

where F_j^n is the FSF flow rate of the j th burner from the n th data set. Next, the library of transformations is used to formulate the generalized sub-prediction model for the i th reforming tube, which is assumed to be dependent on all 96 burners, as follows,

$$\tilde{T}_i^{P,n} = \sum_{g=1}^8 \vec{\alpha}_i^g \cdot f_g(\vec{F}^n) + \alpha_i \quad (4.18)$$

where $\vec{\alpha}_i^g \in \mathbb{R}^{96 \times 1}$ is the generalized parameter vector associated with the g th transformation function, where $g = 1, \dots, 8$ (Eq. 5.2), and $\alpha_i \in \mathbb{R}$ represents ambient air temperature. Then, a basis set of regressors (i.e., \mathbf{S}_{iR}) of the i th reforming tube created by the Bayesian variable selection method developed in the regressor classification layer is utilized in the model-building process which integrates information about the reformer layout and the knowledge that thermal radiation is expected to be the dominant mode of heat transfer in the reformer into the sub-prediction model (i.e., $M_{i,k}$) to set parameters associated with the burners that are not contained in S_{iR} to zero, effectively reducing the number of terms in Eq. 4.18 by a factor of $96/N_{iR}$, where N_{iR} is the cardinality of \mathbf{S}_{iR} , leading significant reduction in the computational cost. Therefore, $M_{i,k}$ can be written as follows,

$$\tilde{T}_{i,k}^{P,n} = \sum_{g=1}^8 \vec{\alpha}_i^{kg} f_g \left(\vec{F}^n \Big|_{S_{iR}} \right) + \alpha_i^k \quad (4.19)$$

where $\vec{F}^n \Big|_{S_{iR}} \in \mathbb{R}^{N_{iR} \times 1}$ is a vector in the design matrix of $M_{i,k}$. The nonlinear sparse regression with MLE is formulated as a constrained optimization problem that is structured based on the L1 regularization technique (i.e., LASSO) because LASSO is known to shrink parameters associated with the irrelevant transformations to zero which further reduces the number of terms in the sub-prediction model (Eq. 4.18) of the i th reforming tube. In addition, theories of thermal radiation discussed in Section 4.1 are integrated into the sub-prediction model by means of equality and inequality constraints (Eqs. 4.21a–4.21c) in the optimization problem. The formulation for the sparse nonlinear regression with MLE is proposed as follows,

$$\min_{\substack{\alpha_i^k \in [298.15, 348.15] \\ \alpha_{ij}^{kg} \in [0, \infty)}} \sum_{n=1}^N \frac{(T_i^n - \tilde{T}_{i,k}^{P,n})^2}{2(\sigma_i^n)^2} + \lambda_i \sum_{g=1}^8 \left\| \vec{\alpha}_i^{kg} \right\|_1 \quad (4.20)$$

subject to

$$\sum_{g=1}^8 \alpha_{il}^{kg} f_g(\vec{F}^0) = \sum_{g=1}^8 \alpha_{ij}^{kg} f_g(\vec{F}^0) \quad \text{if } d_{il} = d_{ij} \quad (4.21a)$$

$$\sum_{g=1}^8 \alpha_{il}^{kg} f_g(\vec{F}^0) \geq \left(\frac{d_{ij}}{d_{il}} \right)^{\beta_l} \sum_{g=1}^8 \alpha_{ij}^{kg} f_g(\vec{F}^0) \quad \text{if } d_{il} < d_{ij} \quad (4.21b)$$

$$\sum_{g=1}^8 \alpha_{il}^{kg} f_g(\vec{F}^0) \leq \left(\frac{d_{ij}}{d_{il}} \right)^{\beta_u} \sum_{g=1}^8 \alpha_{ij}^{kg} f_g(\vec{F}^0) \quad (4.21c)$$

$$\vec{F}^0 = \frac{F_{tot}^{typ}}{96} \quad (4.21d)$$

where l and j are indices of burners that are elements in S_{iR} , α_{ij}^{kg} is the parameter in $M_{i,k}$ associated with the g th transformed FSF flow rate of the j th burner, $\alpha_i^k \in [298.15, 348.15]$ represents an ambient temperature parameter in $M_{i,k}$ and its typical range, λ_i is the tuning parameter in LASSO of the i th reforming tube, d_{ij} and d_{il} are distances from the i th reforming tube to the j th and l th

burners, respectively, $\beta_u=6.0$ and $\beta_l=1.0$ are hyperparameters of the constraints and are chosen by trial and error, and F_{tot}^{typ} is the total FSF flow rate typically reported in the SMR literature. The constraints of Eqs. 4.21a–4.21c are formulated in an effort to integrate the inverse square law of thermal radiation into $M_{i,k}$. Specifically, burners, which are separated from the i th reforming tube by an equal distance and are supplied with the same FSF flow rate, are expected to have the same impact on the i th OTWT as shown in the equality constraint (Eq. 4.21a), whereas burners which are separated from the i th reforming tube by different distances but are supplied with the same FSF flow rate are expected to have different impacts on the i th OTWT as shown in the inequality constraint (Eq. 4.21b). In this particular case, a burner that is situated closer to the i th reforming tube is expected to have a higher impact on the i th OTWT than those that are further away. It is noted that an additional inequality constraint (Eq. 4.21c) is added to the optimization problem to prevent sparse nonlinear regression in an attempt to reduce the number of terms in Eq. 5.1 from falsely presuming that the impact due to a closer burner is indefinitely higher than that due to a further burner given the premise that the two are separated from the i th reforming tube by different distances and are supplied with the same FSF flow rate. It is noted that in the constrained optimization problem (Eqs. 4.20 and 4.21), λ_i directly controls the degree of shrinkage for the parameter vector in $M_{i,k}$. Specifically, large values of λ_i result in a high degree of shrinkage and favor underfitting data-driven models with low levels of complexity. On the contrary, small values of λ_i result in a low degree of shrinkage and favor overfitting data-driven models with high goodness of fit. Therefore, it is desired to use the optimal value of λ_i to balance between the degree of complexity and goodness of fit in data-driven models. In this work, leave-out-one (LOO) cross validation is used to search for the optimal value of λ_i among the proposed values, $\mathbf{S}_\lambda = \{0.1, 0.2, \dots, 1.0, 1.2, \dots, 2.0, 5.0, 10\}$, because the fitting error (i.e., the mean-square error) might not be an adequate representation for the out-of-sample prediction error. In LOO cross validation, the training data (\mathbf{T}_i) is split into sub-training and sub-testing data in such a way that a reformer data set in the training data is assigned to the sub-testing data, and the remaining data sets are assigned to the sub-training data. This procedure generates N different pairs of sub-training and

sub-testing data from the training data (where N is the cardinality of the training data), and then, each pair of the sub-training and sub-testing data is used to derive a sub-prediction model library for the i th reforming tube and to evaluate a corresponding out-of-sample prediction error for each value of λ_i in \mathbf{S}_λ . It is recognized that LOO cross validation is computationally intensive, e.g., the total CPU time is expected to be $\sim N$ times more than that required by an approach that uses the complete training data and the fitting error as the metric to select λ_i , but LOO cross validation provides evidence (i.e., the unbiased estimate of the prediction error) based on which the optimal λ_i can be identified. Specifically, the value of λ_i in \mathbf{S}_λ that yields the least prediction error for out-of-sample predictions is considered to be the optimal λ_i .

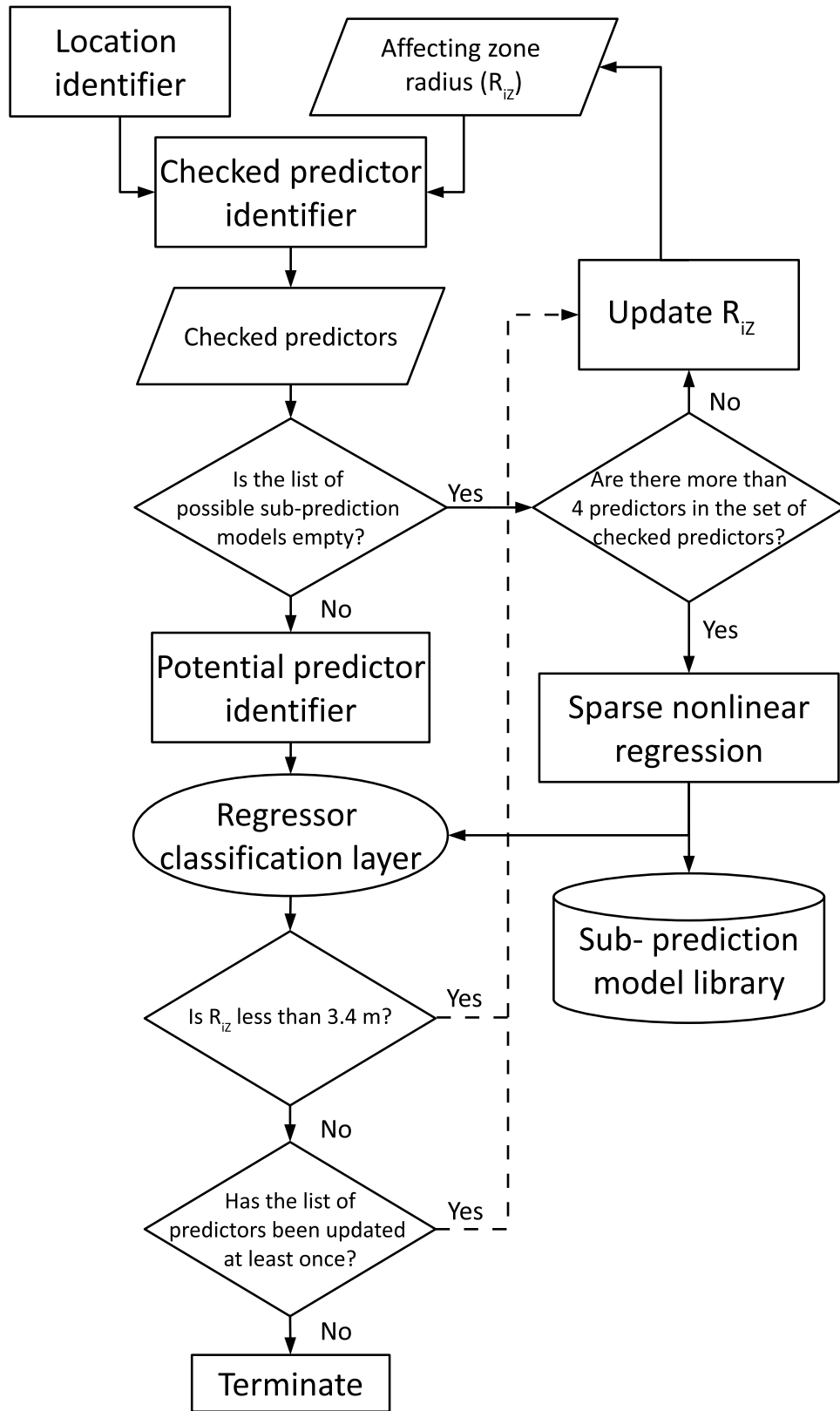


Figure 4.2: Flowchart of the regressor collection layer in the prediction step.

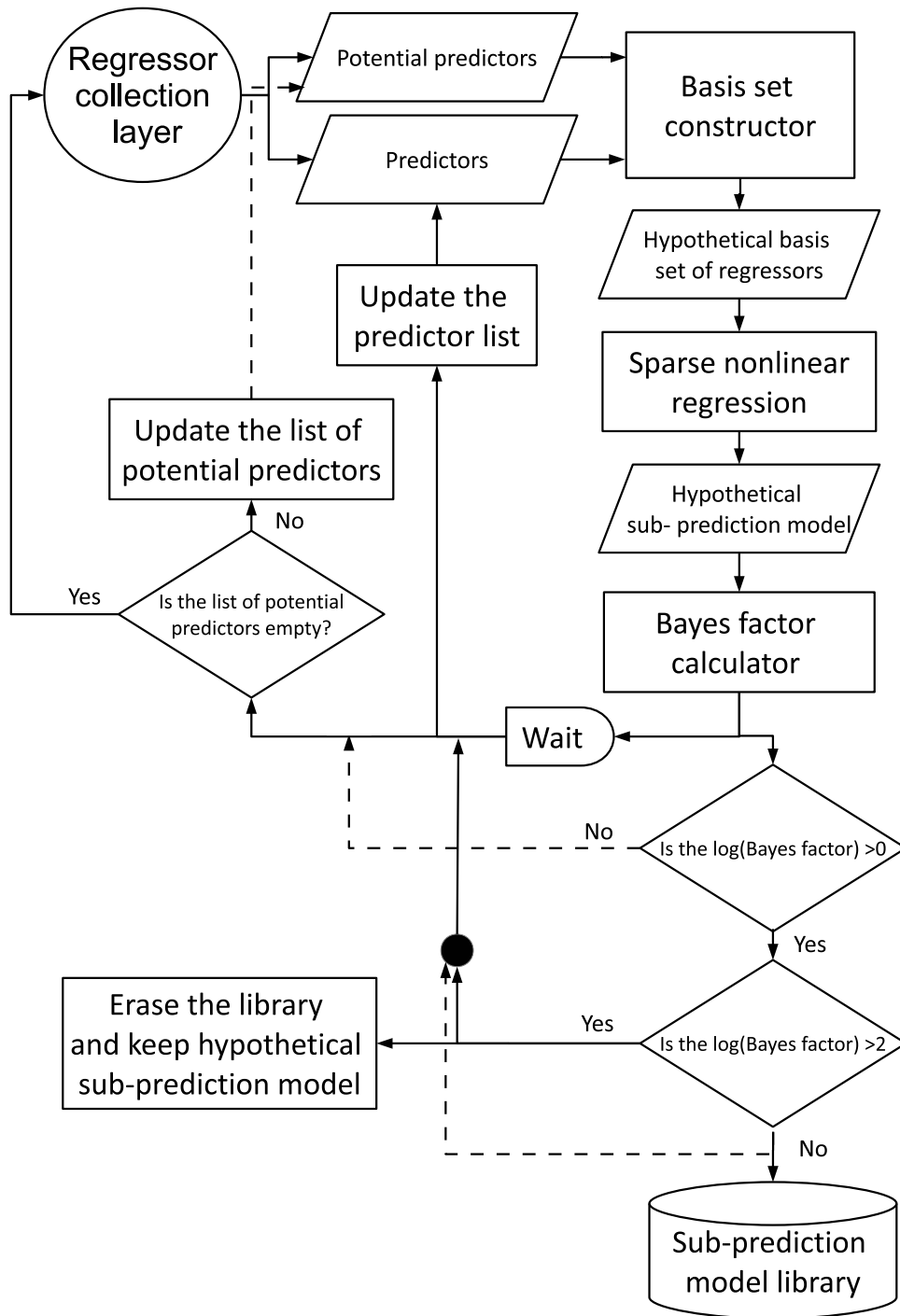


Figure 4.3: Flowchart of the regressor classification layer in the prediction step.

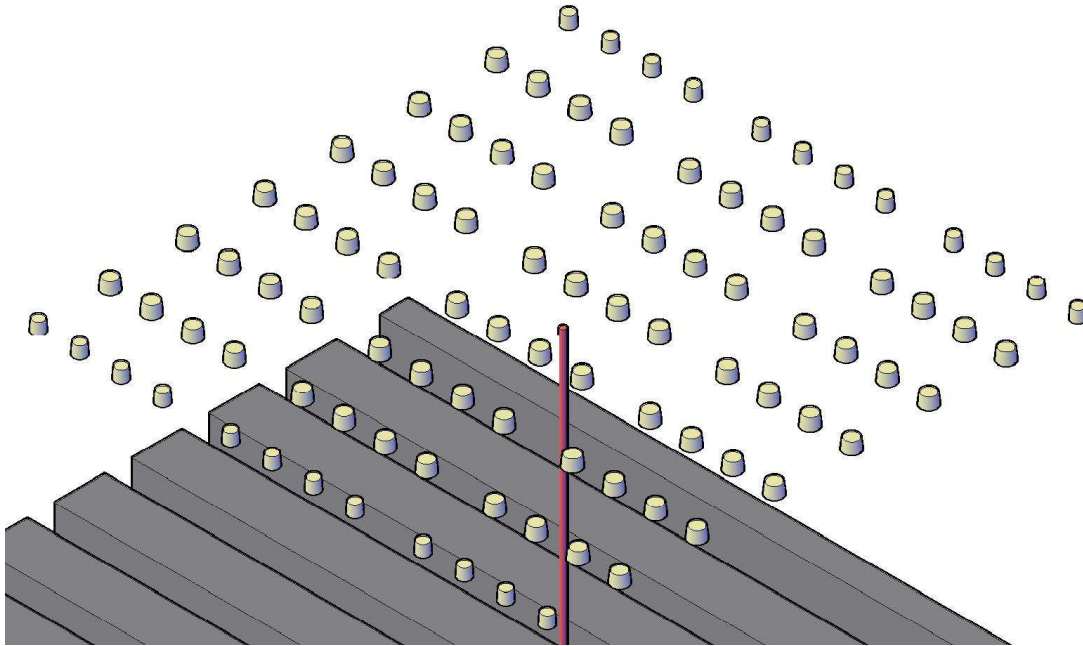


Figure 4.4: A virtual reformer geometry that is created based on the information generated by the location identifier in the regressor collection layer and consists of the i th reforming tube represented by a cylindrical tube and 96 burners represented by the frustum cones.

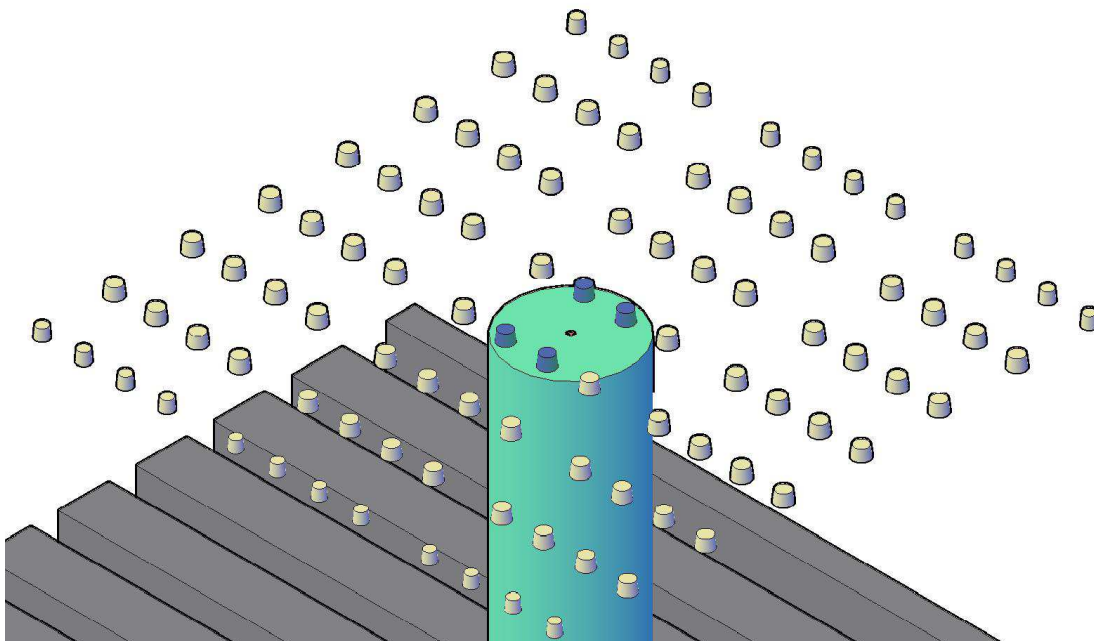


Figure 4.5: The first stage of the multistage affecting zone that is created based on R_{iZ}^1 and the virtual reformer geometry in the first iteration of the prediction step. In Fig. 4.5, the checked predictors in S_{iC}^1 are represented by the four shaded frustum cones and can be visually identified.

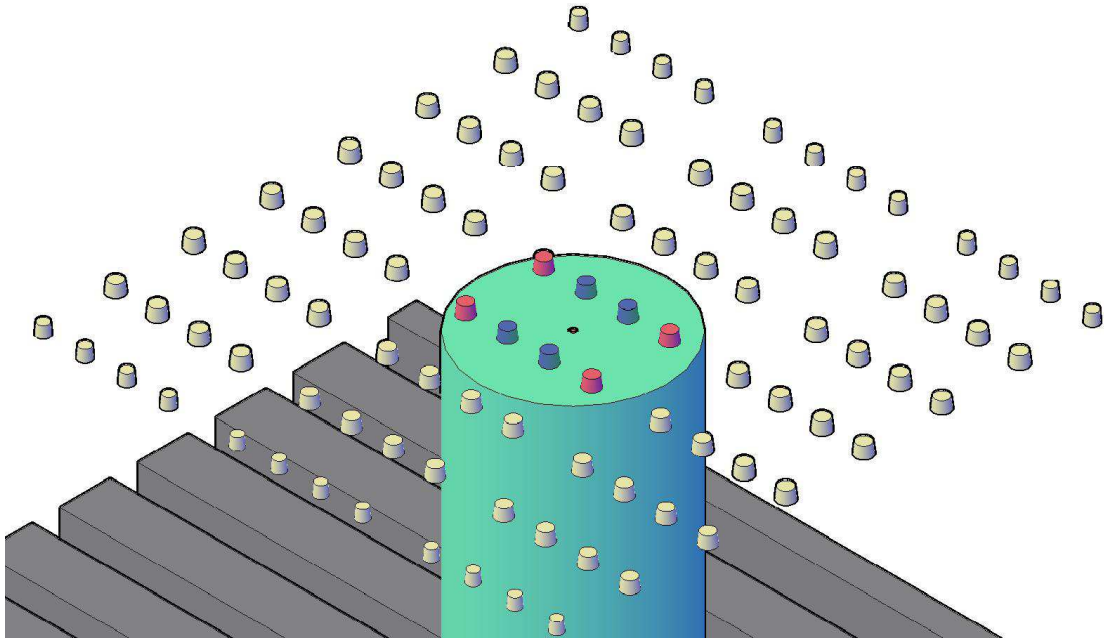


Figure 4.6: The first stage of the multistage affecting zone that is created based on R_{iZ}^j and the virtual reformer geometry in the j th iteration of the prediction step.

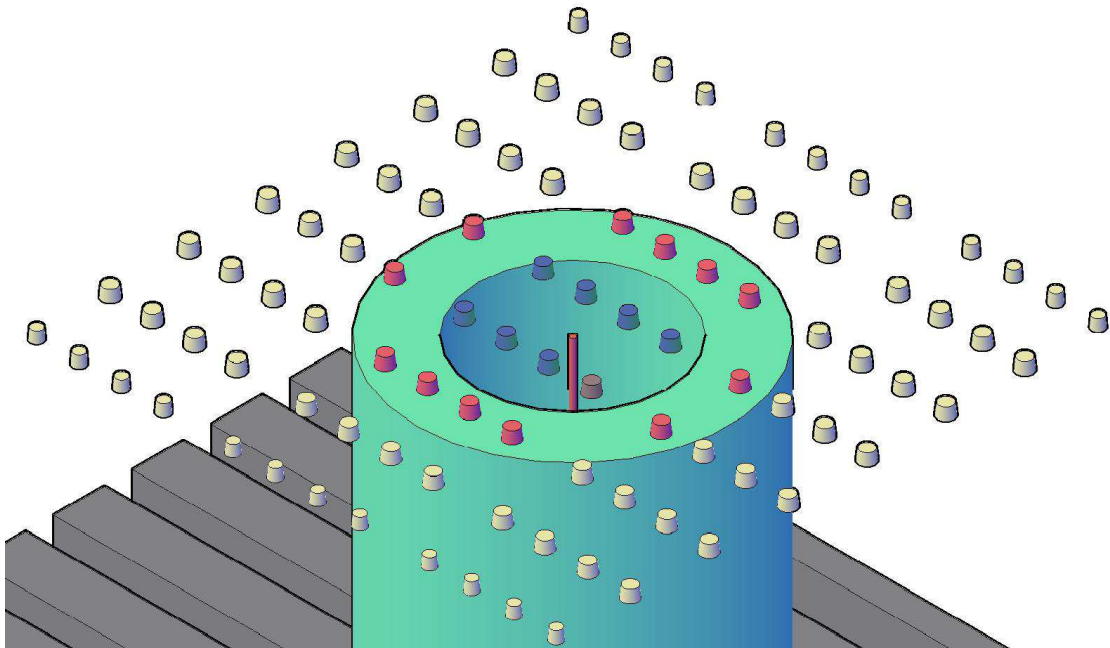


Figure 4.7: The first stage of the multistage affecting zone that is created based on R_{iZ}^{j+1} , R_{iZ}^j and the virtual reformer geometry in the $(j+1)$ th iteration of the prediction step.

4.5 Correction models

In the present work, an algorithm for the correction step is designed based on ordinary Kriging, which is superior to other common interpolation techniques and can yield estimates with minimum variance [26], to improve the predicted OTWT distribution, which is generated from the prediction model for the OTWT distribution using \vec{F}^n and F_{tot}^n , by accounting for the effect of interactions between neighboring reforming tubes on the OTWT distribution. The correction step is also designed to be a distributed algorithm, which derives the correction model for the i th reforming tube from the training data independently of other reforming tubes allowing the correction models for the 336 reforming tubes to be simultaneously created, which expedites the model-building process of the correction model for the OTWT distribution. In the remainder of this section, the underlying process that leads to the temperature variation in the OTWT distribution is discussed to elucidate the use of ordinary Kriging in an attempt to account for the impact of interactions among neighboring reforming tubes on the OTWT distribution, and then, assumptions and equations associated with ordinary Kriging will be explicitly presented.

As noted in Section 4.1, the degree of nonuniformity in the OTWT distributions along the reforming tube length is controlled by the temperature distribution of the furnace-side flow, which is a product of many complex interacting transport phenomena and chemical reactions taking place simultaneously inside the reformer. The analytical deterministic solution for the OTWT distribution modeled as a function of the reformer inputs (e.g., the FSF distribution and FSF flow rate) cannot be easily obtained, and therefore, variations in the OTWT distribution observed in the training data appear to be as though they are the result of a random process. Fig. 4.8 displays the OTWT of each reforming tube as a function of the i th lag ($i=77$ for the 77th reforming tube is chosen in this figure for demonstration purposes), where the lag is defined as the Euclidean distance between the j th and i th reforming tubes where j is different from i . The figure suggests that the mean of the OTWT distribution in each reformer CFD data set in the training data is constant. This realization justifies the assumption that in a sufficiently small neighborhood the underlying process that governs the

variations in the OTWT distribution is intrinsically stationary. Therefore, the spatial correlation of the OTWT among reforming tubes in a sufficiently small neighborhood can be summarized in a spatial variance function (i.e., semivariograms). Under the intrinsic stationarity assumption, the variance function only depends on lag (which is defined as a Euclidean distance between a pair of reforming tubes and is denoted as h) and is calculated using the classical estimator (i.e., the method of moments) from the training data as follows,

$$\widehat{\gamma}_i^n(h) = \frac{1}{2q_i(h)} \sum_{q_i(h)} (T_j^n - T_k^n)^2 \quad (4.22)$$

where $\widehat{\gamma}_i^n(h)$ is the sample semivariogram capturing the spatial correlation of the OTWTs among reforming tubes that are separated by $h \pm 0.15$ m and in the neighborhood of the i th reforming tube (denoted as \mathbf{S}_i^K) created from using the n th reformer CFD data set in the training data, T_j^n and T_k^n are the OTWTs of the reforming tubes that are separated by $h \pm 0.15$ m and in \mathbf{S}_i^K , and $q_i(h)$ is the number of pairs of reforming tubes that are separated by $h \pm 0.15$ m and in \mathbf{S}_i^K . In this work, \mathbf{S}_i^K is defined to be an 8 m by 8 m region centered at the i th reforming tube as shown in Fig. 4.9 so that there are a sufficient number of reforming tubes in \mathbf{S}_i^K , which allows relatively stable regional sample semivariograms to be created for each training data set. The sample semivariograms for \mathbf{S}_{77}^K (the neighborhood of the 77th reforming tube) calculated based on Eq. 4.22 using the training data are shown in Fig. 4.10. It is recognized that the sample semivariograms in \mathbf{S}_{77}^K at a given lag are similar across all training data, which suggests that the spatial correlation among reforming tubes separated by a distance of h m can be modeled to be independent of the FSF distribution and the total FSF flow rate. Therefore, all individual sample semivariograms can be pooled together to create average sample semivariograms as follows,

$$\widehat{\gamma}_i^*(h) = \frac{\sum_{n=1}^N \widehat{\gamma}_i^n(h) q_i(h)}{\sum_{n=1}^N q_i(h)}. \quad (4.23)$$

The average sample semivariograms shown in Fig. 4.11 are expected to be a reasonable represen-

tation of the spatial correlation among reforming tubes in \mathbf{S}_i^K [8].

It is noted from Fig. 4.11 that the average sample semivariograms typically increase with increasing lag, which indicates that the OTWTs of reforming tubes that are closely situated are more highly correlated than the OTWTs of those that are farther apart, with the exception at the lag of approximately 2 m. A detailed analysis of the reformer geometry shown in Fig. 5.2 reveals that the spatial correlation between reforming tubes might also be dependent on directionality in which the reforming tubes are separated. Two new terminologies are introduced to facilitate the discussion of anisotropic sample semivariograms: pairs of reforming tubes within a row are considered to be in the North-South direction and are referred to as North-South pairs, while pairs of reforming tubes in two adjacent rows are considered to be in the East-West direction and are referred to as East-West pairs. It is noted that the adjacent rows of reforming tubes are separated by a distance of approximately 2 m which is the smallest lag between any East-West pair. In addition, the East-West pairs in which reforming tubes are separated by approximately 2 m are expected to be under the influence of a number of common burners, specifically, under the assumption that the four nearest burners to the i th reforming tube are the i th default predictors, the regressor collection layer determines that their sets of regressors always have two common predictors. On the contrary, the North-South pairs in which reforming tubes are separated by approximately 2 m may or may not be under influence of any common burner. This analysis suggests that at the lag of approximately 2 m, the OTWTs of the East-West pairs are expected to be more similar than those of the North-South pairs. Furthermore, the number of East-West pairs at the lag of approximately 2 m is significantly larger than the number of the North-South pairs separated by the same distance due to the reformer layout as shown in Fig. 5.2. Therefore, the average omnidirectional sample semivariograms at the lag of approximately 2 m as shown in Fig. 4.11 might not be used to represent the spatial correlation between the North-South pairs. In this work, North-South and East-West average anisotropic sample semivariograms are evaluated according to Eq. 4.23 using information of the North-South pairs and East-West pairs in \mathbf{S}_i^K , respectively, and are shown in Figs. 4.12–4.13. It is recognized that with the exception at the lag of approximately 2 m at which the East-West pairs exhibit a

strong spatial correlation, the scatter plot of East-West average anisotropic sample semivariograms shown in Fig. 4.12 indicates that when the lag is greater than or equal to 2.4 m, East-West pairs appear to be spatially uncorrelated. Therefore, information of the East-West average anisotropic sample semivariograms will not be utilized in the model-building process of the spatial model (i.e., the correction model) for the i th OTWT. Additionally, it is noted from Fig. 4.13 that when the lag is less than 4 m, North-South pairs are spatially correlated, and North-South average anisotropic sample semivariograms exhibit the expected trend in which semivariance increases with increasing lag; however, when the lag becomes greater than or equal to 4 m, North-South pairs suddenly appear to be spatially uncorrelated. The analysis of the average anisotropic sample semivariograms suggests that variations in the OTWT of reforming tubes separated by a distance greater than or equal to 4 m are spatially uncorrelated so that this information should not be utilized in the model-building process of the correction model for the i th reforming tube. Therefore, the present work only uses information of reforming tubes in \mathbf{S}_i^K and separated by a distance that is strictly less than 4 m to construct the omnidirectional and isotropic average sample semivariograms.

Next, the omnidirectional and anisotropic average sample semivariograms are fitted with linear and exponential functions to generate 4 different theoretical semivariograms, namely, linear omnidirectional, exponential omnidirectional, linear anisotropic and exponential anisotropic theoretical semivariogram models. Then, LOO cross validation is used to identify the most suitable theoretical semivariogram model, which most accurately describes the spatial correlation among neighboring reforming tubes in \mathbf{S}_i^K , to be used in the model-building process of the i th reforming tube. The

linear (Eq. 4.24a) and exponential (Eq. 4.24b) functions [10] are given as follows,

for $h > 0$

$$\tilde{\gamma}_l(h) = \tau_{1,l} + \tau_{2,l}h \quad (4.24a)$$

$$0 \leq \tau_{1,l}, \tau_{2,l} < +\infty$$

$$\tilde{\gamma}_e(h) = \tau_{1,e} + \tau_{2,e} \left[1 - \exp\left(-\frac{h}{\tau_{3,e}}\right) \right] \quad (4.24b)$$

$$0 \leq \tau_{1,e}, \tau_{2,e} < +\infty \quad \& \quad 0 \leq \tau_{3,e} < 4$$

for $h = 0$

$$\tilde{\gamma}_l(h) = \tilde{\gamma}_e(h) = 0 \quad (4.24c)$$

where $\tau_{1,l}$ and $\tau_{2,l}$ are parameters of the linear theoretical semivariogram model, and $\tau_{1,e}$, $\tau_{2,e}$ and $\tau_{3,e}$ are parameters of the exponential theoretical semivariogram model. It is noted that $\tau_{3,e}$ in Eq. 4.24b is related to the range in which variations of the OTWTs are spatially correlated and, therefore, it is reasonable to assume that $\tau_{3,e}$ is less than 4 m. Parameters of theoretical semivariograms are estimated using the method of weighted least squares developed in [10].

Finally, the correction model for the i th reforming tube is formulated as a weighted average OTWT of the neighbors in \mathbf{W}_i^K as follows,

$$\hat{T}_i^{C,n} = \sum_j^{\mathbf{W}_i^K} w_{i,j}^C T_j^n \quad (4.25)$$

where j is an index of a reforming tube in \mathbf{W}_i^K , which is a subset of \mathbf{S}_i^K , and $w_{i,j}^C$ is the correction weighting factor of the j th reforming tube. In this work, \mathbf{W}_i^K is defined to consist of the three nearest northward, three nearest southward, one nearest eastward and one nearest westward neighbors of the i th reforming tube. In the event that the i th reforming tube is missing any of the aforementioned neighbors, \mathbf{W}_i^K is shrunk down accordingly, and the i th OTWT is estimated only using the existing neighbors. For instance, as the 1st reforming tube has neither three nearest northward

neighbors nor one nearest eastward neighbor as shown in Fig. 5.2, the cardinality of \mathbf{W}_1^K is reduced to four, and the 1st OTWT is directly computed as the weighted average OTWT of the three nearest southward and one nearest westward neighbors.

Two different approaches for obtaining $w_{i,j}^C$ associated with elements in \mathbf{W}_i^K are proposed to account for the choice of incorporating directionality into the correction model for the i th reforming tube. Specifically, when an omnidirectional theoretical semivariogram model is used to represent the spatial correlation between reforming tubes in \mathbf{W}_i^K , it is assumed that the i th reforming tube is spatially correlated to all neighbors in \mathbf{W}_i^K , and all $w_{i,j}^C$ in the correction model (Eq. 5.5) are the Kriging weights and can be calculated as follows,

$$\Gamma_i \vec{w}_i^C = \vec{\gamma}_i \quad (4.26a)$$

subject to

$$\Gamma_i \in \mathbb{R}^{N_{i,K}+1 \times N_{i,K}+1} \quad \text{such that,} \quad (4.26b)$$

$$\Gamma_{i,kl} = 0; \quad k = l \text{ where } k, l \in [1, N_{i,K} + 1]$$

$$\Gamma_{i,kl} = \Gamma_{i,lk} = \tilde{\gamma}_i^* (\hat{h}_{kl}) \quad \text{where } k, l \in [1, N_{i,K}]$$

$$\Gamma_{i,(N_{i,K}+1)l} = \Gamma_{i,l(N_{i,K}+1)} \quad \text{where } l \in [1, N_{i,K}]$$

$$\vec{w}_i^C = [w_{i,j}^C, \dots, \lambda_i^C]^T \quad \forall j \in \mathbf{W}_i^K \quad (4.26c)$$

$$\vec{\gamma}_i = [\tilde{\gamma}_i^* (h_{ij}), \dots, 1]^T \quad \forall j \in \mathbf{W}_i^K \quad (4.26d)$$

where Γ_i represents the matrix of semivariances between the neighbors in \mathbf{W}_i^K , $\vec{\gamma}_i$ represents the vector of semivariances between the i th reforming tube and its neighbors in \mathbf{W}_i^K , $\tilde{\gamma}_i^*$ is the best theoretical semivariogram model, which is identified by LOO cross validation as presented at the end of this section, to describe the spatial correlation of reforming tubes in \mathbf{W}_i^K , $N_{i,K}$ is the number of Kriging weights in the correction model for the i th reforming tube, λ_i^C is the Lagrangian multiplier, h_{ij} is the lag between the i th and j th reforming tubes and \hat{h}_{kl} is the lag between the k th and

lth neighbors in \mathbf{W}_i^K . It is noted that the subscripts in \hat{h}_{kl} represent the order in which neighbors are arranged in \mathbf{W}_i^K instead of indices of reforming tubes, and in this study, the neighbors in \mathbf{W}_i^K are arranged in an increasing order of their reforming tube indices. When an anisotropic theoretical semivariogram model is used to represent the spatial correlation between reforming tubes in \mathbf{W}_i^K , it is assumed that the ith reforming tube is spatially correlated to the North-South neighbors but is spatially uncorrelated to the East-West neighbors in \mathbf{W}_i^K . In this scenario, the ith corrected OTWT is defined as an average of two distinct estimates calculated using information of the North-South neighbors and of the East-West neighbors, respectively. It is noted that, as the spatial correlation between the North-South neighbors and the ith reforming tube is captured in the anisotropic theoretical semivariogram model, the estimate calculated using information of the North-South neighbors can be obtained after all $w_{i,j}^C$ associated with the North-South neighbors are calculated as shown in Eq. 4.26. On the other hand, because the ith reforming tube is spatially uncorrelated to the East-West neighbors, the estimate calculated using information of the East-West neighbors is simplified to an average OTWT among the East-West neighbors.

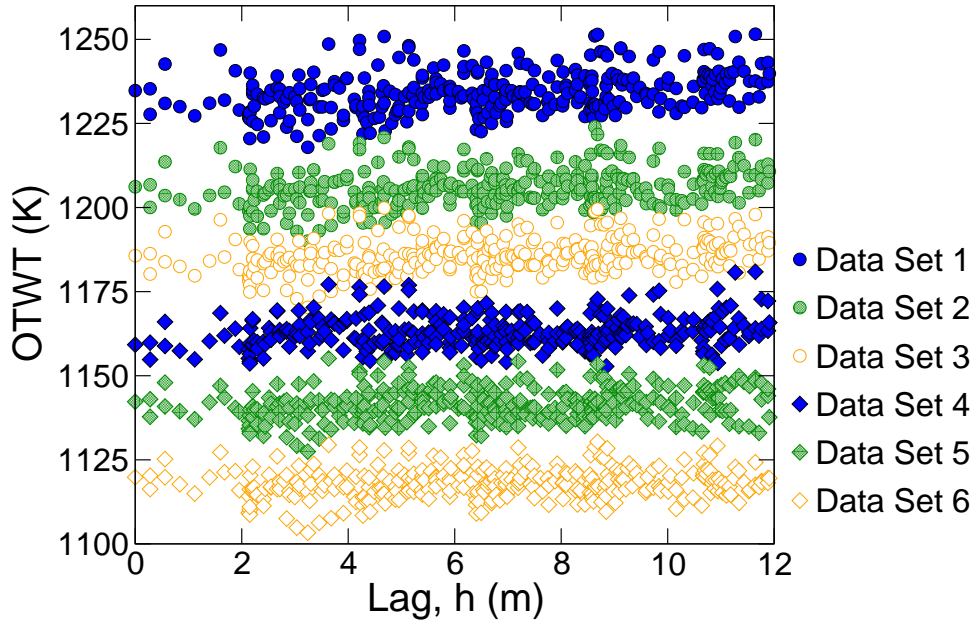


Figure 4.8: The scatter plot of OTWTs of all reforming tubes in six training data sets versus the corresponding distance to the 77th reforming tube, which is referred to as the 77th lag. It is noted that not all reformer CFD data sets in the training data are shown in Fig. 4.8 to avoid cluttering.

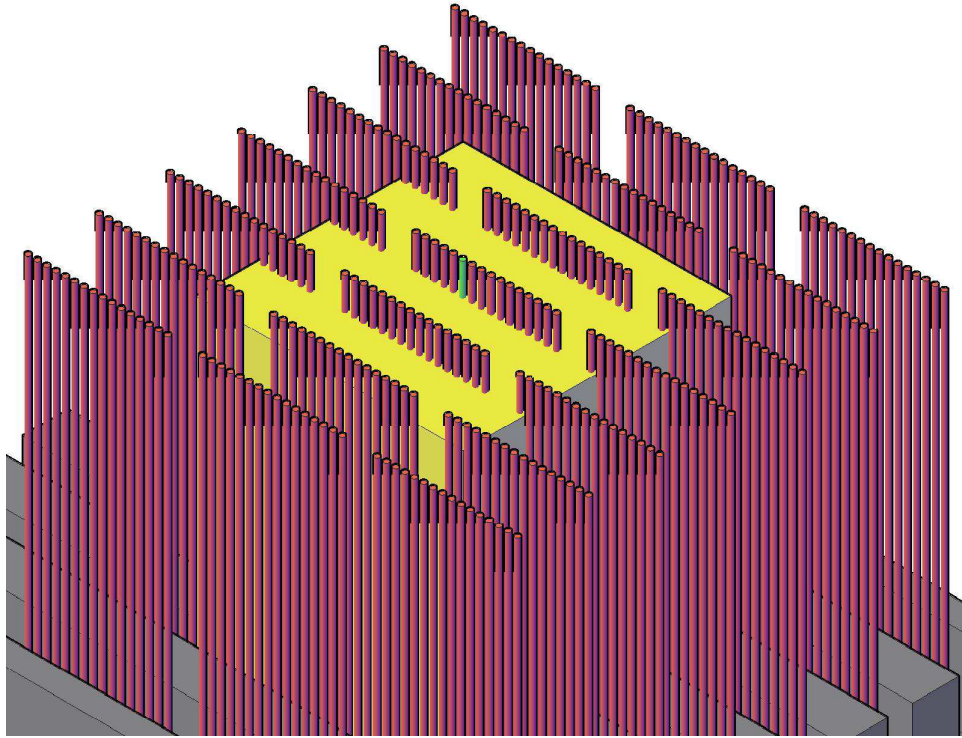


Figure 4.9: The isometric view of the ordinary Kriging neighborhood of the i th reforming tube that is denoted as S_i^K and is defined as an 8 m by 8 m region centered at the i th tube, inside which the underlying process that gives rise to the variations in the OTWT distribution is assumed to be intrinsically stationary.

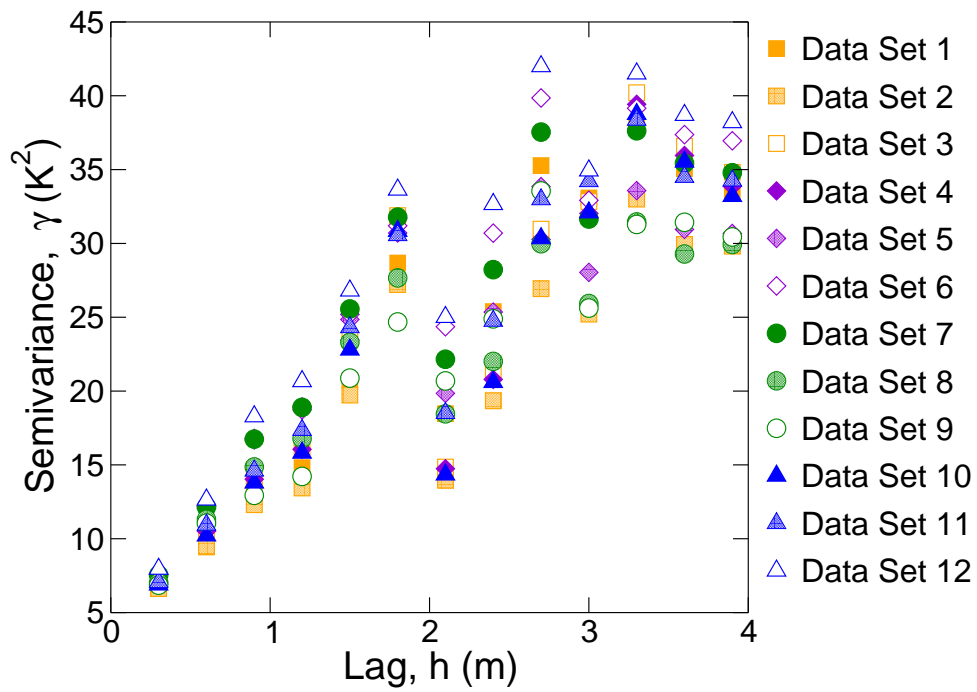


Figure 4.10: Omnidirectional sample semivariograms for S_{77}^K computed by the classical estimator as shown in Eq. 4.22 using the training data. It is noted that not all results generated using reformer CFD data sets in the training data are displayed in Fig. 4.10 to avoid cluttering.

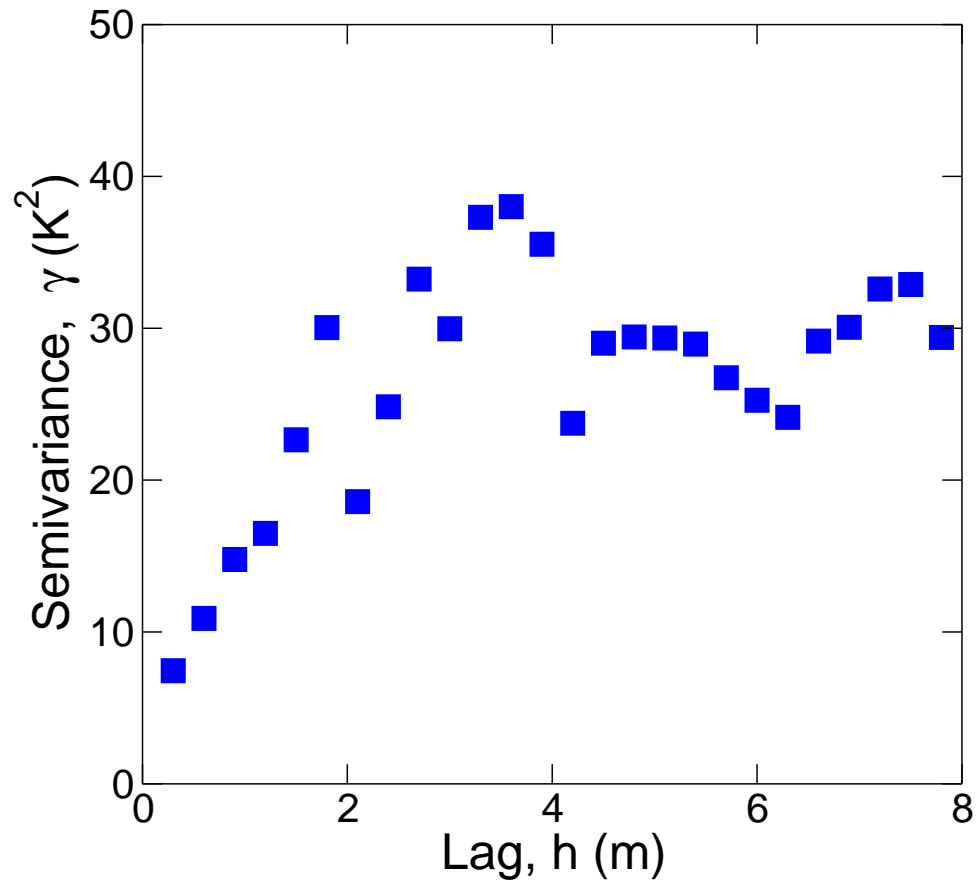


Figure 4.11: Omnidirectional average sample semivariograms for S_{77}^K computed by Eqs. 4.22 and 4.23 using information of all reforming tube pairs in S_{77}^K from the training data.

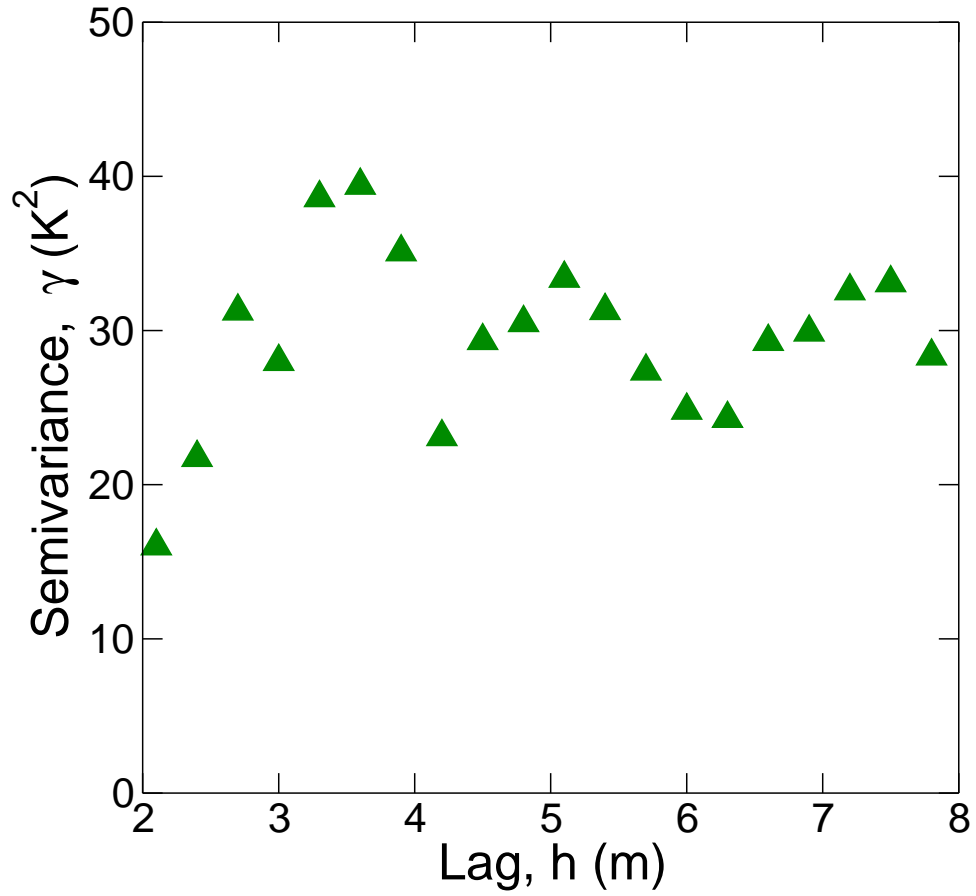


Figure 4.12: East-West anisotropic average sample semivariograms for \mathbf{S}_{77}^K computed by Eqs. 4.22 and 4.23 using information of the East-West pairs in \mathbf{S}_{77}^K from the training data.

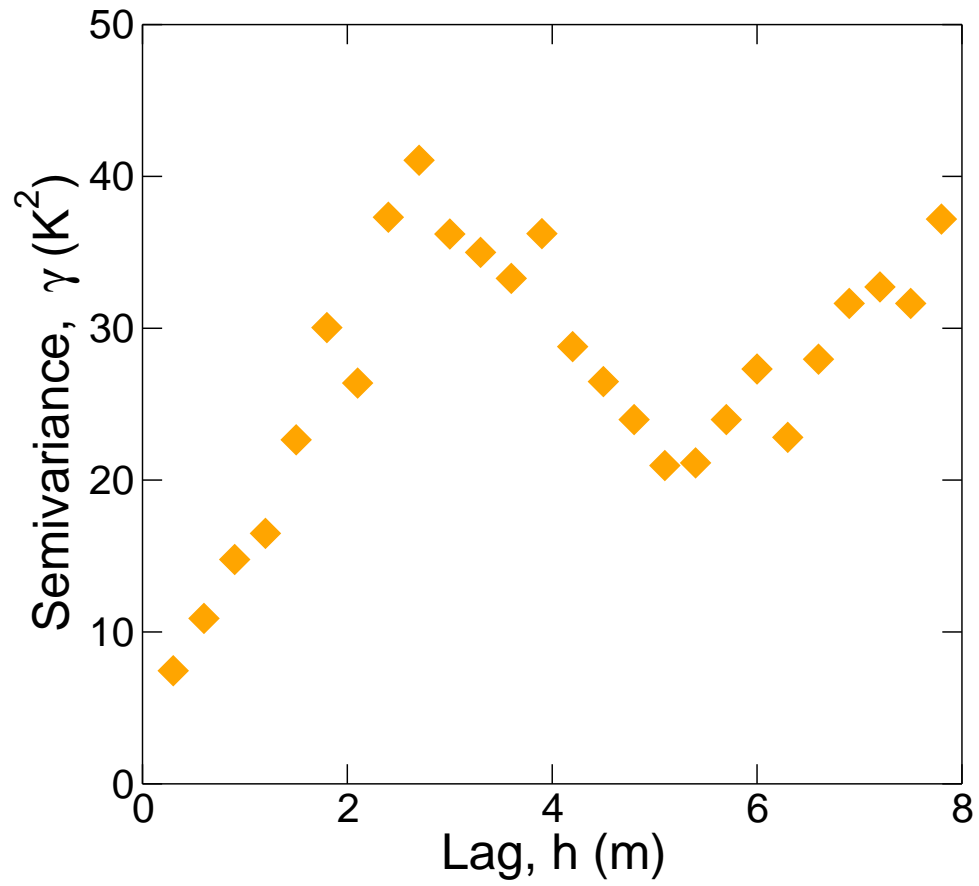


Figure 4.13: North-South anisotropic average sample semivariograms for \mathbf{S}_{77}^K computed by Eqs. 4.22 and 4.23 using information of the North-South pairs in \mathbf{S}_{77}^K from the training data.

4.6 Combined model uniting prediction and correction models

Upon the simultaneous creation of unified prediction models as discussed in Section 4.4 and correction models as discussed in Section 4.5 for 336 reforming tubes from the training data, the data-driven model for the OTWT distribution, which is a function of the FSF distribution and total FSF flow rate and is also able to account for interactions among neighboring reforming tubes, can be assembled. Initially, the prediction models for 336 reforming tubes are pooled to create the prediction model for the OTWT distribution, by which the predicted OTWT distribution can be estimated based on a given FSF distribution and total FSF flow rate, as follows,

$$\begin{pmatrix} \widehat{T}_1^{P,n} \\ \widehat{T}_2^{P,n} \\ \vdots \\ \widehat{T}_{336}^{P,n} \end{pmatrix} = \begin{pmatrix} \sum_{k=1}^{K_1} w_{1,k}^P \widetilde{T}_{1,k}^{P,n} \\ \sum_{k=1}^{K_2} w_{2,k}^P \widetilde{T}_{2,k}^{P,n} \\ \vdots \\ \sum_{k=1}^{K_{336}} w_{336,k}^P \widetilde{T}_{336,k}^{P,n} \end{pmatrix}. \quad (4.27)$$

Then, the correction models for 336 reforming tubes are also pooled to create the correction model for the OTWT distribution, by which the corrected OTWT distribution can be estimated based on the predicted OTWT distribution, as follows,

$$\begin{pmatrix} \widehat{T}_1^{C,n} \\ \widehat{T}_2^{C,n} \\ \vdots \\ \widehat{T}_{336}^{C,n} \end{pmatrix} = \begin{pmatrix} \sum_j^K w_{1,j}^C \widehat{T}_j^{P,n} \\ \sum_j^K w_{2,j}^C \widehat{T}_j^{P,n} \\ \vdots \\ \sum_j^K w_{336,j}^C \widehat{T}_j^{P,n} \end{pmatrix}. \quad (4.28)$$

Next, the data-driven model for the OTWT distribution is formulated as a weighted average of the prediction and correction models for the OTWT distribution as follows,

$$\begin{pmatrix} \widehat{T}_1^n \\ \widehat{T}_2^n \\ \vdots \\ \widehat{T}_{336}^n \end{pmatrix} = w^P \begin{pmatrix} \widehat{T}_1^{P,n} \\ \widehat{T}_2^{P,n} \\ \vdots \\ \widehat{T}_{336}^{P,n} \end{pmatrix} + (1 - w^P) \begin{pmatrix} \widehat{T}_1^{C,n} \\ \widehat{T}_2^{C,n} \\ \vdots \\ \widehat{T}_{336}^{C,n} \end{pmatrix} \quad (4.29)$$

where the optimal value of w^P denoted by \widehat{w}^P is selected among the proposed values, $\mathbf{S}_w = \{0.0, 0.1, \dots, 1.0\}$ by LOO cross validation, which can be carried out in the same manner as discussed in Section 4.4.3. Specifically, the value of w^P in \mathbf{S}_w that yields the least prediction error for out-of-sample predictions is considered to be the optimal w^P .

4.7 Results

The statistical-based model identification approach developed in this work is structured to be entirely parallelized; specifically, the prediction and correction models of the i th reforming tube can be derived simultaneously from the training data and independently of the model-building process of other reforming tubes. This feature allows the optimal LASSO parameter and theoretical semi-variogram model for the i th reforming tube and the optimal weighting factor of the BMA predicted estimates to be determined using leave-out-one cross validation, which is expected to improve the prediction accuracy of the OTWT distribution model for out-of-sample predictions. We note that the model-building process for the OTWT of each reforming tube is identically, independently and simultaneously executed on the shared computing cluster at UCLA, and therefore, the effectiveness of the proposed model identification scheme can be demonstrated using results generated from the model-building process of any reforming tube. In the remainder of this section, the 77th reforming tube is chosen as a representative example because the number of sub-prediction models with high goodness of fit (i.e., 4) and the number of predictors (i.e., 9) for the 77th OTWT make it possible to illustrate the effectiveness of the proposed approach to identify the important burners and to allow the prediction model for the 77th OTWT to account for model uncertainty while forecasting in a concise manner.

The results from LOO cross validation to select the optimal value of λ_{77} (denoted as $\hat{\lambda}_{77}$) from \mathbf{S}_λ are summarized in Fig. 4.14. Specifically, the value of λ_{77} controls the model complexity and goodness of fit as discussed in Section 4.4.3 when the sparse nonlinear regression is formulated as an L1 penalized optimization problem, which is illustrated as shown in Fig. 4.14. It is recognized from Fig. 4.14 that the mean square fitting error increases with increasing values of λ_{77} , and specifically, the fitting error is the largest at the highest values of λ_{77} considered in this work as low-complexity models are favored, while the fitting error is the smallest at the lowest value of λ_{77} as models with high goodness of fit are favored. In addition, Fig. 4.14 reveals that the fitting error is over-optimistic because it is lower than the mean squared prediction error for all values of

λ_{77} , and the fitting error should not be used as the metric for selecting $\hat{\lambda}_{77}$ from \mathbf{S}_λ because the prediction error is not necessarily minimized at the value of λ_{77} which minimizes the fitting error. Specifically, Fig. 4.14 indicates that at $\lambda_{77}=0.4$, the prediction error is minimized, which suggests that the optimal value of λ_{77} is 0.4, i.e.,

$$\hat{\lambda}_{77} = 0.4. \quad (4.30)$$

Thereafter, $\hat{\lambda}_{77}$ is used as the LASSO parameter of the sparse nonlinear regression (Eq. 4.20) in the prediction step algorithm, by which the prediction model for the dependence of the 77th OTWT on the FSF distribution and total FSF flow rate is derived from the complete training data. It is found that this procedure generates four nested sub-prediction models of the 77th reforming tube, which together represent the prediction model for the 77th reforming tube. The four sub-prediction models of the 77th reforming tube, each of which can be used to estimate the 77th OTWT based on a given FSF distribution and total FSF flow rate, are as follows,

$$\tilde{T}_{77,1}^{P,n} = 134.70 \sqrt[5]{F_{18}^n} + 225.49 \sqrt[5]{F_{19}^n} + 141.73 \sqrt[5]{F_{30}^n} + 234.28 \sqrt[5]{F_{31}^n} \quad (4.31a)$$

$$+ 2.54 \exp(F_{18}^n) + 3.17 \exp(F_{19}^n) + 14.45 \exp(F_{32}^n) + 348.15$$

$$\tilde{T}_{77,2}^{P,n} = 51.80 \sqrt[5]{F_{17}^n} + 131.61 \sqrt[5]{F_{18}^n} + 177.63 \sqrt[5]{F_{19}^n} + 134.87 \sqrt[5]{F_{30}^n} \quad (4.31b)$$

$$+ 179.40 \sqrt[5]{F_{31}^n} + 66.49 \sqrt[5]{F_{32}^n} + 10.94 \exp(F_{17}^n) + 1.17 \exp(F_{18}^n)$$

$$+ 0.64 \exp(F_{19}^n) + 6.22 \exp(F_{32}^n) + 348.15$$

$$\tilde{T}_{77,3}^{P,n} = 61.26 \sqrt[5]{F_{17}^n} + 125.22 \sqrt[5]{F_{18}^n} + 166.56 \sqrt[5]{F_{19}^n} + 125.22 \sqrt[5]{F_{30}^n} \quad (4.31c)$$

$$+ 166.56 \sqrt[5]{F_{31}^n} + 60.01 \sqrt[5]{F_{32}^n} + 37.83 \sqrt[5]{F_{43}^n} + 5.40 \exp(F_{17}^n)$$

$$+ 6.39 \exp(F_{32}^n) + 6.63 \exp(F_{43}^n) + 348.15$$

$$\tilde{T}_{77,4}^{P,n} = 61.48 \sqrt[5]{F_{17}^n} + 120.02 \sqrt[5]{F_{18}^n} + 175.72 \sqrt[5]{F_{19}^n} + 120.02 \sqrt[5]{F_{30}^n} \quad (4.31d)$$

$$+ 175.72 \sqrt[5]{F_{31}^n} + 69.04 \sqrt[5]{F_{32}^n} + 21.96 \sqrt[5]{F_{43}^n} + 10.00 \exp(F_{15}^n)$$

$$+ 8.43 \exp(F_{43}^n) + 348.15.$$

At glance, the four sub-prediction models successfully account for the reformer geometry (i.e., the reforming tube and burner arrangement) as only the parameters associated with burners that are situated nearby the *77th* reforming tube are nonzero and also obey the inverse square law for thermal radiation as the parameters associated with burners that are closer to the *77th* reforming tube are larger. The distance between each predictor of the *77th* OTWT and the *77th* reforming tube is detailed in Table 4.1. On closer inspection, it is recognized that out of the eight transformation functions (Eq. 5.2) proposed in the development of the sparse nonlinear regression, only the parameters associated with the quint root and exponential functions are nonzero, and the parameters associated with the quint root function are noticeably larger than those associated with the exponential function (Eq. 4.31). We speculate that the use of the exponential function in the sub-prediction models by the sparse nonlinear regression is because the training data might have suggested that the predictors located further away from the *77th* reforming tube have higher impacts on the *77th*

Table 4.1: Distance from burners in \mathbf{S}_{77R} to the 77th reforming tube

Burner ID	Distance (m)
19th	1.08
31st	1.08
18th	1.44
30th	1.44
32nd	2.32
17th	2.36
43rd	3.21
15th	5.24

OTWT than we previously expect (Eq. 4.21b). This analysis reveals the underlying function that governs the relationship between the 77th OTWT and FSF flow rates of its predictors. Next, the prediction model is created as the weighted average of the four sub-prediction models of the 77th reforming tube using Bayesian model averaging as follows,

$$\hat{T}_{77}^{P,n} = 0.01\tilde{T}_{77,1}^{P,n} + 0.23\tilde{T}_{77,2}^{P,n} + 0.29\tilde{T}_{77,3}^{P,n} + 0.47\tilde{T}_{77,4}^{P,n} \quad (4.32)$$

where the weighting factor associated with each sub-prediction model indicates the level of supporting evidence given by the training data. Then, the training data are used to evaluate the resubstitution accuracy of the prediction model for the 77th reforming tube. The comparison between reformer data from the training data and BMA predicted estimates generated from the prediction model (Eq. 4.32) is shown in Figs. 4.15 and 4.17, and the corresponding residual plot is shown in Fig. 4.16. Specifically, Fig. 4.16 shows that the maximum and average residuals are 2.54 K and -0.01 K, respectively, and Fig. 4.17 shows that all plotted points are close to the diagonal line with the slope of 1 and y-intercept of zero. Therefore, Figs. 4.15, 4.16 and 4.17 show that the prediction model for the 77th reforming tube has a high goodness of fit and provides an excellent description for the dependence of the 77th OTWT on the FSF distribution and total FSF flow rate.

Next, the results from LOO cross validation, which allow the best theoretical semivariogram

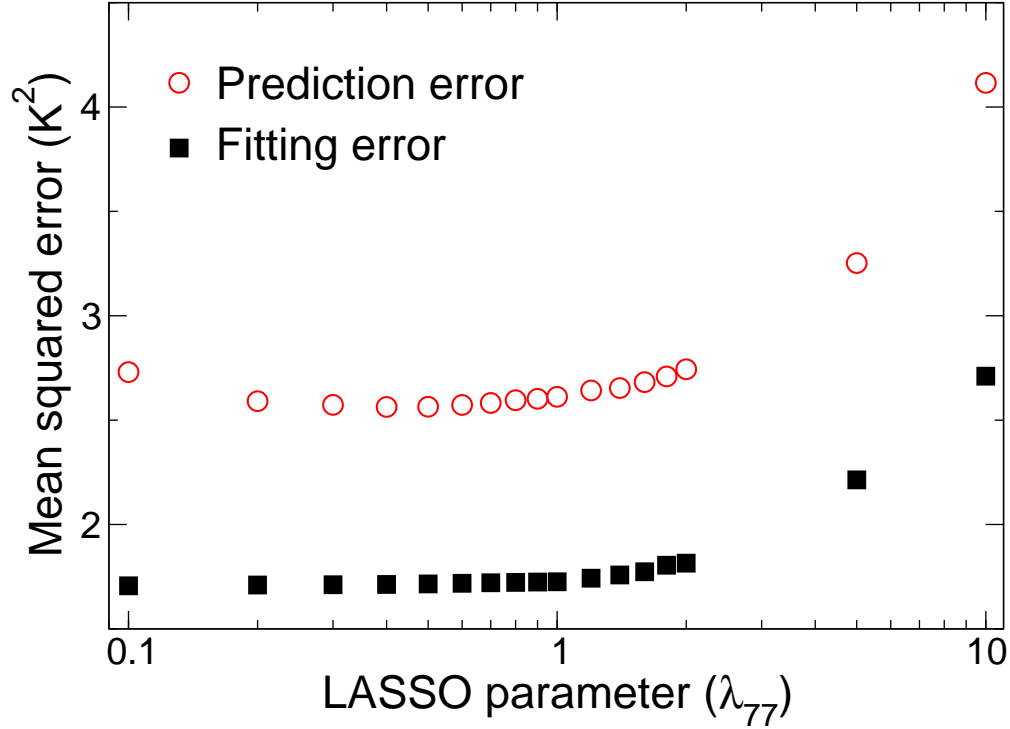


Figure 4.14: Summary of LOO cross validation for selecting the optimal value of λ_{77} from \mathbf{S}_λ in which the mean squared prediction errors are denoted by the empty red circles and the mean squared fitting errors are denoted by the filled black squares.

model (denoted as $\hat{\gamma}_{77}^*$) to be selected among the linear omnidirectional, linear anisotropic, exponential omnidirectional, and exponential anisotropic theoretical semivariogram models so that the spatial correlation among neighboring reforming tubes in \mathbf{S}_{77}^K can be described with adequate accuracy, are summarized in Fig. 4.18. It is noted from Fig. 4.18 that the correction models for the 77th reforming tube created in LOO cross validation using the linear omnidirectional theoretical semivariogram model yield the smallest mean squared prediction error for out-of-sample predictions, and therefore, $\hat{\gamma}_{77}^*$ is assumed to be the linear omnidirectional theoretical semivariogram model. Thereafter, $\hat{\gamma}_{77}^*$ is used as the predetermined theoretical semivariogram model in the correction step algorithm, by which the correction model for the 77th reforming tube is derived from the complete training data as shown in Table 4.2. Table 4.2 shows the expected trend in spatial modeling, i.e., as the distance between a neighbor and 77th reforming tube increases, their OTWT values becomes less correlated. Then, the training data are used to evaluate the resubstitution accuracy of

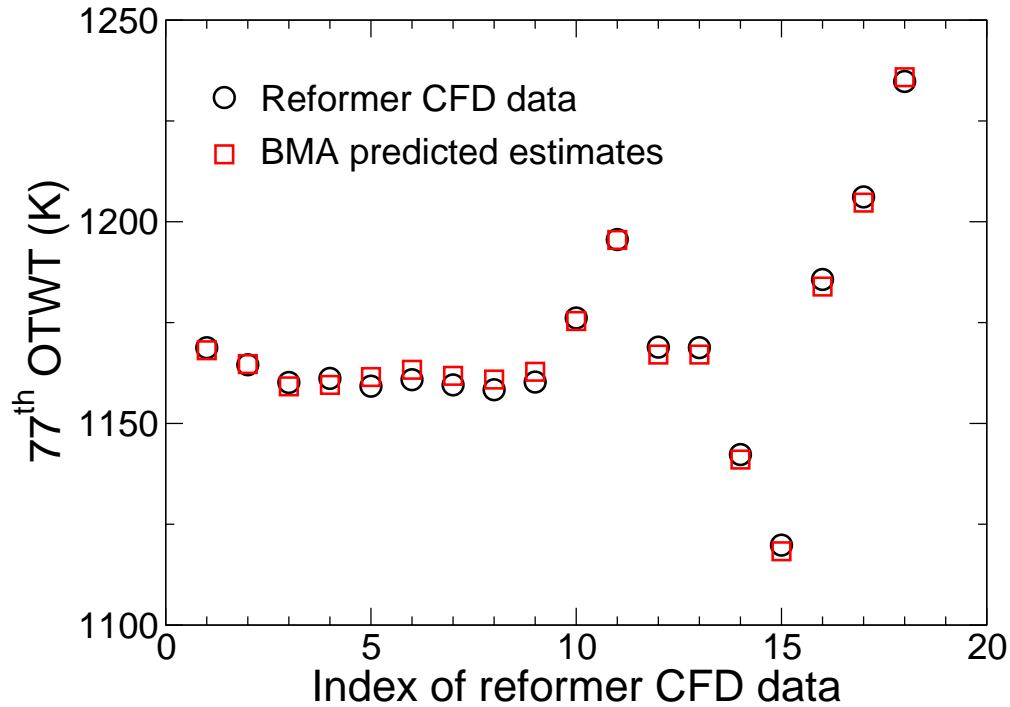


Figure 4.15: Comparison of the 77th OTWT between reformer CFD data from the training data and BMA predicted estimates generated from the prediction model for the 77th reforming tube.

the correction model for the 77th reforming tube. The comparison between reformer data from the training data and corrected estimates generated from the corrected model (Table 4.2) is shown in Figs. 4.19 and 4.21; the corresponding residual plot is shown in Fig. 4.20. Specifically, Fig. 4.20 shows that the maximum and average residuals are 1.63 K and -0.74 K, respectively, and Fig. 4.21 shows that all plotted points are close to the diagonal line with the slope of 1 and y-intercept of zero. Therefore, Figs. 4.19, 4.20 and 4.21 show that the correction model for the 77th reforming tube has a high goodness of fit and provides an excellent description of the 77th OTWT by using information of the neighbors.

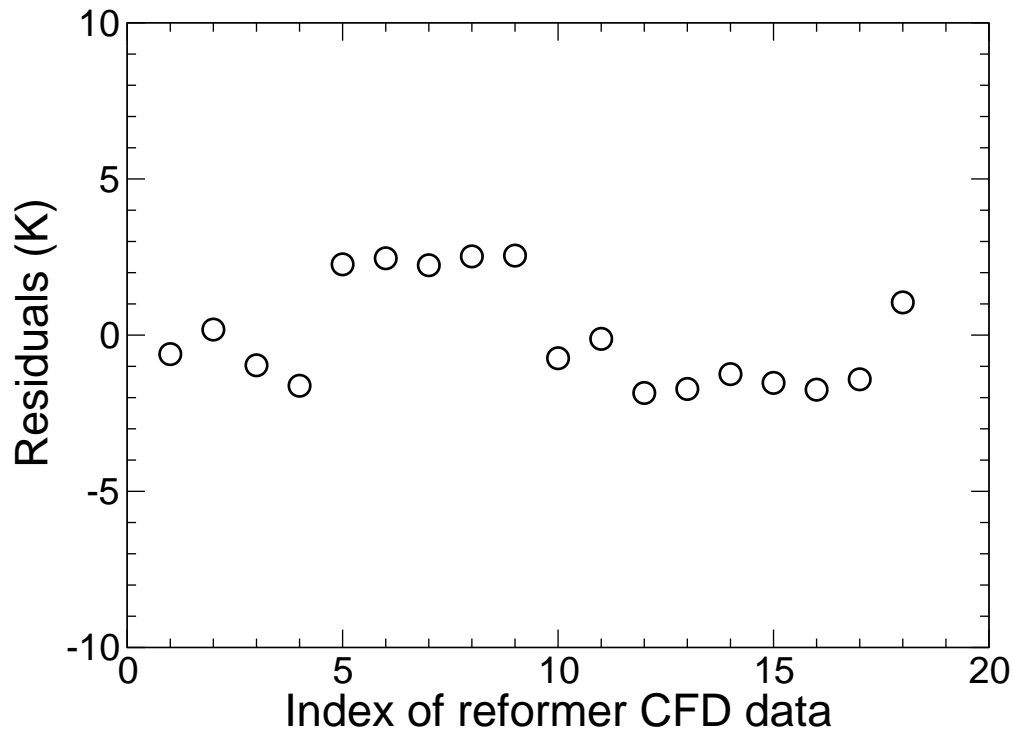


Figure 4.16: Residuals between reformer CFD data from the training data and BMA predicted estimates generated from the prediction model for the 77th reforming tube.

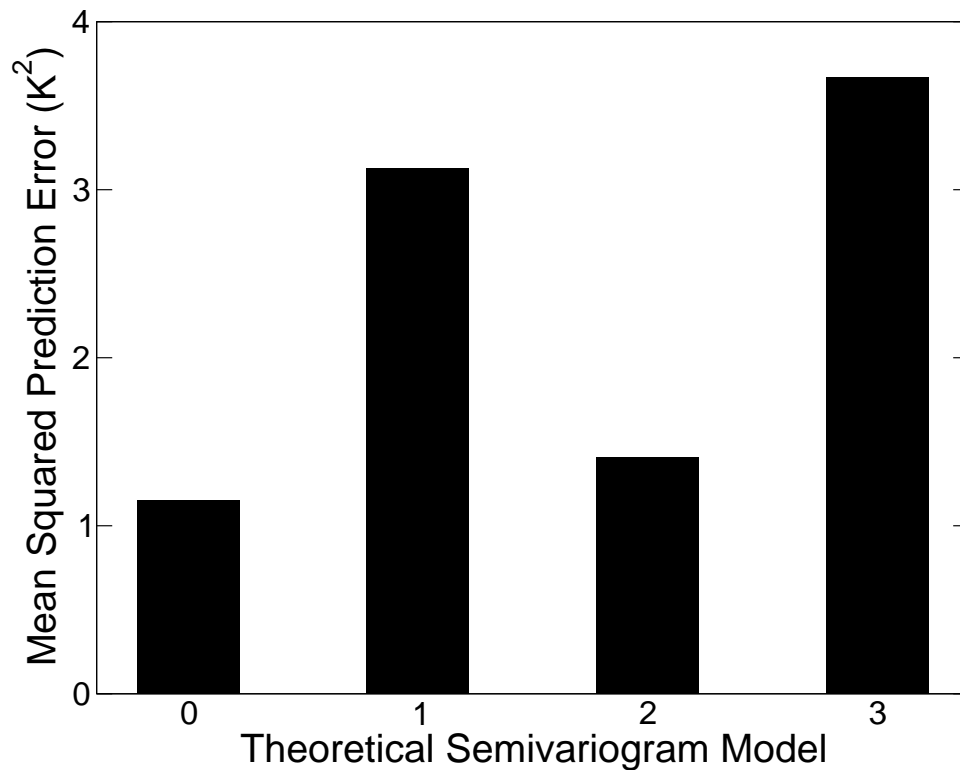


Figure 4.18: A plot of the mean squared prediction error associated with each of the four theoretical semivariogram models considered in the LOO cross validation to select the best theoretical semivariogram to model the spatial correlation among reforming tubes in the S_{77}^K . The values on the horizontal axis, i.e., 0, 1, 2, and 3, correspond to the linear omnidirectional, linear anisotropic,

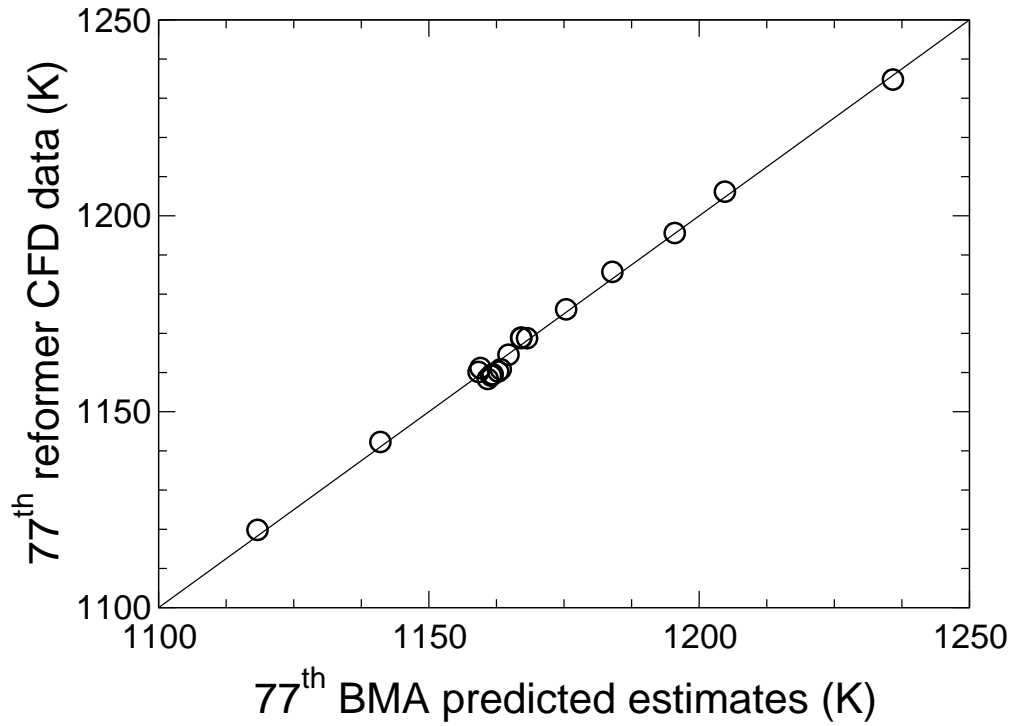


Figure 4.17: Reformer CFD data from the training data versus BMA predicted estimates generated from the prediction model for the 77th reforming tube scatter plots.

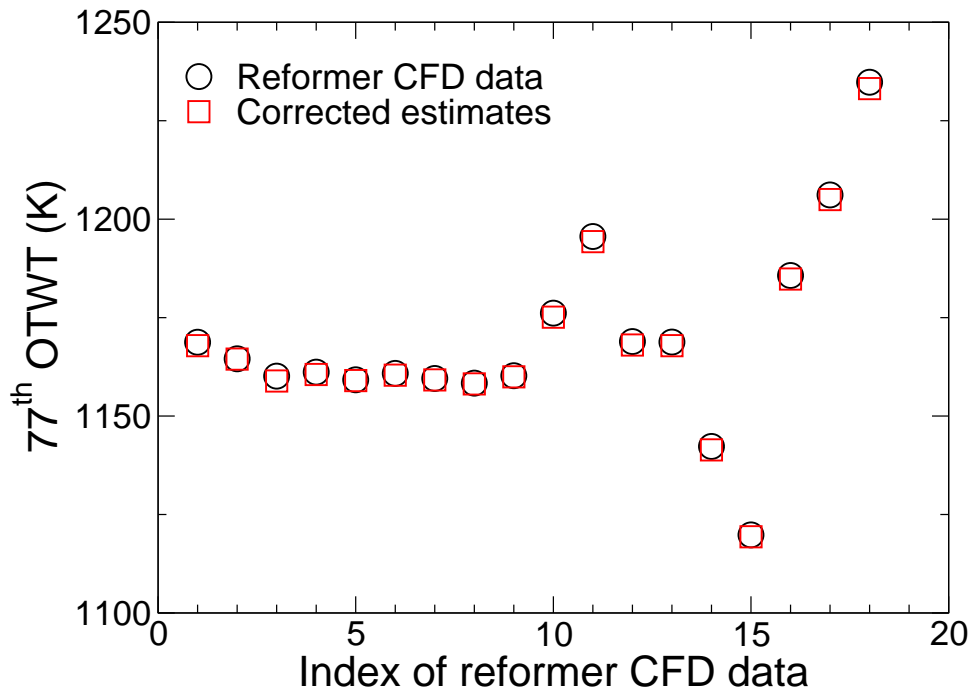


Figure 4.19: Comparison of the 77th OTWT between reformer CFD data from the training data and corrected estimates generated from the correction model for the 77th reforming tube.

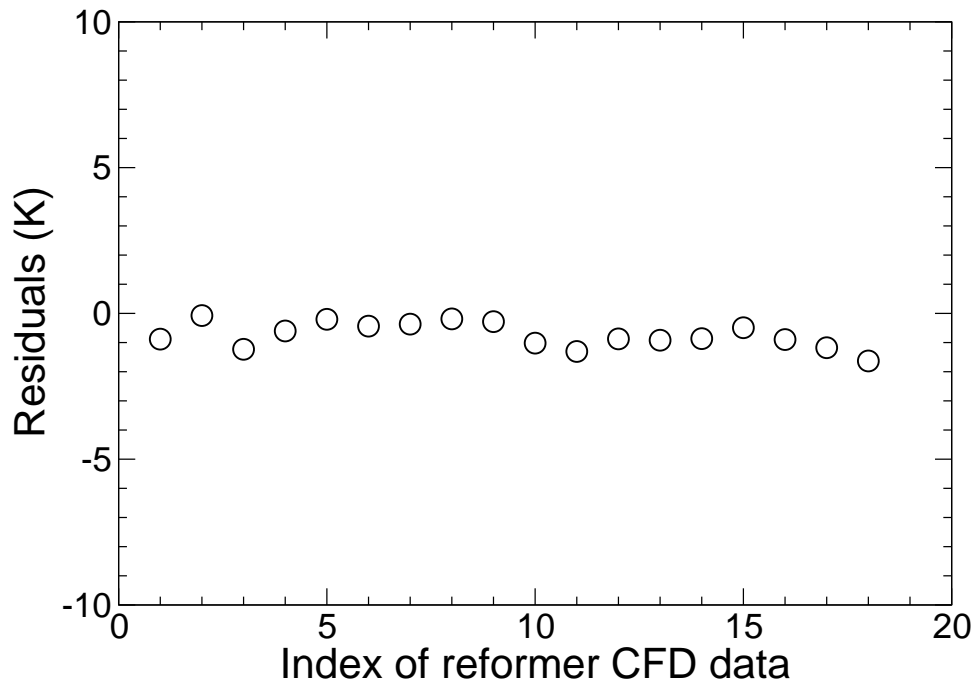


Figure 4.20: Residuals between reformer CFD data from the training data and corrected estimates generated from the correction model of the 77th reforming tube.

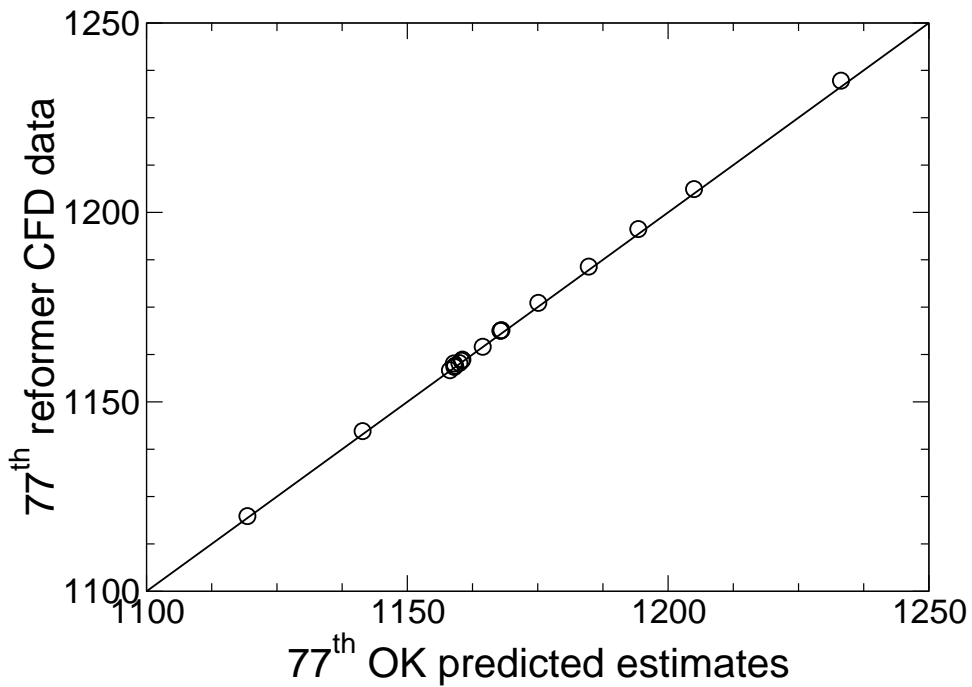


Figure 4.21: Reformer CFD data from the training data versus corrected estimates generated from the correction model for the 77th reforming tube scatter plots.

Table 4.2: Lags, Kriging weights, and directionality of reforming tubes used in the weighted average correction step in calculating the 77th OTWT.

Reforming tube ID	Lag (m)	Kriging weight	Directionality
29	2.13	0.03	Eastward
74	0.84	0.06	Northward
75	0.56	0.13	Northward
76	0.28	0.29	Northward
78	0.28	0.30	Southward
79	0.56	0.15	Southward
80	1.60	0.03	Southward
125	2.13	0.03	Westward

The results from LOO cross validation to select the optimal weighting factor for the BMA predicted estimates from \mathbf{S}_w are summarized in Fig. 4.22. It is noted from Fig. 4.22 that the fitting error decreases with increasing values of w^P , and specifically, the fitting error is at its smallest when the value of w^P becomes 1, which implies that estimates of the OTWT distribution are based entirely on the prediction model for the OTWT distribution, while the fitting error is the largest when the value of w^P becomes 0, which implies that estimates of the OTWT distribution are based entirely on the correction model for the OTWT distribution. This observation is expected because the correction model for the OTWT distribution is derived from the training data, which allows it to have realistic knowledge about spatial correlation among neighboring reforming tubes so that the overall predictability performance of the data-driven model for the OTWT distribution for out-of-sample predictions can be improved. Fig. 4.22 demonstrates the necessity of using the correction model for the OTWT distribution, and specifically, the prediction error is minimized at $w^P=0.9$, which suggests that the correction model for the OTWT distribution improves the out-of-sample predictive performance of the data-driven model for the OTWT distribution. Subsequently,

the prediction models and correction models for 336 reforming tubes derived from the complete training data and the optimal value of w^P are used to formulate the data-driven model for the OTWT distribution. We note that the model for the OTWT distribution depicts a multiple-input multiple-output (MIMO) system and is composed of 336 algebraic equations, which can be solved instantaneously on a standard compute node on a shared computing cluster at UCLA (i.e., the Hoffman2 cluster). Then, the training data are used to evaluate the resubstitution accuracy of the data-driven model for the OTWT distribution. The comparison between reformer data from the training data and estimates generated from the data-driven model for the OTWT distribution is shown in Figs. 4.23–4.24 and Table 4.3. Fig. 4.23 provides a descriptive comparison of the maximum, average and minimum OTWT in each pair of data sets between reformer CFD data in the training data and estimates generated from the data-driven model for the OTWT distribution, Fig. 4.24 provides a visual comparison of the OTWT distribution contour map between the 7th data set in the training data and its corresponding estimate generated from the data-driven model for the OTWT distribution, and Table 4.3 provides an analysis of the deviations between reformer CFD data in the training data and estimates generated from the data-driven model for the OTWT distribution. It is noted that the contour maps shown in Fig. 4.24 created from the 7th data set in the training data and its corresponding estimate generated from the data-driven model for the OTWT distribution are nearly identical. Specifically, the maximum, minimum and average OTWT of the estimated OTWT distribution are adequately close to those in the reformer CFD data as shown in Fig. 4.23, and the maximum and average deviations between the pair as shown in Table 4.3 are 5.6 K and 1.4 K, respectively, with the standard deviation of 1.1 K which is approximately 0.1% of the average OTWT in this reformer data. This evidence indicates that the 7th OTWT distribution generated by the data-driven model is an accurate representation of the corresponding reformer CFD data. In addition, similar conclusions can be drawn from Fig. 4.23 and Table 4.3 for other data sets in the training data. Therefore, it can be concluded that the data-driven model for the OTWT distribution has a high goodness of fit and provides an excellent description for the dependence of the OTWT distribution on the FSF distribution, total FSF flow rate and interactions

among neighboring reforming tubes.

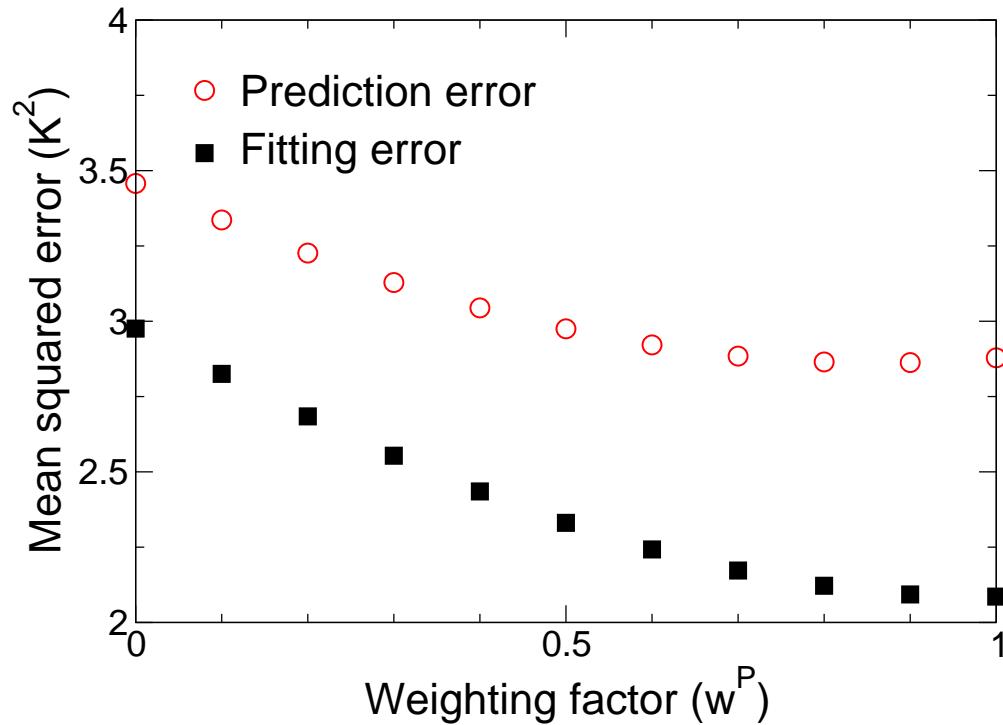


Figure 4.22: Summary of LOO cross validation for selecting the optimal value of w^P from S_w in which the mean squared prediction errors are denoted by the empty red circles and the mean squared fitting errors are denoted by the filled black squares.

Finally, the unbiased testing data are used to evaluate the out-of-sample predictive performance of the data-driven model for the OTWT distribution generated from the proposed integrated model identification scheme. The comparison between reformer data from the testing data and estimates generated from the data-driven model for the OTWT distribution is shown in Fig. 4.25 and Table 4.4. Fig. 4.25 provides a descriptive comparison of the maximum, average and minimum OTWTs in each pair of data sets between reformer CFD data in the testing data and estimates generated from the data-driven model for the OTWT distribution, and Table 4.4 provides an analysis of the deviations between reformer CFD data in the testing data and estimates generated from the data-driven model for the OTWT distribution. Specifically, the maximum, minimum and average OTWT of the estimated OTWT distributions are consistent with those in the reformer CFD data as shown in Fig. 4.25 and the maximum, average and standard deviation of the differences between

Table 4.3: Analysis of the deviations between reformer CFD data in the training data and estimates generated from the data-driven model for the OTWT distribution.

Index of data set	$(\Delta T)_{max}$ K	$(\Delta T)_{ave}$ K	$\sigma_{\Delta T}$ K
1	8.9	2.1	2.5
2	8.1	1.8	1.9
3	18.5	2.2	7.2
4	7.3	1.5	1.9
5	6.7	1.1	1.1
6	6.9	1.1	1.1
7	5.6	1.4	1.1
8	8.1	1.6	2.2
9	7.3	0.9	0.9
10	7.3	1.1	1.0
11	7.5	2.0	2.7
12	7.2	1.3	2.0
13	8.5	1.9	1.6
14	7.7	1.4	1.1
15	2.6	0.7	0.3
16	12.7	2.2	6.1
17	7.2	1.3	1.2
18	8.2	1.0	1.6

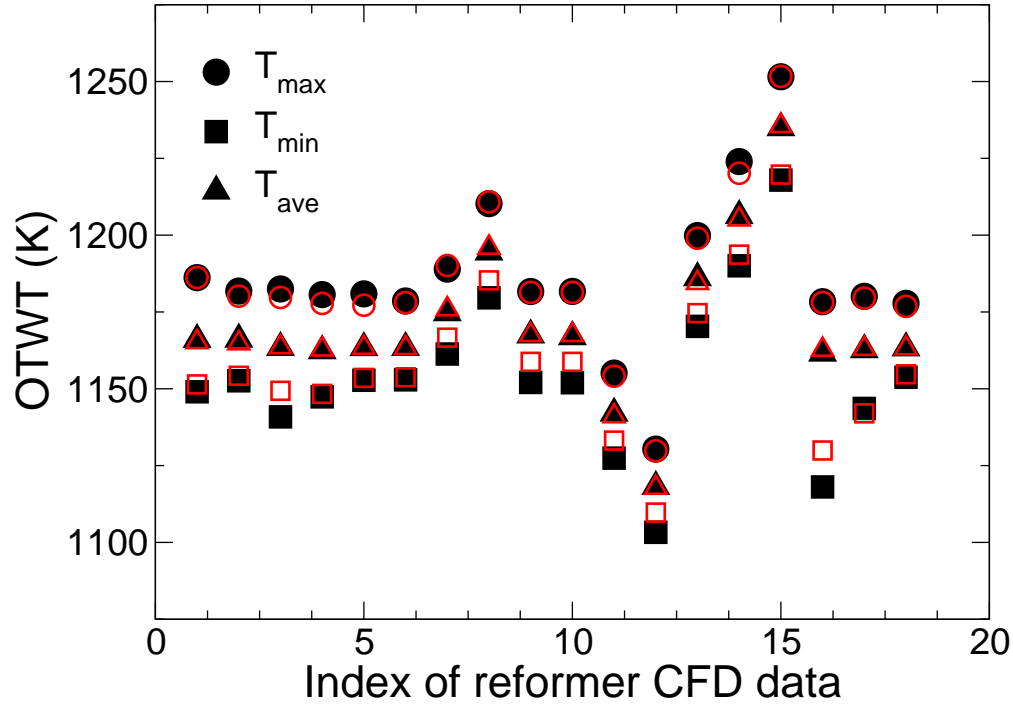


Figure 4.23: Comparison of the maximum (T_{max}), average (T_{ave}) and minimum (T_{min}) OTWTs in each pair of data sets between reformer CFD data in the training data, which are represented by the filled black symbols, and estimates generated from the data-driven model for the OTWT distribution, which are represented by the empty red symbols.

the pairs as shown in Table 4.3 are nearly negligible compared to the corresponding average OTWT in each data set. It is noted that the maximum, average and standard deviation of the differences in the OTWT distributions between the reformer CFD data and estimates generated from the data-driven model for the OTWT distribution in Table 4.3 and Table 4.4 are similar. Therefore, it can be concluded that the data-driven model for the OTWT distribution also has a high out-of-sample prediction performance and provides an excellent description for the dependence of the OTWT distribution on the FSF distribution, total FSF flow rate and interactions among neighboring reforming tubes.

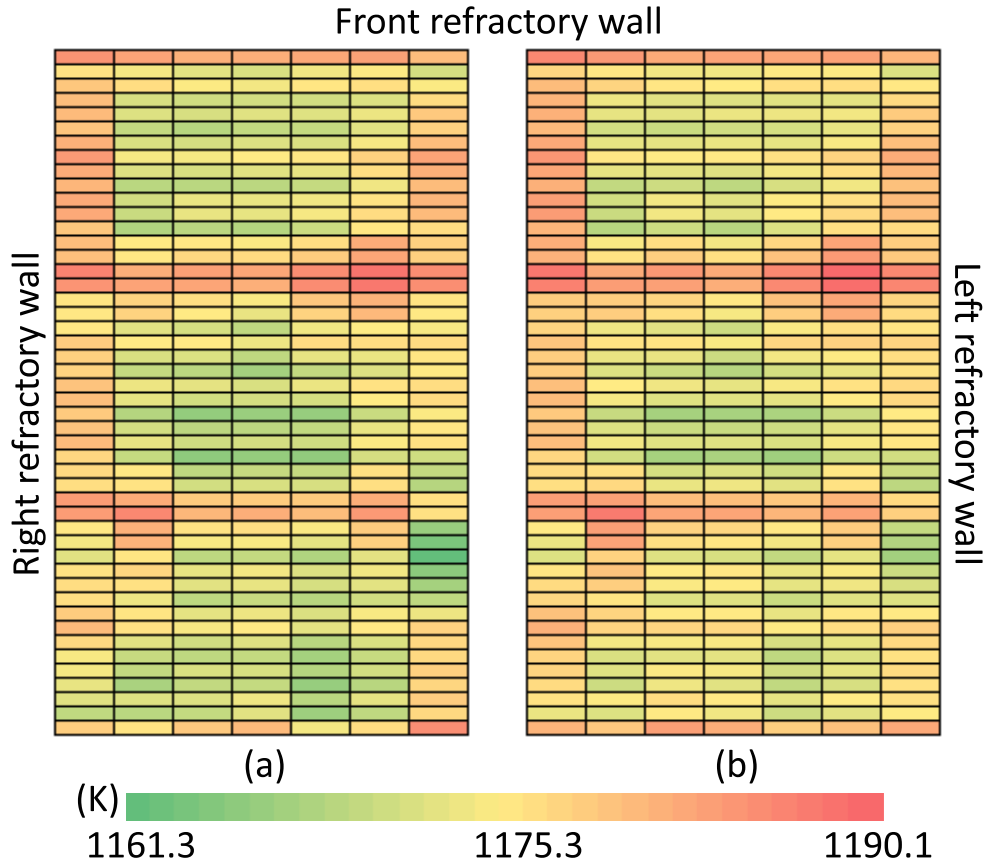


Figure 4.24: Comparison of the OTWT distributions between the 7th data set in the training data (a) and its corresponding estimate generated from the data-driven model for the OTWT distribution (b). In Fig. 4.24, the layout of 336 reforming tubes in the reformer is represented by a table consisting of 336 rectangular cells, in which each cell corresponds to a unique reforming tube in the reformer, i.e., a cell at the bottom right corner of the table represents the 48th reforming tube in the reformer as shown in Fig. 5.2.

Table 4.4: Analysis of the deviations between reformer CFD data in the testing data and estimates generated from the data-driven model for the OTWT distribution.

Index of data set	$(\Delta T)_{max}$ K	$(\Delta T)_{ave}$ K	$\sigma_{\Delta T}$ K
19	8.2	1.6	2.3
20	5.7	0.7	0.6
21	4.3	1.4	1.0

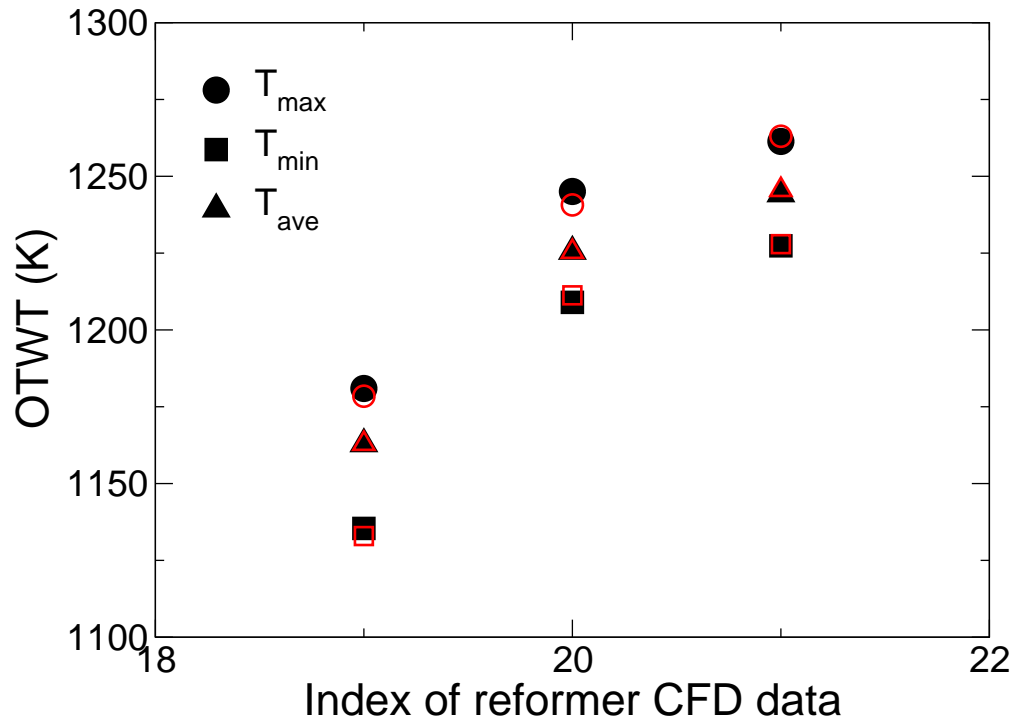


Figure 4.25: Comparison of the maximum (T_{max}), average (T_{ave}) and minimum (T_{min}) OTWTs in each pair of data sets between reformer CFD data in the testing data, which are represented by the filled black symbols, and estimates generated from the data-driven model for the OTWT distribution, which are represented by the empty red symbols.

4.8 Conclusion

The present work developed an integrated model identification scheme that was able to derive a high-fidelity model for the dependence of the OTWT distribution on the FSF distribution, total FSF flow rate and interactions among neighboring reforming tubes from the reformer data. To this end, a high-fidelity reformer CFD model that had been developed and rigorously validated by typical plant data from the SMR literature and actual plant data from our third-party collaborator in our previous work was utilized to facilitate the generation of the reformer database, which was split into the training and testing data. Then, we used Bayesian variable selection, Bayesian model averaging, the BIC approximation, sparse nonlinear regression and theories of thermal radiation to develop the prediction step algorithm in the integrated model identification, from which the prediction model for the OTWT distribution that estimated a predicted OTWT distribution based on a FSF distribution and total FSF flow rate was generated using the training data. Next, we used ordinary Kriging to develop the correction step algorithm in the integrated model identification, from which the correction model for the OTWT distribution that estimated a corrected OTWT distribution based on a predicted OTWT distribution was derived using the training data. Thereafter, we created the data-driven model for the OTWT distribution as a weighted average of the prediction and correction models previously derived from data.

One of our primary interests regarding this work is integrating it in the development of an on-line robust furnace balancing optimizer, which searches for the optimized valve distribution to deliver an optimized FSF distribution and total FSF flow rate to improve the reformer thermal efficiency and compensate for impacts of disturbances on the reformer efficiency. Therefore, it was important that the integrated model identification scheme is computationally efficient so that the optimized FSF distribution and total FSF flow rate can be promptly generated to prevent disturbances from damaging reforming tubes and reducing the reformer service life. In this effort, the prediction and correction steps were structured to be entirely parallelized; specifically, the prediction and correction models of 336 reforming tubes could be derived simultaneously from the

training data and independently of one another. This feature allowed the optimal LASSO parameter and the most suited theoretical semivariogram model for each reforming tube, and the optimal weighting factor of the prediction estimates to be determined using leave-out-one cross validation, which was demonstrated to improve the prediction performance of the data-driven model for the OTWT distribution. Finally, the results from the goodness-of-fit and out-of-sample prediction tests of the data-driven model for the OTWT distribution generated from the integrated model identification scheme demonstrated the high effectiveness of the method proposed in this work. In future work, the integrated model identification scheme can be used to develop an advanced furnace balancing scheme that simultaneously optimizes the FSF distribution and maximizes the total FSF flow rate to decrease the degree of temperature nonuniformity inside the reformer and to increase the reformer efficiency without damaging the reforming tubes and reducing the reformer service life. The ability to adjust the total mass flow rate for the advanced furnace balancing scheme is of special interest for the hydrogen manufacturing industry as it can potentially lead to substantial savings in the re-tubing cost of a reformer.

Chapter 5

Real-time Furnace Balancing for Steam Methane Reforming Furnace

5.1 Introduction

In Chapters 2, 3 and 4, the inherent variation in the outer tube wall temperature (OTWT) distribution, its negative impacts on the reformer thermal efficiency and its mitigation strategies have been the central theme of this dissertation because it poses a major challenge in the estimation of the optimized total furnace-side feed (FSF) flow rate due to the high risk of accelerating the degradation of the microstructure of the reforming tube wall. Specifically, the maximum OTWT along the reforming tube length among all reforming tubes in the reformer operated under a suboptimal fuel distribution can be higher than that in a reformer operated under an optimized fuel distribution with the same total fuel flow rate (Chapter 3). Consequently, the optimized FSF flow rate may not be implemented without the proper distribution of the optimized total fuel flow rate, and the SMR-based hydrogen plant throughput is compromised to retain the reformer service life and to reduce the risk of suffering substantial capital and production losses.

In addition to the challenges associated with the estimation of the optimized firing rate imposed by the physical limitation of the reforming tube wall material and the inherent nonuniformity in the

OTWT distributions, the unstudied dynamic response of the reformer under load alterations poses an additional challenge in the implementation of the optimized firing rate due to the sensitivity of the reforming tube service life to the operating temperature. Specifically, it is believed that the furnace-side temperature is expected to increase immediately in response to a positive step change in the total fuel flow rate due to the rapid combustion of the furnace-side fuel coupled with fast thermal radiative heat transfer in the high temperature combustion chamber. However, it remains unclear that if the additional fired duty can be transferred to the tube-side flow at a sufficient overall rate that would prevent the OTWTs from exceeding the respective steady-state values due to the thermal resistance of the nickel-based catalyst pellets, which are made from an alumina oxide ceramic material with relatively low thermal conductivity. As a result, there is a possibility that a large positive step change in the total fuel flow rate designed to achieve the optimized firing rate may cause the OTWTs of some reforming tubes to temporarily exceed its design temperature causing the degradation of the microstructure of the reforming tube wall to accelerate, which leads to premature failure of the reformer. Hence, designing a robust systematic operating method (i.e., the furnace-balancing scheme) that identifies the optimized firing rate and the corresponding strategic implementation of the maximum total fuel flow rate without accelerating the degradation of the microstructure of the reforming tube wall is of great interest to the hydrogen manufacturing industry.

Motivated by this, the present work utilizes a statistical-based model identification and the furnace-balancing framework to design a real-time robust furnace-balancing scheme that simultaneously identifies the optimized total fuel flow rate and its corresponding optimized valve distribution such that the reformer throughput is maximized within the physical limitation of the reforming tube wall material. Subsequently, the work utilizes the high-fidelity computational fluid dynamic (CFD) model for the reformer to investigate the unstudied dynamic response of the reformer during load alterations to propose a strategic implementation of the optimized total fuel flow rate without causing additional damage to the reforming tubes in the process. The remainder of this manuscript is structured as follows: Section 5.2 presents a high-level description of the

furnace-balancing scheme of which the major components and the basic workflow are introduced, Section 5.3 details the development of the reformer CFD model (Chapter 2) to justify using the reformer CFD model to represent the on-line reformer at the SMR-based hydrogen facility, Sections 5.4 and 5.5 present the key findings, features and capabilities of the statistical-based model identification (Chapter 4) and the valve-to-flow-rate converter (Chapter 3) to highlight their utilities for real-time optimization of the reformer to improve the plant-wise energy efficiency and to reject operational disturbances associated with flow control valves, Section 5.6 introduces readers to the development of a sequential workflow that aims to increase the reformer throughput by maximizing the total fuel flow rate, i.e., the reformer firing rate, without sacrificing the reformer service life in the process, and Section 5.7 addresses the computational challenges associated with the steady-state and transient simulations of the reformer CFD model and the derivation of the data-driven model for the OTWT distribution to emphasize the importance of parallel computing for the purpose of determining the optimized reformer fuel input in real-time using the proposed approach. Finally, in Section 5.8, the goodness-of-fit of the data-driven model for the OTWT distribution is evaluated to justify the use of the model in the development of the balancing procedure, the dynamic response of the reformer to two deterministic step changes in the total fuel flow rate from its nominal value is analyzed to design an appropriate strategy to implement the optimized firing rate estimated by the balancing procedure, and the performance of the furnace-balancing is presented to demonstrate the effectiveness of the proposed approach.

5.2 Overview of the furnace-balancing scheme

In the present work, the integrated furnace-balancing scheme that simultaneously calculates the maximum total fuel mass flow rate and the corresponding optimized valve distribution (which together are referred to as the optimized reformer fuel input) such that the conversion of methane via SMR is maximized, and the maximum OTWT along the reforming tube length among all reforming tubes is strictly less than its design temperature to avoid causing the reforming tubes to fail prematurely is presented for the first time. To this end, the framework for the furnace-balancing scheme that was proposed in Chapter 3, which was used to reduce the temperature nonuniformity inside the combustion chamber at the fixed nominal total fuel flow rate, is utilized in this work. The furnace-balancing scheme is redesigned as shown in Fig 5.1, which makes use of the statistical-based model identification, the valve-to-flow-rate converter, the balancing procedure and the high-fidelity reformer CFD model. Initially, it begins with the statistical-based model identification to derive the data-driven model for the OTWT distribution from the reformer database. Next, it integrates the most up-to-date data-driven model in the balancing procedure to find the optimized reformer fuel input that abides the aforementioned operational specifications. Subsequently, it implements the optimized reformer fuel input as the burner boundary conditions of the reformer CFD model using the strategy designed from the investigation of the transient response of the reformer during load alterations (presented in Section 5.8.2). In the remainder of this manuscript, the key developments and features of our previous work will be revisited in Sections 5.3, 5.4 and 5.5 in an effort to provide readers with sufficient background, and the development of the balancing procedure will be detailed at great length in Section 5.6 for the purpose of clarity.

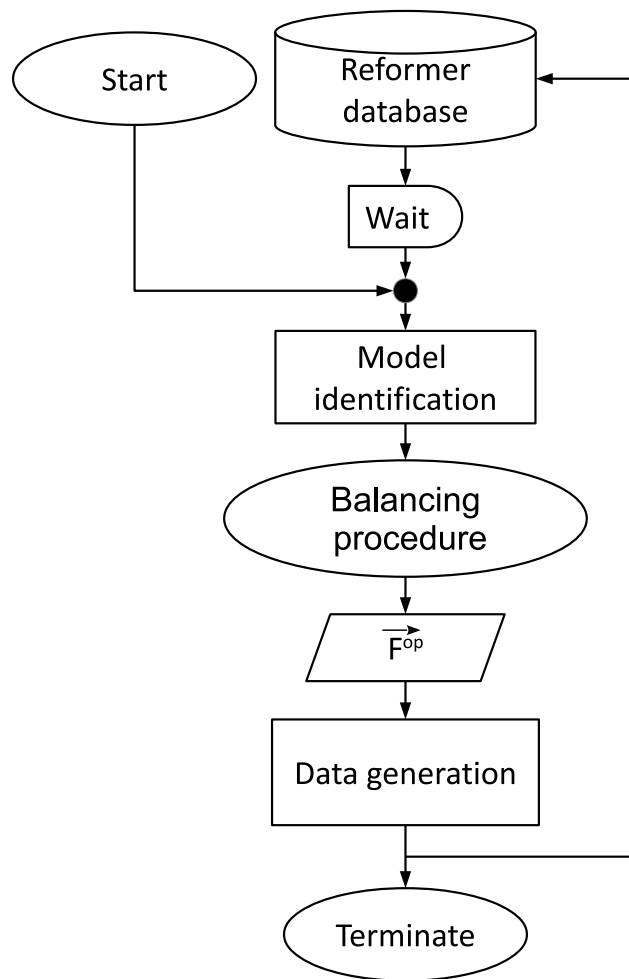


Figure 5.1: Flowchart of the furnace-balancing scheme.

5.3 Reformer CFD model

The high-fidelity reformer CFD model that was first proposed in [57] and further developed in Chapter 3 is a key component of the furnace-balancing scheme and is used to represent the on-line reformer at a commercial SMR-based hydrogen plant. This assumption will be justified by examining the geometry, mesh and development of the reformer CFD model.

The geometry of the reformer CFD model is drawn with a 3D computer-aided design tool and based on the blueprint of the physical counterpart so that it contains all of the important features of the on-line reformer, i.e., seven rows of 48 12.5-m long reforming tubes, six rows of 12 inner-lane burners, two rows of 12 outer-lane burners and eight elongated flue-gas tunnels with extraction ports. Indeed, the reformer geometry as shown in Fig. 5.2 adequately depicts a 16 m x 16 m x 13 m hydrogen producing unit at the SMR-based hydrogen plant. Readers with interest in the structural design and detailed layout of the reformer are advised to study our previous work ([57]).

In addition to the accurate representation of the reformer geometry, the mesh of the reformer CFD model was well crafted. Specifically, during the developing phase of the reformer model ([57]) the generation of the reformer mesh was prioritized because accuracy of converged solutions generated by CFD models depends on the mesh quality. For example, a CFD model created from an insufficiently dense and poor quality mesh is expected to yield inaccurate or even unphysical solutions, and it is also expected to require a higher computational cost compared to CFD models built from a high quality mesh at the same resolution. In [57], we initially provided an in-depth review of two different mesh generation procedures, in which their advantages and disadvantages were studied under the same premise using the reformer geometry, based on which we concluded that the multi-block structured hexahedral mesh generation procedure was more appropriate. Then, we used ANSYS ICEM to create the hexahedral reformer mesh that was characterized to have an acceptable mesh quality. In particular, the reformer mesh has the high averaged orthogonal factor and low averaged ortho skew, which indicate that the mesh has a small number of distorted cells, and the reformer mesh also has the in-range minimum orthogonal factor, in-range max ortho skew

and in-range max aspect ratio, which indicate that the distorted cells in the reformer mesh are not expected to cause convergence difficulties. Finally, we carried out a grid-independent study, and we found that the reformer mesh consisting of ~ 41 million cells allows the reformer CFD model to produce grid-independent solutions. We note that readers who are interested in our rationale for using the multi-block structured hexahedral mesh generation procedure and additional descriptions of the reformer mesh are advised to study our previous work ([57] Chapter 3).

Furthermore, we tailored the ANSYS Fluent model to simulate the known transport phenomena and chemical reactions associated with SMR and the air-combustion process as noted in Section 5.1. Specifically, the effects of turbulence in the furnace-side flow on the transport phenomena, chemical reactions and transport variables associated with the air-combustion process are modeled by the Reynolds-averaged Navier-Stokes (RANS) and Boussinesq hypothesis using the standard $k - \varepsilon$ model coupled with the enhanced wall treatment (EWT) function. We note that the use of the EWT function in the turbulence model has been shown to improve the accuracy of CFD solutions in the near-wall regions for low-Reynolds number meshes. The air-combustion process is modeled by adding source terms in the convective-diffusive species material balances, which are computed using the premixed combustion assumption, the global kinetic model of methane-air combustion ([46]), the global kinetic model of hydrogen-air combustion ([5]) and the finite rate/eddy dissipation (FR/ED) turbulence-chemistry interaction model. Thermal radiative heat transfer within the furnace side between outer walls of reforming tubes, walls of the flue-gas tunnels, refractory walls of the combustion chamber and the furnace-side flow is modeled by adding a source term in the convective-diffusive energy balance, which is computed by the discrete ordinate method, temperature-independent wall emissivity coefficients and the thermal absorptivity of the furnace-side flow. In addition, the thermal absorptivity of the furnace-side flow in the reformer CFD model is assumed to be temperature dependent and modeled by the empirical correlation of the furnace-side thermal emissivity ([43]), Lambert Beer's law and Kirchoff's law. In the tube side, the effects of turbulence in the tube-side flow on the transport phenomena, chemical reactions and transport variables associated with SMR are also modeled by the RANS and Boussinesq hy-

pothesis using the standard $k - \epsilon$ model with the EWT function. The reforming tubes are modeled by the pseudo-homogeneous reactor model, i.e., a continuum approach in which the solid phase is not explicitly modeled and is assumed to co-exist in thermal equilibrium with the fluid phase throughout the reactor volume, using the ANSYS Fluent porous zone function with a void fraction factor of 0.609. The reforming tube wall is modeled by the thin wall model ([34]). SMR is modeled by adding source terms in the convective-diffusive species material balances, which are computed using the global kinetic model of SMR ([64]), the FR/ED model, the catalyst packing factor and the effectiveness factor. We note that the use of the effectiveness factor is critical for accurate simulations of the methane conversion via SMR because it allows the effects of the external mass transfer limitation (as superheated steam and methane must be transferred from the tube-side bulk flow to the external surface of the catalyst pellets) and internal mass transfer limitation (as the reactants must diffuse through the support material to reach the metal active site) on the chemical reaction rates associated with SMR to be simulated. In addition, physical and chemical properties of tube-side and furnace-side species are imported from ANSYS Fluent database, based on which properties of the furnace-side and tube-side flows are computed using appropriate models. For instance, the molecular thermal conductivities and molecular viscosities of the furnace-side and tube-side flows are calculated using ideal-gas mixing law, while the diffusion coefficients of the furnace-side and tube-side flows are calculated using the kinetic theory. Moreover, reforming tubes, catalyst pellets, walls of the combustion chambers and walls of the flue-gas tunnels are assumed to be made of appropriate materials and are encoded all physical properties (e.g., density, thermal conductivity, specific heat capacity and emissivity coefficient) reported in the SMR literature. For example, reforming tubes are typically made from cast creep resistant austenitic steel HP grade, and its catalyst pellets are typically made from nickel-based catalyst dispersed in alpha alumina support. Readers who are interested in our rationales for the proposed modeling strategies for the reformer CFD model, the two-step converging strategy and the data collecting procedure are recommended to study our previous work ([57]).

The steady-state simulation results generated by the reformer CFD model, whose boundary

conditions are modified based on an operating information of the on-line reformer provided by our third party industry collaborator, have been shown to be consistent with typical plant data in the SMR literature and with the plant historian data. Therefore, the reformer CFD model can adequately represent the on-line unit, and simulation results generated by the reformer model, whose boundary conditions are modified based on varying fuel distributions and total fuel flow rates, can be considered to be reliable estimates of the plant data obtained from the on-line unit at equivalent operating conditions. As a result, it is reasonable to use the reformer CFD model to represent the on-line reformer, so that it can be used to study the transient response of the on-line reformer when the total fuel flow rate is increased and to demonstrate the effectiveness of the integrated furnace-balancing scheme.

It is worth noting that at the commercial-scale SMR-based hydrogen plant, the inputs to the furnace side of the reformer are regulated by a system of flow control valves, OTWTs at a finite locations along the reforming tubes inside the furnace are continuously monitored by a system of infrared cameras through peepholes, the synthesis gas composition can be sampled, and the historian data of the on-line reformer are well documented. Therefore, in an effort to simulate a realistic on-site investigation we assume that we have access to the historian data, i.e., the reformer database, which can be reasonably assumed to be a collection of simulation results generated by the reformer model. In this study, the reformer database is populated with 26 steady-state solutions generated by the reformer CFD model under 26 different reformer fuel inputs ([56, 57]). For each data point, only information about the valve positions of all flow control valves, the total fuel flow rate, the fuel flow rates of all burners, the composition of the synthesis gas and the OTWTs of all reforming tubes at a distance 6.5 m away from the reformer ceiling will be utilized, so that the reformer database and the historian plant data collected from the on-line reformer at the SMR-based hydrogen plant are essentially equivalent. The reformer database will be utilized extensively by the statistical-based model identification to create a computationally efficient data-driven model for the reformer controlled variables (i.e., the OTWT distribution) as a function of the reformer manipulated inputs (i.e., the flow control valve distribution and the total fuel flow rate), which will

be detailed in the upcoming section.

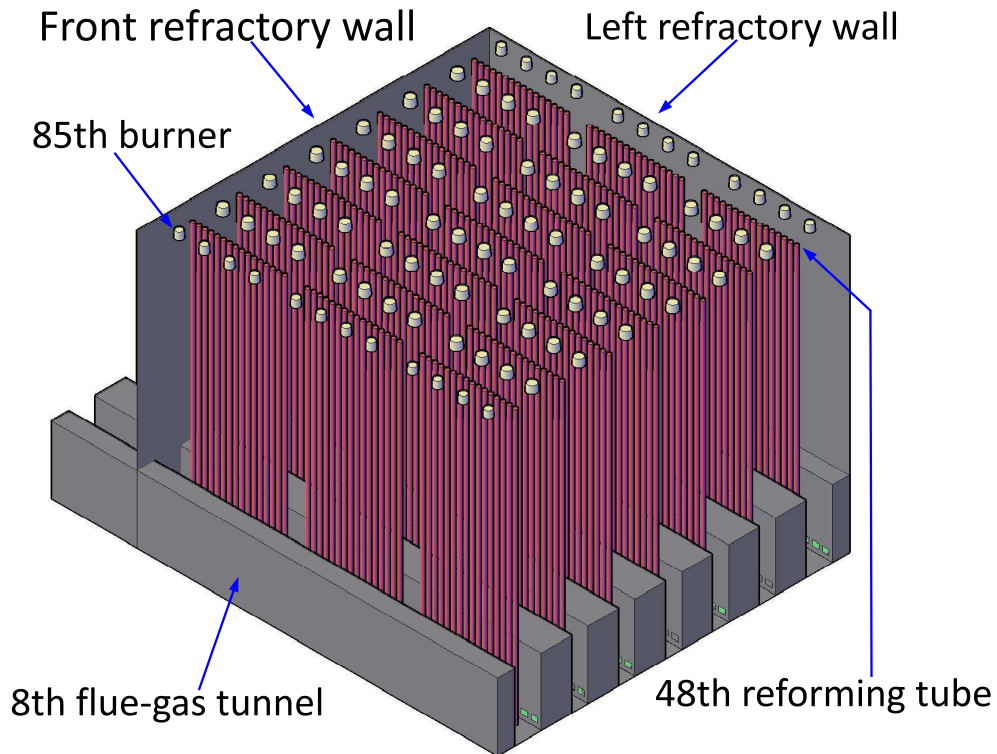


Figure 5.2: Isometric view of the reformer in which the right and back refractory walls are made transparent to display the interior components. The reformer includes 336 reforming tubes (represented by 336 cylinders), 96 burners (represented by 96 frustum cones), and 8 flue-gas tunnels (represented by 8 rectangular intrusions).

5.4 Statistical-based model identification

The statistical-based model identification that was proposed in Chapter 4 is a key component of the furnace-balancing scheme and is used to create a computationally efficient data-driven model for the OTWT distribution as a function of the flow control valve distribution and the total fuel flow rate from the reformer database in an effort to find the optimized reformer fuel input in real-time. The model identification is designed to simultaneously execute two model building processes for each OTWT, i.e., the prediction and correction steps, which create two corresponding data-driven models, namely, the prediction and correction models, respectively. As a result, the prediction and correction estimates of the i th OTWT are computed based on the fuel flow rate distribution and based on the OTWTs of the nearby reforming tubes, respectively.

It is important to note that although the reformer has 96 distinct burners, we have found that the OTWT of the i th reforming tube depends primarily on the fuel flow rates of the nearby burners. This is because more than 95% of the energy absorbed by the reforming tubes is transferred to the outer tube walls by thermal radiation ([58, 47]), while the intensity of thermal radiation decreases with increasing distance between the heat source (i.e., the burners) and the heat sink (i.e., the reforming tubes). Therefore, the model building process for the i th prediction model is designed to iteratively screen for the important predictors for the i th OTWT using Bayesian variable selection, Occam's window, sparse non-linear regression with 11 transformation functions, Bayesian information criterion (BIC) and a first-principles model for thermal radiation. In addition, the model building process is designed to keep tabs on all sub-prediction models for the i th OTWT (which are defined as the data-driven models derived for the purpose of screening for the important predictors) with high goodness of fit, each of which is expected to adequately explain the non-linearity in the dependence of the i th OTWT on its predictors and can be expressed as follows,

$$\tilde{T}_{i,k}^{P,n} = \sum_{g=1}^{11} \hat{\alpha}_i^{kg} f_g \left(\vec{F}^n \Big|_{S_{iR}^k} \right) + \hat{\alpha}_i^k \quad (5.1)$$

where $\tilde{T}_{i,k}^{P,n}$ is an estimate of the i th OTWT computed from the k th sub-prediction model for the i th OTWT ($M_{i,k}^P$) and the n th fuel distribution (\vec{F}^n), S_{iR}^k and $f_g(\cdot)$ are the set of predictors and the g th transformation function used in the identification of $M_{i,k}^P$ by sparse non-linear regression, respectively, $\vec{F}^n \Big|_{S_{iR}^k}$ is the reduced-order n th fuel distribution such that it only retains the fuel flow rates of burners associated with S_{iR}^k , $\hat{\alpha}_i^{kg}$ is the estimated parameter vector corresponding to $f_g(\cdot)$ in $M_{i,k}^P$ and $\hat{\alpha}_i^k$ is the estimated ambient temperature in $M_{i,k}^P$. The 11 transformation functions in sparse non-linear regression are designed to be nonnegative monotonically increasing functions as follows,

$$f_1(\vec{F}^n) = [F_1^n, F_2^n, \dots, F_{96}^n]^T \quad (5.2a)$$

$$f_2(\vec{F}^n) = [(F_1^n)^2, (F_2^n)^2, \dots, (F_{96}^n)^2]^T \quad (5.2b)$$

$$f_3(\vec{F}^n) = [(F_1^n)^3, (F_2^n)^3, \dots, (F_{96}^n)^3]^T \quad (5.2c)$$

$$f_4(\vec{F}^n) = [\sqrt[2]{F_1^n}, \sqrt[2]{F_2^n}, \dots, \sqrt[2]{F_{96}^n}]^T \quad (5.2d)$$

$$f_5(\vec{F}^n) = [\sqrt[3]{F_1^n}, \sqrt[3]{F_2^n}, \dots, \sqrt[3]{F_{96}^n}]^T \quad (5.2e)$$

$$f_6(\vec{F}^n) = [\sqrt[4]{F_1^n}, \sqrt[4]{F_2^n}, \dots, \sqrt[4]{F_{96}^n}]^T \quad (5.2f)$$

$$f_7(\vec{F}^n) = [\sqrt[5]{F_1^n}, \sqrt[5]{F_2^n}, \dots, \sqrt[5]{F_{96}^n}]^T \quad (5.2g)$$

$$f_8(\vec{F}^n) = [\exp(F_1^n), \exp(F_2^n), \dots, \exp(F_{96}^n)]^T \quad (5.2h)$$

$$f_9(\vec{F}^n) = [\sqrt[6]{F_1^n}, \sqrt[6]{F_2^n}, \dots, \sqrt[6]{F_{96}^n}]^T \quad (5.2i)$$

$$f_{10}(\vec{F}^n) = [\sqrt[10]{F_1^n}, \sqrt[10]{F_2^n}, \dots, \sqrt[10]{F_{96}^n}]^T \quad (5.2j)$$

$$f_{11}(\vec{F}^n) = [\sqrt[15]{F_1^n}, \sqrt[15]{F_2^n}, \dots, \sqrt[15]{F_{96}^n}]^T, \quad (5.2k)$$

which is inspired by the observed response of the i th OTWT to varying reformer fuel inputs. For examples, when the fuel flow rates of the predictors for the i th OTWT are increased, the i th OTWT increases. Furthermore, three additional transformation functions (Eqs. 5.2i, 5.2j and 5.2k) are incorporated into the library proposed in Chapter 4 (Eqs. 5.2a–5.2h) to improve the goodness of

fit and forecasting accuracy of the ith prediction model for a wider range of reformer fuel inputs. In an effort to prevent presumptuous bias from being introduced in the derivation of the ith prediction model by our arbitrary choice of the hyperparameter (i.e., LASSO parameter) of sparse non-linear regression, cross-validation methods are used to select the optimized LASSO parameter based on the reformer database. Specifically, Section 5.8.1 will demonstrate the importance of using the optimized LASSO parameter by showing that a LASSO parameter larger than the optimized value allows the model building process to favor underfitting sub-prediction models, while a LASSO parameter smaller than the optimized value allows the model building process to favor overfitting sub-prediction models. Subsequently, instead of treating the “best” sub-prediction model derived from the complete set of important predictors as the ith prediction model, the prediction step combines the ith sub-prediction models with high goodness of fit to derive the ith prediction model using Bayesian model averaging (BMA) and BIC in an effort to account for uncertainty in model selection ([25]). Specifically, the ith prediction model (M_i^P) is formulated as the weighted sum of the ith sub-prediction models as follows,

$$\widehat{T}_i^{P,n} = \sum_{k=1}^{K_i} w_{i,k}^P \widetilde{T}_{i,k}^{P,n} \quad (5.3)$$

where $\widehat{T}_i^{P,n}$ is the prediction estimate of the ith OTWT computed from M_i^P and \vec{F}^n , K_i is the number of sub-prediction models with high model goodness of fit for the ith OTWT and $w_{i,k}^P$ is the BMA weighting factor of $M_{i,k}^P$. Then, a collection of all prediction models arranged in an ascending order of reforming tube IDs is used to define the prediction model for the OTWT distribution (M^P) as follows,

$$\widehat{\vec{T}}^{P,n} = \begin{pmatrix} \widehat{T}_1^{P,n} \\ \widehat{T}_2^{P,n} \\ \vdots \\ \widehat{T}_{336}^{P,n} \end{pmatrix} \quad (5.4)$$

where $\widehat{T}^{P,n}$ is the prediction estimate of the OTWT distribution computed from M^P and \vec{F}^n .

In Chapter 4, we have recognized that OTWTs of neighboring reforming tubes are spatially correlated. Therefore, the model building process for the i th correction model is designed to compute the sample correlation (i.e., the sample semivariograms) among the OTWTs of the reforming tubes in a sufficiently large, predefined neighborhood from the reformer database using the classical estimator. Then, a theoretical semivariogram model is fitted based on the sample semivariograms using the method of weighted least squares ([10]). In an effort to prevent presumptuous bias from being introduced in the derivation of the i th correction model by an ad-hoc and subjective eyeballing approach to select the theoretical semivariogram model, cross-validation methods are used to select the optimized theoretical semivariogram model from a collection of four potential models proposed in Chapter 4. Then, the model building process uses the theoretical semivariogram model to derive the i th correction model using ordinary Kriging modeling. Specifically, the i th correction model (M_i^C) is formulated as the weighted sum of prediction estimates of OTWTs in the i th Kriging neighborhood (denoted as \mathbf{W}_i^K), which contain at most three nearest northward, one nearest eastward, three nearest southward and one nearest westward neighbors of the i th reforming tube, as follows,

$$\widehat{T}_i^{C,n} = \sum_j \mathbf{W}_i^K w_{i,j}^C \widehat{T}_j^{P,n} \quad (5.5)$$

where $\widehat{T}_i^{C,n}$ is a correction estimate of the i th OTWT computed from M_i^C and the prediction estimates of OTWTs in \mathbf{W}_i^K ($\widehat{T}_j^{P,n}$), and $w_{i,j}^C$ is the Kriging weighting factor corresponding to j th reforming tube. Then, a collection of all correction models arranged in an ascending order of reforming tube IDs is used to define the correction model for the OTWT distribution (M^C) as follows,

$$\widehat{T}^{C,n} = \begin{pmatrix} \widehat{T}_1^{C,n} \\ \widehat{T}_2^{C,n} \\ \vdots \\ \widehat{T}_{336}^{C,n} \end{pmatrix} \quad (5.6)$$

where $\widehat{T}^{C,n}$ is the correction estimate of the OTWT distribution computed from M^C and \vec{F}^n . Finally, the data-driven model for the OTWT distribution (M) is formulated as the weighted average of M^P and M^C as follows,

$$\widehat{T}^n = w^P \widehat{T}^{P,n} + (1 - w^P) \widehat{T}^{C,n} \quad (5.7)$$

where w^P is the hyperparameter of M of which an optimized value is estimated by cross-validation methods from a set of 21 possible values, i.e., $\mathbf{S}_w = \{0.00, 0.05, 0.10, \dots, 0.95, 1.00\}$, based on the reformer database. The resulting data-driven model for the OTWT distribution, of which hyperparameters are optimized to minimize out-of-sample prediction errors, incorporates the information about uncertainty in model selection and the spatial correlations in OTWTs among the neighboring reforming tubes into estimating the OTWT distribution based on the fuel flow rate distribution. It is worth noting that the data-driven model for the OTWT distribution is a system of algebraic equations and has been shown to yield estimates of the OTWT distribution for varying reformer fuel inputs instantaneously on a single core machine of the shared computing cluster at UCLA. This feature allows the furnace-balancing procedure, which will be detailed in Section 5.6, to search for the optimal reformer fuel input in real-time.

5.5 Valve-to-flow-rate converter

The valve-to-flow-rate converter that was developed in Chapter 3 is an important component of the furnace-balancing scheme and is used to make our present work a more realistic representation of an on-site investigation, where the reformer fuel input is regulated by a system of manual flow control valves, so that our findings can be brought into practice with little or no changes. It is important to note that fuel lines to burners, of which fuel flow rates are regulated by the flow control valves, are interconnected through a header fuel system with a main header fuel inlet and eight sub-headers fuel pipes as detailed in [32]. This structural design allows the excess fuel feed of burners in the detected overheating regions to be redistributed by partially closing the flow control valves of the corresponding fuel lines. The converter model developed based on the material conservation law as shown in Eq. 5.8 can capture this characteristic through the system of coupled algebraic equations.

In the development of the converter, the following assumptions are made and translated into appropriate mathematical formulations. Two adjacent fuel lines to burners within each burner row are assumed to be regulated by a flow control valve, which forces the fuel flow rates of the associated burners to be the same. The structural layout of the system of manual flow control valves in the reformer can be depicted in an information matrix $[Y]$ as shown in Eq. 5.9c. Next, fuel lines to burners are assumed to be regulated by two types of linear flow control valves with different maximum capacities corresponding to inner-lane and outer-lane burners. The arrangement and identity of burners in the reformer can be captured in an information matrix $[X]$ as shown in Eq. 5.9d. Finally, the pressure of fuel feed in the header fuel system of the reformer is assumed to be sufficiently high so that there will be no backflow for all valve distributions. The model for the converter is formulated as follows,

$$\vec{F} = \delta[X] \cdot [Y] \cdot \vec{V} \quad (5.8)$$

$$\vec{V} \in \mathbb{R}^{48 \times 1} \quad (5.9a)$$

$$\vec{F} \in \mathbb{R}^{96 \times 1} \quad F_i \geq 0 \quad \forall i \in [1, 96] \quad (5.9b)$$

$$[Y] \in \mathbb{R}^{96 \times 48} \quad (5.9c)$$

$$Y_{i,j} = 1.0; \quad i = 2j - 1 \cup i = 2j \text{ where } j \in [1, 48]$$

$$Y_{i,j} = 0.0; \quad i \neq 2j - 1 \cap i \neq 2j \text{ where } j \in [1, 48]$$

$$[X] \in \mathbb{R}^{96 \times 96} \quad (5.9d)$$

$$X_{i,j} = 0.6; \quad i = j \text{ where } i \in [1, 12] \cup [85, 96]$$

$$X_{i,j} = 1.0; \quad i = j \text{ where } i \in [13, 84]$$

$$X_{i,j} = 0.0; \quad i \neq j$$

$$\delta = \frac{F_{tot}}{\|[X] \cdot [Y] \cdot \vec{V}\|_1} \quad (5.9e)$$

where δ is the valve-to-flow-rate proportionality coefficient and \vec{V} is the valve distribution. In this work, we define \vec{V} as the collection of the percent open positions of all flow control valves in the reformer. The converter allows us to formulate the furnace-balancing scheme to use the valve distribution as the manipulated variables as in the on-line reformer, so that the optimized solution generated from our study can be directly applied to the on-line unit to distribute the fuel feed among all burners. The converter also gives us an opportunity to examine the transient response and steady-state behavior of the reformer when the reformer is subjected to common valve related disturbances. It is important to note that the model for the converter allows a fuel distribution to be generated from different valve distributions (which will be discussed in Section 5.6.1); however, these valve distributions are not equivalent in practice. Specifically, among valve distributions that yield the same fuel flow rate distribution, those that deviate further from the fully open valve setting require the fuel feed to the reformer to be at a higher pressure which corresponds to higher operating cost. This information will be used in the formulation of the model-based balancing

procedure, which will be detailed in the upcoming section.

5.6 Balancing Procedure

The balancing procedure is the core component of the furnace-balancing scheme and is used to search for the optimized total fuel flow rate and the corresponding valve distribution such that the conversion of methane via SMR is maximized, and the maximum OTWT along the reforming tube length among all reforming tubes is strictly less than the design temperature of the reforming tube wall material. The balancing procedure is a sequential workflow system, as shown in Fig. 5.3, of which major components are the data-driven model for the OTWT distribution, the valve-to-flow-rate converter and the furnace-balancing optimizer. It is designed to assess the nonuniformity of the current temperature distribution inside the combustion chamber by means of the estimated OTWT distribution calculated from the current valve distribution (denoted as \vec{V}^0) and total fuel flow rate (denoted as F_{tot}^0) using the valve distribution analyzer. Specifically, \vec{V}^0 and F_{tot}^0 are used as inputs for the converter to generate the current fuel distribution (denoted as \vec{F}^0), which is used as an input for M to estimate the current OTWT distribution (denoted as \hat{T}^0). The assumption that \hat{T}^0 is a good representation of the current temperature distribution inside the reformer can be justified because the plant data of the initial OTWT distribution (denoted as \vec{T}^0) belongs to the reformer database from which M is derived, and M is expected to have a high goodness of fit. Next, \hat{T}^0 is processed by the OTWT distribution analyzer, which identifies the maximum value in the OTWT distribution as follows,

$$\hat{T}_{wall,i}^{max} = \left\| \left(\begin{array}{c} \hat{T}_1^i \\ \hat{T}_2^i \\ \vdots \\ \hat{T}_{336}^i \end{array} \right) \right\|_{\infty} \quad (5.10)$$

where $\hat{T}_{wall,i}^{max}$ is the estimated maximum value of the i th OTWT distribution and i is 0. Then, $\hat{T}_{wall,0}^{max}$ is used as an input for the furnace-balancing search indicator, which produces a binary search

indicator (denoted as F_I) as follows,

$$F_I = 1.0 \quad \hat{T}_{wall,0}^{max} < T_{wall}^{max,*} \quad (5.11)$$

$$F_I = -1.0 \quad \hat{T}_{wall,0}^{max} \geq T_{wall}^{max,*} \quad (5.12)$$

where $T_{wall}^{max,*}$ is the maximum allowable OTWT and is a user-specified parameter of the furnace-balancing scheme (a systematic method to estimate $T_{wall}^{max,*}$ will be discussed in Section 5.8.3). Subsequently, F_I is used to guide the heuristic search algorithm that recursively applies incremental changes to the total fuel flow rate followed by evaluating the impact of the adjusted total fuel flow rate on the maximum value of the OTWT distribution, and based on which it reformulates the future action to meet the operational specifications in a finite number of steps. Specifically, $F_I = 1.0$ implies that the total fuel mass flow rate can be increased to increase the methane conversion via SMR, while $F_I = -1.0$ implies that the total fuel mass flow rate must be decreased to avoid causing the reforming tubes to fail prematurely.

In this effort, the heuristic search algorithm is structured to have two sequential modes (referred as the aggressive and conservative modes, respectively) with an identical framework, which begins with the flow rate generator followed by the furnace-balancing optimizer, valve distribution analyzer and furnace-balancing analyzer. In particular, the aggressive search is responsible for identifying the neighborhood of the optimal total fuel flow rate, and the conservative search is responsible for identifying the optimized value such that the operational specifications are satisfied. For instance, when the value of F_I is 1.0, the heuristic search algorithm begins with the aggressive flow rate generator, which recursively applies “large” increments to the total fuel flow rate to approximate the “smallest” upper-bound value, which is defined as the minimum total fuel flow rate that allows the maximum value of the OTWT to exceed $T_{wall}^{max,*}$, as follows,

$$F_{tot}^{i,1} = F_{tot}^0 (1.0 + i\delta_{01}F_I) \quad \text{where} \quad i = 1, 2, 3, \dots \quad (5.13)$$

where $\delta_{01}=10\%$ is the parameter of the aggressive search, $F_{tot}^{i,1}$ is the adjusted total fuel flow rate

at the i th iteration in the aggressive search and $i=1$ is the index of the first iteration. In the i th iteration, $F_{tot}^{i,1}$ is used as an input for the furnace-balancing optimizer which optimizes the valve distribution so that the nonuniformity in the OTWT distribution is minimized. Then, $F_{tot}^{i,1}$ and the corresponding optimized valve distribution (denoted by $\vec{V}^{i,1}$) are used as inputs to the valve distribution analyzer to estimate the maximum value in the corresponding OTWT distribution (denoted by $\hat{T}_{wall,i}^{max,1}$) as discussed previously. Finally, $\hat{T}_{wall,i}^{max,1}$ is used as an input to the aggressive furnace-balancing analyzer, which determines if $F_{tot}^{i,1}$ can be considered to be an approximation of the smallest upper-bound value of the total fuel flow rate. Specifically, when $\hat{T}_{wall,i}^{max,1}$ begins to exceed $T_{wall}^{max,*}$, the aggressive furnace-balancing analyzer classifies $F_{tot}^{i,1}$ as an approximation of the smallest upper-bound value, which is labeled as $F_{tot}^{*,1}$, and terminates the aggressive search.

After the approximation of the smallest upper-bound value is obtained, the heuristic search algorithm continues with the conservative flow rate generator, which gradually applies “small” decrements to the upper-bound value until the reformer returns back into the safe operating regime as follows,

$$F_{tot}^{j,2} = F_{tot}^{*,1} (1.0 - j\delta_{O_2}F_I) \quad \text{where} \quad j = 1, 2, 3, \dots \quad (5.14)$$

where $\delta_{O_2}=1\%$ is the parameter of the conservative search, $F_{tot}^{j,2}$ is the adjusted total fuel flow rate at the j th iteration in the conservative search and $j=1$ is the index of the first iteration. After $F_{tot}^{j,2}$ is computed, an analogous procedure as described in the aggressive search, which begins with the furnace-balancing optimizer followed by the valve distribution analyzer, is executed. Then, the maximum value (denoted by $\hat{T}_{wall,j}^{max,2}$) in the OTWT distribution estimated from $F_{tot}^{j,2}$ and the corresponding optimized valve distribution (denoted by $\vec{V}^{j,2}$) in the j th iteration of the conservative search is used as an input to the conservative furnace-balancing analyzer, which determines if $F_{tot}^{j,2}$ can be considered to be the optimized total fuel flow rate. Specifically, when $\hat{T}_{wall,j}^{max,2}$ begins to drop below $T_{wall}^{max,*}$, which indicates that the operational specifications are satisfied, the conservative furnace-balancing analyzer classifies $F_{tot}^{j,2}$ as the optimized total fuel flow rate, which is labeled as

F_{tot}^{op} , and terminates the conservative search. Finally, F_{tot}^{op} and the corresponding optimized valve distribution (denoted by \vec{V}^{op}) are translated into the optimized fuel distribution (denoted by \vec{F}^{op}), which is strategically applied as the reoptimized burner boundary conditions for the reformer CFD model so that the reforming tubes do not suffer additional damage during the transition to achieve the optimized reformer firing rate.

On the contrary, when the value of F_l is -1.0 , the search direction is reversed. Specifically, the aggressive flow rate generator recursively applies “large” decrements to the total fuel flow rate as shown in Eq. 5.13 to approximate the “largest” lower-bound value, which is defined as the maximum total fuel flow rate that allows the maximum value of the OTWT to approximate $T_{wall}^{max,*}$ from the right. Then, the conservative search gradually applies “small” increments to the lower-bound value as shown in Eq. 5.14 until $\hat{T}_{wall,j}^{max,2}$ begins to exceed $T_{wall}^{max,*}$ indicating that the reformer is leaving the safe operating regime, and at this point, the conservative furnace-balancing analyzer classifies $F_{tot}^{j-1,2}$ as F_{tot}^{op} , and terminates the conservative search. Similarly, F_{tot}^{op} and \vec{V}^{op} are translated into \vec{F}^{op} , which is applied as the reoptimized burner boundary conditions for the reformer CFD model. The heuristic search algorithm proposed in this study can derive F_{tot}^{op} , \vec{V}^{op} and \vec{F}^{op} from any arbitrary initial reformer fuel input so that the operational specifications are satisfied.

5.6.1 Furnace-balancing optimizer

The furnace-balancing optimizer that was developed in Chapter 3 is of the uttermost importance in the heuristic search algorithm and is reformulated to be fully capable of optimizing the valve distribution at any total fuel flow rate to reduce the nonuniformity in the OTWT distribution. Specifically, the improved optimizer aims to minimize the sum of weighted squared differences between the OTWTs at a location 6.5 m away from the reformer ceiling of all reforming tubes and an “ideal” OTWT at a given total fuel flow rate to allow the reformer to be operated under the optimal condition in which the OTWT profiles along the reforming tube length of all reforming tubes are identical. In this subsection, a means to estimate the ideal OTWT at any total fuel flow rate is

presented followed by the discussion of the development of a more robust objective function for the furnace-balancing optimizer.

A thorough analysis of the results reported in Chapter 3 suggests that the average value of the OTWT distribution (denoted by T_{wall}^{ave}) is a good estimator of the ideal OTWT because it is invariant with respect to the valve distribution under a fixed total fuel flow rate. Therefore, the relationship between T_{wall}^{ave} and total fuel flow rate is analyzed by using the reformer database. In particular, Fig. 5.4 shows that T_{wall}^{ave} is, indeed, independent of the valve distribution under a fixed total fuel flow rate, and Fig. 5.5 shows that T_{wall}^{ave} exhibits a strong linear correlation to the total fuel flow rate. Therefore, we can create an estimator for the ideal OTWT as a function of the total fuel flow rate by fitting a linear function using ordinary least squares (OLS) to the plant data presented in Fig. 5.5. The result of the fit is,

$$\widehat{T}_{wall}^{ave} = 2.09F_{tot} + 957.62. \quad (5.15)$$

Then, the furnace-balancing optimizer is formulated using the data-driven model for the OTWT distribution (Eq. 5.7), the valve-to-flow-rate converter (Eq. 5.8), the estimator for the ideal OTWT (Eq. 5.15) and the total fuel flow rate (denoted by F_{tot}^i , which is generated by the flow rate generators of the heuristic search algorithm). Specifically, it is written as a program with the quadratic cost function that aims to minimize the sum of weighted squared deviations of the OTWTs in the OTWT distribution from its average value by optimizing the percent open positions of the functional control valves. The quadratic cost function of the furnace-balancing optimizer has the following form,

$$\min_{\substack{V_j^u \in [60\%, 100\%] \\ j \in [1, 48] \setminus \mathbf{S}_{def}}} \sum_{k=1}^{336} w_k \left(\widehat{T}_{wall,i}^{ave} - \widehat{T}_k^i \right)^2 \quad (5.16)$$

where $V_j^u=100\%$ and $V_j^l=60\%$ are the upper and lower bounds of the percent opening position of the j th flow control valve, respectively, \mathbf{S}_{def} is the set that contains indices of the defective flow control valves, w_k is the weighting factor of the k th reforming tube (which is has been discussed at length in Chapter 3 and will not be elaborated further in this manuscript for brevity), $\widehat{T}_{wall,i}^{ave}$,

and \widehat{T}_k^j are the estimated average OTWT and the estimated k th OTWT, respectively, in the OTWT distribution. It is worth noting that only in a scenario which all flow control valves are functional, and the cardinality of \mathbf{S}_{def} is zero, an optimized valve distribution (denoted by \vec{V}^{op}) calculated by the furnace-balancing optimizer is expected to have multiple equivalent solutions as discussed in Section 5.5. This statement can be mathematically rationalized by first using the model for the converter to solve for \vec{V}^{op} from the optimized fuel distribution (denoted by \vec{F}^{op}) as follows,

$$F_{2j}^{op} = F_{2j-1}^{op} = \delta^{op} X_{2j,2j} Y_{2j,j} V_j^{op} \quad \text{where } j = 1, 2, \dots, 48 \quad (5.17a)$$

$$\delta^{op} = \frac{\sum_{i=1}^{96} F_i^{op}}{\| [X] \cdot [Y] \cdot \vec{V}^{op} \|_1} \quad (5.17b)$$

where F_{2j}^{op} and F_{2j-1}^{op} are the optimized fuel flow rates of the $(2j)$ th and $(2j-1)$ th burners respectively, $X_{2j,2j}$ is the element of the $(2j)$ th row and $(2j)$ th column in $[X]$, $Y_{2j,j}$ is the element of the $(2j)$ th row and j th column in $[Y]$ and V_j^{op} is the optimized percent opening position of the j th flow control valve. Then, the system of non-linear algebraic equations as shown in Eq. 5.17 can be transformed into a system of linear algebraic equations by taking the ratio of all equations in Eq. 5.17(a) to an arbitrarily selected equation as follows,

$$\frac{F_{2j}^{op}}{F_{2k}^{op}} = \frac{X_{2j,2j} Y_{2j,j} V_j^{op}}{X_{2k,2k} Y_{2k,k} V_k^{op}} \quad \text{where } j = 1, 2, \dots, 48 \text{ and } j \neq k. \quad (5.18)$$

It is evident that the system of linear algebraic equations, in which the percent opening positions of the flow control valves are the unknowns, as shown in Eq. 5.18 is underdetermined and is expected to have multiple solutions. However, these valve distributions are by no means the same in a sense of the plant-wise energy efficiency as explained in Section 5.5, and therefore, the valve distribution that deviates the least from the fully open valve setting is considered as the true and unique optimized solution. The task of finding such valve distribution is achieved with the valve optimizer which is developed by exploiting the linear relationship between the percent opening position of the linear flow control valve and the fuel flow rates that it regulates, and the assumption

that the flow control valve to which the maximum fuel flow rate corresponds is fully open. The valve optimizer is formulated as follows,

$$V_{j,eq}^{op} = \frac{\left(\delta^{op}[X][Y] \vec{V}^{op} \Big|_{2j} \right)}{X_{2j,2j} \left\| \delta^{op}[X][Y] \vec{V}^{op} \right\|_{\infty}} \quad (5.19)$$

where $V_{j,eq}^{op}$ is the equivalent optimized percent open position of the j th flow control valve, $\left(\delta^{op}[X][Y] \vec{V}^{op} \Big|_{2j} \right)$ is the fuel flow rate of the $(2j)$ th burner, and $\left\| \delta^{op}[X][Y] \vec{V}^{op} \right\|_{\infty}$ is the maximum fuel flow rate among all burners. The equivalent optimized valve distribution is expected to simultaneously minimize the sum of the weighted squared deviations of all OTWTs in the OTWT distribution from the ideal OTWT, which is computed based on the given total fuel flow rate, and minimizes the required duty of the upstream compression system, and therefore, improves the energy efficiency of the SMR-based hydrogen plant.

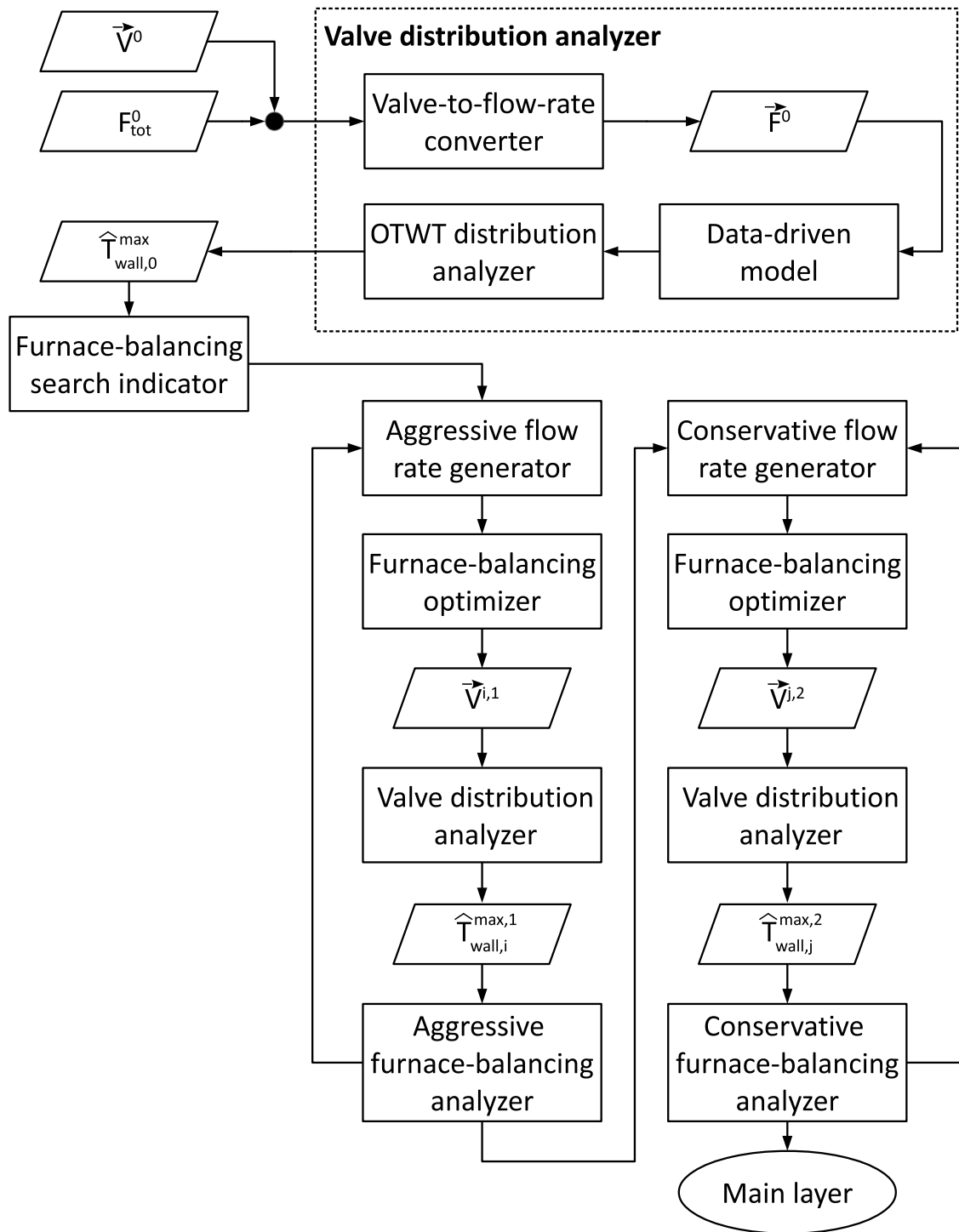


Figure 5.3: Flowchart of the balancing procedure.

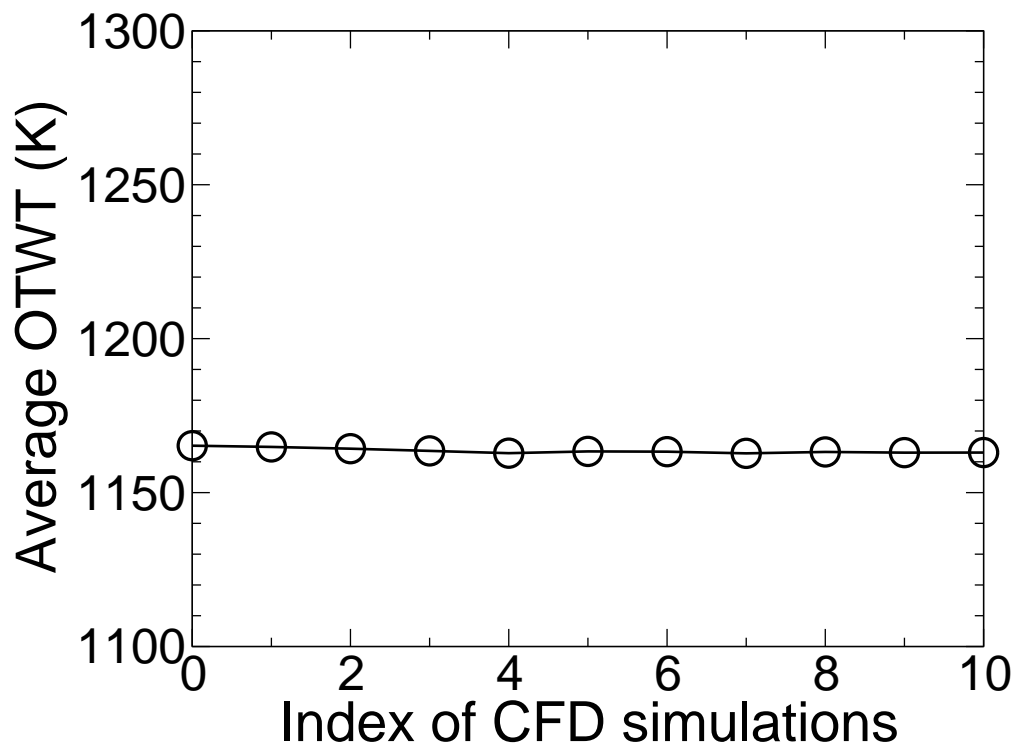


Figure 5.4: Average value of the OTWT distribution when the reformer is operated under the nominal fuel flow rate and varying valve distributions.

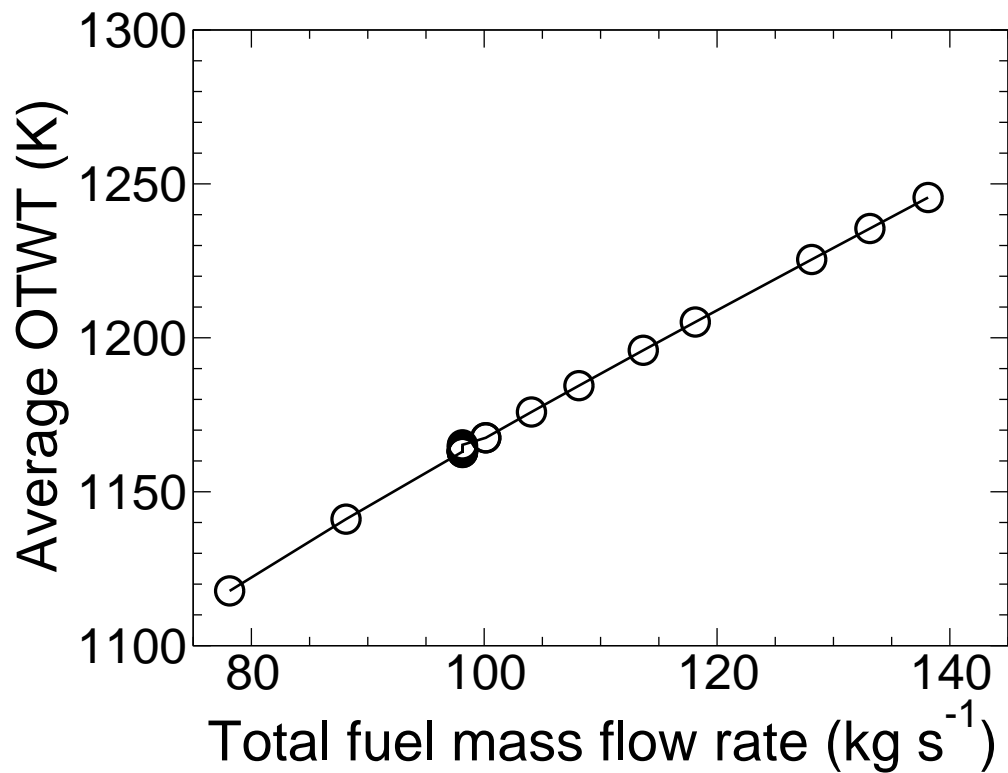


Figure 5.5: Average value of the OTWT distribution when the reformer is operated under varying fuel flow rates and varying valve distributions.

5.7 Parallel Processing

In this section, the computational challenges associated with the steady-state and transient simulations of the reformer CFD model under varying reformer fuel inputs and the derivation of the data-driven model for the OTWT distribution from the reformer database are discussed. Specifically, in all simulations of the reformer CFD model, the furnace-side and tube-side domains are discretized into ~ 41 million control volumes, and in each of which the reformer mathematical model (i.e., a high dimensional system of non-linear partial integro-differential equations with seven independent variables ([44])) is numerically solved or integrated forward in time by the finite volume method. It is evident that the random access memory (RAM), e.g., 32 GB, and the processing speed of a standard high performance workstation are insufficient to keep track of values of transport variables in all control volumes and to compute the numerical solutions of the reformer mathematical model in all control volumes in a practical time frame. In addition, the derivation of M can be viewed as an ensemble of 336 independent model building processes for 336 distinct OTWTs. Each model building process can be viewed as a sub-ensemble of two independent model building processes, i.e., the prediction and correction steps, in which cross validation methods are used to select the optimized hyperparameters to improve the forecasting accuracy of M . To better comprehend the magnitude of the number of computing tasks needed to derive M from the reformer database, we consider the derivation of the data-driven model reported in Chapter 4 as an illustrative example. Specifically, 18 training data sets were used to create the reformer database, and leave-out-one (LOO) cross validation was used to select the optimal lasso parameter from a predefined set of 18 possible LASSO parameters and to select the optimal theoretical semivariogram model from a collection of four potential models. Given this premise, the model building process for the OTWT distribution is expected to require more than 120,000 computing tasks (which will be elaborated at the end of this section), each of which requires the minimum CPU clock time of 10 minutes, which corresponds to a total CPU clock time of ~ 2.3 years. This evidence shows that serial processing on a standard work station is unfit to derive M in

a practical time frame. As a result, all simulations of the reformer CFD model and the derivation of M are executed on the Hoffman2 computing cluster at UCLA.

In this work, we designate 7 private-access high performance compute nodes with the total processing power of 128 cores and system memory of 1640 GB for simulations of the reformer CFD model. Under ANSYS Fluent parallel architecture, the CFD solver uses a core as a host process to create a communication pathway between the CFD solver and the graphical user interface (GUI) of an instance of ANSYS Fluent, and the remaining cores as computing-node processes to numerically calculate the solutions of the Navier-Stoke equations, energy balance and species balances in all control volumes. It is important to note that ANSYS Fluent parallel architecture allows the compute-node processes to be fully linked, so that they can effectively communicate, synchronize and perform global reductions via ANSYS Fluent message-passing interface (MPI). Next, the CFD solver uses the automatic mesh partition and load balancing function to divide the reformer mesh into 127 parts corresponding to the number of compute-node processes followed by assigning a different mesh partition to each compute-node process. Then, 127 compute-node processes simultaneously use the finite volume method to express the reformer mathematical model within each control volume of their respective assigned partitions in the form of algebraic equations by using divergence theorem and second order upwind interpolation algorithm, which are numerically solved. At the end of each iteration, 127 compute-node processes synchronize to calculate the global normalized residuals of all conserved variables, which are used as indicators for the steady-state CFD solver to terminate and for the transient CFD solver to advance to the next time step. We note that the steady-state solutions and transient solutions of the reformer CFD model executed on 7 private-access high performance compute nodes on the Hoffman2 computing cluster using ANSYS Fluent parallel solver can be obtained within a day and 60 days, respectively.

In addition, we exploit the intrinsically distributed structure of the statistical-based model identification and designate our shared computational resources on the Hoffman2 computing cluster to derive M from the reformer data, of which optimized hyperparameters are selected by two times 10-fold cross validation (CV) method. To this end, a massive number of computing tasks are sub-

mitted to the job scheduler of the Hoffman2 cluster, which automatically and optimally dispatches computing tasks. Specifically, 336 job arrays, each of which hosts 460 independent model building processes for the i th CV prediction models are submitted to identify the optimized LASSO parameters for the derivations of the prediction models. Simultaneously, 336 additional job arrays, each of which hosts 80 independent model building processes for the i th CV correction models are submitted to identify the optimized theoretical semivariogram model for the derivations of the correction models. Subsequently, 336 computing tasks for deriving the “forecasting” prediction models and 336 additional computing tasks for deriving the “forecasting” corrections models using the respective optimized hyperparameters are submitted to the job scheduler. Finally, 420 computing tasks for identifying the optimized value of w^P of M are submitted to the job scheduler. The resulting data-driven model for the OTWT distribution, of which hyperparameters are optimized to improve forecasting accuracy using two times 10-fold CV method, can be obtained within a day on the shared computing cluster. Additionally, in the event that new steady-state measurements of the OTWT distribution inside the reformer become available, they can always be integrated into the reformer database, and M can be retrained in real-time. The ability to perform on-line model reidentification is due to the distributed structure of the statistical-based model identification, the availability of the high performance computing cluster and the justifiable use of the previously optimized hyperparameters. Thus, this feature allows the balancing procedure to utilize the most up-to-date data-driven model at all times so that the optimized reformer fuel input is always the most optimal solution.

5.8 Simulation results

5.8.1 Validation of data-driven model for the OTWT distribution

In this subsection, the results generated from two times 10-fold cross-validation studies in the derivation of the data-driven model for the OTWT distribution from the reformer database are used to demonstrate the importance of using the optimized hyperparameters for obtaining accurate estimations of the OTWT distribution. To this end, we consider the derivation of the prediction and correction models for two representative OTWTs, namely, *65th* and *161st* OTWTs, of reforming tubes in two distinct local environments, which are characterized based on their respective proximity to the combustion chamber wall. The results of the cross-validation studies in the derivation of M_{64}^P and M_{161}^P are presented in Figs. 5.6 and 5.7 based on which the corresponding optimized LASSO parameters are chosen. Figs. 5.6 and 5.7 show that choosing an arbitrarily small LASSO parameter to allow the sparse non-linear regression to favor minimizing the CV fitting errors tends to result in overfitting models, which are indicated by small CV fitting errors and large CV forecasting errors. To the contrary, choosing an arbitrarily large LASSO parameter to allow that sparse non-linear regression to favor minimizing the model complexity tends to result in underfitting models, which are indicated by large CV fitting errors and large CV forecasting errors. Next, the results of the cross validation studies in the derivations of M_{64}^C and M_{161}^C are presented in Figs. 5.8 and 5.9, based on which the corresponding optimized theoretical semivariogram models are chosen. Figs. 5.8 and 5.9 show that an incorrect choice of the theoretical semivariogram model to describe the spatial correlation in OTWTs in the Kriging neighborhood can have a detrimental impact on the forecasting and resubstitution accuracy of the respective correction models. Figs. 5.6–5.9 also reveal that the choice of optimized hyperparameters is not universal. In particular, the optimized LASSO parameters for the derivation of M_{64}^P and M_{161}^P are 0.9 and 0.4, respectively, and the optimal theoretical semivariogram models for the derivation of M_{64}^C and M_{161}^C are the exponential anisotropic and linear omnidirectional models, respectively. Subsequently, the results of the cross

validation study in the derivations of M are presented in Figs. 5.10 and 5.11, based on which the optimized value of w^P , denoted by \hat{w}^P , is estimated. $\hat{w}^P=0.65$ indicates that the decision to incorporate information about the spatial correlation in OTWTs among neighboring reforming tubes into M improves its forecasting accuracy and, therefore, justifies the design of the statistical-based model identification. These findings suggest that two times 10-fold cross validation is a reliable accuracy estimation technique to obtain the optimized hyperparameters from the reformer database in a sense that it assesses and compares the forecasting performance of CV data-driven models derived from all given choices of hyperparameters on the basis of root mean square (RMS) errors with low bias. In addition, this evidence suggests that all hyperparameters used in the derivation of M must be independently and optimally selected.

In the remainder of this subsection, we demonstrate that M , which is derived with the optimized hyperparameters estimated from the presented cross-validation studies and the reformer database, has an excellent resubstitution accuracy using the fitting errors as a metric. Fig. 5.12 shows that the descriptive statistics, i.e., the maximum, average and minimum OTWTs, of the estimated OTWT distribution, which is calculated by using the documented reformer fuel inputs and M , are consistent with those of the respective plant data in the reformer database. Specifically, the maximum deviations of the maximum, average and minimum OTWTs between the estimated OTWT distribution and the corresponding plant data are 7.9 K, 2.0 K and 16.9 K, respectively, and are considered to be negligible with respect to the magnitude of the OTWTs. Fig. 5.12 also reveals that M exhibits a common characteristic of interpolation methods, i.e., ordinary Kriging, in which the maximum OTWTs are underestimated, while the minimum OTWTs are overestimated. In addition, due to the use of a sufficiently large training set, i.e., more than 25 data sets, in the derivation of M , the central limit theorem (CLT) can be used to get a quantitative assessment of the fitting errors of the maximum, average and minimum OTWTs between the estimated OTWT distribution and the corresponding plant data. In particular, the mean residual (\bar{e}_j) and residual standard error (s_j) of

the descriptive statistics estimated by M can be computed as follows,

$$\bar{e}_j = \frac{1}{N} \sum_{i=1}^N e_j^i \quad (5.20a)$$

$$s_j^2 = \frac{1}{N-1} \sum_{i=1}^N (e_j^i - \bar{e}_j)^2 \quad (5.20b)$$

where j represents different types of the descriptive statistics, e.g., j is *max*, *min* and *ave* and N is the number of data sets in the reformer database. It is found that the estimated maximum OTWT from M has the mean residual of -3.2 K and the residual standard error of 3.8 K, the estimated minimum OTWT from M has the mean residual of 5.2 K and the residual standard error of 17.6 K, and the estimated average OTWT from M has the mean residual of -0.03 K and the residual standard error of 0.72 K as shown in Fig. 5.13. This finding and the feature of M must be accounted for in the formulation of the model-based balancing procedure that aims to maximize the conversion of methane via SMR within the physical limitation of the reforming tube wall material. Next, we wish to demonstrate that M can also generate adequately accurate estimates for all reforming tubes inside the reformer in addition to the maximum, average and minimum values of the OTWT distribution. In this effort, we create two heat maps of the OTWT distribution from the estimates generated by using M and the optimized reformer fuel input at the nominal total fuel flow rate (as shown in Fig. 5.14(a)) and from the corresponding plant data (as shown in Fig. 5.14(b)) to visually assess the resubstitution accuracy of M . Fig. 5.14 shows that the hot and cold regions in the estimated OTWT distribution are consistent with those in the corresponding plant data. This evidence indicates that M derived by the statistical-based model identification with the optimized hyperparameters estimated from the two times 10-fold cross-validation studies is the reliable model for the OTWT distribution. Therefore, M can be used to create the furnace-balancing optimizer to determine the optimized flow control valve distribution that aims to minimize the degree of nonuniformity in the OTWT distribution at any given total fuel flow rate.

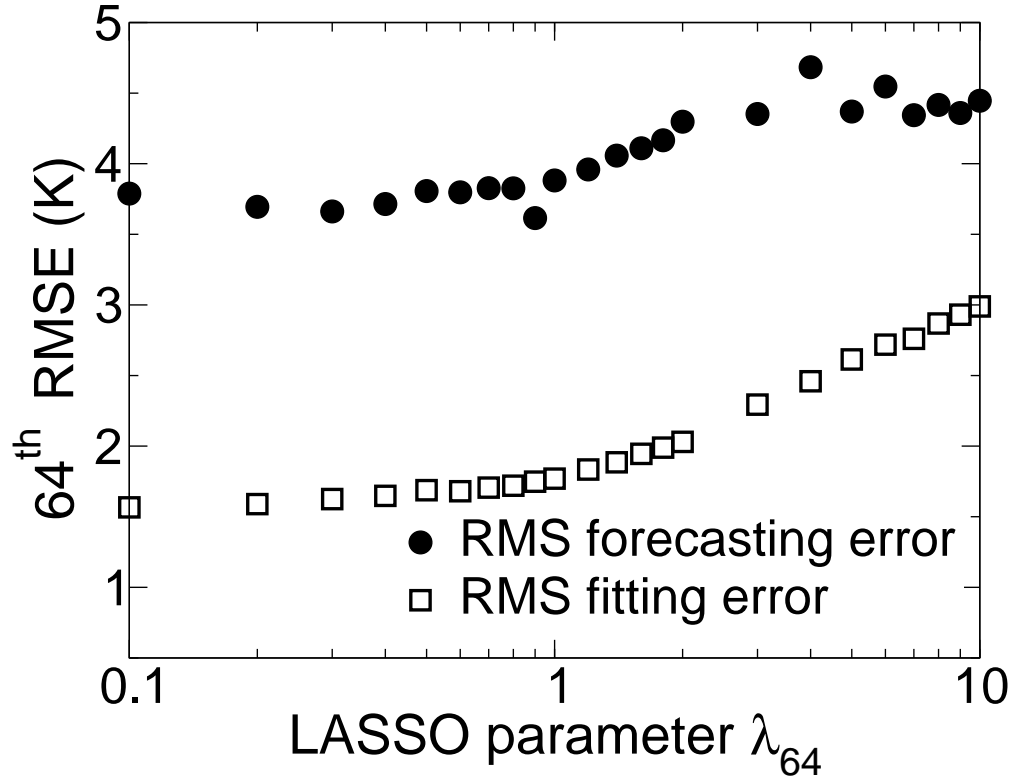


Figure 5.6: RMS fitting and forecasting errors associated with the proposed values of λ_{64} generated from the two times 10-fold cross-validation study in the derivation of M_{64}^P are plotted in empty squares and black circles, respectively.

5.8.2 Dynamic response of the reformer

In this subsection, the transient response of the reformer, and particularly, the OTWT distribution, is investigated when the total fuel flow rate is increased to increase the plant throughput, and based on which we design the appropriate strategy to implement to the maximized total fuel flow rate estimated by the furnace-balancing scheme. To this end, we propose two case studies in which the total fuel flow rate is increased by $\sim 2\%$ (1.8 kg s^{-1}) and $\sim 22\%$ (21.6 kg s^{-1}), respectively, from the nominal flow rate of 98.133 kg s^{-1} . In both cases, the optimized valve distribution identified in Chapter 3 is used to distribute the total flow rate in the reformer operated at higher capacities, and the steady-state solution generated by the reformer CFD model at the nominal total fuel flow rate and the corresponding optimized valve distribution is used as the initial condition. Subsequently,

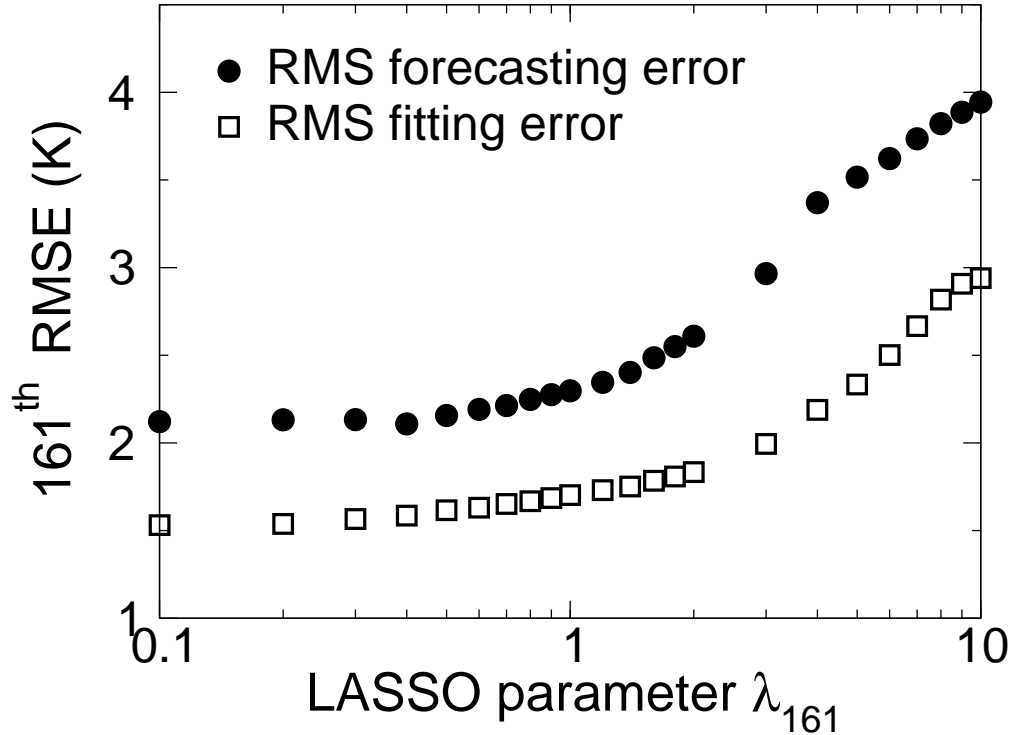


Figure 5.7: RMS fitting and forecasting errors associated with the proposed values of λ_{161} generated from the two times 10-fold cross-validation study in the derivation of M_{161}^P are plotted in empty squares and black circles, respectively.

ANSYS Fluent parallel solver with the explicit step size of 0.5 s and the max iterations per time step of 100 (determined by trial and error) is used to obtain the transient response of the reformer CFD model to step inputs. It is important to note that the predefined max iteration per time step must be sufficiently large so that the ANSYS Fluent parallel solver can iterate to convergence, which is defined by the global normalized residuals of conserved variables of which values are strictly smaller than 10^{-5} , within each time step for a given predefined step size. In an effort to track the convergence progress of the transient simulations of the reformer CFD model, we monitor the mole fractions of hydrogen and unreacted steam in the synthesis gas of the reformer, the OTWTs at a fixed distance of 6.5 m away from the reformer ceiling of 42 representative reforming tubes and the maximum OTWTs across the reforming tube length of a few selected reforming tubes as shown in Fig. 5.15. A transient simulation of the reformer CFD model subjected to a step increase in the total fuel flow rate is said to reach convergence when the monitored transport variables fully

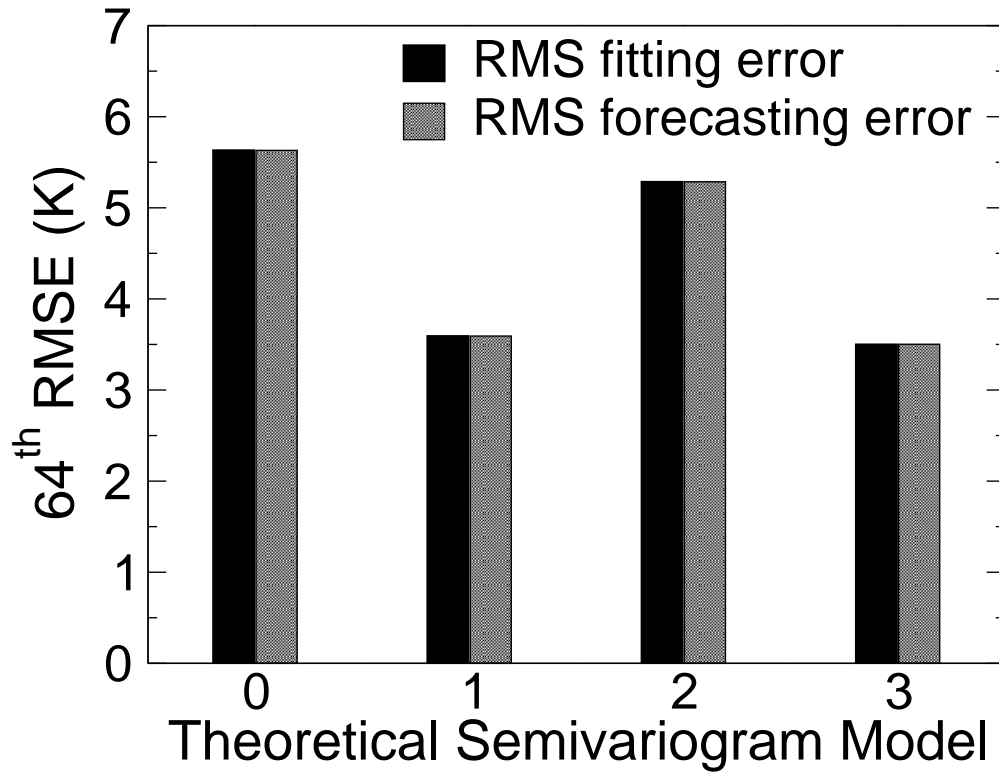


Figure 5.8: RMS fitting and forecasting errors associated with each of the four theoretical semivariogram models (given on the horizontal axis as 0, 1, 2, and 3, which correspond to linear omnidirectional, linear anisotropic, exponential omnidirectional, and exponential anisotropic theoretical semivariogram models, respectively) considered in the two times 10-fold cross-validation study in the derivation of M_{64}^C are plotted in gray and black, respectively.

relax to the steady-state values. In addition, to validate the transient solutions acquired by solving the reformer CFD model with ANSYS Fluent transient solver, we will compare the monitored transport variables recorded at the last sampling time in the transient simulations to those extracted from the converged solutions of the corresponding steady-state simulations.

In the remainder of this subsection, the transient response of the monitored transport variables to the deterministic step changes in which the total fuel mass flow rate is increased by 1.8 and 21.6 kg s^{-1} , respectively, are presented as shown in Table 5.1 and Figs. 5.16–5.20. Table 5.1 shows that the steady-state values of the monitored transport variables generated by the transient simulations are consistent with those generated by the steady-state simulations, which confirms that the phys-

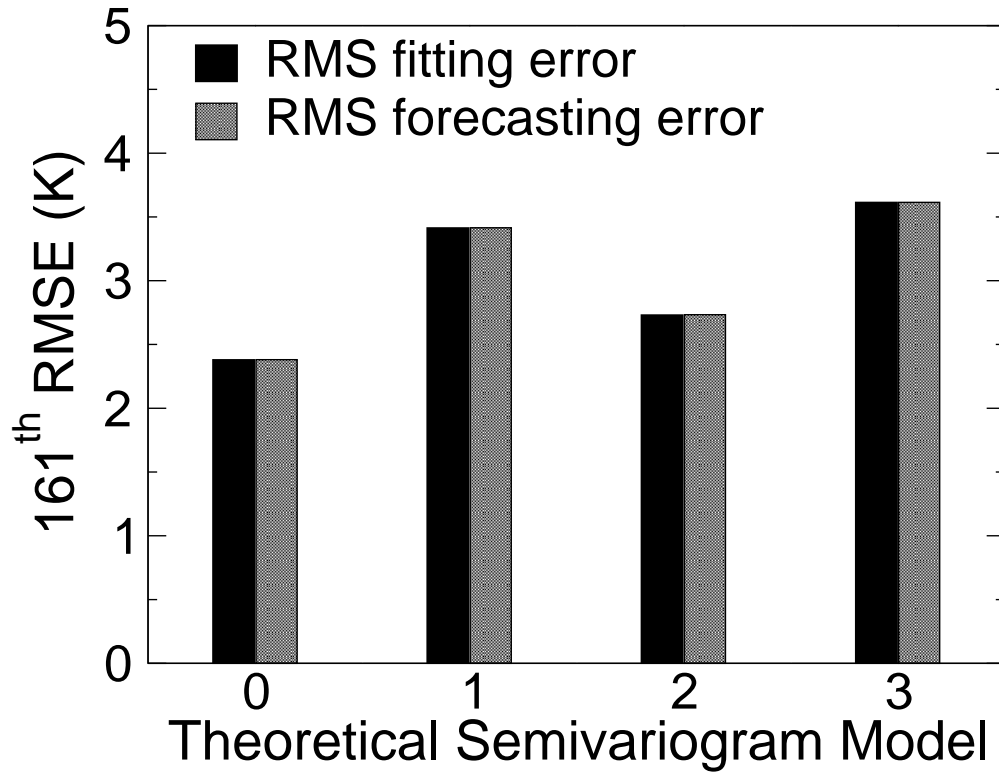


Figure 5.9: RMS fitting and forecasting errors associated with each of the four theoretical semivariogram models (given on the horizontal axis as 0, 1, 2, and 3, which correspond to linear omnidirectional, linear anisotropic, exponential omnidirectional, and exponential anisotropic theoretical semivariogram models, respectively) considered in the two times 10-fold cross-validation study in the derivation of M_{161}^C are plotted in gray and black, respectively.

ical time of 400 s is sufficient for the transient simulations of the reformer CFD model subjected to a step increase in the total fuel flow rate at $t=0$ s to reach steady-state. Specifically, the transient response (shown in Figs. 5.16–5.20) and steady-state values (shown in Table 5.1) of the monitored transport variables indicate that the reformer reaches steady-state within ~ 350 s, and the reformer time constant is independent of the magnitude of the step increase in the total fuel flow rate. It is also interesting to note that the reformer time constant is expected to be insensitive to operational disturbances associated with flow control valves because the disturbances considered in this study can only affect the reformer fuel input, e.g., stuck valves may cause the spatial distribution of the optimized reformer fuel input inside the reformer to become nonoptimal. In addition, the transient

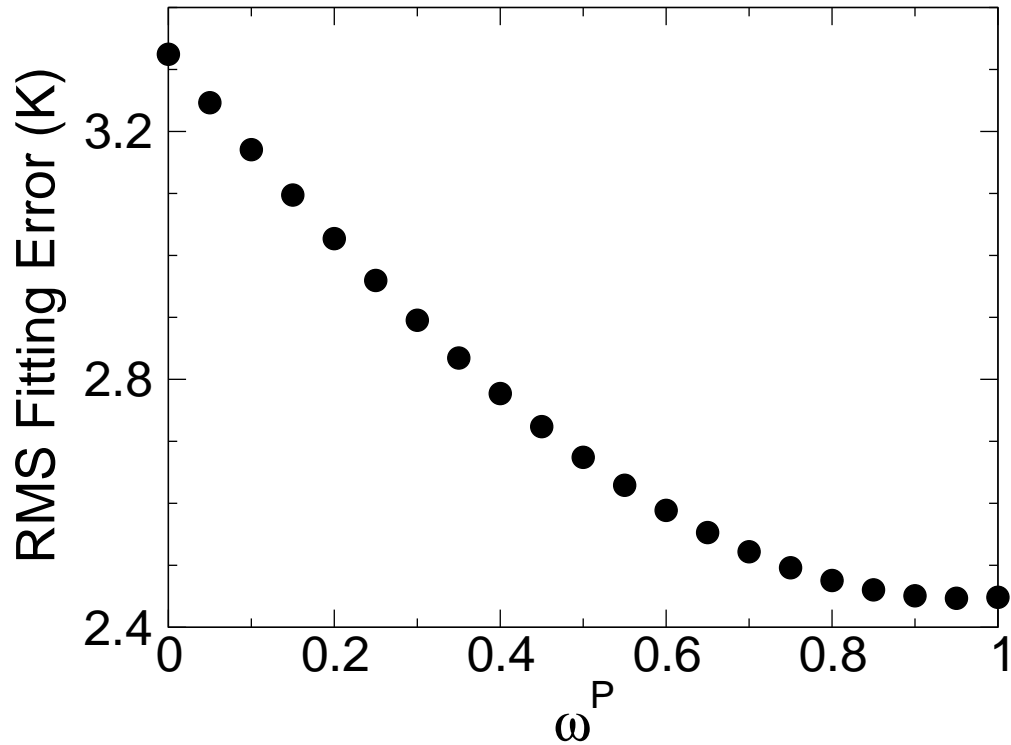


Figure 5.10: RMS fitting errors associated with the proposed values of w^P generated from the two times 10-fold cross-validation study in the derivation of M are plotted in black circles.

response of the OTWTs at a fixed distance of 6.5 m away from the reformer ceiling shown in Figs.5.16 and 5.17 and the transient response of the maximum OTWTs across the reforming tube length shown in Fig. 5.18 exhibit characteristics of first-order systems in which the initial rates of change are the largest, and the monitored OTWTs monotonically reach the new steady-state values. The prior can be explained by the rapid combustion of the furnace-side fuel coupled with fast thermal radiative heat transfer in the high temperature combustion chamber, which allows the reforming tubes to instantaneously experience the step increase in the total fuel flow rate. While the latter is believed to be the result of rapid energy consumption due to the endothermic SMR in the tube side, which prevents the accumulation of thermal energy in the reforming tube wall and, therefore, dismisses all possibility to observe the overshoot response of OTWTs. To the contrary, the transient response of the hydrogen and unreacted steam mole fractions in the synthesis gas as shown in Figs. 5.19 and 5.20 exhibit characteristics of overdamped second order systems, in which

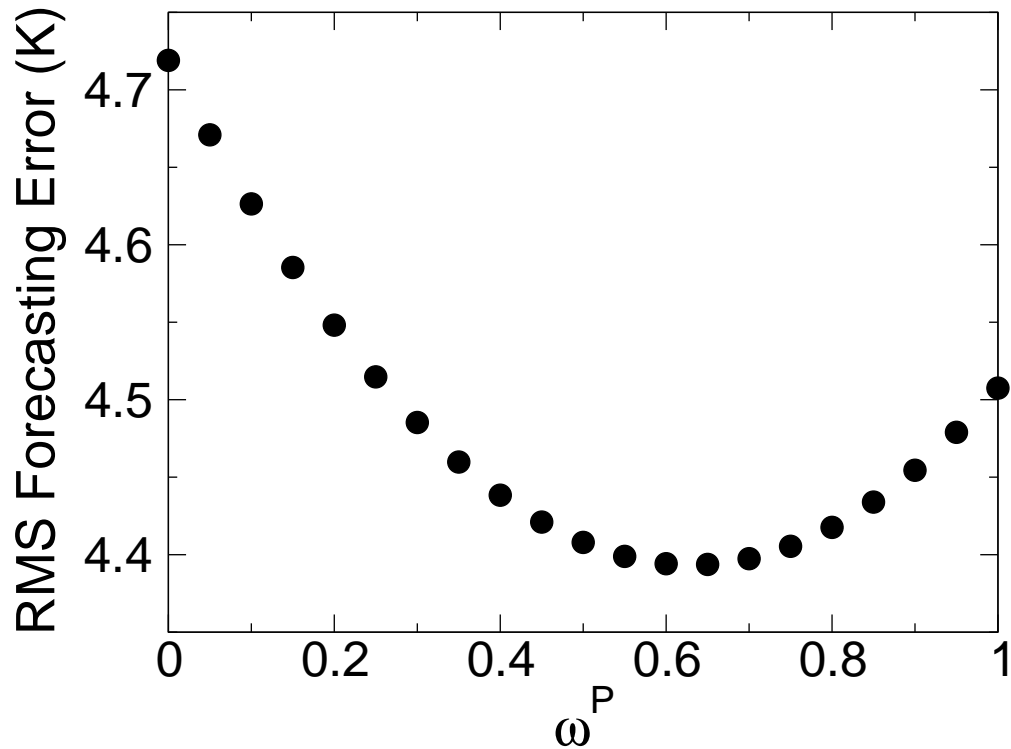


Figure 5.11: RMS fitting errors associated with the proposed values of w^P generated from the two times 10-fold cross-validation study in the derivation of M are plotted in black circles.

the monitored mole fractions reach the new steady-state values without oscillatory; however, the largest rates of change occur well after $t=0$ s, e.g., $t=50$ s. This observation can be justified by the thermal resistance of the reforming tube walls and of the catalyst network. The analysis of the transient response of the monitored transport variables in the proposed case studies supports the assumption that upon a step increase in the total fuel flow rate, the maximum OTWT across the reforming tube length of each reforming tube is expected to monotonically approach its steady-state value without overshoot. The assumption implies that the optimized reformer fuel input predicted by the furnace-balancing scheme in a sense that the steady-state values of the maximum OTWTs across the reforming tube length of all reforming tubes are approaching the design temperature of the reforming tube wall can be implemented in a step change fashion without burning out the reforming tubes. In addition, the transient solutions are valuable resources, which allows us to quantitatively assess the forecasting accuracy of M (derived with the optimized hyperparameters

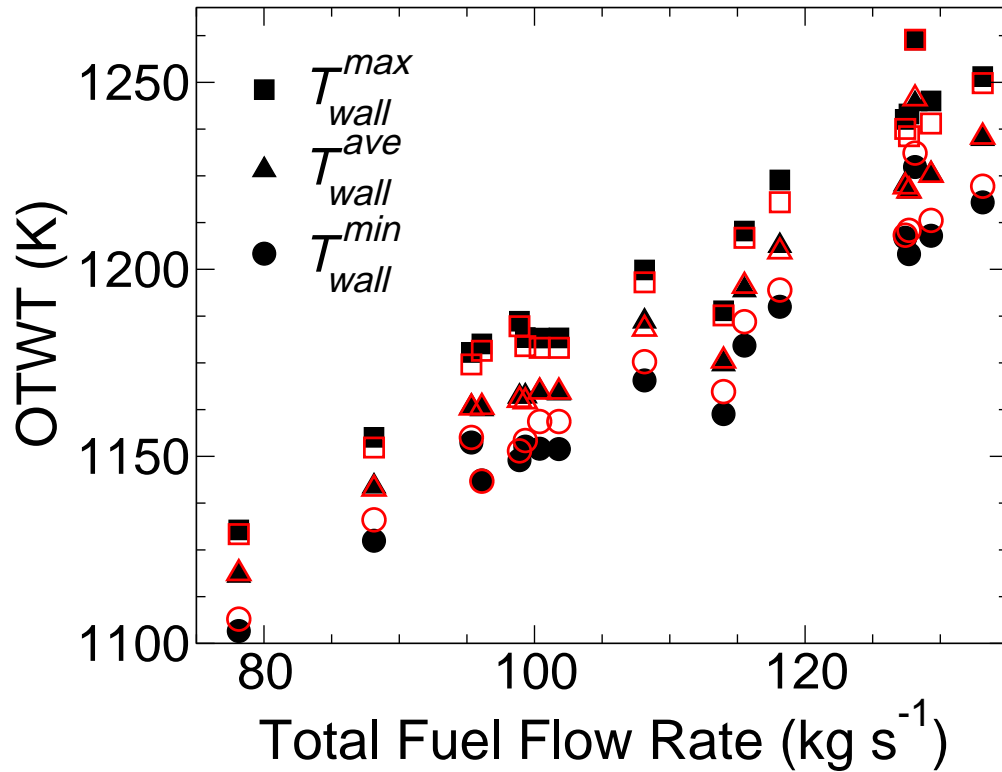


Figure 5.12: Comparison of the maximum, average and minimum values in the OTWT distribution between the plant data (represented by filled black symbols) and the corresponding estimate computed by M (represented by the empty red symbols) at varying total fuel flow rates. In Fig. 5.12, we use jitter to add a small uniform random number on the range from -2% to 2% of the original total flow rate to itself for visual clarity.

estimated from the cross-validation studies and the reformer database) using the forecasting errors as a metric. Fig. 5.21 shows that the forecasting errors of the descriptive statistics between the estimated OTWT distribution, which is calculated by using M and the reformer fuel inputs proposed for the investigation of the reformer dynamic behavior, and the corresponding OTWT distribution, which is documented at the last sampling time in the transient simulations, are within two residual standard error from the mean residual of the respective quantities. Specifically, the maximum residuals of the maximum, average and minimum OTWTs between the estimated OTWT distribution and the corresponding plant data are 6.6 K, 1.1 K and 9.6 K, respectively. Fig. 5.22 shows that the contour heat map of the estimated OTWT distribution generated by using M and the reformer

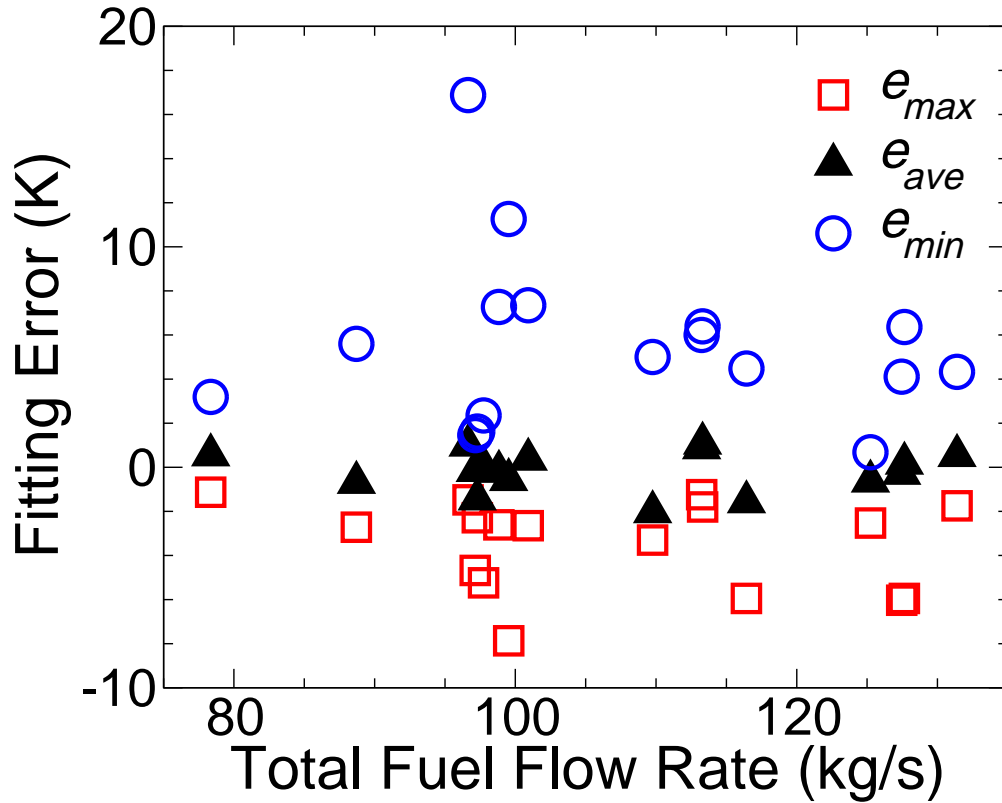


Figure 5.13: Fitting errors of the maximum, average and minimum OTWTs between the estimated OTWT distribution, which is computed using the plant inputs and M , and the corresponding plant data. In Fig. 5.13, we use jitter to add a small uniform random number on the range from -2% to 2% of the original total flow rate to itself for visual clarity.

fuel input designed for the second transient case study (as shown in Fig. 5.22(a)) has similar features (e.g., locations of the hot and cold regions) to that of the corresponding OTWT distribution documented at the last sampling time in the transient simulation (as shown in Fig. 5.22(b)). This analysis justifies the assumption that M is the accurate model for the OTWT distribution in Section 5.8.1. Therefore, it can be stated with high certainty that in the reformer operated under the optimized total fuel flow rate and the corresponding optimized valve distribution predicted by the furnace-balancing scheme, the steady-state values of the maximum OTWTs across the reforming tube length of all reforming tubes are expected to be strictly less than the design temperature of the reforming tube wall.

Table 5.1: Comparison of representatives of the monitored transport variables documented at the last sampling time in the transient simulation of the reformer that is subjected to the positive step change of 21.6 kg s^{-1} in the total fuel flow rate from the nominal value to those extracted from the converged solutions of the corresponding steady-state simulation.

	Steady-state solution	Transient solution	Percent deviation (%)
T_{wall}^{96} (K)	1213.8	1214.7	0.1
T_{wall}^{103} (K)	1205.6	1205.0	0.0
T_{wall}^{111} (K)	1219.5	1219.7	0.0
T_{wall}^{112} (K)	1217.6	1217.9	0.0
T_{wall}^{119} (K)	1203.9	1203.7	0.0
T_{wall}^{127} (K)	1215.4	1214.4	0.1
T_{wall}^{16} (K)	1212.7	1213.0	0.0
T_{wall}^{64} (K)	1217.9	1218.0	0.0
T_{wall}^{160} (K)	1215.0	1213.7	0.1
T_{wall}^{208} (K)	1219.0	1217.7	0.1
T_{wall}^{256} (K)	1221.0	1222.3	0.1
$\ T_{wall}^1\ _{\infty}$ (K)	1245.9	1246.1	0.0
$\ T_{wall}^{63}\ _{\infty}$ (K)	1254.0	1254.6	0.0
$\ T_{wall}^{127}\ _{\infty}$ (K)	1248.7	1247.1	0.1
$\ T_{wall}^{191}\ _{\infty}$ (K)	1265.8	1265.3	0.0
$\ T_{wall}^{223}\ _{\infty}$ (K)	1245.2	1246.3	0.1
$\ T_{wall}^{251}\ _{\infty}$ (K)	1233.2	1233.8	0.0
$\ T_{wall}^{288}\ _{\infty}$ (K)	1253.6	1249.0	0.4
\bar{x}_{H_2}	0.320	0.320	0.0
\bar{x}_{H_2O}	0.500	0.500	0.0

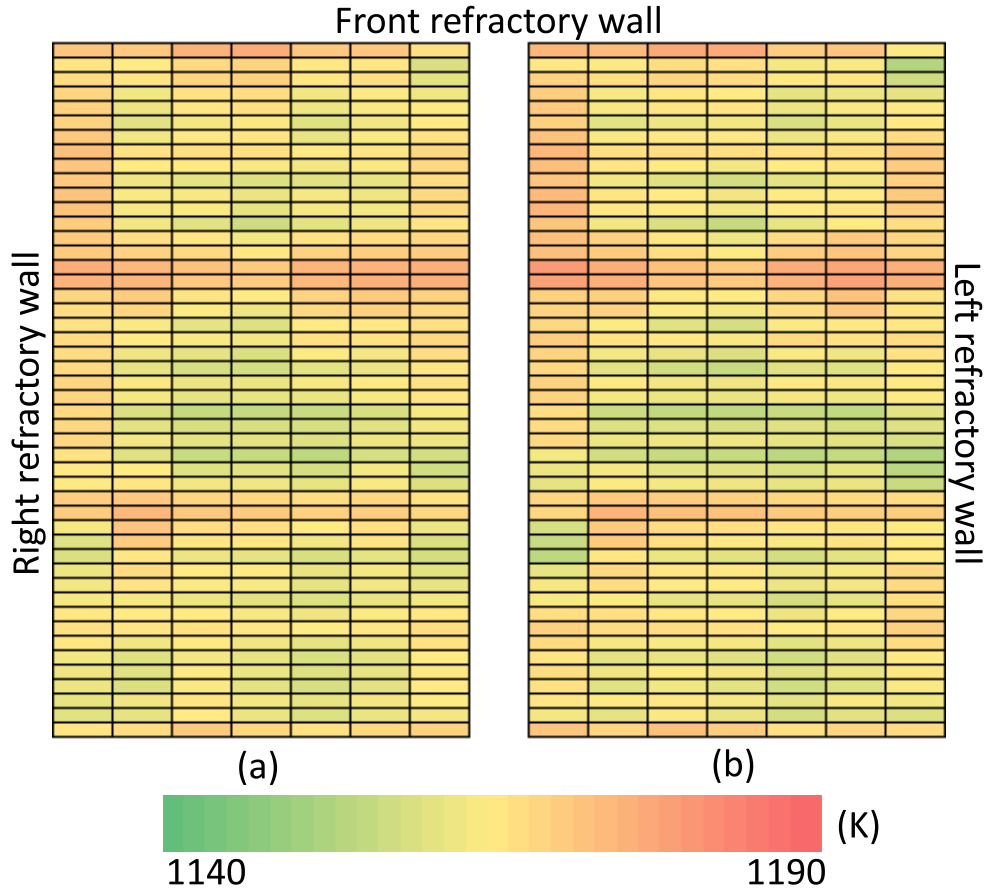


Figure 5.14: Comparison of the estimated OTWT distribution (a), which is generated by using M and the optimized reformer fuel input at the nominal total fuel flow rate, to the respective plant data (b). In Fig. 5.14, each cell represents a unique reforming tube, the location of each cell in the table corresponds to that of the respective reforming tube in the combustion chamber, of which orientation can be visualized by the keywords along the edges and Fig 5.2, and the color of each cell represents the value of the respective OTWT, which is specified by the colorbar.

5.8.3 Validation of the furnace-balancing scheme

In this subsection, we evaluate the performance of the balancing procedure under the following assumptions: all flow control valves in the reformer are operational, the initial total fuel flow rate of $98.133 \text{ kg sec}^{-1}$ is optimally distributed with the optimized valve distribution reported in [56, 57], and the design OTWT of the reforming tube wall (denoted by T_{wall}^{design}) taken from typical plant data has a value of 1300 K. To this end, we propose a systematic approach to estimate the

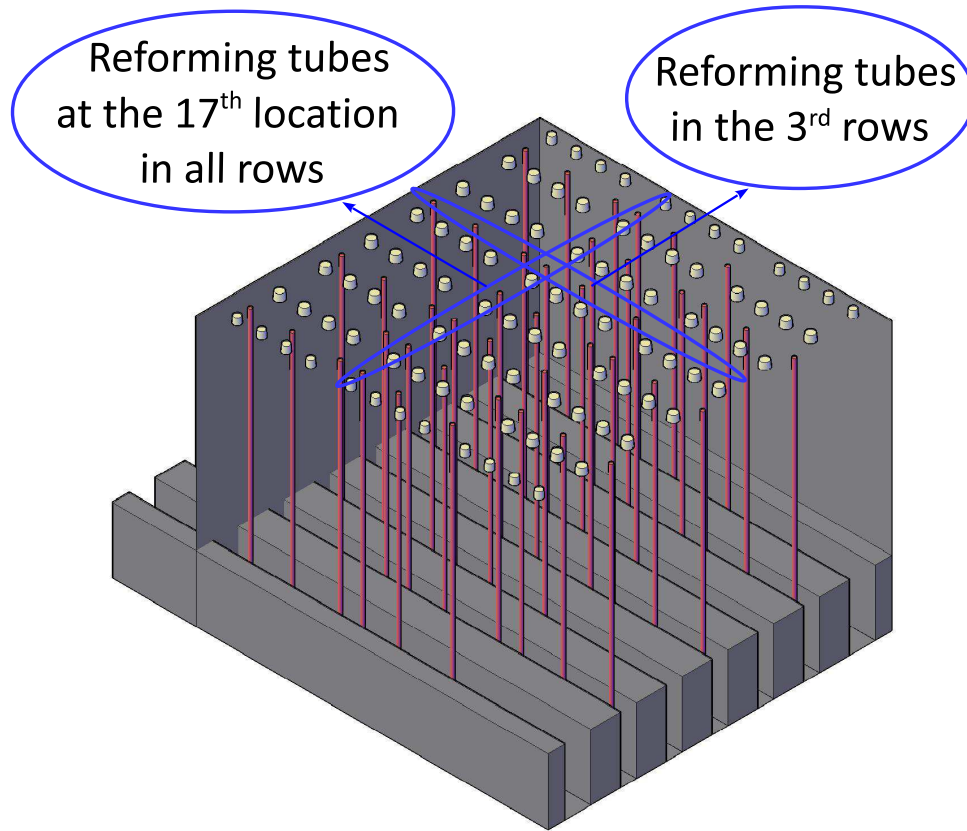


Figure 5.15: Isometric view of the reformer in which the right and back refractory walls are made transparent to display the reforming tubes of which OTWTs at a fixed distance of 6.5 m away from the reformer ceiling are monitored to track the convergence progress of the transient simulations of the reformer CFD model.

maximum allowable OTWT, which is a critical parameter of the furnace-balancing scheme because $T_{wall}^{max,*}$ directly controls the maximum total fuel flow rate and, therefore, the respective optimized valve distribution estimated by the proposed approach. Initially, a deliberate review of the results documented in [56, 57] reveals that the maximum OTWT along the reforming tube length among all reforming tubes (denoted by $T_{wall}^{max,*}$) does not necessarily occur in the OTWT distribution at a location 6.5 m from the reformer ceiling. In fact, the reformer database indicates that $T_{wall}^{max,*}$ is always larger than the maximum value in the OTWT distribution as shown in Fig. 5.23. This finding suggests that if the reformer were to be operated under the total fuel flow rate that permitted the maximum value in the OTWT distribution to be near T_{wall}^{design} , $T_{wall}^{max,*}$ would undoubtedly exceed

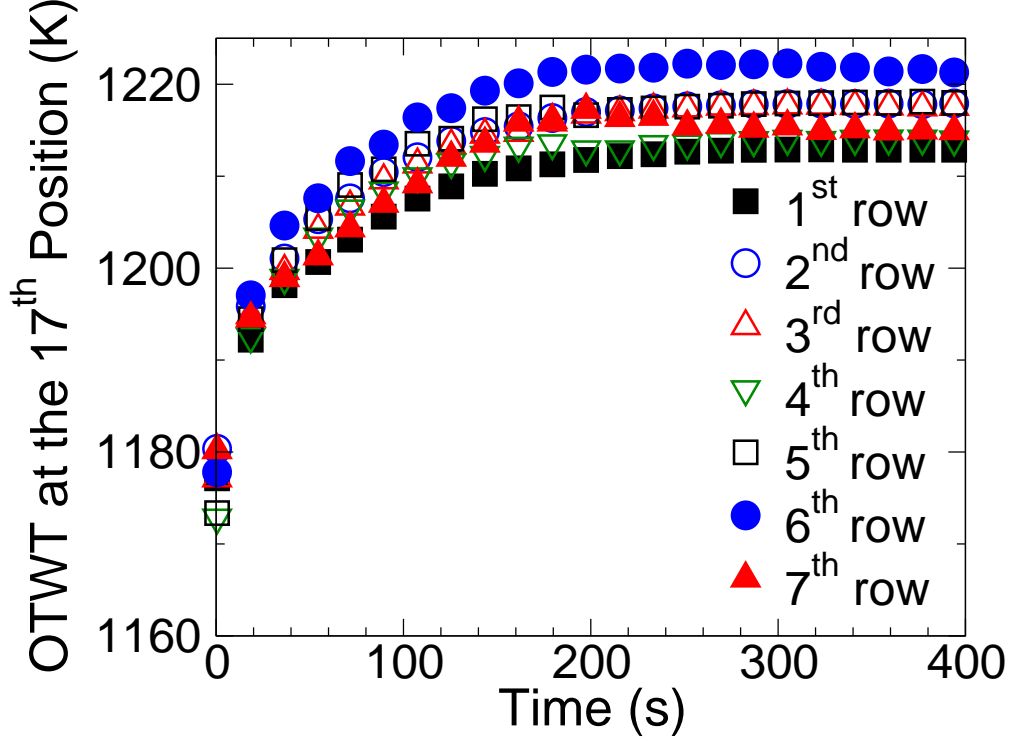


Figure 5.16: The transient response of the OTWTs at a fixed distance of 6.5 m away from the reformer ceiling of the reforming tubes at the 17th position across all rows inside the combustion chamber as shown in Fig. 5.15 to a positive step change of 21.6 kg s^{-1} in the total fuel flow rate from the nominal value.

T_{wall}^{design} , which would accelerate the degradation of the microstructure inside the reforming tube wall and cause the reforming tubes to rupture prematurely. Furthermore, as the maximum total fuel flow rate and the respective optimized valve distribution calculated with the furnace-balancing scheme is implemented in an open-loop control fashion in this work, it is necessary to also account for plant-model mismatch in the estimation of $T_{wall}^{max,*}$. Specifically, the residual analysis of the fitting errors of the data-driven model for the OTWT as presented in Section 5.8.1 provides an efficient means to estimate plant-model mismatch; as a result, $T_{wall}^{max,*}$ can be determined as follows,

$$T_{wall}^{max,*} = T_{wall}^{design} - \max_{1 \leq i \leq 26} \left\{ T_{wall,i}^{max,*} - \left\| \vec{T}_{wall}^i \right\|_{\infty} \right\} - (\bar{e}_{max} + 2.5s_{max}), \quad (5.21)$$

and $T_{wall}^{max,*}$ is found to be $\sim 1260 \text{ K}$. Then, we execute the balancing procedure on our shared

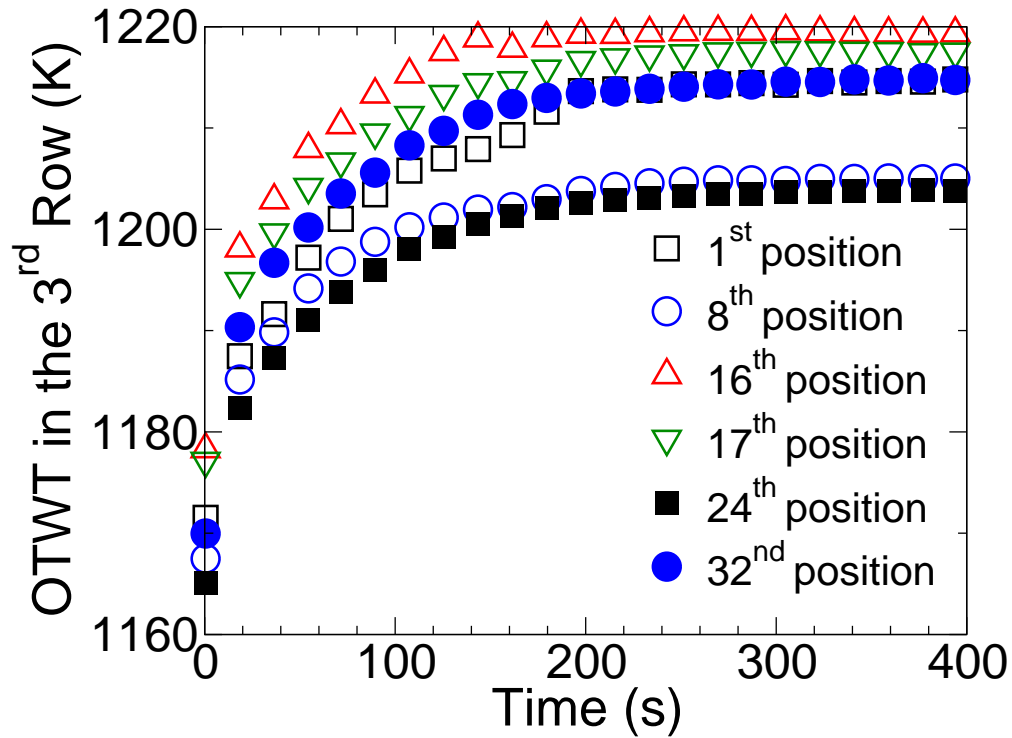


Figure 5.17: The transient response of the OTWTs at a fixed distance of 6.5 m away from the reformer ceiling of six representative reforming tubes along the 3rd row inside the combustion chamber as shown in Fig. 5.15 to a positive step change of 21.6 kg s^{-1} in the total fuel flow rate from the nominal value.

computational resources on the Hoffman2 computing cluster. The CPU clock time of a high performance computing core on the Hoffman2 computing cluster devoted for the balancing procedure to optimize the total fuel flow rate and its spatial distribution inside the reformer to maximize the methane conversion via SMR without violating the physical limitation of the reforming tube wall material is only on the order of a few minutes. This evidence highlights the potential of the balancing procedure for real-time optimization of the reformer to improve the plant-wise energy efficiency and to perform load alterations as well as to reject operational disturbances associated with flow control valves.

In the remainder of this subsection, the results generated from the balancing procedure under the predefined assumptions and $T_{wall}^{max,*}$ of 1260 K are presented as shown in Figs. 5.24 and 5.25. Specifically, Figs. 5.24 and 5.25 indicate that under the initial total fuel flow rate of 98.133 kg

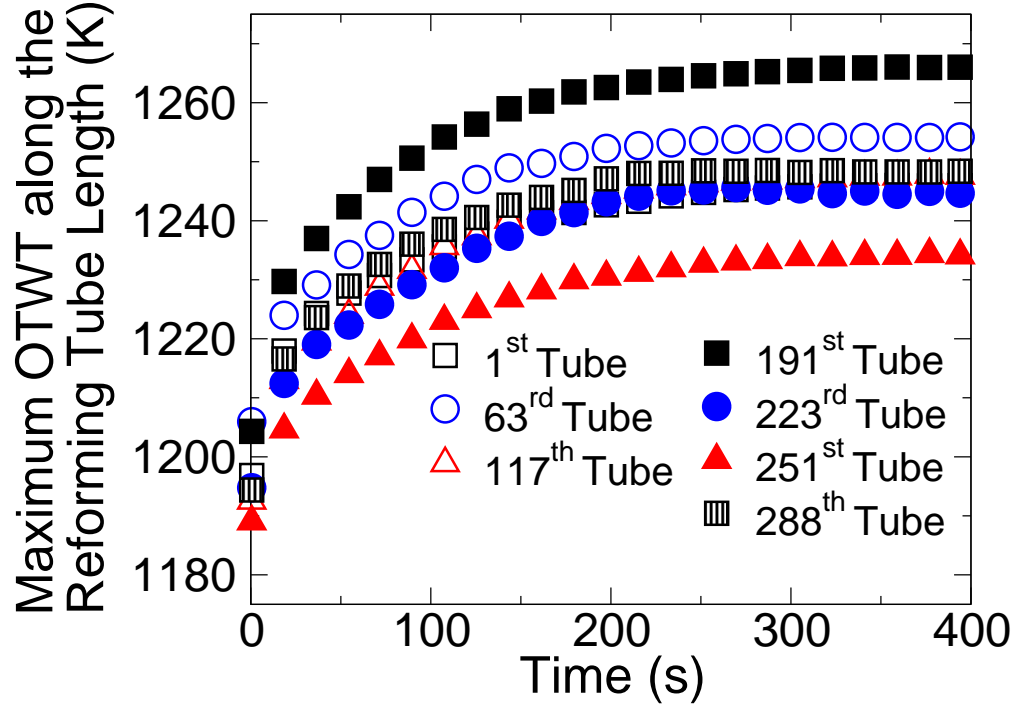


Figure 5.18: Transient response of the maximum OTWTs across the reforming tube length of seven representative reforming tubes at different regions inside the combustion chamber to a positive step change of 21.6 kg s^{-1} in the total fuel flow rate from the nominal value.

sec^{-1} optimally distributed with the respective valve distribution, $\hat{T}_{wall,0}^{max}$ is equal to 1175.25 K , which is smaller than $T_{wall}^{max,*}$; therefore, $\hat{T}_{wall,0}^{max}$ allows the aggressive search recursively to apply large increments to the total fuel flow rate to determine the smallest upper-bound value. In addition, Figs. 5.24 and 5.25 show that in the 4th iteration of the aggressive search, $F_{tot}^{4,1}$ of $137.4 \text{ kg sec}^{-1}$ is identified as the smallest upper-bound value because $\hat{T}_{wall,4}^{max,1}$ is equal to 1260.5 K and is greater than $T_{wall}^{max,*}$. Furthermore, Figs. 5.24 and 5.25 show that the conservative search gradually applies small decrements to the upper-bound value, and in the 1st iteration of the conservative search, $F_{tot}^{1,2}$ of $136.896 \text{ kg sec}^{-1}$ is identified as the optimized total fuel flow rate because $\hat{T}_{wall,1}^{max,2}$ begins to fall below $T_{wall}^{max,*}$ indicating that the reformer has returned into the safe operating regime. Finally, in the main layer of the furnace-balancing scheme, F_{tot}^{op} and the \vec{V}^{op} are translated into \vec{F}^{op} , which is applied as the reoptimized burner boundary conditions for the reformer CFD model in a step increase fashion, and the results are presented as shown in Fig 5.26. Specifically, Fig. 5.26 indicates

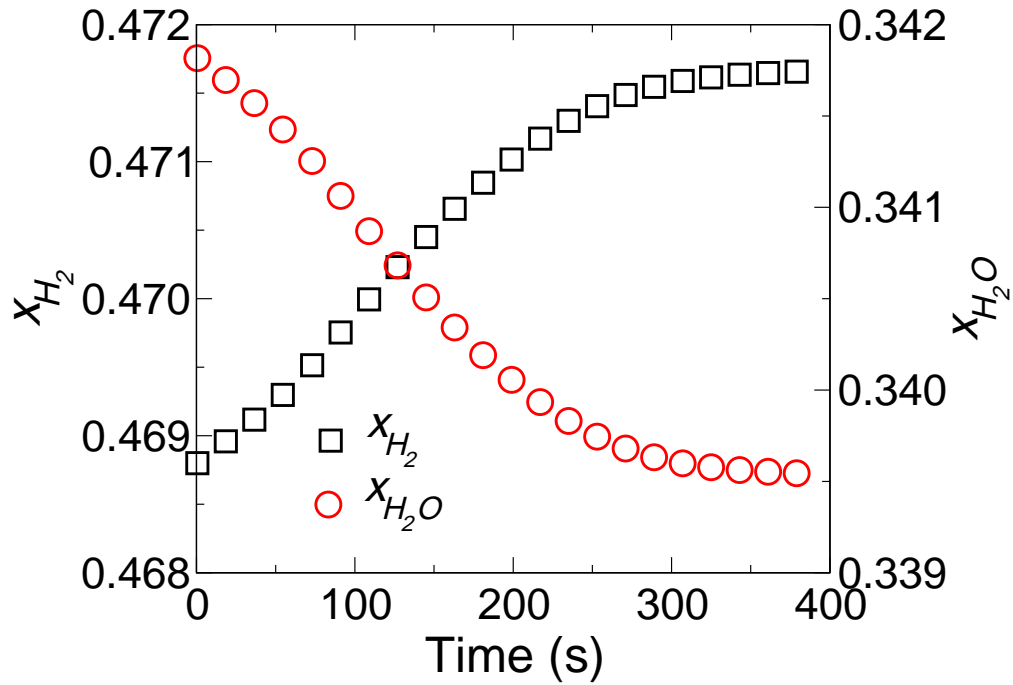


Figure 5.19: Transient response of the hydrogen and unreacted steam mole fractions in the synthesis gas to a positive step change of 1.8 kg s^{-1} in the total fuel flow rate from the nominal value.

that $T_{wall}^{max,*}$ is 1288.35 K, which is less than T_{wall}^{design} , and, therefore, justifies that a positive step change of $38.763 \text{ kg sec}^{-1}$, which is equivalent to $\sim 39.5\%$ increase from the nominal value, in the total fuel flow rate can be applied to achieve the optimized firing rate without accelerating the degradation of the microstructure of the reforming tube wall.

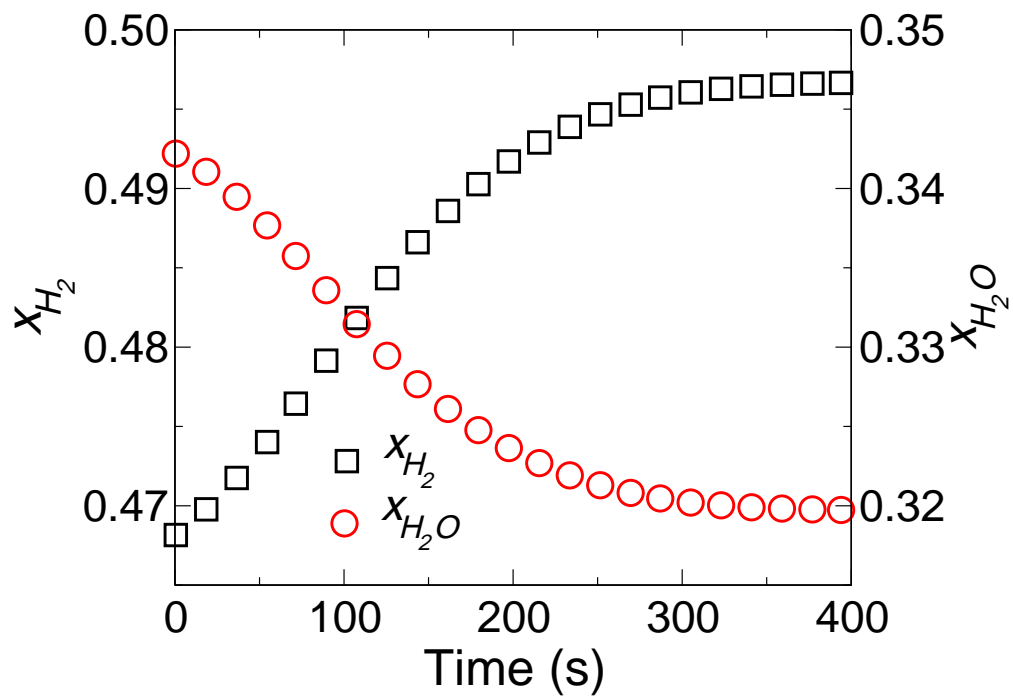


Figure 5.20: Transient response of the hydrogen and unreacted steam mole fractions in the synthesis gas to a positive step change of 21.6 kg s^{-1} in the total fuel flow rate from the nominal value.

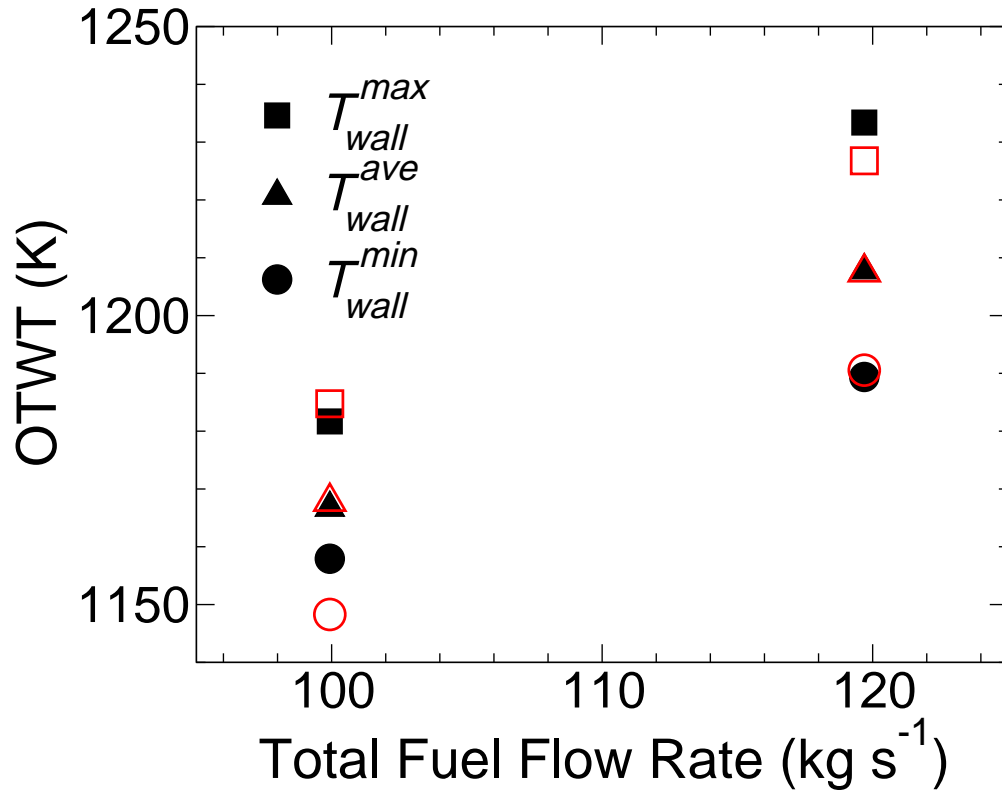


Figure 5.21: Comparison of the maximum, average and minimum values in the OTWT distribution between the plant data (represented by filled black symbols) and the corresponding forecasting estimate (represented by the empty red symbols) computed by M , the two proposed total fuel flow rates and the optimized valve distribution identified in Chapter 3.

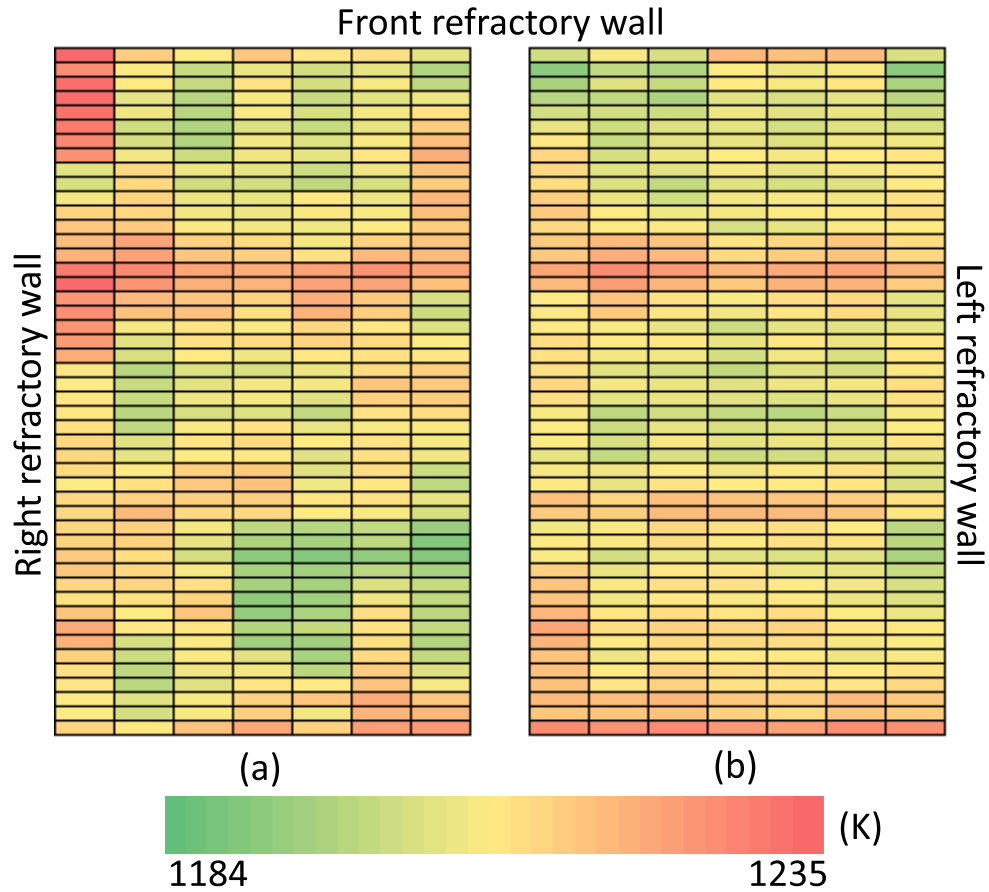


Figure 5.22: Comparison of the estimated OTWT distribution (a), which is generated by using M , the proposed total fuel flow rate for the second case study and the optimized valve distribution identified in Chapter 3, to the respective plant data (b). In Fig. 5.22, each cell represents a unique reforming tube, the location of each cell in the table corresponds to that of the respective reforming tube in the combustion chamber, of which orientation can be visualized by the keywords along the edges and Fig 5.2, and the color of each cell represents the value of the respective OTWT, which is specified by the colorbar.

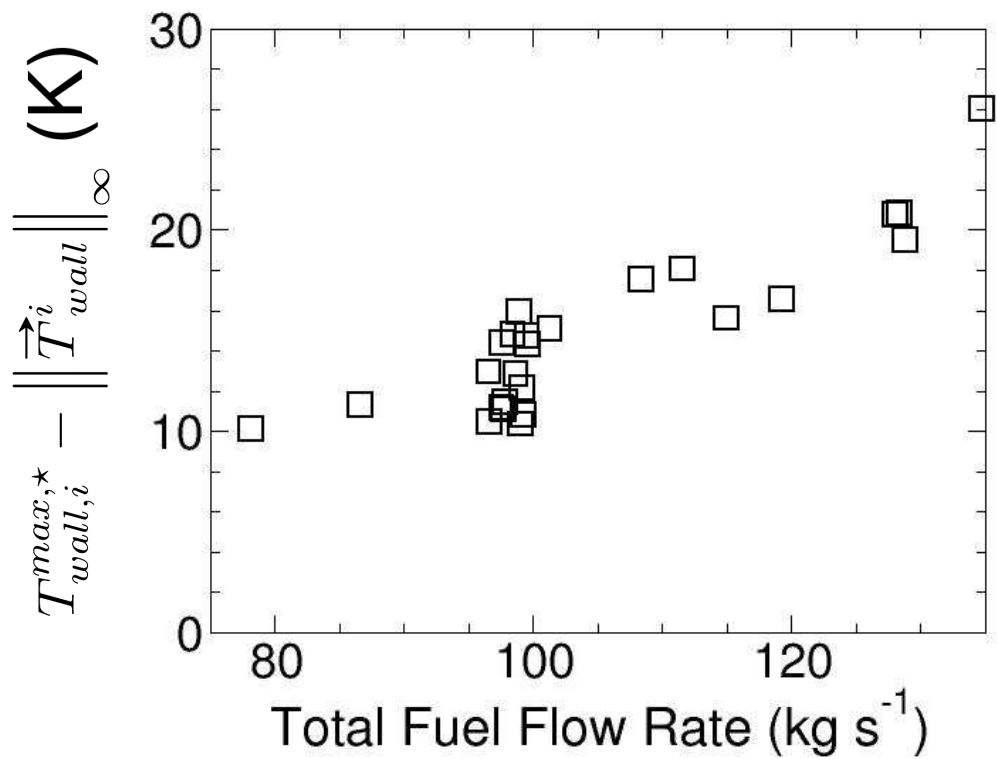


Figure 5.23: Temperature difference between the maximum OTWT along the reforming tube length among all reforming tube ($T_{wall}^{max,*}$) and the maximum value of the OTWT distribution ($T_{wall,i}^{max,*}$) when the reformer is operated under varying total fuel flow rates and varying valve distributions.

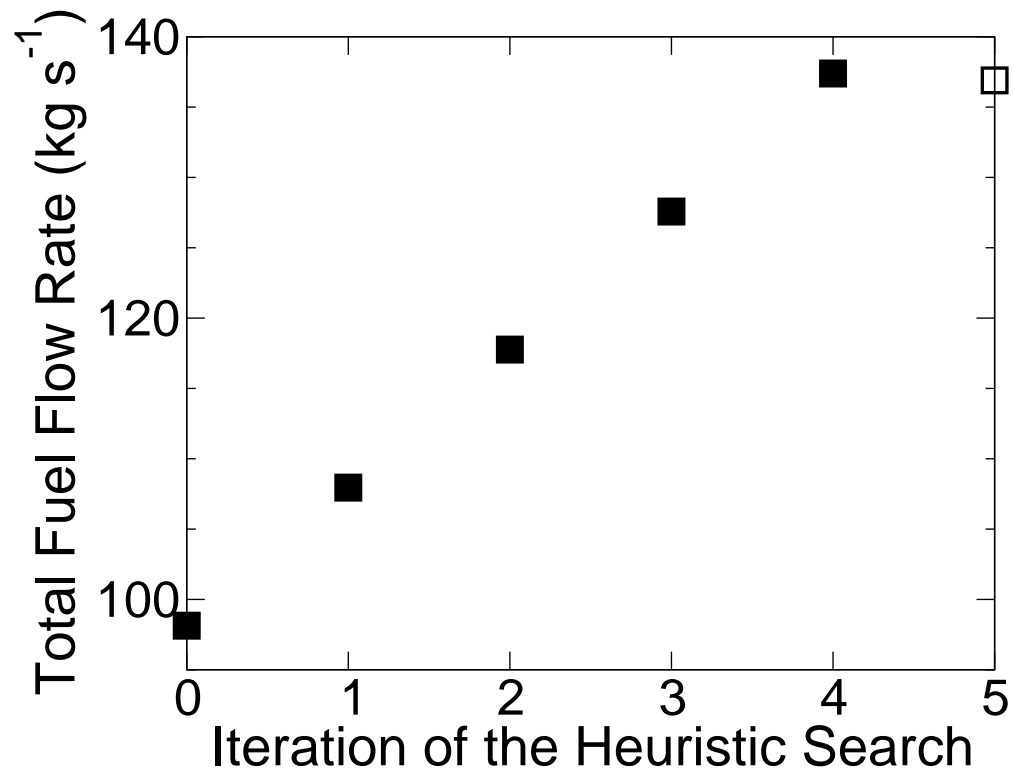


Figure 5.24: Total fuel flow rate generated by the aggressive flow rate generator (represented by the filled symbols) and by the conservative flow rate generator (represented by the empty symbols) in an effort to determine the maximized total fuel flow rate to achieve the desired reformer firing rate without causing premature failure of the reforming tubes.

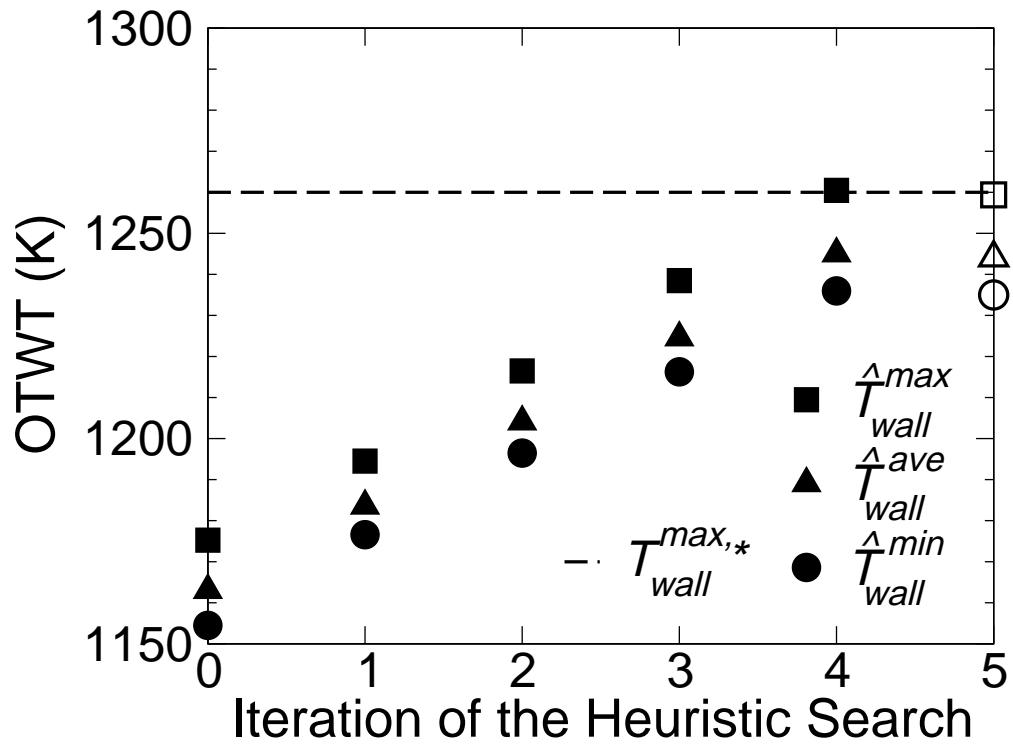


Figure 5.25: Maximum, average and minimum values of the estimated OTWT distribution, which is computed using M with the total fuel flow rate and the respective optimized valve distribution proposed by the aggressive search (represented by the filled symbols) and by the conservative search (represented by the empty symbols) in the process of estimating the maximized total fuel flow rate to achieve the desired reformer firing rate without causing premature failure of the reforming tubes.

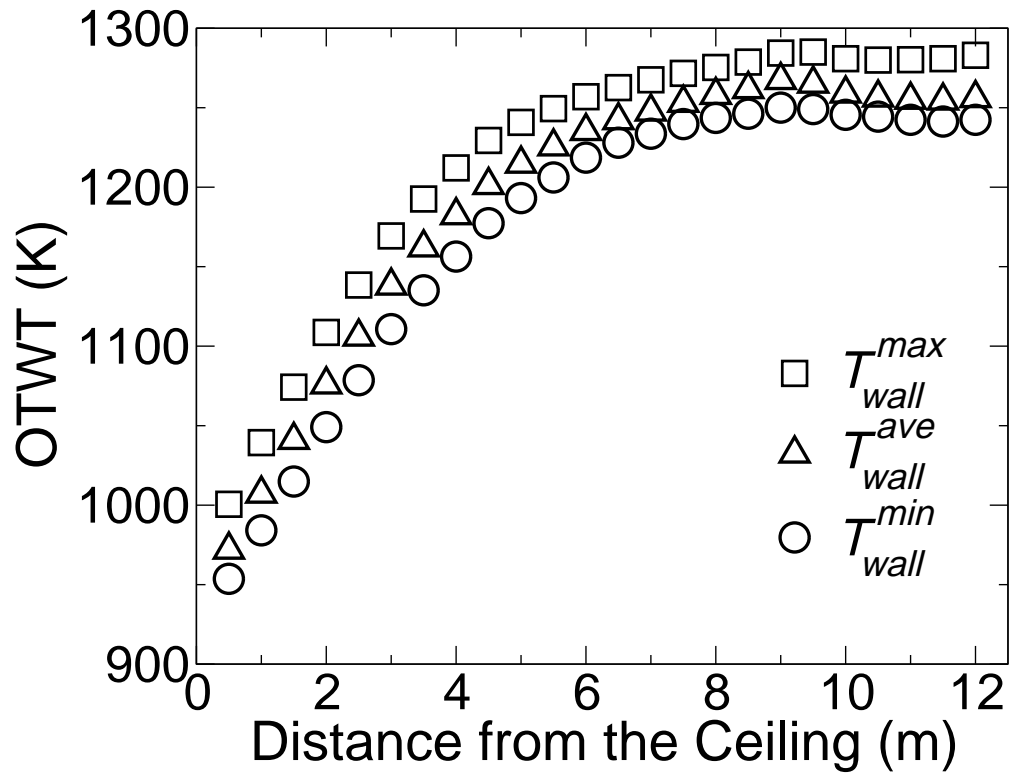


Figure 5.26: Maximum, average and minimum OTWT profile along the reforming tube length among all reforming tubes generated by the reformer CFD model in which the boundary conditions are adjusted based on the maximized total fuel flow rate and the corresponding optimized valve distribution that are identified by the balancing procedure.

5.9 Conclusion

In this work, a furnace-balancing scheme that simultaneously searches for the optimized total fuel flow rate and the respective optimized valve distribution to increase the methane conversion via SMR without accelerating the degradation of the microstructure of the reforming tube wall material was proposed. To this end, a high fidelity CFD model for the reformer, assumed to represent the on-line unit at an SMR-based hydrogen facility, was used to characterize the previously unstudied dynamic behavior of the reformer. Specifically, the reformer that was initially operated under the nominal total fuel flow rate and the respective optimized valve distribution was subjected to two deterministic step changes in the total fuel flow rate. The corresponding evolution of the mole fractions of hydrogen and unreacted steam in the synthesis gas, the OTWTs at a fixed distance of 6.5 m away from the reformer ceiling and the maximum OTWTs across the reforming tube length of a few selected reforming tubes was analyzed, based on which positive step changes in the total fuel flow rate to achieve the optimized firing rate in the reformer were deemed appropriate. It is important to note that the transient simulations of the reformer CFD model were only computationally feasible with the use of 7 private-access high performance compute nodes with the total processing power of 128 cores and system memory of 1640 GB on the Hoffman2 computing cluster.

Then, the furnace-balancing framework, the statistical-based model for the OTWT distribution and the valve-to-flow rate converter developed in our previous work were integrated with the heuristic search algorithm to design the robust balancing procedure. In the balancing procedure, a series of computing tasks is executed to estimate the maximum value of the initial OTWT distribution based on information from the initial reformer input. This information and the user-defined maximum allowable OTWT are used to guide the aggressive search to identify the neighborhood of the optimal total fuel flow rate and, subsequently, the conservative search to identify the optimized value of the optimal total fuel flow rate such that the operational specifications are satisfied. The optimized total fuel flow rate and the corresponding optimized valve distribution were used to

adjust the boundary conditions of the reformer CFD model, and the results demonstrated that the optimized total fuel flow rate could be increased from 98.133 to 136.896 kg sec⁻¹ in a step change fashion without accelerating the degradation of the microstructure of the reforming tube wall.

Chapter 6

Conclusions

This dissertation developed a systematic framework for creating and simulating a computational fluid dynamics (CFD) model for an industrial-scale steam methane reforming furnace at an SMR-based hydrogen plant. The reformer CFD model was used to improve our understanding of the physiochemical processes occurring in the tube side and furnace side during the endothermic conversion of methane, to assess impacts of varying the furnace-side feed (FSF) distribution on the inherent variability in the outer tube wall temperature (OTWT) at a fixed height, and to study a reformer dynamic response to step change inputs of the total FSF flow rate. Additionally, this dissertation also details a framework and practical considerations for developing a real-time furnace balancing scheme including plant-model mismatch in the estimation of the OTWT distribution, uncertainty in model selection for the OTWT distribution, and uncertainty in estimating the maximum OTWT across the reforming tube length among all reforming tubes. Finally, the furnace balancing scheme was used to improve the reformer thermal efficiency by increasing the total FSF flow rate while keeping the reformer in a safe operating regime and maintaining the expected service life of the reformer.

In Chapter 2, a CFD model for a steam methane reformer was developed within ANSYS Fluent framework, and in particular, the source terms that are integrated into the standard convective-diffusive transport equations of momentum, energy and material to enable a commercial CFD

solver to simulate the physiochemical processes in the tube side and the furnace side as well as their thermal interactions during the catalytic conversion of methane to hydrogen were explained. Specifically, the lean combustion of the furnace-side feed, i.e., the source terms in the material transport equations, was modeled by the finite rate/eddy dissipation turbulence-chemistry interaction model and the global reaction schemes with the premixed combustion assumption. Additionally, thermal radiative heat transfer rate between the interior combustion chamber, the outer reforming tube wall and the furnace-side flow, i.e., the source term in the energy transport equation, was modeled by the discrete ordinate method, and the absorption coefficient of the furnace-side flow was modeled by an empirical correlation for estimating the radiative properties of a homogeneous gas flow, Kirchhoff's law, and Lambert Beer's law. Furthermore, the effects of turbulence on the furnace-side transport variables was simulated by the standard $k - \epsilon$ turbulence model with ANSYS enhanced wall treatment function. In the tube side, the catalytic bed of the reforming reactor, i.e., the source term in the momentum transport equation, was modeled by the continuum approach with ANSYS porous zone function, the effectiveness factor and catalyst packing factor, and SMR, i.e., the source terms in the material transport equations, was modeled by the global reaction scheme. Additionally, the wall of the reforming reactor was modeled by ANSYS thin wall function, and the effects of turbulence on the tube-side transport variables was also simulated by the standard $k - \epsilon$ turbulence model with ANSYS enhanced wall treatment function. Subsequently, publicly available SMR-based plant data was used to derive equivalent boundary conditions of the reformer CFD model. The simulation results generated by the reformer CFD model with boundary conditions derived from available SMR-based plant data were shown to be consistent with phenomena observed in reformers and SMR-based industrial plant data, and the simulation results generated by the reformer CFD model with boundary conditions provided by our industry collaborator were shown to be in close agreement with the plant data recorded from the on-line industrial-scale reformer at the SMR-based plant. Therefore, the CFD model can be considered as an adequate representation of the reformer and as an effect tool that furthers our understanding of the inherent variability in the outer tube wall temperature distribution at a fixed height and allows

cost-effective operating conditions to be explored.

In Chapter 3, a furnace-balancing scheme that optimizes the valve distribution at the nominal total FSF flow rate to minimize the inherent nonuniformity in the OTWT distribution such that the reformer thermal efficiency can be increased while maintaining the expected service life of the reformer was developed. The CFD data showed when the reformer CFD model implemented with the optimized valve distribution predicted by the furnace-balancing scheme, the variability in the OTWT distributions in the high temperature region and the maximum OTWT along the reforming tube length among all reforming tubes were reduced compared to the baseline case in which the reformer CFD model implemented with a uniform FSF distribution. In addition, the CFD data also showed that when the flow control valve system of the reformer was defective, which prevented the pre-optimized valve distribution from being implemented, the furnace-balancing scheme was able to find an alternative input that also reduced the variability in the OTWT distributions as well as the maximum OTWT. This result confirmed that it is possible to improve the reformer thermal efficiency and increase the throughput of the SMR-base plant by optimizing the reformer input.

In Chapter 4, a statistical-based model identification that can be used to derive a data-driven model for the OTWT distribution as a function of the FSF distribution, total FSF flow rate and interactions among neighboring reforming tubes was developed. Specifically, Bayesian variable selection, Bayesian model averaging, the BIC approximation, sparse nonlinear regression and theories of thermal radiation were used to develop the prediction step algorithm, which was used to derive the prediction model such that the OTWT distribution can be estimated from the reformer input. In addition, ordinary Kriging was used to develop the correction step algorithm, which was used to derive the correction model such that the OTWT distribution can be estimated from the interaction among the reforming tubes. Subsequently, the prediction and correction models were used to formulate the data-driven model to estimate the OTWT distribution from the reformer input while accounting for the interaction among neighboring reforming tubes. The results from the re-substitution and forecasting tests showed that the data-driven model for the OTWT distribution has a high goodness of fit and a high predictability, which demonstrated the robustness of the proposed

model identification.

In Chapter 5, a real-time furnace-balancing scheme that simultaneously maximizes total FSF flow rate and identifies the corresponding optimized valve distribution in real-time such that the reformer thermal efficiency is maximized within the physical limitation of the reforming tube wall material was developed. To this end, insights and developments from Chapters 3 and 4 including the framework for the furnace-balancing scheme, the statistical-based model identification and the valve-to-flow-rate converter were integrated with a heuristic search algorithm to create a real-time balancing procedure. Specifically, the balancing procedure evaluates the initial variability in the OTWT distribution by using the respective reformer input and the data-driven model for the OTWT distribution, based on which it establishes the starting direction of the heuristic search algorithm that identifies the maximized total FSF flow rate and the corresponding valve distribution to improve the reformer thermal efficiency while maintaining the expected service life of the reformer. Subsequently, the reformer CFD model developed in Chapter 2 was used to characterize the reformer response to step change inputs of the reformer input such that an optimal strategy to implement the maximized total FSF flow rate can be implemented without jeopardizing the expected service life of the reformer. Additionally, the reformer CFD model was also used to demonstrate that the optimized reformer input predicted by the real-time balancing procedure was more optimal than the nominal reformer input in the sense that the total FSF flow rate and the average hydrogen mole fraction of the reformer effluent stream were increased by $\sim 40\%$ and $\sim 4\%$, respectively, while the maximum OTWT across the reforming tube length among all reforming tubes was kept below the design temperature of the tube wall material.

In summary, this dissertation has provided a systematic framework for creating and simulating a CFD model for an industrial-scale reformer at an SMR-based hydrogen plant and, subsequently, a framework for designing and evaluating a real-time furnace balancing scheme such that the reformer thermal efficiency, measured by means of the average hydrogen composition of the reformer effluent stream, can be improved by increasing the total FSF flow rate without compromising the expected service life of the reformer in the presence of the inherent variability in the OTWT distri-

butions along the reforming tube length. The results documented in this dissertation are expected to allow the SMR-based hydrogen plant to be operated at a higher plant efficiency and achieve a substantial economic benefit by reducing operational costs.

Bibliography

- [1] A. Aguirre, A. Tran, L. Lao, H. Durand, M. Crose, and P. D. Christofides. CFD modeling of a pilot-scale steam methane reforming furnace. In *Advances in Energy Systems Engineering*, pages 75–117. 2017.
- [2] A. Alvino, D. Lega, F. Giacobbe, V. Mazzocchi, and A. Rinaldi. Damage characterization in two reformer heater tubes after nearly 10 years of service at different operative and maintenance conditions. *Engineering Failure Analysis*, 17:1526–1541, 2010.
- [3] ANSYS Inc. *ANSYS Fluent Theory Guide 15.0*. 2013.
- [4] M. Balat. Potential importance of hydrogen as a future solution to environmental and transportation problems. *International journal of hydrogen energy*, 33:4013–4029, 2008.
- [5] S. P. M. Bane, J. L. Ziegler, and J. E. Shepherd. Development of one-step chemistry models for flame and ignition simulations. Technical report, GALCIT Report GALCITFM:2010.002, 2010.
- [6] L. Barreto, A. Makihiro, and K. Riahi. The hydrogen economy in the 21st century: a sustainable development scenario. *International Journal of Hydrogen Energy*, 28:267–284, 2003.
- [7] M. Batdorf, L. A Freitag, and C. Ollivier-Gooch. Computational study of the effect of unstructured mesh quality on solution efficiency. In *Proceedings of the 13th AIAA Computational Fluid Dynamics Conference*, Snowmass, CO, 1997.

- [8] R. A. Bilonick. Risk qualified maps of hydrogen ion concentration for the new york state area for 1966–1978. *Atmospheric Environment*, 17:2513–2524, 1983.
- [9] S. L. Brunton, J. L. Proctor, and J. N. Kutz. Discovering governing equations from data by sparse identification of nonlinear dynamical systems. *Proceedings of the National Academy of Sciences*, 113:3932–3937, 2016.
- [10] N. Cressie. Fitting variogram models by weighted least squares. *Journal of the International Association for Mathematical Geology*, 17:563–586, 1985.
- [11] M. Crose, J. S. Kwon, A. Tran, and P. D. Christofides. Multiscale modeling and run-to-run control of PECVD of thin film solar cells. *Renewable Energy*, 100:129–140, 2017.
- [12] H. I. de Lasa, G. Dogü, and A. Ravella, editors. *Chemical Reactor Technology for Environmentally Safe Reactors and Products*, volume 225 of *NATO ASI Series*. Springer Science & Business Media, Dordrecht, The Netherlands, 1992.
- [13] A. L. Dean, B. M. Kimberley, A. P. Brant, and M. R. Troy. Mathematical modeling of an industrial steam-methane reformer for on-line deployment. *Fuel Processing Technology*, 92:1574–1586, 2011.
- [14] Y. Ding and E. Alpay. Adsorption-enhanced steam–methane reforming. *Chemical Engineering Science*, 55:3929–3940, 2000.
- [15] R. Duan, W. Liu, L. Xu, Y. Huang, X. Shen, C. Lin, J. Liu, Q. Chen, and B. Sasanapuri. Mesh type and number for the CFD simulations of air distribution in an aircraft cabin. *Numerical Heat Transfer, Part B: Fundamentals*, 67:489–506, 2015.
- [16] I. Dybkjaer. Tubular reforming and autothermal reforming of natural gas—an overview of available processes. *Fuel Processing Technology*, 42:85–107, 1995.
- [17] S. Ergun and A. A. Orning. Fluid flow through randomly packed columns and fluidized beds. *Industrial & Engineering Chemistry*, 41:1179–1184, 1949.

- [18] B. C. R. Ewan and R. W. K. Allen. A figure of merit assessment of the routes to hydrogen. *International Journal of Hydrogen Energy*, 30:809–819, 2005.
- [19] P. Ferreira-Aparicio, M. J. Benito, and J. L. Sanz. New trends in reforming technologies: from hydrogen industrial plants to multifuel microreformers. *Catalysis Reviews*, 47:491–588, 2005.
- [20] T. M. Fragoso, W. Bertoli, and F. Louzada. Bayesian model averaging: A systematic review and conceptual classification. *International Statistical Review*, 86:1–28, 2018.
- [21] G. F. Froment and K. B. Bischoff. *Chemical Reactor Analysis and Design*. Wiley, New York, 1990.
- [22] J. Gong, S. Tu, and K. Yoon. Damage assessment and maintenance strategy of hydrogen reformer furnace tubes. *Engineering Failure Analysis*, 6:143–153, 1999.
- [23] K. Guan, H. Xu, and Z. Wang. Analysis of failed ethylene cracking tubes. *Engineering Failure Analysis*, 12:420–431, 2005.
- [24] R. B. Gupta. *Hydrogen fuel: production, transport, and storage*. CRC Press, 2008.
- [25] J. A. Hoeting, D. Madigan, A. E. Raftery, and T. Volinsky. Bayesian model averaging: a tutorial. *Statistical Science*, 14:382–401, 1999.
- [26] M. R. Holdaway. Spatial modeling and interpolation of monthly temperature using kriging. *Climate Research*, 6:215–225, 1996.
- [27] Hydrogen Production Expert Panel. Report of the hydrogen production expert panel: A subcommittee of the hydrogen & fuel cell technical advisory committee. Technical report, United States Department of Energy, 2013.
- [28] H. Jeffreys. Some tests of significance, treated by the theory of probability. *Mathematical Proceedings of the Cambridge Philosophical Society*, 31:203–222, 1935.

- [29] W. P. Jones and B. E. Launder. The prediction of laminarization with a two-equation model of turbulence. *International Journal of Heat and Mass Transfer*, 15:301–314, 1972.
- [30] R. E. Kass and A. E. Raftery. Bayes factors. *Journal of the American Statistical Association*, 90:773–795, 1995.
- [31] A. Kumar, M. Baldea, and T. F. Edgar. Real-time optimization of an industrial steam-methane reformer under distributed sensing. *Control Engineering Practice*, 54:140–153, 2016.
- [32] A. Kumar, M. Baldea, T. F. Edgar, and O. A. Ezekoye. Smart manufacturing approach for efficient operation of industrial steam-methane reformers. *Industrial & Engineering Chemistry Research*, 54:4360–4370, 2015.
- [33] M. Kuroki, S. Ookawara, and K. Ogawa. A high-fidelity CFD model of methane steam reforming in a packed bed reactor. *Journal of Chemical Engineering of Japan*, 42:S73–S78, 2009.
- [34] L. Lao, A. Aguirre, A. Tran, Z. Wu, H. Durand, and P. D. Christofides. CFD modeling and control of a steam methane reforming reactor. *Chemical Engineering Science*, 148:78–92, 2016.
- [35] D. Latham. *Masters Thesis: Mathematical Modeling of An Industrial Steam Methane Reformer*. Queen’s University, 2008.
- [36] B. E. Launder and B. I. Sharma. Application of the energy dissipation model of turbulence to the calculation of flow near a spinning disc. *Letters in Heat and Mass Transfer*, 1:131–137, 1974.
- [37] R. G. Lemus and J. M. M. Duart. Updated hydrogen production costs and parities for conventional and renewable technologies. *International Journal of Hydrogen Energy*, 35:3929–3936, 2010.

- [38] Y. Luan, Y. Chyou, and T. Wang. Numerical analysis of gasification performance via finite-rate model in a cross-type two-stage gasifier. *International Journal of Heat and Mass Transfer*, 57:558–566, 2013.
- [39] D. Madigan and A. E. Raftery. Model selection and accounting for model uncertainty in graphical models using Occam’s window. *Journal of the American Statistical Association*, 89:1535–1546, 1994.
- [40] D. Madigan, A. E. Raftery, J. C. York, J. M. Bradshaw, and R. G. Almond. Strategies for graphical model selection. In *Selecting Models from Data*, pages 91–100. 1994.
- [41] B. F. Magnussen. The eddy dissipation concept: A bridge between science and technology. In *ECCOMAS Thematic Conference on Computational Combustion*, Lisbon, Portugal, 2005.
- [42] B. F. Magnussen and B. H. Hjertager. On mathematical modeling of turbulent combustion with special emphasis on soot formation and combustion. In *Symposium (International) on Combustion*, pages 719–729, 1977.
- [43] A. Maximov. *Thesis for the Degree of Doctor of Science: Theoretical Analysis and Numerical Simulation of Spectral Radiative Properties of Combustion Gases in Oxy/air-fired Combustion Systems*. Lappeenranta University of Technology, 2012.
- [44] S. C. Mishra and M. Prasad. Radiative heat transfer in participating media—A review. *Sadhana*, 23:213–232, 1998.
- [45] E. M. A. Mokheimer, M. I. Hussain, S. Ahmed, M. A. Habib, and A. A. Al-Qutub. On the modeling of steam methane reforming. *Journal of Energy Resources Technology*, page 012001, 2015.
- [46] D. G. Nicol. *Ph. D. Thesis: A Chemical Kinetic and Numerical Study of NO_x and Pollutant Formation in Low-emission Combustion*. University of Washington, 1995.

- [47] A. Olivieri and F. Vegliò. Process simulation of natural gas steam reforming: Fuel distribution optimisation in the furnace. *Fuel Processing Technology*, 89:622–632, 2008.
- [48] A. J. M. Oprins and G. J. Heynderickx. Calculation of three-dimensional flow and pressure fields in cracking furnaces. *Chemical Engineering Science*, 58:4883–4893, 2003.
- [49] G. Pantoleontos, E. S. Kikkinides, and M. C. Georgiadis. A heterogeneous dynamic model for the simulation and optimisation of the steam methane reforming reactor. *International Journal of Hydrogen Energy*, 37:16346–16358, 2012.
- [50] X. D. Peng. Analysis of the thermal efficiency limit of the steam methane reforming process. *Industrial & Engineering Chemistry Research*, 51:16385–16392, 2012.
- [51] A. E. Raftery, D. Madigan, and C. T. Volinsky. Accounting for model uncertainty in survival analysis improves predictive performance. *Bayesian Statistics*, 5:323–349, 1996.
- [52] J. R. Rostrup-Nielsen. *Catalysis: Science and Technology*. Springer-Verlag, Berlin, Germany, 1984.
- [53] J. R. Rostrup-Nielsen and T. Rostrup-Nielsen. Large-scale hydrogen production. *Cattech*, 6:150–159, 2002.
- [54] Y. Seo, D. Seo, Y. Seo, and W. Yoon. Investigation of the characteristics of a compact steam reformer integrated with a water-gas shift reactor. *Journal of Power Sources*, 161:1208–1216, 2006.
- [55] A. P. Simpson and A. E. Lutz. Exergy analysis of hydrogen production via steam methane reforming. *International Journal of Hydrogen Energy*, 32:4811–4820, 2007.
- [56] A. Tran, A. Aguirre, M. Crose, H. Durand, and P. D. Christofides. Temperature balancing in steam methane reforming furnace via an integrated CFD/data-based optimization approach. *Computers & Chemical Engineering*, 104:185–200, 2017.

- [57] A. Tran, A. Aguirre, H. Durand, M. Crose, and P. D. Christofides. CFD modeling of a industrial-scale steam methane reforming furnace. *Chemical Engineering Science*, 171:576–598, 2017.
- [58] A. Tran, M. Pont, A. Aguirre, H. Durand, M. Crose, and P. D. Christofides. Bayesian model averaging for estimating the spatial temperature distribution in a steam methane reforming furnace. *Chemical Engineering Research and Design*, 131:441–463, 2018.
- [59] S. R. Turns. *An Introduction to Combustion: Concepts and Applications*. McGraw-Hill, Boston, MA, 1996.
- [60] R. Vuthaluru and H.B. Vuthaluru. Modelling of a wall fired furnace for different operating conditions using FLUENT. *Fuel Processing Technology*, 87:633–639, 2006.
- [61] A. Wächter and L. T. Biegler. On the implementation of an interior-point filter line-search algorithm for large-scale nonlinear programming. *Mathematical Programming*, 106:25–57, 2006.
- [62] M. H. Wesenberg and H. F. Svendsen. Mass and heat transfer limitations in a heterogeneous model of a gas-heated steam reformer. *Industrial & Engineering Chemistry Research*, 46:667–676, 2007.
- [63] Z. T. Wilson and N. V. Sahinidis. The ALAMO approach to machine learning. *Computers & Chemical Engineering*, 106:785–795, 2017.
- [64] J. Xu and G. F. Froment. Methane steam reforming, methanation and water-gas shift: I. intrinsic kinetics. *AIChE Journal*, 35:88–96, 1989.
- [65] D. Zheng, B. Wu, J. Fleitz, R. Trajkovski, and C. Q. Zhou. CFD simulation of a hydrogen reformer furnace. In *Proceedings of the 14th International Heat Transfer Conference*, pages 233–244. American Society of Mechanical Engineers, 2010.